Hydrogen Adsorption on Selected Metal Organic Frameworks

A
Thesis
Submitted in
Partial fulfillment of the
Requirements for the Degree of

DOCTOR OF PHILOSOPHY

By

DEBJYOTI SAHU

Centre for Energy
Indian Institute of Technology Guwahati
Guwahati – 781039, Assam, India

July 2014

Dedicated
To
My
Parents
&
Family

Certificate

It is certified that the work contained in the thesis entitled "**HYDROGEN ADSORPTION ON SELECTED METAL ORGANIC FRAMEWORKS"**, by **DEBJYOTI SAHU** (Roll No. 09615108), has been carried out under our supervision and that this work has not been submitted elsewhere for a degree.

Date:

Dr. Sasidhar Gumma

Associate Professor
Department of Chemical Engineering &
Center for Energy

Dr. Anil Verma

Associate Professor
Department of Chemical Engineering &
Center for Energy

Acknowledgement

At the end of this journey I would like to thank all people without whom this work would not be done. First, I would like to thank my supervisors Dr. Sasidhar Gumma and Dr. Anil Verma for their immense guidance during the PhD work. Many hours of scientific discussions that I had with them are priceless, and they made a huge impact on this work.

I would like to express my gratitude to my 'Doctoral Committee' members, Prof. Gopal Das, Dr. Biplab Mondal and Dr. Chandramohan Somayaji for their helpful advices.

I am also thankful to Centre for Scientific and Industrial Research, New Delhi, India for financial support through project grant 01(2522)/11/EMR-II.

I am thankful to Dr. C. V. Sastri, Department of Chemistry, IIT Guwahati for his helpful advice and there are no words which can help to express my deepest gratitude!

I would like to thank all employees at Department of Chemical Engineering, Central Instruments Facility (CIF), Centre for Nanotechnology, Dr. Ajay Kalamdhad from Department of Civil Engineering and Prof. P. K. Giri from Department of Physics for the instrumentation and other facilities.

I am thankful to Prof. Pranab Goswami, Head, Centre for Energy, IIT Guwahati, former Head, Prof. A. K. Ghoshal and all the staff members of the center for their support throughout my stay at IITG campus.

I am grateful to my valued colleagues Prashant Mishra, Abhik Bhattacharjee, Satyannarayana Edubilli, Nitun Das, Amrita Difusa, Pruthviraj Medikonda, Mudit Baurai, Pradip Das, Roopak Kishore, Shravanthi L. and all other friends from IIT Guwahati for their relentless effort in completing this work.

I acknowledge the help and advice of my friends Pratyush Chakraborty from University of Florida, Gainesvile, FL, USA, Dr. Supriyo Roy from Indian Institute of Science, Bangalore and Dr. Avijit Ghosh from Haldia Institute of Technology. Their love and support mean a lot to me.

I am also thankful to Mata Amritanandamayee Math, Amritpuri and School of Engineering, Bangalore, Amrita Vishwa Vidyapeetham, for their love and respect for my work.

Debjyoti Sahu

Guwahati, India

Abstract

One of the major challenges for a hydrogen based economy is in the design of an efficient system for storing hydrogen. The most common method to store hydrogen in gaseous form is in steel tanks, although lightweight composite tanks designed to endure higher pressures are also becoming popular. Adsorption based storage system is widely being explored for a hydrogen storage vessel filled with a suitable solid adsorbent that can achieve a higher energy density (as opposed to that of a vessel with no adsorbent) at the same temperature and pressure conditions. The US DoE hydrogen storage target, 2017 for an adsorption based system is about 5.5 wt% (and 40 g L^{-1} volumetric storage capacity) at 233- 333 K with a maximum delivery pressure of 5-12 bar. Since adsorption is primarily a material driven technology a large volume of research today focuses on development and understanding of hydrogen adsorption on a variety of adsorbents. In the present work, metal organic frameworks which are a class of porous materials are evaluated for their hydrogen adsorption characteristics over a wide range of temperature and pressure. In addition, attempt will be made to understand the effect of metal (Li/Pd/Pt) doping on the hydrogen adsorption characteristics on these structures.

Hydrogen adsorption measurements have been performed for a wide range of temperature (90 -298 K) and pressure on selected adsorbents (viz. Cu-BTC, Cr-BDC, MOF-205, Mg-DOBDC, Ni-DABCO, Zn-BDC, Co-DOBDC and a mesoporous silica material i.e. MCM-41). The choice of MOFs was governed by a wide variation in their surface characteristics. While pore volume is necessary for reaching high hydrogen storage capacities at saturation, at intermediate conditions (pressure/uptake capacities) DOBDC MOFs which have unsaturated metal sites exhibit better gravimetric uptake capacities for hydrogen.

The hybrid porous materials like MOFs can be modified by doping them suitably to enhance their hydrogen adsorption capacities. At ~90 K (50 bar) MOF-205 is found to adsorb near to 5.8 wt% (excess) H_2. At similar conditions, the saturation capacities for Cu-BTC and Cr-BDC MOFs were about 3.39 and 3.9 wt%. Cu-BTC/Li and Cr-BDC/Li, the Li doped sample of respective MOFs exhibit an improvement in the pore volume and hydrogen uptake (4.27 and 6.02 wt% respectively). It is significant to note that after the Li doping, saturation uptake on Cr-BDC is close to large pore volume and surface area containing MOF like MOF-205 (which has larger organic linkers). To the best of our knowledge, the surface area and pore volume are best reported till date for Cu-BTC and Cr-BDC based adsorbents. The saturation hydrogen uptake capacity of Cu-BTC/Li also exceeds all other Cu-BTC based adsorbents, while that of Cr-BDC/Li matches with an earlier report in literature where an NH_4F wash was performed on as synthesized Cr-BDC sample.

Palladium supported graphene oxide (Pd-IGO) and platinum activated carbon (Pt-AC) are used to synthesize composites of Cu-BTC and Cr-BDC. Some of these composites exhibit enhanced hydrogen uptake; however, at high contents of Pd-IGO or Pt-AC in the composites, the uptake capacities decrease (more so in case of Cu-BTC composites which have smaller pore volume). An additional doping of Li onto the Pt-AC or Pd-IGO composites of Cu-BTC and Cr-BDC, improves their hydrogen uptake capacity. Nevertheless, the gravimetric uptake capacities of all the composites are lower than that Li doped Cu-BTC and Cr-BDC samples. In contrast, the enhancement in adsorption enthalpies of MOF composites was better than that of Li doped Cu-BTC or Cr-BDC, especially at high contents of Pd-IGO and Pt-AC in the composites.

CONTENTS

CHAPTER 1 – Introduction

		Page No
1.1	Background on Hydrogen Energy	1
1.2	Conventional Storage System	2
1.3	Adsorption Based Storage System	3
1.4	Research Objectives	4

CHAPTER 2 – Literature Survey

2.1.	Hydrogen Adsorption on a Solid Surface	9
2.2.	Hydrogen Adsorption on Porous Materials	12
	2.2.1 Zeolites	12
	2.2.2 Allotropes of Carbon	14
	2.2.3 Mesoporous Silica Materials	15
	2.2.4 Metal Organic Frameworks (MOFs)	16
2.3.	Strategies of Enhanced Hydrogen Uptake on MOFs	17
	2.3.1. MOFs with Open Metal Sites	17
	2.3.2. Catenation of MOFs	20
	2.3.3 Large Pore MOFs	21
	2.3.4 Alkali Metal Doping in MOFs	25
	2.3.5. Heavy Metal Impregnation in MOFs	29
	2.3.6. MOF Composites	32
	2.3.7. Heavy Metal Doped MOF Composites	33

2.4 Summary 35

CHAPTER 3 – Experimental Methods

3.1 Characterization Techniques 47

3.1.1 Transmission Electron Microscopy 47

3.1.2 Field Emission Scanning Electron Microscopy 48

3.1.3 Thermogravimetric Analysis 49

3.1.4 X-ray Diffraction Analysis 50

3.1.5 Atomic Absorption Spectroscopy 51

3.1.6 Flame Photometry 51

3.1.7 Nitrogen Adsorption Studies 52

3.2 Gravimetric Adsorption Measurements 55

3.3 Definition of Adsorbed Amount (Uptake Capacity) 56

3.3.1 Absolute Adsorption 57

3.3.2 Excess Adsorption 57

3.3.3 Net Adsorption 57

3.3.4 Determination of Buoyancy Volume for Various Reference States 58

3.4 Isotherm Modeling 60

3.5 Estimation of Volume of Adsorptive Hydrogen Storage Vessel 62

3.6. Estimation of Bulk Gas Density 63

3.7. Details of Experimental System used for Gas Adsorption Measurements 64

3.8. Experimental Protocol 66

3.8.1 Sample Activation 66

3.8.2 Helium Buoyancy Measurement 67

3.8.3 Hydrogen Isotherm Measurement 68

3.8.4 Sample Regeneration 68

3.8.5 Isothermal Bath 69

3.9. Experimental Conditions 69

3.10 Hydrogen Uptake on Palladium Nanoparticles 70

3.10.1 Synthesis of Palladium Nanoparticles 71

3.10.2 Material Characterization 72

3.10.3 Pressure Composition Isotherm 73

3.11 Summary 76

CHAPTER 4 – Hydrogen Adsorption on Selected Metal Organic Frameworks

4.1 Background 89

4.2 Structures of Adsorbents Studied 91

4.2.1 Zn-BDC 91

4.2.2 Ni-DABCO 91

4.2.3 MOF-205 92

4.2.4 Cu-BTC 92

4.2.5 Cr-BDC 93

4.2.6 Mg-DOBDC and Co-DOBDC 94

4.3 Material Synthesis 94

4.3.1 Synthesis of MCM 41 94

4.3.2 Synthesis of Zn-BDC 94

4.3.3 Synthesis of Ni-DABCO 95

4.3.4 Synthesis of MOF-205 95

4.3.5 Synthesis of Cu-BTC 97

4.3.6 Synthesis of Cr-BDC 97

4.3.7 Synthesis of Mg-DOBDC 98

4.3.8 Synthesis of Co-DOBDC 98

4.4. Characterization of Adsorbents 99

4.4.1 Thermogravimetric Analysis 99

4.4.2 XRD Analysis 101

4.4.3 Surface Area and Pore volume Analysis 102

4.5 Excess Adsorption Isotherms 103

4.5.1 Hydrogen Uptake on Various Adsorbents 103

4.5.2 Henry's Constant 106

4.5.3 Enthalpy of Adsorption 107

4.6 Net Adsorption 108

4.7 Volume of Adsorptive Hydrogen Storage Vessel 110

4.8 Summary 111

Chapter 5 – Effect of Lithium Doping of MOFs on their Hydrogen Adsorption Characteristics

5.1 Background 135

5.2 Material Synthesis 136

5.3 Material Characterization 136

5.3.1 Elemental Analysis 136

5.3.2 TGA Analysis 137

5.3.3 XRD Analysis 139

5.3.4 IR Analysis 139

5.3.5 Surface Area and Pore Volume 140

5.4 Hydrogen Adsorption Measurements 141

5.4.1 Excess Adsorption Isotherm 141

5.4.2 Net Adsorption 145

5.5 Summary 146

CHAPTER 6 – Effect of Heavy Metal Doping on Hydrogen Adsorption in Selected Metal Organic Frameworks

6.1 Background 159

6.2 Material Synthesis 161

6.2.1 Graphene Oxide 161

6.2.2 Improved Graphene Oxide 162

6.2.3 Palladium Supported Graphene Oxide and Palladium Supported Improved Graphene Oxide 162

6.2.4 Composites of Cu-BTC 163

6.2.5 Cr-BDC Composites 164

6.2.6 MOF-205/Pt-AC Composite 166

6.2.7 Doping of Li into the MOF Composites 166

6.3 Material Characterization 167

6.3.1 TEM Imaging 167

6.3.2 AAS Analysis 167

6.3.3 XRD Analysis 168

6.3.2 Specific Surface Area and Pore Volume of MOF Composites 169

6.4 Hydrogen Adsorption on MOF Composites 172

6.4.1 Isotherms on MOF-205 Composite 172

6.4.2 Hydrogen Adsorption on Cu-BTC/Pt-AC and Cu-BTC/AC Composites 173

6.4.3 Hydrogen Adsorption on Cu-BTC/IGO Cu-BTC/Pd-GO and Cu-BTC/Pd-IGO Composites 176

6.4.4 Hydrogen Adsorption on Cr-BDC/IGO, Cr-BDC/Pt-AC and Cr-BDC/Pd-IGO Composites 179

6.4.5 Correlation between Pore Volume and Maximum Hydrogen Uptake Capacity 182

6.5 Summary 182

CHAPTER 7 – Conclusions and Future Scope

7.1 Conclusions 213

7.2 Future Scope 219

REFERENCES

List of Abbreviations

DOE –Department of energy

ACs – Activated carbons

Pt/AC – Platinum catalyst supported on activated carbon

ENG – Expanded natural graphite

GO – Graphene oxide

CNTs –Carbon nanotubes

SWCNTs – Single-walled carbon nanotubes

MOFs – Metal-organic frameworks

IRMOFs – Isoreticular metal-organic frameworks

FCC-Face centered cubic

BCC –Body-centered cubic

BET – Brunauer-Emmett-Teller

BJH – Barrett, Joyner, and Halenda

DFT – Density functional theory

DMF –N, N'-dimethylformamide

DSC – Differential scanning calorimetry

DTA – Differential thermal analysis

DTG- Derivative thermogram

FCC – Face-centered cubic

PCI – Pressure composition isotherm

GCMC – Grand canonical Monte Carlo

BTB –Benzene tribenzoate

BDC-Benzene dicaroxylate

BTC-Benzene tricarboxylate

HCl – Hydrochloric acid

HF- Hydrofluoric acid

HPLC – High-performance liquid chromatography

IR – Infrared

MIL- Materials Institute Lavoisier

HKUST- Hong Kong University of Science and Technology

IUPAC – International union of pure and applied chemistry

RT – Room temperature

FESEM – Field emission scanning electron microscopy

TEM – Transmission electron microscopy

TGA – Thermo-gravimetric analysis

XRD – X-ray diffraction

1D/3D – 1 dimensional/3 dimensional

Nomenclature

λ = radiation wavelength (Å)

d= distance between two successive crystallographic planes (Å)

M= Molecular weight (g mol^{-1})

n_p = Micropore volume (cc g^{-1})

P/P_0 = Relative pressure

M_{ads} = Gibbs' excess amount adsorbed (g)

M_0 = Mass of sample and bucket (g)

M_t = Mass of sample and bucket after adsorption/ desorption (g)

V_s = Impenetrable solid volume (cc)

$V_{buoyancy}$ = Buoyancy volume (cc)

V_{bucket} = Bucket volume (cc)

V_M = Molar volume (cc)

W = Gas adsorbed (wt%)

W_{max} = Saturation loading/ uptake capacity (wt%)

N = Gas adsorbed (mol kg^{-1})

β = Henry's constant (mol kg bar^{-1})

ΔH_{ads} = Enthalpy of adsorption (kJ mol^{-1})

R = Universal gas constant (8.314 J mol^{-1} K^{-1})

Q_{st} = Isosteric heat (kJ mol^{-1})

V_{empty_tank} = Tank volume without adsorbent (L)

N_{net} = Net amount adsorbed (mol kg^{-1})

ρ_{solid} = Bulk density of the solid (kg L^{-1})

ρ_{gas} = Gas molar density (g cc^{-1})

List of Figures

Figure 2.1: A Generic reaction Equation for the Reversible Hydrogenation and Dehydrogenation

Figure 2.2: A Typical Pressure Composition Isotherm plot

Figure 2.3: Schematic Diagrams Depicting Framework Structures of two Common Zeolites Types

Figure 2.4: Schematic Diagrams Representing Graphene

Figure 3.1: Diffraction of Incident X-rays from the Family of Parallel Atomic Planes

Figure 3.2: Different type of N_2 Adsorption Isotherms

Figure 3.3: Gravimetric adsorption measurement setup

Figure 3.4: (a): Equilibrium between Adsorbate and Adsorbent; (b): Reference state for Absolute Adsorption; (c): Reference state for Excess Adsorption; (d): Reference state for net Adsorption Framework

Figure 3.5: The Schematic of Experimental Setup for Gas Adsorption Measurement

Figure 3.6: TEM image of Pd Nanoparticle Synthesized in 9 hours

Figure 3.7: FESEM image of Pd Nanoparticle Synthesized in 18 hours

Figure 3.8: Powder XRD Pattern of Palladium Nanoparticle; Intensity in Arbitrary Units Plotted Against 2θ

Figure 3.9: (a) TEM Image of Nanoparticles, (c) An Icosahedrons Particle Detected by HRTEM (c) SAED shows Diffraction from 5 Reflection Planes Surrounding the Core

Figure 3.10: Hydrogen Uptake on Palladium Nanoparticles at Low Pressure

Figure 3.11: Pressure composition isotherm on palladium nanoparticles compared to work reported in the literature

Figure 3.12: Hydrogen Uptake on Palladium Nanoparticles at High Pressure

Figure 4.1: Crystal Structure of Zn-BDC

Figure 4.2: Crystal Structure of Ni-DABCO MOF

Figure 4.3: Crystal structure of MOF-205

Figure 4.4: Crystal Structure for Cu-BTC MOF

Figure 4.5: View of the Structure of Cr-BDC

Figure 4.6: Crystal structure of (a) Mg-DOBDC, (b) Co-DOBDC

Figure 4.7: Thermograms of Adsorbents Studied

Figure 4.8: Powder XRD patterns of Adsorbents Studied

Figure 4.9: N_2 Adsorption Isotherms at 77 K for Various Adsorbents Studied

Figure 4.10: H_2 Adsorption Isotherms of MCM-41

Figure 4.11: H_2 Adsorption Isotherms of Zn-BDC

Figure 4.12: H_2 Adsorption Isotherms of Ni-DABCO

Figure 4.13: H_2 Adsorption Isotherms of MOF-205

Figure 4.14: H_2 Adsorption Isotherms of Cu-BTC

Figure 4.15: H_2 Adsorption Isotherms of Cr-BDC

Figure 4.16: H_2 Adsorption Isotherms of Co-DOBDC

Figure 4.17: H_2 Adsorption Isotherms of Mg-DOBDC

Figure 4.18: Variation of Henry's Constants with Temperature

Figure 4.19: Henry's Constant for H_2 Adsorption at Room Temperature for Studied MOFs and MCM-41

Figure 4.20: Enthalpy of Adsorption for H_2 at Zero Coverage for Studied MOFs and MCM-41

Figure 4.21: Variation of Hydrogen Saturation Uptake Capacity with Pore Volume for Adsorbents Studied

Figure 4.22: Net Adsorption Isotherms of MCM-41

Figure 4.23: Net Adsorption Isotherms of Zn-BDC

Figure 4.24: Net Adsorption Isotherms of Ni-DABCO

Figure 4.25: Net Adsorption Isotherms of MOF-205

Figure 4.26: Net Adsorption Isotherms of Cr-BDC

Figure 4.27: Net Adsorption Isotherms of Cu-BTC

Figure 4.28: Net Adsorption Isotherms of Co-DOBDC

Figure 4.29: Net Adsorption Isotherms of Mg-DOBDC

Figure 4.30: Tank Volume required to store 1 kg of H_2 with Different Adsorbents

Figure 4.31: Tank Volume required to store 1 kg of H_2 with MCM-41 as Adsorbent

Figure 4.32: Tank Volume required to store 1 kg of H_2 with Zn-BDC as Adsorbent

Figure 4.33: Tank Volume required to store 1 kg of H_2 with Ni-DABCO as Adsorbent

Figure 4.34: Tank Volume required to store 1 kg of H_2 with MOF-205 as Adsorbent

Figure 4.35: Tank Volume required to store 1 kg of H_2 with Cu-BTC as Adsorbent

Figure 4.36: Tank Volume required to store 1 kg of H_2 with Cr-BDC as Adsorbent

Figure 4.37: Tank Volume required to store 1 kg of H_2 with Mg-DOBDC as Adsorbent

Figure 4.38: Tank Volume required to store 1 kg of H_2 with Co-DOBDC as Adsorbent

Figure 5.1: Thermograms of Cu-BTC/Li and Cr-BDC/Li compared to Parent MOFs

Figure 5.2: X-ray Diffractogram of Cu-BTC/Li and Cr-BDC/Li compared to Parent MOFs

Figure 5.3: IR Patterns of (a) Cu-BTC and (b) Cr-BDC samples

Figure 5.4: N_2 Adsorption Isotherms at 77 K on Cu-BTC/Li and Cr-BDC/Li samples compared to Parent MOFs

Figure 5.5: H_2 Adsorption Isotherms of Cu-BTC/Li

Figure 5.7: Comparative Excess Adsorption Isotherms of (a) Cu-BTC at 297 K, (b) Cu-BTC at 101 K

Figure 5.8: Comparative Excess Adsorption Isotherms: (a): Cr-BDC at 297 K, (b) Cr-BDC at 92 K (c) Cr-BDC at 165 K

Figure 5.9: Variation of Saturation loading with Pore volume

Figure 5.10: Henry's constants for Cu-BTC/Li and Cr-BDC/Li Compared to Parent MOFs

Figure 5.11: Henry's constant at Room Temperature for Cu-BTC/Li and Cr-BDC/Li Compared to Parent MOFs

Figure 5.12: Enthalpy of Adsorption at Zero Coverage for Cu-BTC/Li and Cr-BDC/Li Compared to Parent MOFs

Figure 5.13: Net Adsorption Isotherms of Cu-BTC/Li

Figure 5.14: Net Adsorption Isotherms of Cr-BDC/Li

Figure 5.15: Volume of Vessel required to store 1 kg of H_2 at 100 bar using Cr-BDC/Li and Cr-BDC

Figure 6.1: TEM Image of Improved Graphene Oxide

Figure 6.2: TEM Image of Pd nanoparticles deposited on Improved Graphene Oxide

Figure 6.3: Powder XRD Pattern for Cu-BTC composites

Figure 6.4: Powder XRD Pattern for Cr-BDC composites

Figure 6.5: Powder XRD Pattern for MOF-205 Composite

Figure 6.6: N_2 Adsorption Isotherm at 77 K on Pt-AC, MOF-205 and MOF-205/2.3Pt-AC Composite

Figure 6.7: N_2 Adsorption Isotherm at 77 K on AC, Pt-AC, Cu-BTC and Cu-BTC/XPt-AC Composites

Figure 6.8: N_2 Adsorption Isotherm at 77 K on Cu-BTC and Cu-BTC/3.7Pd-GO, Cu-BTC/3.3IGO, Cu-BTC/XPd-IGO Composites

Figure 6.9: N_2 Adsorption Isotherm at 77 K on Cr-BDC, Cr-BDC/1.4IGO, Cr-BDC/1.9Pt-AC Composites

Figure 6.10: N_2 Adsorption Isotherm at 77 K on Cr-BDC and Cr-BDC/XPd-IGO Composites

Figure 6.11: N_2 Adsorption Isotherm at 77 K on Cu-BTC and Cu-BTC/XPt-AC/Li Composites

Figure 6.12: N_2 Adsorption Isotherm at 77 K on Cu-BTC, Cu-BTC/3.7Pd-GO/Li, Cu-BTC/XPd-IGO/Li Composites

Figure 6.13: N_2 Adsorption Isotherm at 77 K on Cr-BDC, Cr-BDC/1.9Pt-AC/Li Composite

Figure 6.14: N_2 Adsorption Isotherm at 77 K on Cr-BDC and Cr-BDC/XPd-IGO/Li Composites

Figure 6.15: Variation of Surface Area and Pore Volume with Doping for Cu-BTC/XPt-AC and Cu-BTC/XPt-AC/Li Composites

Figure 6.16: Variation of Surface Area and Pore Volume with Doping for Cu-BTC/XPd-IGO and Cu-BTC/XPd-IGO/Li Composites

Figure 6.17: Variation of Surface Area and Pore Volume with Doping for Cr-BDC/XPd-IGO and Cr-BDC/XPd-IGO/Li Composites

Figure 6.18: H_2 Adsorption Isotherms of MOF-205 (91 K, triangle), MOF-205/2.3Pt-AC (93 K, filled triangle)

Figure 6.19: H_2 Adsorption Isotherms of MOF-205(296 K, diamond), MOF-205/2.3Pt-AC (298 K, filled diamond)

Figure 6.20: H_2 Adsorption Isotherms of Cu-BTC (101 K, circle), Cu-BTC/1.2Pt-AC (91 K, open triangle), Cu-BTC/1.2AC (91 K, dash), Cu-BTC/1.2Pt-AC/Li (92 K, filled triangle)

Figure 6.21: H_2 Adsorption Isotherms of Cu-BTC (297 K, circle), Cu-BTC/1.2Pt-AC (297 K, triangle), Cu-BTC/1.2AC (296 K, dash), Cu-BTC/1.2Pt-AC/Li (297 K, filled triangle)

Figure 6.22: H_2 Adsorption Isotherms of Cu-BTC (101 K, circle), Cu-BTC/1.2Pt-AC (91 K, triangle), Cu-BTC/3.3Pt-AC (91 K, square), Cu-BTC/7.1Pt-AC (90 K, diamond), Cu-BTC/11Pt-AC (92 K, cross), Cu-BTC/31Pt-AC (101 K, dot)

Figure 6.23: H_2 Adsorption Isotherms of Cu-BTC (297 K, circle), Cu-BTC/1.2Pt-AC (297 K, triangle), Cu-BTC/3.3Pt-AC (296 K, square), Cu-BTC/7.1Pt-AC (296 K, diamond), Cu-BTC/11Pt-AC (296 K, cross), Cu-BTC/31Pt-AC (298 K, dot)

Figure 6.24: H_2 Adsorption Isotherms of Cu-BTC (101 K, circle), Cu-BTC/1.2Pt-AC/Li, (92 K, filled triangle), Cu-BTC/3.3Pt-AC/Li (100 K, filled square), Cu-BTC/7.1Pt-AC/Li (99 K, filled diamond), Cu-BTC/11Pt-AC/Li (99 K, star)

Figure 6.25: H_2 Adsorption Isotherms of Cu-BTC (297 K, circle), Cu-BTC/1.2Pt-AC/Li (297 K, filled triangle), Cu-BTC/3.3Pt-AC/Li (297 K, filled square), Cu-BTC/7.1Pt-AC/Li, (297 K, filled diamond), Cu-BTC/11Pt-AC/Li (297 K, star)

Figure 6.26: Variation of Henry's constants for Hydrogen Adsorption with Dope % for Cu-BTC/XPt-AC composites

Figure 6.27: Variation of Henry's constants for Hydrogen Adsorption with Dope % for Cu-BTC/XPt-AC/Li Composites

Figure 6.28: Variation of Adsorption Enthalpy for Hydrogen with Dope % for Cu-BTC/XPt-AC Composites

Figure 6.29: H_2 Adsorption Isotherms of Cu-BTC (101 K, circle), Cu-BTC/3.7Pd-GO (90 K, square), Cu-BTC/3.7Pd-/GO/Li (297 K, filled square), Cu-BTC/3.7Pd-IGO (106 K, triangle), Cu-BTC/3.7Pd-IGO/Li (97 K, filled triangle), Cu-BTC/3.3IGO (97 K, plus)

Figure 6.30: H_2 Adsorption Isotherms of Cu-BTC (297 K, circle), Cu-BTC/3.7Pd-GO (296 K, square), Cu-BTC/3.7Pd-/GO/Li (297 K, filled square), Cu-BTC/3.7Pd-IGO (297 K, triangle), Cu-BTC/3.7Pd-IGO/Li (298 K, filled triangle), Cu-BTC/3.3IGO (297 K, plus)

Figure 6.31: H_2 Adsorption Isotherms of Cu-BTC (101 K, circle), Cu-BTC/3.7Pd-IGO (106 K, triangle), Cu-BTC/8Pd-IGO (102 K, diamond), Cu-BTC/10Pd-IGO (113 K, cross), Cu-BTC/37Pd-IGO (91 K, dash)

Figure 6.32: H_2 Adsorption Isotherms of Cu-BTC (297 K, circle), Cu-BTC/3.7Pd-IGO (297 K, triangle), Cu-BTC/8Pd-IGO (295 K, diamond), Cu-BTC/10Pd-IGO (297 K, cross), Cu-BTC/37Pd-IGO (297 K, dash)

Figure 6.33: H_2 Adsorption Isotherms of Cu-BTC (101 K, circle), Cu-BTC/3.7Pd-IGO/Li (97 K, filled triangle), Cu-BTC/8Pd-IGO/Li (98 K, diamond), Cu-BTC/10Pd-IGO/Li (95 K, star)

Figure 6.34: H_2 Adsorption Isotherms of Cu-BTC (297 K, circle), Cu-BTC/3.7Pd-IGO/Li (298 K, filled triangle), Cu-BTC/8Pd-IGO/Li (296 K, diamond), Cu-BTC/10Pd-IGO/Li. (296 K, star)

Figure 6.35: Variation of Henry's Constants for Hydrogen Adsorption with Dope % for Cu-BTC/XPd-IGO Composites

Figure 6.36: Variation of Henry's Constants for Hydrogen Adsorption with Dope % for Cu-BTC/XPd-IGO/Li Composites

Figure 6.37: Variation of Adsorption Enthalpy for Hydrogen with Dope % for Cu-BTC/XPd-IGO Composites

Figure 6.38: H_2 Adsorption Isotherms Cr-BDC (92 K, circle), Cr-BDC/1.4IGO (90 K, cross), Cr-BDC/1.9Pt-AC (90 K, square), Cr-BDC/1.9Pt-AC/Li (91 K, filled square), Cr-BDC/1.9Pd-IGO (92 K, triangle), Cr-BDC/1.9Pd-IGO/Li (104 K, filled triangle)

Figure 6.39: H_2 Adsorption Isotherms Cr-BDC (297 K, circle), Cr-BDC/1.9Pt-AC (298 K, square), Cr-BDC/1.9Pt-AC/Li (298 K, filled square), Cr-BDC/1.9Pd-IGO (297 K, (triangle), Cr-BDC/1.9Pd-IGO/Li (298 K, filled triangle)

Figure 6.40: H_2 Adsorption Isotherms of Cr-BDC (92 K, circle), Cr-BDC/1.9Pd-IGO (92 K, triangle), Cr-BDC/4.6Pd-IGO (107 K, dash), Cr-BDC/6.4Pd-IGO (101 K, diamond), Cr-BDC/21Pd-IGO (95 K, cross)

Figure 6.41: H_2 Adsorption Isotherms of Cr-BDC (297 K, circle), Cr-BDC/1.9Pd-IGO (297 K, triangle), Cr-BDC/4.6Pd-IGO (297 K, dash), Cr-BDC/6.4Pd-IGO (296 K, diamond), Cr-BDC/21Pd-IGO (297 K, cross)

Figure 6.42: H_2 Adsorption Isotherms of Cr-BDC (92 K, circle), Cr-BDC/1.9Pd-IGO/Li (104 K, filled triangle), Cr-BDC/6.4Pd-IGO/Li (96 K, filled diamond), Cr-BDC/21Pd-IGO/Li (103 K, star)

Figure 6.43: H_2 Adsorption Isotherms of Cr-BDC (297 K, circle), Cr-BDC/1.9Pd-IGO/Li (298 K, filled triangle), Cr-BDC/6.4Pd-IGO/Li (296 K, filled diamond), Cr-BDC/21Pd-IGO/Li (295 K, star)

Figure 6.44: Variation of Henry's Constants for Hydrogen Adsorption with Dope % for Cr-BDC/XPd-IGO Composites

Figure 6.45: Variation of Henry's Constants for Hydrogen Adsorption with Dope % for Cr-BDC/XPd-IGO/Li Composites

Figure 6.46: Variation of Adsorption Enthalpy for Hydrogen with Dope % for Cr-BDC/XPd-IGO Composites

Figure 6.47: Variation of Saturation Loading of Hydrogen with Pore Volume for Various Adsorbents Considered.

List of Tables

Table 1.1: Hydrogen Storage Target for Adsorption Based Storage

Table 2.1: Hydrogen Uptake on Selected Zeolites, Allotropes of Carbon and Silica based Material

Table 2.2: Selected Organic Linkers as MOF Constructor

Table 2.3: Hydrogen Uptake on Selected MOFs

Table 2.4: Hydrogen Uptake Capacity of MOFs with Open Metal Sites

Table 2.5: Hydrogen Uptake on Large pore MOFs

Table 2.6: Hydrogen Uptake (77 K, 1 bar) on Cation Doped MOFs and Functionalized MOFs

Table 2.7: Hydrogen uptake on Selected MOF Composites

Table 3.1: Colour of Flame for different Alkali Metals

Table 3.2: Packing Densities for Adsorbents

Table 3.3: Constants Associated with the Equation of State (EoS)

Table 3.4: Details of Major Instruments in the Gravimetric Adsorption Measurement Unit

Table 3.5: Experimental Conditions for Adsorbent Samples

Table 4.1: Physical Properties of Adsorbents Studied

Table 4.2: Activation Conditions for Adsorbents Studied

Table 4.3: Maximum H_2 Uptake, Henry's Constants and Enthalpy of Adsorption for Adsorbents Studied

Table 4.4; Langmuir Isotherm Model Parameters for H_2 Adsorption on Adsorbents Studied

Table 5.1: Surface area and Pore volume of various Cu-BTC and Cr-BDC MOFs

Table 5.2: H_2 Uptake at Saturation, Henry's constant and Enthalpy of adsorption for Cu-BTC/Li and Cr-BDC/Li compared to parent MOFs

Table 6.1: Composition and Doping Levels of different MOF composites

Table 6.2: Surface area, Pore volume, Saturation uptake, Henry's Constant and Enthalpy of Adsorption for Hydrogen Uptake on Various Cu-BTC Composites

Table 6.3: Surface area, Pore volume, Saturation uptake, Henry's Constant and Enthalpy of Adsorption for Hydrogen Uptake on Various Cr-BDC Composites

Table 6.4: Surface Area, Pore volume, Saturation uptake, Henry's Constant and enthalpy of Adsorption for Hydrogen Uptake on MOF-205 Composite

CHAPTER 1

Introduction

1.1. Background on Hydrogen Energy

Hydrogen is a prospective source or energy carrier for the future because it is clean and sustainable. Commercially viable hydrogen can be produced from a variety of feedstock. These include fossil resources, such as natural gas and coal, as well as renewable resources, such as biomass and water. Renewable energy sources e.g. solar, wind, wave or hydro-power can be utilized for hydrogen production. A variety of technology can be employed for large scale production, including chemical, biological, electrolytic, photolytic and thermo-chemical processes [IEA website]. Each technology is in a different stage of research and development, and each one of them offers unique opportunities, advantages as well as challenges. Local availability of resources, the state of the art technology, industrial applications and demand, policy issues, and costs will influence the choice of the various options for hydrogen production [AFDC website]. Dating back to the late 1920's, it was the electrolysis of water used to produce pure hydrogen. In the 1960s, the industrial hydrogen production shifted slowly towards a fossil-based feedstock, which is the main source for hydrogen production today. Fuel cell used in spacecraft as well as eco-friendly automobiles use commercial hydrogen [Toyota website].

Many countries have recognized hydrogen based energy system as a partial substitute to the conventional oil based system. Depleting resources of fossil fuel may reduce production and supply in future. Air pollution is a collateral damage while using fossil fuel. Hydrogen-oxygen fuel cell overcame such environmental impacts as it produces no

harmful or greenhouse gas. Hydrogen is light weight gas hence diffuses fast; burns in colourless flame. It has very low boiling point of ~20 K hence lot of energy needed to liquefy and maintaining that temperature. Therefore one of the challenges for migration to hydrogen based fuel lies in designing an efficient storage system.

1.2. Conventional Storage System

A typical hydrogen cylinder made up of steel weighs ~75 kg contain 1.22 kg of hydrogen at 150 bar pressure and at room temperature. In some countries cylinders are filled upto a pressure of 300 bar [Schalpbach and Zuttel, 2001]. There are some safety issues that still have not been resolved, such as the problem of rapid loss of H_2 in case of an accident. The long-term effect of hydrogen on the materials under cyclic or cold conditions is also not fully understood. Material embrittlement can be analyzed by using new ad-hoc fracture mechanics techniques and improved by suitable reinforcement. Stronger and low-cost construction materials (carbon fibers composite) are also being developed [Dyntek Solutions website]. Compressed gas technology involves a compressor and ultra-high pressure technology involves pressure booster. Developing an efficient and clean (oil free) 1000-bar pressure booster is also needed for better compression. Developing hydride-type compressors utilizing waste heat or solar energy is also a challenge. Recovery of the compression energy during vehicle operation (braking) can be helpful in energy saving in a hydrogen vehicle. Nevertheless compression to very high pressures has huge energy penalty.

Carbon fiber reinforced composite tanks are being developed recently for commercial application. Although they are costlier than steel tanks, these tanks are lighter and hence of interest. There are several advantages with composite tanks. Their low weight meets key targets and the tanks are already commercially available, well-engineered and safety-

tested, after extensive prototyping experience. They do not require internal heat exchanger and may be used for storing hydrogen at cryogenic temperature and at high pressure with extra fittings.

The most commonly used method to store hydrogen in liquid form is to cool it down to ~20 K. Other options include storing hydrogen as a constituent in other liquids, such as $NaBH_4$ solutions, rechargeable organic liquids, or anhydrous ammonia NH_3 [Wang and Kang, 2008, Wu, 2003]. Cryogenic hydrogen, usually simply referred to as liquid hydrogen, has a density of 70.8 kg m^{-3} at its normal boiling point 20 K (critical pressure 13 bar, critical temperature 33 K). Although the density of liquid hydrogen is much better than that of compressed gas (~ 30-50 kg m^{-3} even at 700 bar), about 30-40% of the energy is lost while maintaining liquid H_2 at such low temperature. The other disadvantage associated with liquid H_2 is the boil-off loss that happens even in the best insulated cryogenic containers. On the other hand, the main advantage with liquid H_2 is the high storage density that can be reached at relatively low pressures. Liquid hydrogen use has been demonstrated in commercial vehicles (BMW), and may also be utilized to partially meet the needs in an aircraft fuel system. It provides the best weight advantage over any other H_2 storage system. Capture of boil-off liquid, re-liquefaction and economic thermal insulation may alleviate some of the associated problems.

1.3. Adsorption Based Storage System

Another alternative widely being explored is based on adsorption of hydrogen onto a solid material (adsorbent); a hydrogen storage vessel filled with a suitable solid adsorbent can achieve a higher energy density (as opposed to that of a vessel with no adsorbent) at the same temperature and pressure conditions. Adsorption based storage system is widely recognized as a material driven technology for the successful commercialization and

market acceptance of hydrogen powered vehicles. In addition, the physical properties of the adsorbate molecules also play an important role. The U.S. Department of Energy (DOE), in collaboration with automotive industry majors, established specific technical targets for on-board hydrogen storage system to focus on material development for hydrogen storage [Satyapal *et al.*, 2007]. Salient features of the target are represented in Table 1.1. Storing sufficient hydrogen for on-board vehicular application without compromising consumer requirements (driving range, cost, safety, performance, passenger and cargo space etc.), is the ultimate goal of such efforts.

The US DOE hydrogen storage target, 2017 for an adsorption based system is about 5.5 wt% (and 40 g L^{-1} volumetric storage capacity) considering a refueling range in excess of 300 miles. However, future generation cars may be light weight and more fuel efficient therefore lower values than the target may be realistic. New adsorbents are being developed and studied for hydrogen uptake both theoretically and experimentally. While, hydrogen storage capacity of traditional porous materials like carbons [Campesi et al., 2010, Srinivas *et al*., 2010], zeolites [Takagi *et al*., 2004, Langmi *et al*., 2005] etc. has been studied for a long time, interest in storage in Metal organic frameworks (MOFs) is a more recent phenomenon. Pure MOF can rarely achieve 5.5 wt% H_2 at 233-333 K. Therefore modifying the MOF structure to enhance the uptake at room temperature is being explored recently [Wang and Yang, 2008, Suh *et al*., 2012]

1.4. Research Objectives:

To seek suitable hydrogen storage material adsorption measurement on selected MOFs are carried out. Adsorption based storage is basically a material driven technology; a large volume of research today focuses on development and understanding of hydrogen adsorption on a variety of adsorbents. Hydrogen adsorption depends on the availability of

high binding energy sites at low pressures and availability of large surface area/pore volume at high pressures. In order to exploit the structural diversity of MOFs and synthesize adsorbents with tailor made structures for targeted applications, it is essential to understand the role of each of the constituents in the adsorbent framework. In an effort to understand this behavior, frameworks with widely different characteristics were chosen for this study. Two categories of MOFs *i.e.* coordinatively saturated metal sites containing MOFs (MOF-5, MOF-205, Ni-DABCO) and coordinatively unsaturated (*cus*) metal sites containing MOFs (Cu-BTC, Cr-BDC, Mg-DOBDC, Co-DOBDC) are chosen for this work. These materials cover a wide range of surface area starting from 623 m^2 g^{-1} (Zn-BDC) to 4590 m^2g^{-1}. One silica based material MCM-41 (pore volume 1.48 cc g^{-1} and surface are 919 m^2 g^{-1}) is also chosen for comparing the results. Adsorption isotherms for hydrogen uptake on these materials will be measured over a wide temperature and pressure range; experimental data for hydrogen uptake at cryogenic temperatures (between 77 and 273 K) is rather limited in literature. On the other hand, such data is essential if adsorbent based hydrogen storage systems are to be developed at these temperatures; success of such systems in the cryogenic temperature range seems more likely since even with the best performing adsorbents today, the hydrogen uptake at ambient temperature is rather poor.

A careful analysis of experimental data will be performed to obtain important parameters such as Henry's constant and enthalpy of adsorption. Enthalpy of adsorption at zero loading and Henry's constant also determine the energy required to release the adsorbed molecules during regeneration [Bae and Snurr, 2010].

In the second part of the work, attempts will be made to dope the MOFs with a light alkali metal (Li) for enhancing the hydrogen adsorption of selected MOFs. Being light

metal lithium will not substantially increase the weight of the MOF framework after doping and hence the penalty on the gravimetric storage capacity is expected to be minimal. While some literature exists on Li doping in metal organic frameworks, most of the reports are for frameworks which have rather poor hydrogen uptakes on the pure MOF itself; although some reports indicate improvement in hydrogen storage capacity the final result is still well below the desired target. However, many theoretical studies indicate that Li doping should considerably increase hydrogen uptake capacity of MOFs. Attempt will be made to dope Li into some of well-studied MOFs in literature viz. Cu-BTC and Cr-BDC.

In the final part of this work, heavy transition metals (such as Palladium and Platinum) which are known to have strong affinity for hydrogen adsorption will be used for doping of selected MOF materials. MOF composites containing varying amounts of Pd on graphene oxide (Pd-GO) and Pt on activated carbon (Pt-AC) will be synthesized and the hydrogen adsorption of these materials will be evaluated. Although the specific surface area and pore volume are expected to decrease (due to structural distortion) but they are likely to exhibit better hydrogen loading than the pure MOF. There are reports in literature indicating efforts to dope MOFs with heavy transition metals; some reports even report exceptional enhancement in hydrogen uptake due to so called spillover effect. However, such results are few, far in between and reproducibility is limited to laboratories across the globe.

MOFs are known to have widely different surface area and pore volume and other adsorption characteristics based on the laboratory of their origin. One of the objectives of the work would be to compare the results of transition metal doping to that of Li doping on MOFs synthesized in our laboratory; such a work would eliminate unwarranted

differences in the pure MOF properties and the differences can be attributed directly to the doping. Finally, to the best of our knowledge there are no reports in literature where MOFs are doped with both transition metals as well as light metal such as Li. While transition metal doping is known to increase vertical interactions of hydrogen molecules with the surface (and thereby the enthalpy of adsorption improves significantly), literature indicates that Li plays a more subtle role in increasing the uptake capacity and improvement in adsorption enthalpies are minimal. On the other hand, transition metals are heavy and significantly add to the mass of the framework offsetting some of the improved gravimetric uptake. It would be interesting to see the effect of combined doping of both Pd (or Pt) and Li into the MOF structures.

Tables

Table 1.1: Hydrogen Storage Target for Adsorption Based Storage [DOE website]

Storage Parameter	**Units**	**2017**	**Ultimate**
Gravimetric Capacity	wt%	5.5	7.5
Volumetric Capacity	gH_2/L	40	70
Operating temperature	K	233/333	233/333
Minimum and maximum delivery temperature	K	233/358	233/358
Cycle life (1/4 tank to full)	cycles	1500	1500
Minimum delivery pressure from storage system *	bar	5	3
Max delivery pressure from storage system *	bar	12	12
System fill time (5 kg of H_2)	min	3.3	2.5

*for a H_2-O_2 fuel cell vehicle

CHAPTER 2

Literature Survey

In order to overcome the challenges posed by storage of hydrogen as a liquid or compressed gas, alternate hydrogen storage technologies are being explored. These technologies include storage of hydrogen on materials with which it forms a chemical bond (metals or their alloys forming metal hydrides/complex metal hydrides) and on high surface area materials where it is physisorbed. First, a brief introduction and examples of materials used in chemically and physically bound hydrogen are given. In the next section, a review of literature on hydrogen physisorption on various porous materials is presented, followed by techniques used for enhancement of hydrogen adsorption on metal organic frameworks (MOFs). The literature available on the effect of doping of MOFs with alkali/alkali earth metals and heavy transition metals on their hydrogen adsorption characteristics as well as hydrogen adsorption on MOF composites with activated carbon and graphene oxide are also discussed.

2.1. Hydrogen Adsorption on Solid Surface

A tank can be filled with selected metal or metal alloy powder to store more hydrogen than an empty tank at similar conditions. Selected metals (or alloy) either in the bulk or as nanoparticles can adsorb hydrogen. Hydrogen moleculeschemically bind with the metal to form metal hydride. This phenomenon is called chemisorption [Janot*et al*., 2005]. Many metals (Pt/Pd) and alloys (Mg_2Ni for example) react with hydrogen to form a reversible metal hydride which when heated releasesthe entire amount of bound hydrogen [*de*-Jongh and Adelhelm, 2009]. A generic reaction is shown in Figure 2.1. In order to understand this behavior it is helpful to consider the pressure–composition isotherm (PCI)

for a metal hydride. A representational isothermis given in Figure 2.2, which shows that as the pressure increases the hydrogen uptake increases. Above the pressure corresponding to point A on the isotherm, the metal will form a hydride. The stored hydrogen can be released by reducing the pressure of the system to a level below that of the plateau pressure. The plateau pressure increases with temperature; hence stable at a given temperature and pressure will decompose, when the temperature is increased suitably (such that the plateau pressure at new temperature is higher than system pressure). The maximum achievable storage capacities vary widely (15 wt% and 150 kg m^{-3} for $Mg(BH_4)_2$, 4 wt% and 90 kg m^{-3} for Mg_2NiH_4, and 2 wt% and 120 kg m^{-3} for $LaNi_5H_6$).

The metals and alloys which can form low temperature hydrides e.g.Pd nanoparticles, $LaNi_5$ and FeTi, (at <353 K, 1 bar) are based on heavy transition metals and therefore have low gravimetric hydrogen storage capacities [Sahu*et al*., 2014, Yartys*et al*., 2008]. These materials have volumetric capacities even superior to that of liquid hydrogen [Zuttel, 2004].Because of the low gravimetric capacity for the interstitial metal hydrides, there has been a lot of interest in higher capacity materials such as magnesium hydride (with a storage capacity of 7.6 wt% and maximum delivery capacity of 4.2 wt%). However, this material has high regenerationtemperature of 553 K (at 1 bar). Complex metal hydrides(e.g. Na_2LiAlH_6,$TiV_{0.9}Mn_{1.1}$)are extensively studied and well reported in literature [Huot*et al*., 2008, Bogdanovicand Schwickardi,1997]. Titanium-based catalysts enable sodium alanate to be reversibly dehydrogenated (having a theoretical capacity of 7.5 wt%).Reported literature is availableon lithium amide and tetra-hydrido-borates of lithium, magnesium and a number of transition elements. While the complex metal hydridesmay have the potential to reach theUS DOE target 2017,their dehydrogenation enthalpy is considerably high, hence limited applicationis expected. In order to reduce the

enthalpy of adsorption a catalyst (also called a destabilizing agent) is introduced. The regenerationtemperature is defined as $\Delta H_{ads}/\Delta S$; where ΔH_{ads} and ΔS are the change in enthalpy and entropy for the dehydrogenation process. $LiBH_4$ and MgH_2 mixture [Vajo*et al.*, 2005] is an example ofmulti-component system where a destabilizing agent is added to a hydride or complex hydride; this new mixture has a regeneration temperature of 438 K at1 bar in comparison with 553 K (for MgH_2) and 683 K(for $LiBH_4$).

In contrast to metals or metal alloys porous materials can also be used to fill a hydrogen storage tank to enhance the storage capacity. In this case, the hydrogen molecule does not dissociate on the surface, rather they adhere to the surface through *vander* Waals (or other electrostaticforces) but no chemical bond is formed. The strength of these interactions for hydrogen is weak with an enthalpy of adsorptionΔH_{ads}($-\Delta H_{ads}$ is also referred as isosteric heat, Q_{st}), between 4 to 10 $kJmol^{-1}$. These weak interactions mean considerably lower desorption/ regeneration temperatures; but at the same time hydrogen molecules easily overcome the weak interactions with the surface and are not as strongly bound as in case of chemisorption with metals.

Typically, hydrogen adsorption on porous material is measured at liquid nitrogen temperature,77 K since reasonable hydrogen adsorption is observed on most porous materials at these temperatures and quantification/comparison is often easier. Hydrogen storage at 77 K using a porous material is easier than using a liquid hydrogen storage to be maintained at 20 K (about thrice the energy is required). Thus, it is also of interest to know the adsorption capacity of a porous material at a suitable intermediate cryogenic temperature and liquid nitrogen temperature is often conveniently chosen for this purpose.

Sinceadsorption is a surface phenomenon, research is now focused on developing high surface area materials with higher hydrogen uptake capacity. Porous materials that

have been studied for hydrogen adsorption include are allotropes of carbon like carbon nanotubes (CNTs) [Porier*et al*., 2006], zeolites [Langmi*et al*., 2005], metal–organic frameworks (MOFs) [Czaja*et al*., 2009] and polymers of intrinsic microporosity (PIMs) [Budd *et al*., 2007].

2.2.Hydrogen Adsorption on Porous Materials

2.2.1.Zeolites

Zeolites are three dimensional alumina-silicate structures (tetrahedron) consist of Si^{4+} and Al^{3+} ions. The general formula of zeolites is $M_{x/z}[(AlO_2)_x(SiO_2)_y]\cdot mH_2O$, where M is the non-framework exchangeable cation. The Si-O-Si or Al-O-Al bonds are very flexible, therefore the tetrahedral units can be linked in a several different network topologies;twenty eightsuchstructures are physically realizable. Zeolites arestable at high temperature, pressure andin harsh chemical environments [Schüth*et al*., 2002].In order to maintain the electro neutrality of the structure, for everySi^{4+} substituted with an Al^{3+} there is an additional metalion (usually alkali and alkali earth metal ions) in the structure. The ion exchange capacity depends on thesize of the accommodating pores and on the charge of the cation. Due to the presence ofstrong electrostatic forces inside the pores, highly polar sites on the surface are available for adsorption. Most zeolites are synthesized from aluminosilicate gel by a hydrothermal process [Szostak, 1998]. Zeolites also occur naturally. Zeolites can have a very open microporous structure with different framework types depending on the assembly of the tetrahedral building units. This assembly is determined by the Si to Al ratio.

Figure 2.3 shows schematics of different zeolites. In zeolite type A (Fig 2.3. a) the sodalite cages, which are truncated octahedron tertiary subunitsare connected with each

other throughthe square faces to from a cubic framework. In zeolite types X and Y (Fig 2.3 b) the cages areconnected through the hexagonal faces; the zeolites X and Y differ only in the Si/Alratio.The through channels of the zeolites create a honeycomb-like structure. Zeolites have specific surface areaof the order of 500 to 800 m^2 g^{-1}. The internal surface and pores/channels afford zeolites to exchangeions,physisorbmoisture and gas molecules.Zeolites have been extensively usedin the industry for gas adsorption, catalysis and water purification by ion exchange [Guisnetand Gilson, 2002] and also forremoval ofradioactive nuclei from nuclear waste[Attfield, 2002].

Makarova*et al*. [1994] measured H_2 uptake at 77 K on a number of hydrogen-exchanged zeolites. They correlated the total adsorption capacity at a given pressure as an inverse function of pore size. Best performing material was H-mordenite followed by H-ZSM-5 and zeolite X and Y respectively. The highest observed hydrogen uptake was 0.7 wt% at 0.65 bar in H-mordenite, but fitting of the data to the Dubinin equation predicted that considerably higher capacities can be achieved at higher pressures in zeolite X and Y. Ruthven and Farooq [1994] reported that CaNaA (LTA) can adsorb 0.44 wt% at 77 K , 0.1 bar. Kazansky*et al*. [1998] studied hydrogen adsorption at 77 K on various isostructural zeolites, NaY and NaX with different Si/Al ratios. The amount of hydrogen adsorbed was found to increase in the sequence NaY (Si/Al = 2.4; 56 Na^+ per unit cell) <NaX (Si/Al = 1.4; 80 Na^+) <NaX (Si/Al = 1.2; 87 Na^+) <NaX (Si/Al = 1.05; 94 Na^+) with adsorption corresponding to 1.2 wt% reported for NaX (Si/Al = 1.05) at 0.6 bar. The correlation between the amount adsorbed and the number of Na^+ in the zeolite structure indicated that the cations act as the adsorption sites. The strength of the adsorbate-adsorbent interaction is expected to decrease with increasing framework basicity due to reduction in effective positive charge on the Na^+ ions. Stéphanie-Victoire*et al.*[1998] carried out adsorption studies on molecular hydrogen isotopes on NaA at cryogenic

temperature (40–120 K) at pressures up to 0.8 bar using the Dubinin model. They documented a capacity of 1.9 wt% loading of H_2, but significantly the value at 77 K is two-third of its value at 40 K, indicating that the zeolite was far from saturated at 77 K. The isosteric heats of adsorption ($-\Delta H_{ads}$) strongly depends on coverage, decreases from 10.7 kJ mol^{-1} at loading levels of 0.5 H_2 molecules per unit cell to 6.2 kJ mol^{-1} at 10 H_2 per unit cell. Nijkamp*et al*. [2001] performed hydrogen adsorption measurements on a various carbonaceous, Si/Al-based materials and on zeolites, at 77 K and pressures up to 1 bar. They reported that adsorption of hydrogen under these conditions was dependent on the presence of a large volume of micropores with a suitable diameter. A capacity of 0.72 wt% was recorded for zeolite ZSM-5 and 0.54 wt% for the mesoporous silica material MCM 41. Forster *et al*. [2003] examined H_2 adsorption in the zeolitic nickel phosphates VSB1 and VSB5 at 77 K. A stronger adsorption found in the latter was related to the presence of coordinatively unsaturated framework Ni^{2+}cations. However, the storage capacities remained below 1 wt% at 1 bar. Jhung*et al*. [2005] measured adsorption capacities in a range of porous materials including zeolites, finding a maximum capacity at 77 K and 1 bar of 1.4 wt% in SAPO34.

2.2.2. Allotropes of Carbon

There are different allotropes of carbon like carbon nanotubes (CNT), activated carbon, fullerene etc. that can adsorb hydrogen. Activated carbon has high surface area whereas CNT have lower surface area.There exists more scope of activating or functionalizing the surface of graphene or grahene oxide (GO). Graphene is a popular allotrope of carbon and is being investigated widely as potential candidate for hydrogen storage. Talyzin and co-workers synthesized bulk amounts of powdered graphene by thermal exfoliation of graphite oxide [Talyzin*et al*., 2011]. Material produced by this

method is multi-layer graphite sheets with 2-15 graphene layers (Figure 2.4). Physically graphene is similar to activated carbon but has a smaller surface area of the order of 600-1000 m^2g^{-1} (although the theoretical surface area for single layer graphene ~2500 m^2g^{-1}). Maximum hydrogen uptake in a graphene-like material with a surface area of 640 m^2g^{-1} was estimated as 0.72 wt% at 298 K, 100 bar and which is on the same level as for ACs with comparable surface area [Srinivas*et al*., 2010].

2.2.3. MesoporousSilica Materials

Mesoporous silica materials exhibit pores with diameters in the range between 2-50 nm. Mesoporous silica materials like MCM-48, SBA-15 and MSU-1 serve as templates for synthesis of well-tailored carbon materials [Vix-Guterl*et al*., 2005]; they also find applications in drug delivery [Wang, 2009]. Some of the interesting characteristics of mesoporous materials include the ease of synthesis, very low density and good thermal stability. Due to the large pore sizesthese materials also have considerable pore volume; therefore in principle they can adsorb significant amounts of hydrogen inside these pores. The presence of well-defined, ordered and connected pore systems can enhance the dynamics of the gas diffusion in the material and in combination with high specific surface area offer potential for hydrogen storage. But large pore size materials translate to weak interactions with the hydrogen molecules (especially when the surface is neutral)and hence cannot adsorb significant hydrogen at lower pressures.Reported literature suggests that modification of the structure is necessary to enhance surface area and hydrogen affinity by metal doping [Sheppard and Buckley, 2008, Acatrinei*et al*., 2009]. Mesoporous materials can be used as a host or template material in which metal particles can be confined to control their growth. A comparison of reported hydrogen

uptake on some zeolites, allotropes of carbon and silica materials is presented in Table 2.1.

2.2.4. Metal Organic Frameworks (MOFs)

Metal organic frameworks are typically Cu/Zn/Ni/Al or other metal atom structures bridged with aromatic rings forming a complex compound [Rosi*et al*., 2003, Baeand Snurr, 2010]. These materials have an extremely high surface area, highly versatile and allow for many structural modifications [Fereye*t al*., 2003].MOFs are porous material readily synthesized by coordinative bonding of metal atoms with organic linkers (see Table 2.2) [Li *et al*., 1999]. The metal building block is generally cationic and binds with electrostatic interaction to form an organometallic compound where the linker is anionic [Kaye and Long., 2008, Nouar*et al*., 2009]. These materials are widely being investigated for their potential application in gas separation, gas storage and catalysis [Eddaoudi*et al*., 2000, Chen *et al*., 2001, Fletcher *et al*., 2005]. Numerous reviews summarize the fast growing research efforts in the field. The most comprehensive ones are by Ferey[2008], Kitagawa *et al*.[2004],Rowsell and Yaghi [2004] and Suh*et al*. [2012]. Adsorption characteristics in MOFs depend on the geometry of the linker as well as the saturation (coordinated) level of the metal atom. MOFs have gained attention over other conventional porous materials due to their high surface area, larger pore volume, and tunable structure. However, some MOFs degrade on exposure to water vapor [Chowdhury*et al*., 2009].

A thumb rule correlating the relation between the surface area and hydrogen loading predicts 1.5 wt% of H_2 adsorption at 77 K and 1 bar for every 1000 m^2g^{-1} is optimum.As an example, Cu-BTC (with specific surface area of ~1500 m^2g^{-1}) has a typical hydrogen storage capacity of 2.25 wt% at 77 K and 1 bar. However, surface area alone does not

dictate the hydrogen capacity but the pore geometry and pore volume also has an effect [Frost and Snurr, 2007] along with the framework elements where the metal atoms can provide stronger adsorption sites (open metal sites) [Suh*et al*., 2012]. In general these porous materials have good recyclability as the material itself does not undergo any significant change through the adsorption/desorption process.

If MOFs or other porous materials are chosen for storing hydrogen a convenient cryogenic temperature such as 77 K, additional liquid nitrogen to keep the fuel tank and its contents at 77 K during refueling since physisorption is exothermic. The problems associated with handling cryogenic temperatures can be overcome if the hydrogen is coordinated strongly with the substrate and storage can be achieved at room temperature. However, enthalpy of interactionneeded in such a scenario would be significantly higher (~20 kJ mol^{-1} at 298 K)[Baeand Snurr, 2010]. MOFs having open metal site offer extra binding energy and asuitableLi doped MOF or a Pt/Pd doped MOF can increase the enthalpy of adsorption [Li and Yang, 2006, Stucket*et al*., 2010] in principle. A comparison of hydrogen uptake capacities for various MOFs reported in literature is given in Tables2.3- 2.5.

2.3. Strategies of Enhancement of Hydrogen Uptake in MOFs

2.3.1. MOFs with Open Metal Sites

On the basis of both experimental and computational studies, it has been documentedthat the coordinatively unsaturated (*cus*-) metal centers (open metal sites) enhance adsorption enthalpy at zero coverage (ΔH_{ads}) in a MOF. H_2 molecules can directly interact with these cus-metal sites. The metal-H interactions in a MOF have been confirmed by NMR experiments by several researchers [Dinca*et al*., 2006, Yan *et al*.,

2010, Peterson *et al*., 2006]. Zhou et al., studied different M-DOBDC MOFs (M= Mg/Mn/Co/Ni/Zn) and showed Ni-DOBDC has better hydrogen affinity than the rest though all of them have same coordination number 6 [Zhou *et al*., 2008]. In order toexpose the open metal sites in the MOFs, the coordinating solvent molecules need to beremovedto the maximum possible extent. The room temperature H_2 storage capacities of the MOFs with open metal sites are much higher than those without saturated metal sites. However, if the surface area is smaller than 3000 $m^2 g^{-1}$, the effect of the open metal sites on the room temperatureH_2 storage capacities is rather minor.The saturation uptake capacities on selected MOFs are given in Table 2.4.

Suh's group made a comparison of the H_2 storage capacitiesfor three iso-structural MOFs with and without open metalsites. The MOFs,SNU-4 and SNU-5'have no open metal site, whereas SNU-5 has open metal sites [Lee *et al*., 2008]. The BET surface area and pore volumein SNU-5 having open metal sites are 1.4-1.7 times greater thanthose of SNU-4 and SNU-5'. The H_2adsorptioncapacities of SNU-5 are much higher than those of SNU-4 andSNU-5'; at 77 K and 1 bar. H_2 uptake is 2.07 wt%for SNU-4, 1.83 wt% for SNU-5', and 2.87 wt% for SNU-5 respectively. They calculated H_2uptake per unit volumeof the MOF on a dry basis (after desolvation), which indicated thatSNU 5adsorbs at least 1.2 timeshigher amount ofH_2than SNU-4. Enthalpy of adsorption (ΔH_{ads}) at zero coverage for SNU-4, SNU-5',and SNU-5 were 5.96-7.24, 5.91-6.53, and 4.43-11.60 kJ mol^{-1}respectively.

Wang *et al.*documented that alignment of open metalsites affects the H_2 adsorption [Wang et al., 2008].Porous coordination networks, PCN-12 and PCN-12'structure shape iscuboctahedra; while in PCN-12 the open metal sites are aligned, in PCN-12' these openmetal sites are out of alignment.The dissimilar alignments significantly affected the

hydrogen uptakes on theseMOFs. The H_2 uptake capacities of PCN-12 andPCN-12' are 3.05wt%and 2.40wt%, respectively, at 77Kand 1 bar.NMR studies of PCN-12 indicate thatH_2 strongly prefers aligned Cu(II) sites compared to non-aligned Cu(II) sites.These results suggest that the presence of open metal sites in a MOF leads to the higher H_2 uptake capacity and higher enthalpy of adsorption.

Yaghi and co-workers weresuccessful in coordinating metal into rigid metal-oxygen-carbon clusters (by using carboxylate linker of terephthalic acid) with the points of extension to obtain entities known as secondary building units (SBUs) [Yaghi*et al*., 2003]. Zn-BDC [Li *et al*., 1999] is the first synthesized MOFs based on this concept of SBUs. The concept of SBUs has been used to develop variousstructures of MOF [Kim *et al*., 2001]. However, Zn-BDC MOF does not have any unsaturated metal site. MOFs constructed of metal clusters with coordinating solvent molecules as secondary building units (SBU), located at the framework nodes have the potential to generate open metal sites. The removal of the coordinating solvent molecules by thermal evacuation brings coordinative unsaturation in the metal sites. The most common SBUs for such purposes are the bimetallic paddle-wheel units of $M_2(O_2CR)_4$ ($M=Cu^{2+}$, Zn^{2+}, and Cd^{2+}), where solvent molecules are coordinated at the axial sites [Krungleviciute*et al*., 2007].

Among heterocyclic azolate-based frameworks, Mn-BTT, exhibits highest hydrogen uptake capacity (5.1 wt %) as well as enthalpy of adsorption (10.1 kJ mol^{-1}) [Dinca*et al*., 2006]. Single crystal XRD indicated that the chloride centered, square-planar $[Mn_4Cl]^{7+}$ units are linked with eight trigonal planar BTT ligands to form the anionic, three-dimensional sodalite-type structure. The solvent molecules occupy the sixth coordination site on each Mn(II) ion, while charge balance is provided by Mn complexes. Similar isostructuralsodalite frameworks, Cu-BTT and Fe-BTT also show high enthalpy of

adsorption of 9.5 and 11.9 kJ mol^{-1}, respectively [Sumida *et al*., 2010]. The strongest binding site is located just 2.47 and 2.17 Å away from the exposed Cu(II) and Fe(II) metal sites, respectively. The highest enthalpy of adsorption at zero coverage of MOFs reported so far is 15 kJ mol^{-1} for SNU-15 [Cheon and Suh, 2009], favorably close to meet the DOE target [Lochan and Gordon, 2006]. It has fluorite-like network generating 3D channels. In the as-synthesized MOF, each Co(II) ion coordinates to terminal aqua ligand, and Co-Co distances are 3.550 Å and 3.428 Å. Such high enthalpy of adsorption in SNU-15 might be attributed to the Co-Co distance that makes it possible for a H_2 molecule to bind in a side-on fashion.

2.3.2.Catenation of MOFs

Catenation or interpenetrationmakespore size narrower and hence adsorption uptake capacity at low pressures usually improves [Tranchemontage*et al*., 2008, Suh*et al*., 2012]. Zhou and co-workers compared the H_2 adsorption capacities of the MOFs that are chemically identical but with catenated and non-catenated structures [Ma *et al*., 2008, Ma *et al*. 2007]. The catenated PCN-6 and non-catenated PCN-60 have the general formula $Cu_3(TATB)_2$. The volumetric H_2 adsorption measurements for the samples activated at 323 K showed that catenated PCN-6 adsorbed 1.74 wt%, while PCN-60 adsorbed 1.35 wt% at 77 K and 1 bar. When the samples were activated at 423 K the adsorption capacity increased slightly, PCN-6 to 1.9 wt% and PCN-60 to 1.62 wt%. The larger improvement in H_2 adsorption of PCN-60 was due to availability of open metal sites. However, the available Cu^{2+} sites in PCN-6 were blocked because of the catenation, thereby resulting aonly marginal improvement of H_2 adsorption. However, the catenated structures adsorb more H_2 gas than the non-catenated structures at low pressure. Theoretical calculations also predict that interpenetration is beneficial for hydrogen storage at low temperature and

low pressures, but at ambient temperature, the adsorption capacity decreases significantly [Ryan *et al*., 2006].

2.3.3. Large Pore MOFs

The pore volume of MOFs is an important factor in determining its total uptake capacity for hydrogen. In an attempt to enhance the hydrogen uptake capacity of MOFs, several researchers have attempted to construct MOFs with large organic linkers/ large pores to enhance the pore volume of the materials. Most reported large pore MOF is MOF-177 [Foy*et al*., 2006, Saha and Deng, 2010]. Structure has similarity with MOF-5; it is constructed from [Zn_4O] clusters and 4,4',4''-benzene-1,3,5-triyltribenzoate (BTB). Each [Zn_4O] unit is connected to six carboxylate groups and each tricarboxylate ligand connects to three [Zn_4O] units to form the network. MOF-177 has high specific surface area of 4750 m^2 g^{-1} and a pore volume of 1.59 cm^3 g^{-1} [Foy*et al*., 2006]. ThisMOFadsorbs 7.5 wt % of H_2 at 77 K and 70 bar.

In many MOFs the metal coordinates with more than one organic linker or functional groups (OH, OF etc.). Two chromium based MOFs, $Cr_3OF(BTC)_2$ (MIL-100) and $Cr_3OF(BDC)_3$ (MIL-101) are such MOFs but they have totally different topologies from MIL-53 [Fereyet *al*., 2003, Latrocheet *al*., 2006]. They contain trimeric Cr^{3+},octahedral clusters coordinating with water molecules (or Fluorine) and thus provide unsaturated metal sites upon desolvation. This zeotype structure was constructed by the connection of large hybrid super tetrahedron and generated large mesopores. After removal of the solvent molecules, the accessible pore diameters are 25 and 29 Å for MIL-100, and 29 and 34 Å for MIL-101. Two different treatments were reported to form MIL-101a with unreacted BDC and MIL-101b without unreacted BDC present inside the pores. For MIL-101a, the Langmuir surface was ~4000 m^2 g^{-1}, and maximum H_2 adsorption capacities

were 4.5 wt% at 77 K and 40 bar and 0.36 wt% at 298 K and 86 bar. For MIL-101b (Langmuir surface area 5500 m^2g^{-1}), adsorption capacities were phenomenal 6.1 wt% at 77 K and 80 bar. Furthermore, MIL-101b has high enthalpy of adsorption (9.3-10.0 kJ mol^{-1}) at low coverage, which is larger than that of MIL-100 (5.6-6.3 kJ mol^{-1}). The high enthalpy of adsorption in MIL-101b was explained by the presence of strong adsorption sites at each corner close to the trimers of chromium octahedra.

A series of MOFs, NOTT-100to NOTT-111 were constructed from Cu^{2+} paddle-wheel SBUs and long tetra-carboxylic acids [Lin *et al*., 2006, Yang *et al*., 2009]. On activation, all of them have similar structures and stoichiometry, except NOTT-104.NOTT 104 has inter-penetrated (catenated) structure but it is unstable after desolvation. These MOFs show high H_2 uptake due to large pore volumes as well as the presence of Cu(II). NMR studies indicated that the open Cu(II) sites are the strongest adsorption sites in the pores, but the enthalpy of adsorption is similar to other MOFs in this series. The adsorbate-adsorbent interaction is affected by the ligandstructure near the paddle-wheel SBUs. The high heat of adsorption at low H_2 loading was observed for NOTT-106 and NOTT-107, and it is due to the exposed Cu(II) sites as well as methyl groups exposed to the pores. Fluorine and methyl groups functionalized MOFs have lower pore volumes and lower H_2 capacities and the lower enthalpy of adsorption. The size of organic linkers in NOTT-103 (naphthalene ring) and NOTT-110 (phenanthrene group) result in high surface area/pore volume and hence higher H_2 uptake.

Large pore MOFs have slightly less enthalpy of adsorption because large cavities make the electrostatic interaction weaker. However, NOTT 200 has high enthalpy of adsorption of 9 kJ mol^{-1} because of doubly interpenetrated (catenated) structure. In the NOTT series, large cavities are formed in the fused polyhedral frameworks, for

example,NOTT-112 [Yan *et al*., 2009].It adsorbs 2.3 wt% of H_2 at 78 K and 1 bar. The high H_2 adsorption capacity at low pressure is attributed to available Cu(II) centers and narrow channel of the linker (See Table 2.5 for saturation loading);enthalpy of adsorption at zero coverage is 5.64-4.74 kJ mol^{-1}. The high H_2 uptake is attributed to the high surface area and large pore volume created bypolyaromatic ligands [Yan *et al*., 2010]. NOTT-116, also shows high H_2 uptake, contains open metal sites, and its apparent BET surface area is 4664 m^2 g^{-1}. The framework has pores with sizes around 1.6, 2.0, and 2.6 nm. NOTT-116 adsorbs 1.9 wt % of H_2 at 78 K and 1 bar, and the enthalpy of adsorption is 6.7 kJ mol^{-1} at zero coverage. It has little less capacity than NOTT-112 may be because of its larger pore diameter.Schroder and coworkers reported H_2 uptake capacity of NOTT 140 as 6.0 wt% at 77 K, 20 bar. The enthalpy of adsorption was 4.15 kJ mol^{-1} at zero surface coverage [Tan *et al*., 2011]. The relatively low enthalpy of adsorption is due to the different alignment of the vacant Cu(II) sites. Contrary to other NOTT series that have the exposed Cu(II) sites in the pores of the cages, NOTT-140 has the Cu sites that locate outside the cages, which results in reduced affinity for H_2.

Zhou and coworkers have reported a series of isostructural MOFs, which were synthesized from dendritic hexacarboxylate ligands and copper paddle-wheel SBUs, namely, PCN-61, PCN-66, PCN-68 and PCN-69 [Yuan *et al*., 2010, Yuan *et al*., 2011]. PCN series of MOFs generate open Cu(II) sites. Among the activated PCNs, PCN-61, PCN-66, PCN-68, and PCN-69 show high surface areas as well as high H_2 uptake capacities.Saturation pressure at cryogenic temperatureis lowest for PCN-61 and highest for PCN-68, coincident with the increase in surface area.Total H_2 uptake capacity for PCN-68 is 7.32 wt% at 77 K. However, these frameworks have relatively low $\Delta H_{ads,0}$, 6.36 kJ mol^{-1} for PCN-61, 6.22 kJ mol^{-1} forPCN-66, and 6.09 kJ mol^{-1} for PCN-68 respectively, despite the presence of open Cu(II) sites. Even though the surface area of

PCN-69 is greater than PCN-61, its H_2 uptake capacity is smaller than any of the series. However, PCN-69 shows a slightly higher $\Delta H_{ads,0}$(8.14 kJ mol^{-1}) at zero coverage because of the twisted ligand creating pockets and concaves in the pores, which enhance adsorbate-adsorbent interaction.

Koh*et al* [2008] suggested coordination copolymerization of topologically different linkers with identical coordinating functionality. They combined symmetrical dicarboxylate and tricarboxylate, which should be connected with [Zn_4O] octahedral SBUs. For example, [$Zn_4O(BDC)(BTB)_{4/3}$] (UMCM-1) was obtained from H_2BDC and H_3BTB. On the octahedral building unit, two BDC linkers are nearby and the other four positions are occupied by BTB linkers, which construct an octahedral cage. If ditopic ligand BDC was replaced with T_2DC, 2,5-thiophenedicarboxylate (TDC) and NDC, different coordinations are formed, which provided the frameworks with different topologies, UMCM-2, UMCM-3, and MOF-205, respectively. All MOFs (UMCM-1 UMCM-2, UMCM-3, UMCM-4, UMCM-5, MOF-205, and MOF-210) prepared by this technique demonstrated BET surface areas ranging from 3500 to 6240 m^2 g^{-1} and the high pore volumes ranging from 1.64 to 3.60 cm^3 g^{-1} [Koh*et al*., 2010]. UMCM-2, [$Zn_4O(T_2DC)(BTB)_{4/3}$], showed high H_2 uptake (excess 6.88 wt%) at 77 K and 46 bar. MOF-210 constructed from BTE and BPDC exhibited excessH_2 uptake of 8.6 wt% at 77 K and 56 bar with an absolute adsorption of 17.6 wt% at 77 K and 80 bar [Furukawa *et al*., 2010]. This H_2 uptake is the highest and excess is the second after NU-100 (>9 wt%) among the reported values.

A summary of uptake capacities in various large pore MOFs is given in Table 2.5.

2.3.4.Alkali Metal Doping in MOFs

In order to increase hydrogen storage capacity at ambient temperature or at low pressure, hydrogen affinity of MOF surface should be increased. The MOF should have a binding energy of 15-25 kJ mol^{-1} for sufficient H_2 storage [Lochanand Gordon, 2006, Baeand Snurr, 2010]. One of the approaches to enhance the enthalpy of adsorption is exchanging the counter-cations included in the anionic framework with metal ions that can interact with H_2 molecules more strongly. Theoretical studies were performed on metal-doped MOFs and the results suggested hydrogen adsorption can be significantly increased than that on the pure MOF. For example, Goddard and coworkers reported that Li-doped MOFs can significantly improve H_2 uptake capacities at ambient conditions [Han and Goddard, 2008, Han and Goddard, 2007]. The results suggest that Li atoms prefer to bind at the centers of the hexagonal aromatic rings, but Li atoms at the adjacent rings are located exactly on the opposite sides. In a computational study Mavrandonakis*et al*. showed that the incorporation of Li cation into an organic linker containing sulfonate group of IRMOF-14 enhances the hydrogen adsorption capacity even at room temperature [Mavrandonakis*et al*. 2009]. In another computational study, Kolntzas*et al*. incorporate lithium alkoxide groups in the organic linker itself; GCMC simulations indicate that hydrogen molecules tend to adsorb near the positions of the Li atoms and room temperature hydrogen uptake shows significant improvement [Klontzas et al, 2008].

Eddaoudi and co-workers have synthesized anionic zeolite-like MOF structures, rho-ZMOF [Nouar*et al*., 2009]. They exchanged the dimethylammoniumcations in the ZIFs with Na^+, Li^+, and Mg^{2+} by soaking ZMOFs in a solution of the corresponding metal salt and obtained the fully exchanged products at room temperature after 18 h. Contrary to their expectations, the H_2 uptake amount and the enthalpy of adsorption did not increase

drastically compared to those for the unsubstituted ZMOFs. The single crystal XRD of rho-ZIF/Mg indicated that Mg^{2+} ions were coordinatively saturated with six aqua ligands. The exchanged metal cations retained the aqua ligands even after the activation hence direct interaction between the cation and adsorbed hydrogen did not take place. Consequently, the adsorption isotherms for three samples including DMA^{+}, Li^{+}, and Mg^{2+} were almost similar.

Dinca and Long reported that Mn^{2+} ions in an anionic framework, Mn-BTT, could be exchanged with a variety of metal ions such as Li^{+}, Cu^{+}, Fe^{2+}, Co^{2+}, Ni^{2+}, Cu^{2+}, and Zn^{2+}[Dincaand Long, 2007]. The original material shows the enthalpy of adsorption of 10.1 kJ mol^{-1} and those cation-exchanged materials exhibits marginal drop in enthalpy of adsorption for Li^{+} (8.9 $kJmol^{-1}$), Cu^{+} (9.9 kJ mol^{-1}), Ni^{2+} (9.1 $kJmol^{-1}$), Cu^{2+} (8.5 $kJmol^{-1}$), and Zn^{2+} (9.6 $kJmol^{-1}$) respectively and a slight increase in case of Fe^{2+} (10.2 kJ mol^{-1}) and Co^{2+} (10.5 kJ mol^{-1}). Yang et al. reported the kinetics and hysteresis of the H_2 adsorption directly related to cation exchange [Yang *et al*., 2009]. NOTT-200 which was synthesized in the presence of piperazine (ppz), has a doubly interpenetrated anionic structure with three kinds of channels with sizes of 6.6 Å ×4.4 Å (channel A), 4.3 Å ×4.1 Å (channel B), and 4.6 Å ×1.0 Å (channel C). Single crystal X-ray analysis proved that the NH^{2+} group of the piperazine located in channel B, which forms hydrogen bonds with the oxygen atoms of the ligand. This MOF shows big hysteretic N_2 and H_2 adsorption isotherms due to the entrapment of H_2 and ppz^{2+} inside the channel B. When the ppz^{2+}cation is substituted with Li^{+} by immersion of the MOF in a LiCl solution, structure created was called NOTT-201. NOTT-201 shows enhanced H_2 adsorption capacity from 0.96 wt % to 1.02 wt % at 78 K and 1 bar as well as increased enthalpy of adsorption from 9.0 kJ mol^{-1} to 10.1 kJ mol^{-1}.

Mulfort and Hupp reported a MOF $Zn_2(NDC)_2(diPyNI)$ doped with 5 mol% Li^+cations. This was obtained by the cation exchange of a doubly interpenetrated structure containing redox active ligand N,N-di-(4-pyridyl)-1,4,5,8-naphthalene tetracarboxy di-imide (diPyNI) with a Li salt solution in DMF. The Li^+ doped material showed the H_2 uptake of 1.63 wt% at 77 K and 1 bar, which is considerably higher than 0.93 wt% in the original material [Mulfortand Hupp, 2007]. The enthalpy of adsorption also increased from 5.5 kJ mol^{-1} to 6.1 kJ mol^{-1} after the Li^+ ion doping. The unusual enhancement in the hydrogen loading (more than 60 H_2 atoms / Li cation) is rationalized due to framework displacement and/or increase in polarizability of the strut due to reduction with Li. In other works they reduced the organic linker of doubly interpenetrated $Zn_2(NDC)_2(diPyNI)$ and triply interpenetrated $Zn_2(NDC)_2(diPyTz)$ (diPyTz = 3,6-di(4-pyridyl)-1,2,4,5-tetrazine) with an alkali metal (Na, Li, and K) naphthalenides. All alkali metal doped MOFs exhibits enhanced N_2 and H_2 sorption properties.The order of average enthalpy of adsorption for $Zn_2(NDC)_2(diPyNI)$/3M is $Li^+ > Na^+ > K^+$, which corresponds to the ratio of cation charge to radius. This must be related with the strength of the interaction between the alkali cations and quadrupole moment of H_2. However, a triply interpenetrated framework, $Zn_2(NDC)_2(diPyTz)$, represents the different ΔH_{ads} order ($K^+ > Na^+ > Li^+$). Although the results represent enhanced hydrogen uptakes at 77 K and 1 bar by doped metal cations, they do not claim a direct relationship between hydrogen sorption capacities and enthalpy of adsorption. They indicated that the catenated structures might cause adsorption site heterogeneity [Mulfort*et al*., 2009, Nouar*et al*., 2009]. The improved N_2 and H_2 uptakes are not attributed to the direct access of the gas molecules to the doped metal cations directly, but cation induced displacement of the catenated MOF [Mulfortand Hupp, 2008; Mulfort*et al*., 2009]. The authors thus conclude that direct reduction of suitable framework struts as

another method for doping Lithium into the framework. However, in such cases framework displacement is reasoned to be the major cause for enhancement of hydrogen uptake rather than the direct interaction of the hydrogen molecules with the dopant.

In another work Mulfort*et al*. reported the effect of non-catenated hydroxyl functionalized MOF by exchanging the proton of the hydroxyl group with Li or Mg cations. They achieved lithium loading by exchanging (via soaking) the initially present guest solvent molecules (DMF) with more volatile THF and then stirring the MOF in an excess of Li-[$O(CH_3)_3$] in CH_3CN/THF. The extent of lithium loading is controlled by adjusting the stirring duration and speed. When the Li^+/Zn^{2+} ratio was about 0.20, the BET surface area, the pore volume and the H_2 uptake increase marginally (1.23 to 1.32 wt%, at 77 K, 1 bar). While the isosteric heat of H_2 adsorption at zero loading remained almost the same (6.3 kJ mol^{-1}), it increased to about 6.6 kJ mol^{-1} at higher H_2 loadings in case of Li doped MOF (in case of undoped MOF it decreases to 4.7 kJ mol^{-1}). While doping with Mg also produced similar results at a Mg^{2+}/Zn^{2+} of about 0.86, higher Mg doping (Mg^{2+}/Zn^{2+} ratio > 2) resulted in loss of surface area and inferior H_2 loadings, although isosteric heat increased slightly. They hypothesize that the metal remains naked in the structure at low to intermediate doping and as a result the hydrogen uptake enhances by about 2 molecules per dopant atom [Mulfort*et al*., 2009].

Himsl*et al*. exchanged the protons of hydroxyl pendants in MIL-53(Al) with lithium by using lithium di-isopropyl amide (LDA). By chemical analysis, it was found that 15% of the acidic framework protons were exchanged with lithium. The apparent BET surface area of MIL-53(Al)/Li were 1384 m^2 g^{-1}, which is smaller than that of the pure MIL-53 (1566 m^2 g^{-1}). The H_2 uptake capacities at 77 K and 1 bar were 0.5 wt% and 1.7 wt% for pure MIL-53(Al) and MIL-53(Al)/Li, respectively. The enhancement of the H_2 storage in

MIL-53(Al)/Li was not only due to the lithium doping but also due to the temperature-induced structural transformation. The isosteric heat of H_2 adsorption clearly demonstrated the impact of Li^+ doping on hydrogen sorption. Compared with the virgin MOF which has an adsorption enthalpy of 5.8-4.4 kJ mol^{-1}, MIL-53(Al)/Li has enthalpy of adsorption 11.6-6.4 kJ mol^{-1}, which approaches the theoretical maximum value of ca. 13 kJ mol^{-1}[Himsl*et al*., 2009].

Xiang *et al*. [2012] reported the effect of Li doping (using lithium napthalenide) in Cu-BTC and Cr-BDC on their hydrogen adsorption properties. While, the surface area and pore volume of the MOFs decrease significantly after doping they report that the hydrogen uptake increases by more than 40% compared to undoped MOFs. While, no other study in literature reports such results, it is worth mentioning that such a behavior is not supported by earlier studies or theoretical models. Frost and Snurr [Frost and Snurr, 2007] demonstrated that at intermediate loadings surface area plays and important role while at higher loadings micropore volume is important. Moreover, the loadings reported in the work of Xiang et al. for parent Cu-BTC and Cr-BDC MOFs are considerably lower than those reported elsewhere in literature. Table 2.6 lists the effect of metal doping on hydrogen storage capacities of some MOFs.

2.3.5. Heavy Metal Impregnation in MOFs

While the doping of light metal atoms into the MOF structures introduces point charges thereby increasing the binding energy for the hydrogen molecules, the interaction energies are still small and resultant metal-hydrogen complexes are unlikely to be stable at room temperature [Klontzas*et al*., 2008]. Another approach is to introduce transition metals into the structure to produce a stable scheme through Kubas type interaction

(where the d orbitals of the metal interact with the antibonding orbitals of hydrogen), thereby enhancing the hydrogen storage capacities.

Several researchershave also reported improved hydrogen physisorption properties for metal organic frameworks and ordered mesoporous carbons by deposition of Pd nanoparticles using incipient wetness impregnation (Table 2.7). Kaskel and co-workers deposited 1 wt% Pd to form Zn-BDC/Pd using palladium acetylacetonate as precursor and chloroform as solvent. Reduction in hydrogen atmosphere and subsequent drying are performed at 473 K. The deposition of Pd led to a significant decrease in surface area ($958 m^2 g^{-1}$) and pore volume ($0.39 cm^3 g^{-1}$) compared to pure Zn-BDC ($2885 m^2 g^{-1}$, $1.18 cm^3 g^{-1}$), indicating also partial destruction of the MOF structure during synthesis. Although the nature of palladium is not characterized, it is also reported that when 1 wt% of palladium is impregnated in the Zn-BDC by immersion of Zn-BDC in a chloroform solution of $Pd(acac)_2$ followed by H_2 reduction; the hydrogen storage capacity of Zn-BDC increased from 1.15 wt% to 1.86 wt% at 77 K and 1 bar [Sabo *et al*., 2007].

Suh and coworkers documented the fabrication of small palladium nanoparticles (3.0-0.4 nm, 3 wt% Pd) in a redox-active MOF (SNU-3) without using a reducing agent and stabilizer (caping agent), and reported the enhanced H_2 adsorption capacity of the MOF containing the Pd-NPs [Cheon and Suh, 2009]. The hydrogen storage capacity of the MOF containing 3 wt% Pd-NPs increases to about 1.48 wt% of H_2 at 77 K and 1 bar (from 1.03 wt% for pure MOF).To check with the spillover effect they calculated enthalpy of adsorption. SNU-3/Pd has less enthalpy of adsorption,6.62 kJ mol^{-1} than pure SNU-3 (8.11 kJ mol^{-1}) hence no 'Spillover' is reported. Pd nanoparticles can be incorporated inside a MOF crystal like core-shell [Zhao *et al*., 2014] or just placing it near to the surface (by creating a crystal defect) [Park *et al*., 2011]. In order tosynthesizea

novel catalyst Gao and coworkers prepared Zn-BDC/Pd, by a chemical method atroom temperature [Gao*et al*., 2010].The catalyst consisted of highly dispersed Pd-NPs (about 3–6 nm) on Zn-BDC with a moderate surface area ($533 m^2 g^{-1}$).Similarly,Zn-BDC/Pd and Zn-BDC/Ruhave also been successfully synthesized by gas phase loading [Turner *et al*., 2008].

Latroche and co-workers studied the hydrogen sorption properties of Pd and a Pd_xNi_y alloy deposited on ordered mesoporous carbons replicated from SBA-15 [Campesi*et al*., 2009]. Hydrogen uptake measurements showed that the addition of Pd and Pd_xNi_y increase the hydrogen uptake at room temperature. In case of Pd activated carbon, the capacity at room temperature is found to be eight times higher than activated carbon (0.08 wt% instead of 0.01 wt% at 5 bar); Pd_xNi_y activated carbon yielded three fold increase (0.027 wt% instead of 0.01 wt% at 5 bar).

Recently a series of Pd-doped Cr-BDC samples with different Pd content (1, 3 and 5 wt %) and valence state have been prepared by Li and co-workers [Qin *et al*., 2014]. These composites are used as adsorbents for toluene adsorption and hydrogen storage. With 3wt% Pd content the surface area decreases from 3190 to 2850 $m^2 g^{-1}$ whereas H_2 uptake improves from 0.28 wt% to 0.64 wt% at 298 K, 73 bar (see Table 2.8). The hydrogen storage studies indicates that the reversible storage capacities on the Cr-BDC/Pd samples at room temperature are enhanced by a factor of 1.5–2.3 compared with that of the pure Cr-BDC [Qin *et al*., 2014].

Pd nanoparticles embedded in the metal organic framework MIL-100(Al) have been successfully synthesized by incipient wetting [Zlotea*et al*., 2010]. The corresponding MIL-100(Al)/Pd composite synthesized by Zlotea and co-workers reported high metal contents (10 wt%) without degradation of parent material. Most of the highly dispersed

Pd NPs (average dia 2.5 nm) are located within the pores of MIL-100(Al). This changed the textural properties with a loss of specific surface area (went down from 1200 to 380 m^2 g^{-1}) and of micropore volumes (went down from 0.4 to 0.12 cm^3 g^{-1}). The loss of excess hydrogen storage at 77 K has been correlated with the decrease of the specific surface area and pore volume after Pd impregnation. At room temperature however, the hydrogen uptake in the composite is enhanced significantly; at about 80 bar the uptake capacity increased from 0.19 to 0.35 wt% after incorporating Pd. This was attributed to the formation of Pd hydride and partially due to the so called "spillover" effect. They did not estimate enthalpy of adsorption to support it further.

Heavy transition metal nanoparticles embedded in MOFs are not so recycleable for H_2 adsorption and desorption. Pt doping in MOF-177 is reported by Proch*et al*. [2008]. Surface area and pore volume decreases from 5600 m^2 g^{-1}, 1.69 cc g^{-1} 867 m^2 g^{-1}, 0.39 cc g^{-1} respectively. MOF-177/Pt adsorbed 2.5 wt % of H_2 at room temperature and 144 bar in the first adsorption cycle. Again, in the second cycle, the uptake capacity considerably decreased to 0.5 wt %, which was close to the value of pure MOF-177. They stated this difference is due to the formation of Pt-hydride in the first cycle, from which hydrogen could not be desorbed at room-temperature.

2.3.6. MOF Composites

MOF composites are being recently synthesized for potential application in the field of energy and environment. Carbon dioxide and hydrogen adsorption capacities of MOF composites are better than virgin MOFs owing to the synergetic effect of its constituent MOF as well as the other substrate used in the composite such as activated carbon (AC), Graphene Oxide(GO), Expanded Natural Graphite (ENG) etc. [Kumar *et al*., 2013]. Graphene oxide (GO), rich with functional groups is a prospective constituent to

construct graphene-based hybrid composites [Liu *et al*., 2013]. Petit and Bandosz have reported the formation of MOF/GO composites via interactions between oxygen groups of GO and metallic centers of MOF, where the synergetic effect between MOF units and GO layers was responsible for enhanced adsorption amounts on $Zn(MeIM)_2$, (MeIM = 2-methyl imidazolate) compared to the pure MOF [Petit and Bandosz, 2010 , Petit and Bandosz, 2011]. Recently, the nanosized Cu-BTC and ZIF-8 have been induced by the incorporation of GO component. Similarly, Bajaj and coworkers synthesized Cr-BDC/AC composite under hydrothermal conditions by adding AC in different proportions during the synthesis. To reduce the unutilized voids in Cr-BDC by incorporating microporous activated carbon pores of MOF enhances its volumetric hydrogen storage capacity [Rallapalli*et al*., 2011]. Siegel and coworkers successfully synthesized Zn-BDC/ENG (expanded natural graphite) composites. They concluded that introducing a small of amounts of ENG to compacted Zn-BDC provides a simple way to enhance thermal properties with only modest decreases in the hydrogen storage amounts [Purewal et al., 2012]. Hydrogen uptake capacity in selected hybrid composite is shown in Table 2.7.

2.3.7. Heavy Metal Doped MOF Composites

Although some results of doping transition metals in carbons and MOFs indicate that hydrogen uptake capacity can be improved, incorporation of transition metals effectively into the MOF structure and the considerable contribution of the heavy transition metals have to reduction in gravimetric storage capacity remains a major challenge [Klontzas*et al*., 2008; Mavrandonakis et al., 2009]. In order to overcome the difficulty, an alternate methodology is suggested in literature, where transition metals are introduced into the MOF structure by synthesis of a MOF composite with materials such as activated carbon, graphene oxide etc. The carbonaceous materials (activated carbon or graphene) may be

pre-loaded with transition metals such as Platinum or palladium to desired percentage thereby effectively incorporating Pd/Pt into the MOF structure. Considerably low loading quantities of transition metals can be achieved in addition to avoiding difficulties associated with clustering. There are also reports in literature that suggest metals such as Pt/Pd result in enhanced loading of hydrogen in highly porous materials such as activated carbon and MOFs due to so called spillover effect [Wang and Yang, 2008], if a successful "bridge" can be created between the metal and the substrate (MOF). Since MOF bridging technique necessary to achieve the spillover effect is highly uncertain, doping nanoparticles through in-situ synthesis method into MOF/GO units exhibits more controllable and reliable synthesis procedure [Zhou *et al*., 2014].

The use of Pd as a hydrogen adsorbent itself is restricted because of its high price and low hydrogen content. However, it can be used in low concentrations as an effective catalyst for dehydrogenation facilitating spillover effect. Spillover is a phenomenon known from heterogeneous catalysis and describes the transport of an activated species adsorbed on a first surface onto another surface that does not adsorb hydrogen readily under the same conditions [Conner *et al*., 1995]. Enhancing the contact between the source and receptor is very crucial to achieve successful the spillover effect.Pt or Pd bridged to MOF with carbon as support result in hydrogen spillover and improved capacity. Hydrogen molecules first dissociate on the Pd nanoparticles to form hydrogen atoms that then spill over to the MOF/carbon support[Wang and Yang, 2008]. The enthalpy of adsorption reported was higher for the modified MOF. Even though the hydrogen uptake capacity is low compared to supported metal hydride system, these studies show that hydrogen storage in classical physisorption systems can be considerably improved by using catalysts [Wang and Yang, 2010].

Li and Yang reported thatby physically mixing 5 wt% Pt on activated carbon (AC) with MOF and then building the carbon bridge between them secondary spillover is facilitated. The hydrogen uptakes at 298 K of bridged Zn-BDC and IRMOF-8 have been improved greatly compared to those of unbridged-MOFs [Li and Yang, 2006]. Similarly, the enhancement of hydrogen storage capacities is also observed on bridged-MOF-177 [Li and Yang, 2007], Cr-BDC and MIL-53 [Liu *et al*., 2007, Li and Yang, 2008].However, contradictory reports on spillover effect are available in the literature [Luzan*et al*., 2010]. The reproducibility of hydrogen spillover enhancement by bridge-building method was affected by many factors, including contacts between the dissociation source and receptor, metal particle sizes and doping method, etc. [Campesi*et al*., 2010, Stucke*et al*., 2010].Table 2.7 lists representative literature reports on hydrogen storage capacities of various heavy metal doped MOFs and their composites.

2.4. Summary

This literature review indicates more variation in the adsorption uptakes for MOFs than that for other porous adsorbents such as zeolites, mesoporous silica and allotropes of carbon. MOFs seem to have variable pore size and structures and thereby allow for easy functionalization and tuning to enhance hydrogen adsorption. Adsorption uptakes in both gravimetric and volumetric scale are found to be somewhat higher on MOFs than that on other porous adsorbents at room temperature as well as at cryogenic temperature. While significant studies are done at 77 K and at room temperature adsorption on MOFs, the research work reported on adsorption at intermediate cryogenic temperatures on MOFs is rather limited.

Later part of this literature review includes discussion on literature available on modification of MOF structures via post synthesis modification procedure.

Cationexchange and/or doping of alkali /alkali earth materials enhances hydrogen uptake in some MOFs. Synthesis and hydrogen adsorption properties of MOF composites and composites doped with transition metals such as Pt and Pd are also reviewed. Some of these composites perform better than pure MOF constituent. While a few research groups report that MOF structures can be modified for enhanced hydrogen uptake via spillover effect, these results were not reproducible readily. While, the theory behind spillover effect itself is not challenged, the successful synthesis and performance of a material exhibiting spillover effect is still confined to the laboratories of extremely few research groups only.

The literature review indicates that a systematic study on hydrogen adsorption at intermediate temperatures for a variety of MOFs is rather limited. While a few reports exist in literature on alkali metal and heavy metal doping to enhance hydrogen adsorption characteristics of some of the well-studied MOFs in literature (such as Cu-BTC and Cr-BDC), the alkali metal doping does not seem to significantly enhance their hydrogen adsorption characteristics. The results of heavy metal doping are even more confusing with varying degrees of success; while some groups report successful synthesis of material exhibiting spillover effect, others report doped materials exhibit a drop in gravimetric hydrogen storage capacity. With this background this thesis aims to carry out the research objectives mentioned in Chapter 1.

Figures

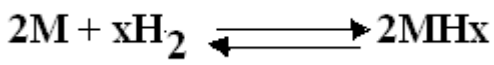

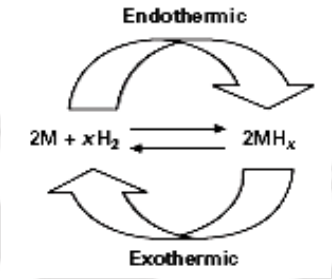

Figure 2.1: A Generic reaction Equation for the Reversible Hydrogenation and Dehydrogenation [Walker, 2008]

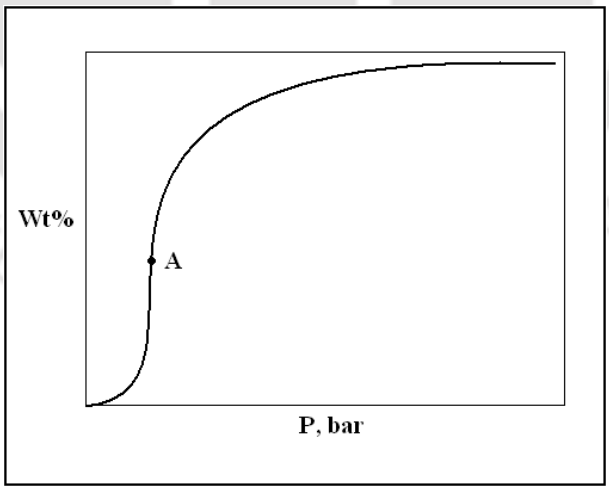

Figure 2.2: A Typical Pressure Composition Isotherm [Walker, 2008].

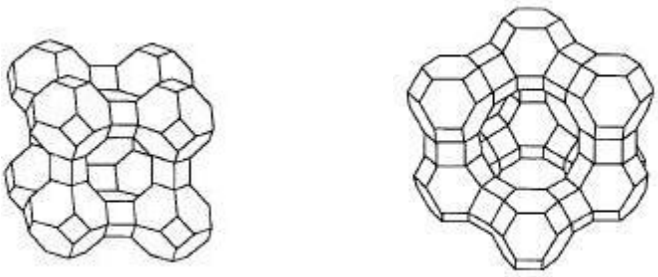

(a) (b)

Figure 2.3: Schematic Diagrams Depicting Framework Structures of two Common Zeolites Types (**a**) Zeolite A (**b**) Zeolite X or Y **[**Yang, 1997, Ruthven and Sun, 1984**]**.

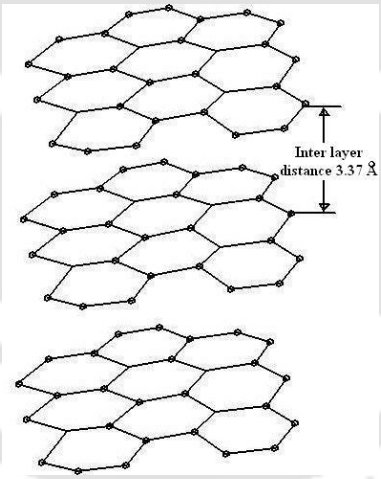

Figure 2.4: Schematic Diagrams Representing Graphene [Geim and Novoselov, 2007]

Tables

Table 2.1: Hydrogen Uptake on Selected Zeolites, Allotropes of Carbon and Silica based Material.

Adsorbent	**T, K**	**P, bar**	**Wt%**	**SSA_{BET} (m^2g^{-1})**	**Pore Volume (ccg^{-1})**	**References**
Activated Carbon	233	60	0.98			
	298	60	0.5	3000	1.3	[Zhou *et al*., 2004]
Multi wall CNT	298	100	0.24	137	NA	
Single wall CNT	77	1	1.7			[Takagi *et al*., 2004]
	303	30	0.25	710	0.25	
Graphene	77	10	1.2		NA	
	123	10	0.6	640		[Srinivas*et al*., 2010]
	298	10	0.1			
Zeolite CaX	77	15	2.19	669	NA	[Langmi*et al*., 2005]
ZSM-5	303	30	0.3	330	0.15	[Takagi *et al*., 2004]
MCM-41	77	35	1.6	1017	0.73	[Sheppard *et al*., 2005]
	77	1	0.44	1324	NA	[Wu *et al*., 2009]

Table 2.2: Selected Organic Linkers as MOF Constructor

Organic Linker	**Organic Linker**
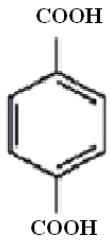 Terepthalic Acid (BDC) BDC is used to synthesize MOF-5, MIL-53, MIL-101 etc.	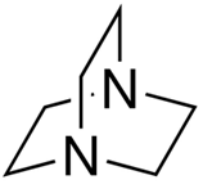 1,4-Diazabicyclo[2.2.2]Octane (DABCO)
Together BDC and DABCO is used to synthesize M-DABCO (M= Ni, Cu, Zn)	
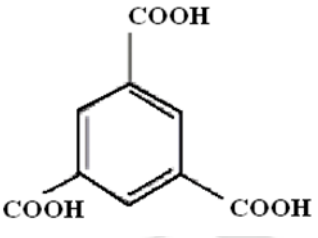 Trimsic Acid (BTC) BTC is used to synthesize Cu-BTC, MIL-100 etc.	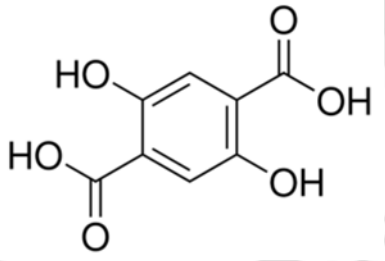 2,5-Dihydroxy Terepthalic Acid (DOBDC) DOBDC is used to synthesize M-DOBDC (M= Fe, Co, Ni, Mg, Mn)

<table>
<tr>
<td> 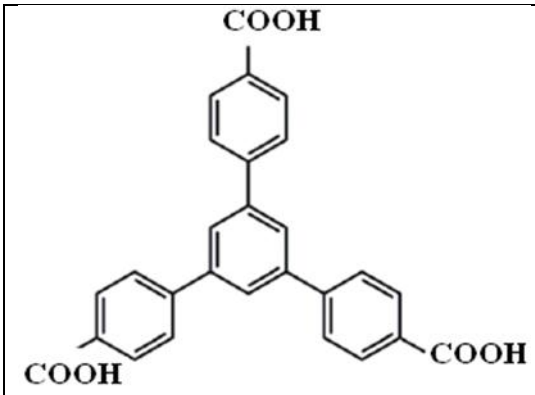

Benzene Tribenzoic acid

BTB is used to synthesize MOF-177</td>
<td> 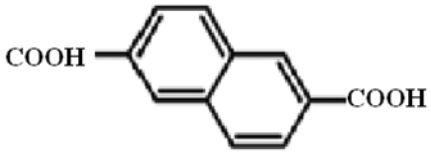

Napthalene 2,6-dicaroxilic Acid (NDC)

NDC is used to synthesize Al-NDC</td>
</tr>
<tr>
<td colspan="2">Together BTB and NDC are used to synthesize MOF-205

Together NDC and DABCO are used to synthesize Zn(NDC)dabco, Cu(NDC)dabco</td>
</tr>
</table>

Table 2.3: Hydrogen Uptake on Selected MOFs.

Adsorbent	**T, K**	**P, bar**	**Wt%**	**SSA_{BET}, m^2g^{-1}**	**Pore Volume, cm^3g^{-1}**	**References**
Co(NDC)DABCO	77	1	2.45	1502	0.82	
	298	17.2	0.89			[Chun *et al*., 2008]
Zn-BDC or MOF-5 or IRMOF-1	77	20	4.5	2833	1.13	[Rosi*et al*., 2003, Foy *et al*., 2006]
	298	20	1	2833	1.13	
	293	20	0.12	832	0.3	[Luzan*et al*., 2009]
	101	20	0.85	623	0.38	[Sahu*et al*., 2013]
	136	20	0.6			
	169	20	0.25			
Ni(BDC)DABCO	77	50	3.76	1809	NA	
	299	50	0.65			[Song *et al*., 2011]
	145	50	2.39	1904[$]	0.98[$]	[Sahu*et al*., 2013]
	192	80	2.4			
SNU-4	77	50	3.7	1460*	0.53	[Lee *et al*., 2008]
Be-BTB	77	25.7	6.04	4030	1.48[§]	[Sumida *et al*., 2012]
	298	95	1.01			

*Langmuir surface area; [$]Mishra et al., 2013; [§]measured with Ar

Table 2.4: Hydrogen Uptake Capacity of MOFs with Open Metal Sites

Adsorbent	**T, K**	**P, bar**	**Wt%**	**SSA_{BET}, m^2g^{-1}**	**Pore Volume, cm^3g^{-1}**	**References**
Cu-BTC or HKUST-1	77	50	3.8	1482	0.83	[Liu *et al*., 2007]
	175	50	1			
	298	50	0.3			
Mg-DOBDC or MOF 74	77	80	3.2	1800	0.66	[Sumida *et al*., 2011]
	298	80	0.5			
	101	80	3.6	1048	0.58	[Sahu*et al*., 2013]
	133	80	3.2			
	192	80	2.4			
Ni-DOBDC	77	10	3	1056	0.44	[Zhou *et al*., 2008]
Co-DOBDC	77	10	2.5	1027	0.48	
PCN-10	77	20	4.33	1779*	0.67	[Wang *et al*., 2008]
PCN-11	77	20	5.05	2442*	0.91	
PCN-12	77	1	3.05	2425*	0.94	
PCN-12’	77	1	2.4	1962*	0.73	
SNU-5	77	50	5.22	2850	1	[Lee *et al*., 2008]
	298	100	0.5			
MIL-53 (Cr)	77	16	3.1	1026	0.59	[Fereyet *al*., 2003]
MIL-53 (Al)	77	16	3.8	1020	0.56	
	293	50	0.37	NA	NA	[Liu *et al*., 2007]
Mn-BTT	77	90	5.1	2100	0.795	[Dinca et al., 2006]

*Langmuir surface area

Table 2.5: Hydrogen Uptake on Large pore MOFs

Adsorbent	**T, K**	**P, bar**	**Wt%**	**SSA_{BET}, m^2g^{-1}**	**Pore Volume, $cm^3\ g^{-1}$**	**References**
Cr-BTC	77	26.5	3.28		1	
or MIL 100	298	73	0.15	2700*		[Latroche*et al*., 2006]
Cr-BDC	77	80	6.1		1.9	
or MIL-101	297	80	0.43	5500*		
	136	80	2.5		1.52	[Sahu*et al*., 2013]
	165	80	1.7	2927		
MOF-177	77	70	7.5	3275[#]	2.65[#]	[Foy *et al*., 2006]
or Zn-BTB	298	100	0.62			[Li *et al*., 2007]
NOTT-112	77	40	7.07	3800	1.62	[Yan et al., 2009]
NOTT-116	77	27	6.4	4664	2.17#	[Yan et al., 2010]
NU-100	77	56	9.95	6143	2.82	[Farha et al., 2010]
PCN-61	77	33	6.24	3000	1.36	[Yuan *et al*., 2010]
PCN-68	77	50	7.32	5109	2.13	
MOF-200	77	46	7.33	4530	3.59	[Furukawa *et al*., 2010]
MOF-205	77	35	7.02	4460	2.16	
MOF-210	77	65	8.73	6240	3.6	

*Langmuir surface area; #measure with Ar; [#]Saha and Deng, 2010;

Table 2.6: Hydrogen Uptake (77 K, 1 bar) on Cation Doped MOFs and Functionalized MOFs

MOF/dopant	**Wt%**	**SA_{BET} m^2g^{-1}**	**Wt%**	**V_{Pore} cm^3g^{-1}**	**SA_{BET} m^2g^{-1}**	**References**
	Pure MOF		**After doping**			
Cu-BTC/Li	2.41	1587	3.5	0.51	795	[Xiang *et al*., 2012]
rho-ZMOF/Mg			0.91[$]	NA	NA	[Nouar*et al*., 2009, Liu *et al*., 2006]
rho/ZMOF/Li	0.95[$]	1067*	0.91[$]	NA	NA	
Mn-BTT/Fe			2.21	NA	2033	
Mn-BTT/Co			2.12	NA	2096	
Mn-BTT/Ni	2.23	2057	2.29	NA	2110	[Dinca and Long, 2008]
Mn-BTT/Li			2.06	NA	1904	
Cr-BDC/Li	2.37	2537	3.39	1.38	1840	[Xiang *et al*., 2012]
Zn(NDC)diPyTz/Li	1.12	400	1.46	0.19	526	
Zn(NDC)diPyTz/Na			1.6	0.21	558	[Mulfort*et al*., 2009]
Zn(NDC)diPyTz/K			1.51	0.2	509	
NOTT-206/Li	0.73	138	0.89	0.2	475	
NOTT-200/Li	0.94	180	1	0.24	580	[Yang *et al*., 2011]
NOTT-208/Li	1	687	1.3	0.3	729	

[$]at 78 K, 0.95 bar, *****Langmuir surface area

Table 2.7: Hydrogen uptake on Selected MOF Composites

MOF	**T, K**	**P, bar**	**wt%**	**V_{Pore} cm^3g^{-1}**	**SA_{BET} m^2g^{-1}**	**References**
SNU-3/Pd	77	1	1.48	0.21	242	[Cheon and Suh, 2009]
	298	95	0.3			
Cr-BDC/Pd (3%)	298	73	0.64	1.25	2449	[Qin *et al*., 2014]
Cr-BDC/Pd (5%)	298	73	0.48	1.2	2385	
Zn-BDC/ENG (1%)	77	44	4.66	NA	2584	
Zn-BDC/ENG (5%)	77	40	4.94	NA	2781	[Purewal*et al*., 2012]
Zn-BDC/CNT	77	1	1.5	0.765	2900	
	298	100	0.6			[Yang *et al*., 2009]
Cr-BDC/AC	77.4	60	10.1	2.61	3555	[Ralapalli*et al*., 2013]
Cu-BTC/GO	77	40	3.58	0.64	1532	[Liu *et al*., 2013]
IRMOF-8/Pt-AC	298	100	0.85	0.59	1175	[Wang *et al*., 2011]
IRMOF-8/Pt-AC	298	69	4.7	NA	400	[Tsao*et al*., 2009]
IRMOF-8/Pt-AC	298	75	2.5	NA		[Miller *et al*.,2009]
Cr-BDC/Pd-GO	77	40	3.1	0.33	380	
	298	40	1.9			[Zlotea*et al*., 2010]
MOF-177/Pt-AC	298	100	1.5	NA	NA	[Li and Yang, 2006]
Cr-BDC/Pt-AC	298	50	1.14	NA	NA	
MIL-53/Pt-AC	298	50	0.63	NA	NA	[Liu *et al*., 2007]
Cr-BDC/Pt-AC	298	100	1.5	NA	2580	
Cu-BTC/Pt-AC	298	100	1.1	NA	1116	[Yang and Wang, 2008]
Co-DABCO/Pd-AC	298	100	0.31	NA	NA	
Zn-DABCO/Pd-AC	298	100	0.41	NA	NA	[Lin *et al*., 2014]

CHAPTER 3

Experimental Methods

This chapter outlines various methods used for characterization of MOF materials synthesized in this work. A brief on the experimental protocol for measurement of adsorption uptake, the definition of adsorption uptake and the methodology followed for conversion of raw experimental data into various types of adsorption uptakes (absolute, excess, net etc.) are also presented. Finally, some preliminary results for hydrogen sorption on palladium nanoparticles which were used to understand the synthesis of Pd nanoparticles (necessary for synthesis of MOF composites as discussed later) are presented. These preliminary studies were also used to understand the limitations of the gravimetric hydrogen uptake measurement unit used in this study.

3.1. Characterization Techniques

3.1.1. Transmission Electron Microscopy

Transmission electron microscopy (TEM) is a tool for the characterization of structure and morphology of nanoparticles. Selected area electron diffraction (SAED) attached to it provides information about crystallinity of the sample. In the TEM setup electron beams generated by the electron gun are accelerated to energy level of 50 – 300 keV, highly focused and directed towards the sample. Electrons interact strongly with atoms of the sample by both elastic and inelastic scattering; the sample should not be thicker than ~200 nm to allow transmission. Behind an objective lens, an objective aperture is placed in the back focal plane. By the positioning of the objective aperture on specific positions in the back focal plane, two kinds of images can be obtained. An image is formed when aperture allows only transmitted electrons to pass through the bright-field (BF). In the dark field

(DF) mode the aperture can be positioned to pass only diffracted electrons. This is called selected area electron diffraction (SAED) analysis. The transmitted or diffracted signal from the sample is magnified by a system of electromagnetic lenses and finally is visible as an image on the fluorescent screen [Egerton *et al*., 2005, Amrita Virtual Laboratory]. Except diffraction and spatial imaging, the inelastically scattered high-energy electrons produced in TEM cause electronic excitation of the atoms of the sample under investigation. It is possible to obtain the chemical composition of the specimen using energy dispersive X-ray spectra (EDS) attached to the TEM setup.

TEM (Jeol, JEM 2100) in the bright field mode with an accelerating voltage of 200 kV was used in this work; this instrument allows resolutions up to 1 nm. In this work, Pd nanoparticles and Pd nanoparticles doped ion graphene oxide were characterized using TEM. First, the samples were dispersed in 2-propanol and transferred on 300 mesh copper grid with carbon film on top (Pacific Grid-Tech); the samples were then dried under vacuum before mounting.

3.1.2. Field Emission Scanning Electron Microscopy

A field emission scanning electron microscope (FESEM) analyzes the surface topography and morphology. The electron beam generated from the field emitter (tungsten), focused by several magnetic lenses, hits the sample and electrons from the beam collide with the electrons from the specimen. As a result of elastic scattering highly energetic (>50 eV) back scattered electrons (BSE) are reflected in back scattered mode. Due to inelastic collisions secondary electrons (SE) essentially have lower energy (2-50 eV). The detected signals are amplified and transferred to a computer; an image of the chosen area is obtained with typical resolution upto 1 nm [Reimer *et al*., 1998]. In the backscattered mode incident electrons are elastically scattered with higher energy by the

sample under investigation. Sample is coated with either gold or palladium using a sputtering unit to enhance the scattering by increasing the conductivity of the surface. The brightness of the image formed by backscattered electrons depends on the atomic number of the element constituting the sample. Darker images are formed when the light elements are present in the sample whereas heavier elements appear bright. FESEM provides narrow probing beams at low as well as high electron energy, resulting in improved resolution.

FESEM (Zeiss, Sigma) was used in a secondary electron mode to obtain the images of the Pd nanoparticles. Sample dispersed in 2-propanol was dropped on an aluminum foil, dried under vacuum overnight and then coated with gold.

3.1.3. Thermogravimetric Analysis

Thermogravimetric analysis (TGA) is a method of thermal analysis in which changes in physical and chemical properties of materials are measured as a function of increasing temperature (with constant heating rate), or as a function of time (with constant temperature and/or constant mass loss). TGA plot can be interpreted to understand physical change in a material with change of temperature, such as second-order phase transitions like vaporization, sublimation, absorption, adsorption, and desorption. TGA plot can be interpreted for chemical phenomena including chemisorption, dehydration, decomposition, and solid-gas reactions (e.g., oxidation or reduction). TGA may also be useful for predicting (1) degradation mechanisms [Narayanan *et al*., 1997], (2) determination of organic content in a sample, and (3) determination of inorganic (e.g. ash) content in a sample.

A Mettler TOLEDO analyzer (model no. TGA/SDTA851^e) and NETZSCH analyzer (model no. STA449 F3 Jupiter) have been deployed for TGA analysis of the adsorbents to

understand the thermal stability of the materials as well as to determine the temperature needed for activation of the samples prior to hydrogen adsorption measurements (degassing).

3.1.4. X-ray Diffraction Analysis

X-ray diffraction (XRD) technique is an important characterization technique which is commonly used for determining the structural of materials. All atoms in crystalline materials are considered as sets of parallel crystallographic planes which are characterized by Miller indices (h k l). Diffraction maxima occur when a certain set of crystallographic planes fulfill conditions for constructive interference provided by the Bragg's law (see Figure 3.1) [Luzan, 2012]:

$$2d \sin\theta = n\lambda \qquad (3.1).$$

where θ is the angle between the incident beam and the crystallographic plane, d is the distance between two successive crystallographic planes, λ is a radiation wavelength, and n is an integer number. X-ray tube, the detector, and the sample are located on the focusing circle. The X-ray tube is fixed, and the detector moves along the goniometer circle with an angular speed which is two times that of the sample (the rotational axes of the sample and of the detector coincide). During the XRD analysis the detector is always at 2θ angle and the sample surface is always at θ angle with respect to the incident beam. The detector scans around the sample in the specified 2θ intervals and records the angle and the intensity of diffracted radiation.

Pd nanoparticles as well as MOFs used in this work were characterized using PXRD. These XRD measurements are carried out for synthesized materials using monochromatic

Cu-Kα radiation source (λ=1.54178 Å). A Bruker D8 Advance instrument operating at 40 kV and 40 mA is used to analyze the samples.

3.1.5. Atomic Adsorption Spectrometry (AAS)

Atomic absorption spectrometry (AAS) is an analytical technique that measures the concentrations of certain elements in a sample. In an AAS, the sample is atomized/vaporized and converted into the ground state (free atoms) in the vapor phase. Atoms of different elements absorb different characteristic wavelengths of light. To determine metal ion concentration using flame mode this instrument uses air-acetylene or nitrous oxide- acetylene burner. For example with Cu, a lamp containing Cu emits light from excited Cu atoms that produce a proper mix of wavelength to be absorbed by any Cu atom present in the sample. The amount of light absorbed is proportional to the number of Cu atoms. A calibration curve is constructed first by using standard samples and is subsequently used to estimate the concentration of metal in unknown sample solution.

In this study, AAS (Varian, 55B) is used to quantify amounts of Cu in Cu-BTC MOF, Cr in Cr-BDC MOF and Pd in Pd impregnated improved graphene oxide (Pd-IGO) material. Typically about 2 mg of dry sample is digested in 0.6 cm^3 conc. HCl (27%) and diluted with water to a suitable level for further analysis.

3.1.6. Flame Photometry

Flame photometry (FP) principle is based on the fact that the compounds of the alkali and alkaline earth metals can be thermally dissociated in a flame and that some of the atoms produced will be further excited to a higher energy level. When these atoms return to the ground state they emit radiation which lies in the visible region of the spectrum. Each element will emit radiation at a wavelength specific for that element. The Table 3.1

given at the end details the measurable atomic flame emissions of the alkali and alkaline earth metals in terms of the emission, wavelength and the colour produced.

Over certain ranges of concentration the intensity of the emission is directly proportional to the number of atoms returning to the ground state which in turn is proportional to the absolute quantity of the species atomized in the flame, i.e. light emitted is proportional to sample concentration. When the light is emitted by the element at characteristic wavelength, the intensity of that light is measured by a photo-detector. Photo detector generates electrical signal which is proportional to sample concentration. FP (Systronics, Model No. 128) is used to quantify the amount of Li in Cu-BTC/Li and Cr-BDC/Li MOFs. About 2 mg of dry MOF is dissolved in 0.6 cm^3 conc. HCl and subsequently diluted with water to a suitable level for further analysis. A calibration procedure involves analysis of standard samples (of known Li concentration) prepared from a Li salt.

3.1.7. Nitrogen Adsorption Measurements

The porosity of an adsorbent is measured from its nitrogen physisorption at 77 K. The basic principle is to measure the amount of nitrogen adsorbed by the sample and applying theoretical models to convert this amount into physical properties of the sample such as surface area, pore volume, pore size distribution etc. The amount of nitrogen n adsorbed by the material depends on temperature T, equilibrium pressure P, and on the nature of the adsorbent.

$$n = f(P, T, \text{adsorbent}) \tag{3.2}$$

If a specific nitrogen-material system is maintained at a constant temperature T ($T < T_c$ for nitrogen), the amount adsorbed is plotted against the relative pressure (P/P_0) and

the shape of the isotherm can used to deduce whether the adsorbent is a microporous, mesoporous, or a non-porous material.

IUPAC classification of some types of nitrogen adsorption isotherms [Barett *et al*., 1951], is given in Figure 3.2. Type I isotherms are normally measured on microporous adsorbents, e.g. MOFs, activated carbon. Type II isotherms are measured on mesoporous adsorbents. Type III isotherm is found in case of a material having micropores as well as mesopores such as MCM 41. Materials with Type III isotherm do not adsorb nitrogen by layers but nitrogen molecules are clustered around some favorable adsorption sites. Typically, these materials have relatively weak interaction with nitrogen molecules particularly at low pressure, e.g. Pd nanoparticles. Mesoporous adsorbents normally exhibit Type IV isotherms (dotted line in Fig. 3.2) where the monolayer-multilayer adsorption on mesopore walls is followed by capillary condensation.

3.1.7.1. Specific Surface Area

Different models (methods) are applied to interpret nitrogen adsorption isotherm data. *The Brunauer-Emmett-Teller (BET) method* is normally used to estimate specific surface area of the material. This method is based on the following equation:

$$\frac{1}{(\frac{P}{P_0}-1)n} = \frac{1}{Cn_m} + (\frac{C-1}{Cn_m})\frac{P}{P_0} \qquad (3.3)$$

where n is the amount of nitrogen adsorbed at pressure P, n_m is the amount of nitrogen forming a monolayer of surface coverage, and C is a constant which is related to the adsorption energy in the first adsorbed monolayer (C value is typically between 50 and 250). A plot of $\frac{1}{(\frac{P}{P_0}-1)n}$ against relative pressure (P/P_0) yields a straight line with a slope

$\frac{C-1}{Cn_m}$ and an intercept of the line $(C\ n_m)^{-1}$; this plot can be used to obtain n_m. The monolayer coverage n_m can be then converted into surface area S using

$$S = \frac{n_m}{M_r} N_A \sigma \tag{3.4}$$

where M_r is a molecular weight of nitrogen, N_A is the Avogadro constant, and σ is the cross-sectional area of one nitrogen molecule. The linearity range of $\frac{1}{(\frac{P}{P_0}-1)n}$ against relative pressure is different for different types of materials and should be carefully chosen. In this work, a relative pressure (P/P_0) range between 0.05 and 0.3 was used in the BET surface area calculation for all the samples analyzed in Autosorb iQ whereas in Beckman Coulter Surface area analyzer this range is set at 0.05 -0.2.

3.1.7.2. Pore Volume

Dubinin's theory is commonly used to describe pore filling in microporous materials. This theory is described by a general equation for fractional micropore filling:

$$\ln(\frac{n}{n_p}) = -2(\frac{A}{bE_0}) \tag{3.5}$$

where n_p is micropore volume, A is an expression for the "adsorption potential", E_0 is the "characteristic" energy for a standard vapor (normally benzene) and b is a constant [Dubinin, 1960].

$$A = -RT\ln(\frac{P}{P_0}) \tag{3.6}$$

The main disadvantages of Dubinin's method are that this method assumes a homogeneous surface of the material and is not specific towards the pore shape. Other methods are developed for specific pore geometry. For example, the Saito and Foley

method assumes cylindrical pores [Satio and Foley, 1997] whereas the Cheng and Yang method assumes spherical pores [Cheng and Yang, 1994]. Nitrogen adsorption analysis also provides information about the pore size distribution by the model proposed by Barrett, Joyner, and Halenda (BJH). This model is described by the modified version of the Kelvin equation [Barett *et al*., 1951]:

$$r_k RT = -2\gamma V_M \ln\left(\frac{P}{P_0}\right) \qquad (3.7)$$

where r_k is the Kelvin pore radius, γ is the surface tension of nitrogen at its boiling point, V_M is the molar volume of liquid nitrogen, T is the nitrogen boiling temperature, and P/P_0 is the relative pressure. The equation describes successive emptying of pores with radius r_k by lowering relative pressure, P/P_0. The total pore volume calculation was performed at a pre-determined relative pressure of 0.98.

All measurements in this work were performed on one of the two instruments available in our laboratory 1) Quantachrome (Autosorb iQ MP) and 2) Beckman Coulter (SA 3100). Latter is used for pure Zn-BDC and pure Cr-BDC MOFs only.

3.2. Gravimetric Adsorption Measurement

In measurement of adsorption uptake capacity of a sample using gravimetry the adsorbent is placed in a bucket, activated under appropriate condition and sealed (A simple gravimetric setup is shown in Figure 3.3). At this condition the signal from the microbalance under vacuum is due to the mass of the sample and the bucket only (M_0). The sample is then allowed to equilibrate with the gas of interest at equilibrium pressure P and temperature T (at a gas molar density of ρ_{gas}); the mass of the sample changes to its equilibrium value M_t and this signal from the microbalance is recorded. The change in the weight is a result of adsorption occurring on the solid surface and the buoyancy force

acting on the sample and bucket. The equilibrium microbalance signal M_t is related to the Gibbs' excess amount adsorbed, M_{ads} by the relation,

$$M_{ads} = M_t - M_0 + V_{buoyancy}\ \rho_{gas} \tag{3.8}$$

The last term on RHS accounts for the buoyancy correction necessary to convert "raw" experimental measurements into appropriate amount adsorbed as discussed in the next section (Section 3.3). The density of the gas is usually obtained from an appropriate Equation of State (Section 3.4).

3.3. Definition of Adsorbed Amount (Uptake Capacity)

In general, any experiments to measure adsorbed amount require a correction term (last term in Eq. 3.8) as discussed above. In adsorption literature several "types" of adsorption are defined based on the reference state to calculate the buoyancy volume [Do, 1998] or locating the so-called Gibbs dividing surface. The common reference states used in adsorption literature are given in Figure 3.4 [Gumma and Talu, 2010].

A large volume of literature exists discussing the merits and demerits for each case and it is still an ongoing debate in the international adsorption community. However, each one of the reference states has its own advantages and in the following section three such reference states *viz.* absolute adsorption, excess adsorption and net adsorption are briefly explained. This is necessary to perform calculations of actual benefits of using an adsorbent for hydrogen storage as elaborated later.

Consider an adsorbent placed inside a tank that is in equilibrium with the bulk gas surrounding it as shown in Figure 3.4 (a). Near the vicinity of the solid the gas density is somewhat higher than that in the bulk due to adsorption. However, the gas density far away from the surface (outside the pores) is equal to that of the bulk gas density.

3.3.1. Absolute Adsorption

Figure 3.4 (b) shows the reference state for absolute adsorption. The gas molecules exist in the non-shaded "available" volume of the tank at the same conditions (temperature and pressure) as that in Figure 3.4 (a). Thus, the density of molecules in the non-shaded region of this figure is same as that of the bulk density is case (a). The shaded black region is considered to be unavailable for the gas at the reference state conditions. The difference between the number of gas molecules between the two cases (a) and (b) is called as the absolute amount adsorbed. On a normalized basis, the difference per unit mass of adsorbent is the so called specific absolute amount adsorbed.

3.3.2 Excess Adsorption

Figure 3.4 (c) (bottom left) shows the reference state for excess adsorption. The gas molecules exist in the non-shaded "available" volume of the tank at the same conditions (temperature and pressure) as that in Figure 3.4 (a). Thus, the density of molecules in the non-shaded region (including that inside the pores) of this Figure 3.4 (c) is same as that of the bulk density is case (equilibrium). The shaded black region is the so called "impenetrable solid volume" that is unavailable for the gas. The difference between the number of gas molecules between the two cases (a) and (c) is called as the excess amount adsorbed. Thus, excess amount is equivalent to the number of additional gas that can be accommodated in the "penetrable" region of the tank due to adsorption. By far this is the most commonly used reference state in adsorption literature.

3.3.3. Net Adsorption

Figure 3.4 (d) shows the reference state for net adsorption. The gas molecules exist in the total volume of the tank at the same conditions (temperature and pressure) as that in

Figure 3.4 (a). Note that in this reference state the total volume of the tank is considered available to the gas unlike in the earlier two cases. Further, the density of molecules in the tank at the reference state is same as that of the bulk density is case (a). The difference between the number of gas molecules between the two cases (a) and (d) is called as the net amount adsorbed. Thus, net amount is equivalent to the number of additional gas that can be accommodated in the total volume of the tank (as opposed to that in the penetrable volume only for case of excess) due to adsorption. From a practical perspective for evaluation of adsorbents for hydrogen (or natural gas) storage this reference state is most convenient [Gumma and Talu, 2010].

3.3.4. Determination of Buoyancy Volume for Various Reference States

In order to calculate the amount adsorbed based on any one (absolute, excess or net) reference states, it is necessary to correct the microbalance signal with appropriate buoyancy correction term as described in Eq 3.8.

The buoyancy volume for net adsorption is the buoyancy acting on the bucket alone (excluding the sample). This is usually obtained *via* Eq. 3.8, by using a convenient gas to record the microbalance signal of the bucket only (in the absence of any sample) at several densities of the surrounding bulk gas. In the absence of adsorbent sample, the change in microbalance signal is solely due to buoyancy of the bucket assembly (irrespective of the gas used) and hence LHS of Eq. 3.8 is zero. The slope of microbalance signal against bulk gas density is thus directly related to the buoyancy volume (of the bucket in this case). Argon was used as probe gas to obtain buoyancy of the bucket for data reported in this work. In net adsorption only bucket experience buoyancy force therefore

$$V_{buyoancy\ ,\ net} = V_{bucket} \tag{3.9}$$

In case of excess adsorption the impenetrable solid volume also experiences the buoyancy force and

$$V_{buyoancy\ ,\ excess} = V_{bucket} + V_s \tag{3.10}$$

where V_s is the impenetrable solid volume. The buoyancy volume is calculated again from the change in microbalance signal on the bucket and sample assembly. However, since a porous solid sample adsorbs the probe gas, LHS of Eq (3.8) is non-zero unlike in the previous case when only the bucket is used to measure the buoyancy volume. LHS of Eq (3.8) is zero in presence of a sample only if the sample does not adsorb the probe gas. Hence, helium is conventionally chosen as a non-adsorbing probe gas to obtain impenetrable solid volume (and hence $V_{buoyancy}$ for excess adsorption). With non-adsorbing helium assumption the LHS of Eq. 3.8 is zero; the slope of microbalance signal against helium density is related to the buoyancy volume for excess adsorption.

In case of absolute adsorption the impenetrable solid volume as well as the pores also experiences the buoyancy force and

$$V_{buyoancy\ ,\ absolute} = V_{bucket} + V_s + V_p \tag{3.11}$$

where V_p is the pore volume. In addition to non-adsorbing helium assumption to measure the second term in Eq (3.11), a suitable experimental technique is necessary to measure the pore volume of the adsorbent. Several methods which combine a suitable measurement with appropriate theoretical models can be used to estimate the pore volume of a sample as discussed earlier (Section 3.1.7).

In summary, the buoyancy volume is fixed on the basis of the reference state. In case of net adsorption, the buoyancy correction is needed only for forces acting on the bucket. It needs to be determined only once for the given experimental system. For excess adsorption, the buoyancy correction for the impenetrable solid volume is also needed and needs to be determined from an assumption (non–adsorbing helium) for each adsorbent sample. In this work non-adsorbing helium assumption at 298 K is used for determination of buoyancy volume for excess adsorption. Finally, in case of absolute adsorption an additional experiment is necessary to determine the pore volume.

3.4. Isotherm Modeling

Excess adsorption isotherms can be suitably modeled to calculate important thermodynamic parameters such as Henry's constant and enthalpy of adsorption. A Langmuir equation is used to model the obtained experimental excess adsorption isotherms. Langmuir equation can be represented as (Eq. 3.12):

$$W = \frac{W_{max}\, bP}{1 + bP} \tag{3.12}$$

where W is the amount adsorbed in wt%, P is the pressure in bar, and W_{max} is the saturation loading in wt%. *b* is the affinity parameter and its temperature dependency is expressed by

$$b = b_0 \exp\left(b_1 / T\right) \tag{3.13}$$

Henry's law states that the amount adsorbed is proportional to pressure at zero pressure and Henry's constant is defined as the slope of the isotherm at the limit of zero pressure. Mathematically, Henry's constant, β, is written as

$$\beta = \lim_{P \to 0} \left(\frac{N}{P} \right) \tag{3.14}$$

N is amount adsorbed in mol kg^{-1} adsorbed at pressure P. The amount adsorbed, W is related to N via relation given in Eq. 3.15.

$$N = \left(\frac{10 \times W}{Mw} \right) \tag{3.15}$$

where M_w is the molecular weight of the adsorbate. Unless otherwise explicitly noted, all amounts adsorbed in this work indicate excess adsorption (both N and W). The Henry's constant (β, mol kg bar^{-1}) is used to characterize the adsorbate affinity for an adsorbent. For the Langmuir model, combining Eqs. 3.12, 3.14 and 3.15 yields

$$\beta = \left(\frac{W_{\max} \times b \times 10}{Mw} \right) \tag{3.16}$$

Enthalpy of adsorption is also a measure of the strength of adsorbate-adsorbent interaction and is used to characterize the adsorption properties of any adsorbent. It also shows how easily an adsorbent can be regenerated. Enthalpy of adsorption is often calculated from the following expression

$$\Delta H_{ads} = -R \left. \frac{\partial (\ln P)}{\partial (1/T)} \right|_N \tag{3.17}$$

where R is the universal gas constant (8.314 J mol^{-1} K^{-1}). At the limit of zero loading, the slope of ln β against inverse of T (K^{-1}) will directly give the derivative term on LHS of Eq. 3.17.

In case of Langmuir Equation (Eq 3.12), the enthalpy of adsorption is constant with loading and is directly equal to b_1R (b_1 is the coefficient used in Eq. 3.13). In literature enthalpy of adsorption is also commonly represented as isosteric heat ($Q_{st} = -\Delta H_{ads}$).

3.5. Estimation of Volume of Adsorptive Hydrogen Storage Vessel

The volume of the tank required to store 1 kg of hydrogen is an indicator for the benefit achieved using of adsorptive storage. The mass of hydrogen chosen above (1 kg) is the typical requirement of a light motor vehicle for a run of about 100 km [Schlapbach and Zuttel, 2001]. The following procedure is used to calculate the volume of hydrogen storage tank with and without adsorbent.

(a) Without adsorbent : The volume (in liters) of tank V_{empty_tank} necessary to store 1 kg of hydrogen at desired temperature T and pressure P is given by

$$V_{empty\_tank} = \frac{1000}{\rho_{H_2}\{T, P\}\, M_{w,H_2}} \tag{3.18}$$

where ρ_{H_2} is molar density of hydrogen in kmol m^{-3} at T and P, obtained from a suitable EoS (ideal gas law was used for ease in calculation here). M_{w,H_2} is the molar mass of hydrogen in kg $kmol^{-1}$ (2.01588 kg mol^{-1} taken from recent literature [Wieser, 2006].

(b) With adsorbent: The volume of tank V_{tank} (in liters) containing an adsorbent necessary to store 1 kg of hydrogen is calculated from

$$V_{tank} = \frac{1000}{\left(N_{net}\{T, P\}\,\rho_{solid} + \rho_{H_2}\{T, P\}\right) M_{w,H_2}} \tag{3.19}$$

where $N_{net}\{T, P\}$ is the net amount adsorbed in mol kg^{-1} at T and P, and ρ_{solid} is the bulk density of the solid in kg $liter^{-1}$. Only when N_{net} is positive $V_{tank} < V_{empty\_tank}$ and tank filled with an adsorbent will need a smaller volume than compressed hydrogen tank at similar conditions; otherwise no advantage exists in using an adsorbent for storing hydrogen. Thus, net adsorption has direct application for evaluating benefits of hydrogen

storage. While other reference states for adsorption can also be used in Eq. (3.19) none of them are as straightforward. It is also worth mentioning that when N_{net} is positive, the maximum benefit is derived when adsorbent is well packed (thereby enhancing its bulk density, ρ_{solid}).The best results are achieved when one approaches the crystal density of the material; unnecessary voids (intraparticle, intracrystalline etc.) only tend to decrease the advantage offered by the adsorbent. For sake of comparison alone, the packing bulk density of the solid used in calculation for tank volume in Eq. (3.19) is taken to be the packing density of the powdered sample. Typically, a syringe is packed with about 1 to 2 ml of solid adsorbent and the mass of adsorbent is measured to calculate its "packing" density. The packing densities thus obtained are given in Table 3.2.

3.6. Estimation of Bulk Gas Density

The bulk gas density of helium is obtained from virial equation of state truncated up to second virial coefficient at the desired temperature. In terms of second virial coefficient, the density can be represented by Eq. 3.20.

$$\rho_{gas} = \left(\frac{-1 + \sqrt{1 + 4 B_{gas} \frac{P}{RT}}}{2 B_{gas}} \right) M_w \qquad (3.20)$$

where M_w is molar mass of the gas, P is pressure, T is the temperature, R is gas constant and B_{gas} is the gas phase second virial coefficient. The temperature dependency of the second virial coefficient for helium is obtained from [Chowdhury, 2010]

$$B_{gas} = 0.014 - \frac{0.0354}{T} - \frac{0.0595}{T^3} + \frac{361}{T^8} - \frac{794}{T^9} \qquad (3.21)$$

For better accuracy, density of hydrogen is obtained using the equation of state (EoS) suggested by Lemmon *et al.*, [2008]. The density values for H_2 predicted from this EoS matches well with the reported data in NIST Chemistry Webbook [NIST website].

$$Z(P,T) = \frac{P}{\rho RT} = 1 + \sum_{i=1}^{9} a_i \left(\frac{100\ K}{T}\right)^{bi} + \left(\frac{P}{1MPa}\right)^{ci} \qquad (3.22)$$

where pressure P is in MPa and T in K. The parameter values for a_i, b_i and c_i used in Eq. 3.22 are given in Table 3.3.

3.7. Details of Experimental System used for Gas Adsorption Measurements

This section described the details of the experimental system used for gravimetric hydrogen adsorption measurements and the experimental protocol followed. The details of major instruments used in this experimental system are given in Table 3.4.

3.7.1. Feed Section*:* The feed section comprises of three pneumatic on-off valves *viz*. H1, H2 and H3, three needle valves (N1, N2 and N3) and one mass flow controller (MFC). The gas is fed into the system through the assembly of these set of valves. Helium is sent into the system through MFC for a better control of the overall flow during activation and regeneration of the moisture trap. During the adsorption measurements, pure hydrogen gas (better than 99.99%) is sent through an inline moisture trap (~1 liter SS tank filled with molecular sieve 4A). Otherwise for a low adsorbing species like H_2 any trace quantity of impurities will also lead to erroneous measurements. This tank is purged with helium at 523 K at regular intervals to remove the adsorbed moisture.

3.7.2. Manifold*:* The manifold constitutes the central portion of the setup and connects the feed section to the balance assembly/sample chamber. All the pressure transducers are mounted on to the manifold.

3.7.3. Sample Chamber*:* The magnetic suspension balance (MSB) has a bucket containing the adsorbent which is enclosed in a high pressure chamber. The inlet section consists of one on-off valve (H4) and one filter (F1). Additionally, in the outlet section

we have one filter (F2), needle valve (N4) and on-off valve (H6) respectively. The needle ensured that the chamber can be depressurized slowly to prevent spillage of the adsorbent.

The magnetic suspension balance (Rubotherm, GmbH) measures the mass (weight) of the bucket. The balance is divided into two parts, 1) balance chamber containing the bucket (sample) and sinker, 2) assembly of the electronic components. The adsorbent is placed in a bucket inside the balance chamber; the bucket is hanged down through a permanent magnet which itself is suspended by an electromagnet. The electromagnet on the other hand is attached to the load cell of a Sartorius microbalance. A PID controller keeps the position of the permanent magnet fixed. The force transmitted to the microbalance is equal to the weight of the bucket and the sample. Thus, weight recorded by the microbalance is directly related to the mass of the solid sample. The electromagnet and the balance electronics are completely isolated from the balance chamber which enables the instrument to be used at extreme temperature, pressure conditions and in corrosive environments [Rubotherm website].

3.7.4. Vent/Vacuum Section: The complete system is vented from high pressure to atmospheric pressure by operating the pneumatic valve H12, whereas the vacuum line was connected through valve H13 to a vacuum pump. The vacuum pump is capable of achieving pressures below 1.5 m torr.

3.7.5. Pressure measurement Section: The pressure measurement section comprises of four pressure transducers of different ranges. It enables to measure pressures from very low (P1), atmospheric (P2), high (P3) and very high (P4) with accuracy and precision.

3.7.6. Temperature measurement Section: Various thermocouples (K type) with appropriate temperature indicators are installed into the system for measuring temperature with an accuracy of ± 1 K.

3.7.7. Auxiliary Section (Vacuum pump, air compressor to operate pneumatic valves, Solenoid valves, Refrigerated and heated circulator): Several auxiliary/supporting machineries are installed for smooth functioning of the system. As is already mentioned in the above section, the vacuum pump is used for evacuating the complete system; the air compressor is used for operating the pneumatic valves which on the other hand are operated through a series of solenoid valves being controlled from an electric control panel. Circulating water bath is used for maintaining the experimental temperature from 293 K to 364 K. Heating mantle is used to maintain the temperature from 373 K to 573 K. A cryocan is used to maintain the constant temperature during equilibration of sample with hydrogen at cryogenic temperatures.

3.8. Experimental Protocol

3.8.1. Sample Activation

A. The solid adsorbent is loaded into the bucket and mounted into the balance. Depending on the bulk density of the adsorbent, this quantity varied between 0.25 to 2 grams for the experiments performed in this work; the quantity is usually determined by the amount that can be loaded into the bucket and larger samples masses are possible with dense samples.
B. The balance chamber is sealed and system was ensured to be leak free.
C. The system is then evacuated by a vacuum pump.

D. Activation of the adsorbent is performed to remove moisture, solvent and other impurities adsorbed on to the adsorbent. The activation temperature is selected based on TGA analysis data; as explained later for all samples, this temperature is more than 473 K. The activation time for the freshly prepared sample is varied between 3 to 12 hours. However, for subsequent activations (in between two isotherms) of the same sample, only 2-6 hours of activation is sufficient.

E. Activation is assumed to be complete when change in sample weight was less than 0.010 mg in a time of ~30 minutes. During the activation process, the adsorbent was exposed to the desired temperature with a flow of He (about 33 cc min^{-1}) under vacuum. High temperature and vacuum ensure desorption of adsorbed impurities while the helium flow helps in purging of desorbed impurities. After complete activation, the balance chamber is thoroughly evacuated and sealed. The chamber is then allowed to reach desired experimental temperature by immersing it in a suitable isothermal bath. The choice and operation of isothermal bath is described later.

3.8.2. Helium Buoyancy Measurement

As described in the previous section, the buoyancy volume of the bucket and sample are determined with non-adsorbing helium assumption to correct raw experimental measurements into excess amount adsorbed.

A. In this measurement, the sample is first activated as described in earlier section (3.8.1). The experimental temperature is then set to ~ 298 K.

B. Helium is then introduced into the balance chamber via valve H3 in incremental doses to desired target pressure. After each dose, sufficient equilibration time is allowed and the signal of the microbalance along with the pressure is recorded.

C. Typically, 5-7 experimental points in between 0-26 bar are recorded for measurement of buoyancy volume using helium.

3.8.3. Hydrogen Isotherm Measurements

A. In this measurement, the sample is first activated as described in earlier section (3.8.1). The experimental temperature is then set to desired temperature using an isothermal bath. The choice and operation of isothermal bath is described later.
B. Hydrogen is then introduced into the balance chamber via valve H2 in incremental doses to desired target pressure. After each dose, sufficient equilibration time is allowed and the signal of the microbalance along with the pressure is recorded. The equilibration time is varied anywhere between 10 to 30 minutes, depending on the material and system conditions. The mass of the sample is constantly monitored in ae a computer connected to the balance. When change in sample mass is less than 0.01 mg for 10 minutes, equilibrium is assumed.
C. After completion of isotherm measurement over the desired pressure range (details of experimental pressure range for various samples are listed Table 3.5) the balance chamber is evacuated.
D. Typically 15-20 experimental points were recorded for each isotherm.

3.8.4. Sample Regeneration

A. Once measuring an isotherm of a particular temperature is completed, the adsorbent is regenerated to remove adsorbed hydrogen previous run. Typically evacuation coupled with a purge of helium for few minutes would regenerate.
B. It is always ensured that the "true sample weight" is reached before start of each new run. In case, the true mass of the sample is not achieved by simple evacuation (and/or

helium purge), the sample is activated at high temperature as described earlier (in section 3.8.1).

3.8.5. Isothermal Bath

In this work a combination of isothermal baths were used depending on the required temperature.

(1) At temperatures above between 253 and 353 K, an isothermal water bath from Jeio Tech (details given in Table 3.4) was used.

(2) At temperatures below 253 K, a homemade isothermal bath is used. A mixture of methanol and liquid nitrogen was used to maintain the temperature [Rondeu and Harrah, 1965]. During experiments, temperature fluctuations were within a range of ± 2 K. The intermittent addition of excess liquid nitrogen was done manually to maintain the desired temperature.

(3) Temperatures above 353 K were achieved by immersing the balance chamber in a jacketed electric heater assembly. The temperature control was achieved by regulating the energy supply to the heater and balance chamber was controlled within ± 2 K.

3.9. Experimental Conditions for Hydrogen Adsorption Measurements

The adsorption equilibria of various gases on various metal organic frameworks MOFs and their composites were measured gravimetrically in a magnetic suspension balance (Rubotherm, GmbH) over a wide range of temperature and pressure. The experimental conditions for each of the measurements are listed in Table 3.5.

3.10. Hydrogen Uptake on Palladium Nanoparticles

As already mentioned the objective of this preliminary work is two-fold. (1) Controlled synthesis of palladium nanoparticles (Pd-NP) and (2) Measure the hydrogen adsorption uptake on this model material (which has been widely studied in literature) using the gravimetric adsorption unit in our laboratory.

The Palladium (Pd) is a noble metal and the bulk of its hydride contains less than 1 wt% hydrogen. It is one of the most important model systems for hydrogen–metal interaction. It is chosen for this study to understand the differences in the hydrogen adsorption behavior on nano-sized particles as opposed to that of the bulk material. As discussed in later chapters of this thesis, palladium nanoparticles are also used for heavy metal doping of metal organic frameworks by first depositing them onto graphene oxide (GO). The synthesis technique for palladium nanoparticles discussed in this section will also be used in their deposition on GO.

An extensive review of the effect of the particle size on the interaction between palladium and hydride has been published by Pundt et al. [Pundt and Kirchheim, 2006]. Two striking observations are that there are important differences between Pd nanoparticle and bulk Pd, that the scatter in the data for the Pd nanoparticles is very large. Higuchi et al. reported that thin film of Pd can store only 0.15-0.3 wt% of hydrogen [Higuchi *et al*., 2006]. However, nanostructures show different behavior than their bulk analogs.

Preparation of Pd-PVP nanoparticles by single stage reduction using polyol process, which were subsequently used for Suzuki coupling reaction, was reported by El-Sayed's group [Narayanan and El-Sayed, 2003]. After glycol reduction, separation of the nanoparticles from the viscous solution is very crucial and few methods are reported in

the literature. Xiong *et al*. used inorganic membrane [Xiong *et al*., 2005] to separate the Pd nanoparticle, whereas, Yamauchi *et al*. separated these particles by precipitation [Yamauchi *et al*., 2008]. Hydrogen adsorption capacity on Pd nanoparticles reported in literature varies over a wide range, since it depends on the size of the particles. Yamauchi et al. reported a maximum loading of about 0.7 wt% for 2.6 nm Pd particles and about 0.88 wt% for 7 nm particles at 393 K and 10 bar. Kishore et al. reported marginally better loading for 70 nm particles (0.53 wt%) than 4 nm particles (0.46 wt%) at 323 K and 10 bar [Kishore *et al*., 2005]. Narehood et al. reported maximum loading for 2-3 nm particles to be 1.08 wt% at 323 K and 0.8 wt% at 363 K and 5 bar [Narehood *et al*., 2009]. Harinouchi et al. reported loading of 0.6 wt% at 373 K and 10 bar for a similar particle size [Harinouchi *et al*., 2006].

3.10.1. Synthesis of Palladium Nanoparticles

Palladium (II) Chloride (Spectrochem), Ethylene Glycol (Merck), and Polyvinyl Pyrrolidone (CDH Lab.) were used without further purification. In three separate conical flasks ethylene glycol was heated up to 393 K for 2 h to remove moisture. In the first flask, 900 mg of $PdCl_2$ was added to 252 cm^3 ethylene glycol and 0.1 cm^3 conc. HCl at 333 K and filtered subsequently. In the second flask, 5.64 g PVP was is added to 252 cm^3 ethylene glycol at 393 K. In the third flask, 480 cm^3 of ethylene glycol was kept at 393 K. During the reaction, solutions from first and second flask were added simultaneously at a rate of 2.1 cm^3 min^{-1} to the third flask at 398 K. The contents of the third flask were stirred at 1200 RPM during this process. The contents of the flask were allowed to react for about 7 hours. Proper precautions were taken to ensure that no temperature gradient exists in the reaction medium. As the reaction proceeded, initial pale orange color solution turned black, due to formation of Pd nanoparticles.

Initially, several preliminary experiments were conducted to understand the effect of reaction time, temperature and concentration of Cl^- ions. Higher is the temperature faster will be the reduction hence particles will agglomerate. Cl^- ions prevent aggregation so that it stabilizes the reduction for a homogeneous growth [Wiley *et al*., 2004]. If the duration is less then particles size would be small with lesser yield. Thus, the duration of reaction as 6 to 7 hours and a temperature of 398 K were chosen after several trials to obtain nanoparticles of size ~10 nm. Methanol was added to the reactant solution in 1:1 ratio and centrifuged for 45 min at 10000 RPM to separate the nanoparticles. The filtrate from all the centrifuge tubes was collected in a ceramic crucible and air dried at 353 K for about 6 hours.

3.10.2. Material Characterization

Crystalline nanoparticles formation starts at 30-40 minutes of the reaction. Brown solution starts becoming dark. Initially, a few small particles of 2-3 nm are formed. These particles are known as seeds [Bisson *et al*., 2009]. As the reaction proceeds these seeds grow to form bigger size crystals. This phenomenon is called 'Ostwald Ripening' [Narayanan and El-Sayed, 2004]. Samples were collected at several time intervals for characterization. Once 9 hours of reaction time has elapsed, homogeneous distribution of palladium nanoparticles of 10-20 nm was observed by TEM (Figure 3.6). At longer times, after 18-20 hours 200-300 nm particles were formed and shown in FESEM image (Figure 3.7).

The X-ray diffraction pattern of purified Pd nanoparticle is shown in Figure 3.8. These patterns are characterized by several intense peaks between the diffraction angles of 30^o and 90^o. The peaks can be indexed to those reflection from (111), (200), (220), (311), and (222) planes of nano-crystalline Pd as reported in literature [Kishore *et al*.,

2005]. Scherrer formula based on the full width of half maximum (FWHM) can approximate the average crystal size. Individually each peak can be selected to determine the average particle size and the intense peak at 40^o estimates a particle size of about 19 nm.

TEM image shown in Figure 3.9.(a) confirm that most of the particles are in nanometer size. Three shapes distinctively can be figured out are icosahedrons (looks like a hexagon from top), cubes (looks like a square or rhombus from top) tetrahedron (looks like a triangle from the top). HRTEM was used to spot a single icosahedron and its image is shown in Figure 3.9.(b). Selected Area Electron Diffraction (SAED) patterns are a projection of the reciprocal lattice, with lattice reflections showing as sharp diffraction spots. SAED pattern of Pd nanoparticles obtained in this work are shown in Figure 3.9.(b). There are 5 planes for which d-spacing can be calculated from SAED as 0.3 nm, 0.3 nm, 0.19 nm, 0.19 nm and 0.16 nm respectively. These values are close to d-spacing approximated by XRD). BET surface area of Pd nanoparticles (synthesized in 7 hours) is 2.5 m^2g^{-1} is close to literature report of 10 m^2g^{-1} [Kishore *et. al*. 2005]. These particles are thus non-porous and the hydrogen uptake would be mainly due to chemisorption.

3.10.3. Pressure Composition Isotherm

First the sample (Pd nanoparticles) was degassed at 473 K in helium atmosphere to remove solvent and other impurities. Isotherms of hydrogen uptake on sample were measured gravimetrically as explained earlier (Section 3.2). Isotherm measurements were carried out at 293 K, 324 K, 364 K and 392 K, in the pressure range of 0-26 bar.

Most important aspect in the measurement of the hydrogen adsorption isotherm data is in achieving the equilibrium. Sufficient equilibrium time is necessary to allow

hydrogen to completely penetrate the inter lattice planes of the adsorbent particles. The thermodynamic aspects of metal-hydrogen interactions are usually understood from pressure composition isotherm. Equilibration times in excess of 20-30 minutes were allowed after injection of H_2 at predetermined pressure. Figure 3.10 shows the pressure composition (PC) isotherms of Palladium nanoparticles.

Each isotherm exhibits three distinct regions. Surface adsorption due to weak van der Waal's force attained within 0.4 bar, denoted as α phase in Figure 3.10 (for all the measured temperatures). Sub-surface adsorption happens within 0.6 bar denoted as α+β phase. Hydrogen adsorption is a continuous process; within the lattice planes hydrogen will form bonds with palladium atom making way for more hydrogen molecules to get adsorbed at its surface; this is denoted as the β phase in Figure 3.10. The maximum loading we have observed corresponds to a value of x = 0.55 for β-PdH_x system. Particle size also has an influence on the relative stability of the hydride. Therefore, Yamauchi et al., reported smaller is the crystal size lesser is the hydrogen uptake capacity of Pd NPs. However, conflicting results are reported; for example Narehood *et al.* [2009] achieved higher hydrogen uptake even on particle sizes lesser than those used by Yamauchi et al. [2008].

A comparison of hydrogen uptake on various Pd NP reported in literature is shown in Figs. 3.11(a) and (b). Kishore *et al*. [2005] took different sizes of Pd NPs and measured the isotherms at 323 K, 4 nm particles were found to saturate with 0.43 wt% H_2 whereas 70 nm particles were saturated with 0.52 wt% H_2. 10-40 nm particles used in this work saturate with 0.5 wt% hydrogen at 324 K i.e., which is higher than the uptake at room temperature (0.41 wt% at 293 K). Kuji *et al*., [2002] reported higher hydrogen uptake at 298 K than at 323 K (0.88 wt% and 0.86 wt% respectively) but both Yamauchi et al.

[2008] and Kishore *et al*. [2005] reported high uptake at 323 K than at 298 K. Narehood et al. [2009] reached 0.98 wt% at 323 K which is close to maximum uptake reported of 1.06 wt% on ~13 nm particles [Rather *et al*., 2007]. At 393 K hydrogen uptake on 7 nm particles saturates with 0.27 wt% H_2 [Yamauchi *et al*., 2008] whereas 10-40 nm particles studied in this work saturates with 0.36 wt% H_2 at 392 K. However Kuji *et a*l. [2002] reported higher saturation uptake on 10 nm particles (0.77 wt% at 353 K and 0.65 wt% at 373 K). At 363 K Narehood *et al*. [2009], reported uptake capacity of 0.86 wt% which is higher than the loading in this work (0.45 wt% at 364 K).

It is not easy to approximate the value of enthalpy of adsorption (ΔH_{ads}) if there is a scatter in the data points in the isotherm. ΔH_{ads} estimated from the virial plot in this work is -21 kJ mol^{-1}. Enthalpy of adsorption calculation in chemisorption depends on the stability of the hydride, increases (absolute value) with decreasing particle size, due to the higher stability of the sub-surface hydride. ΔH_{ads} for the 2.6 nm Pd nanoparticle was -34.6 kJ mol^{-1}, whereas for the 7 nm Pd nanoparticles the value was -31 kJ mol^{-1}, respectively [Yamauchi *et al*., 2008]. Harinouchi and coworkers also obtained ΔH_{ads} of -36.1 kJ mol^{-1} for 2.1 nm particles which confirms that ΔH_{ads} depends on the particle size. Pd nanoparticles as such are not stable at elevated temperatures as they tend to sinter, especially when hydrogen is present, therefore scope of using Pd NP beyond 393 K for hydrogen storage is limited.

Hydrogen uptake at different temperatures upto 26 bar is shown in Figure 3.12. Adsorption at 293 K and 1 bar pressure is about 0.38 wt%. This value is significantly higher than those for porous adsorbents like graphene [Srinivas *et al*., 2010], carbon nanotube [Porier *et al*., 2006], zeolites [Langmi *et al*., 2005], common MOFs like MIL 101 [Latroche *et al*., 2006], HKUST-1 [Liu *et al*., 2007] etc. At 324 K and 1 bar even

higher loading is observed (0.5 wt%). Similarly, 0.48 wt% loading is observed at 364 K and 1 bar. But loading decreases to 0.36 wt% at 392 K and 1 bar. Metal organic frameworks, zeolite and other porous material predominantly exhibit physisorption [Bae and Snurr, 2010]. In contrast, the Pd nanoparticles have chemical affinity towards hydrogen leads to chemisorption [Janot *et al*., 2005, de-Jongh and Adelhelm, 2009]. At favorable temperature and pressure, hydrogen molecules reach the inter-lattice planes of Pd crystals to form the hydride.

3.11. Summary

In this chapter, details of various characterization techniques used in this study were summarized. Major hardware of the gravimetric adsorption unit and the hydrogen adsorption measurement protocol are detailed. In addition, the definition of various types of adsorption, the reference states used for defining adsorbed amount are discussed. The details of additional experiments and the methodology for conversion of raw experimental data into desired amount adsorbed are discussed. The EoS used for calculation of bulk gas density for helium and hydrogen are summarized. The procedure involved in calculation of volume of an adsorptive storage vessel for hydrogen is presented. Finally, the synthesis of palladium nanoparticles and measurement of hydrogen storage on these nanoparticles as a preliminary study for hydrogen uptake measurements using the gravimetric unit employed are presented.

Figures

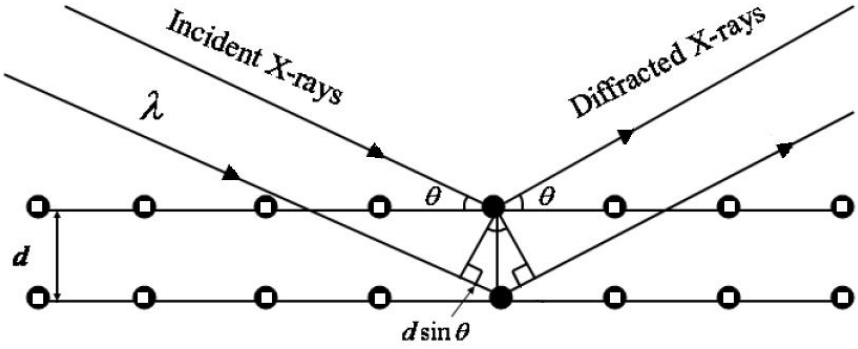

Figure 3.1: Diffraction of Incident X-rays from the Family of Parallel Atomic Planes

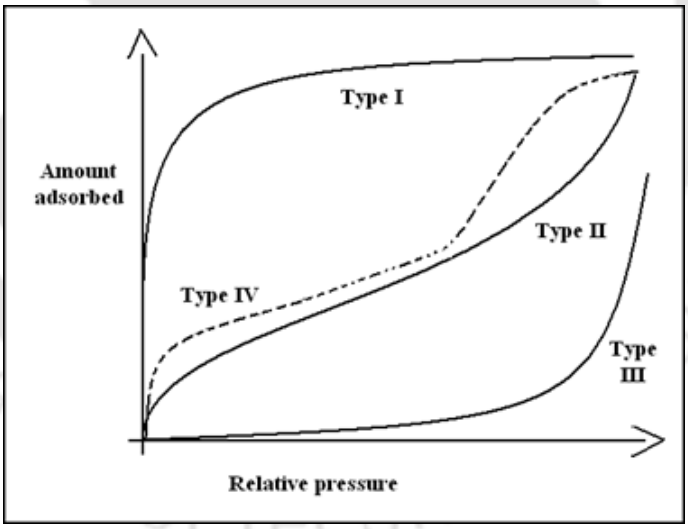

Figure 3.2: Different type of N_2 Adsorption Isotherms [Amrita Virtual Laboratory]

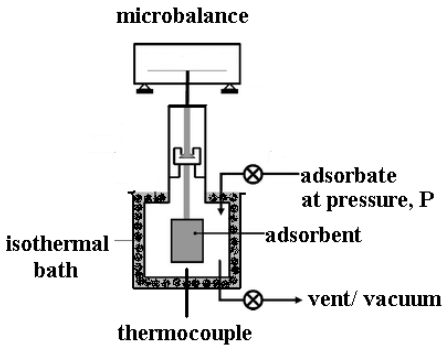

Figure 3.3: Gravimetric adsorption measurement setup

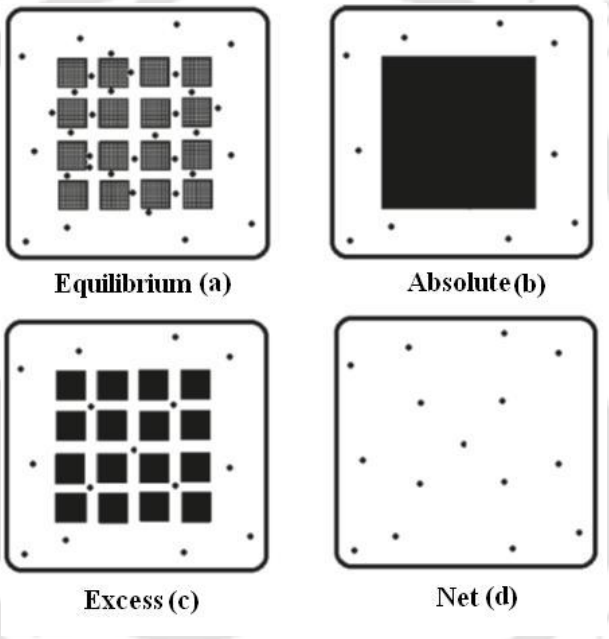

Figure 3.4: (a): Equilibrium between Adsorbate and Adsorbent; (b): Reference state for Absolute Adsorption; (c): Reference state for Excess Adsorption; (d): Reference state for net Adsorption Framework [Gumma and Talu, 2010]

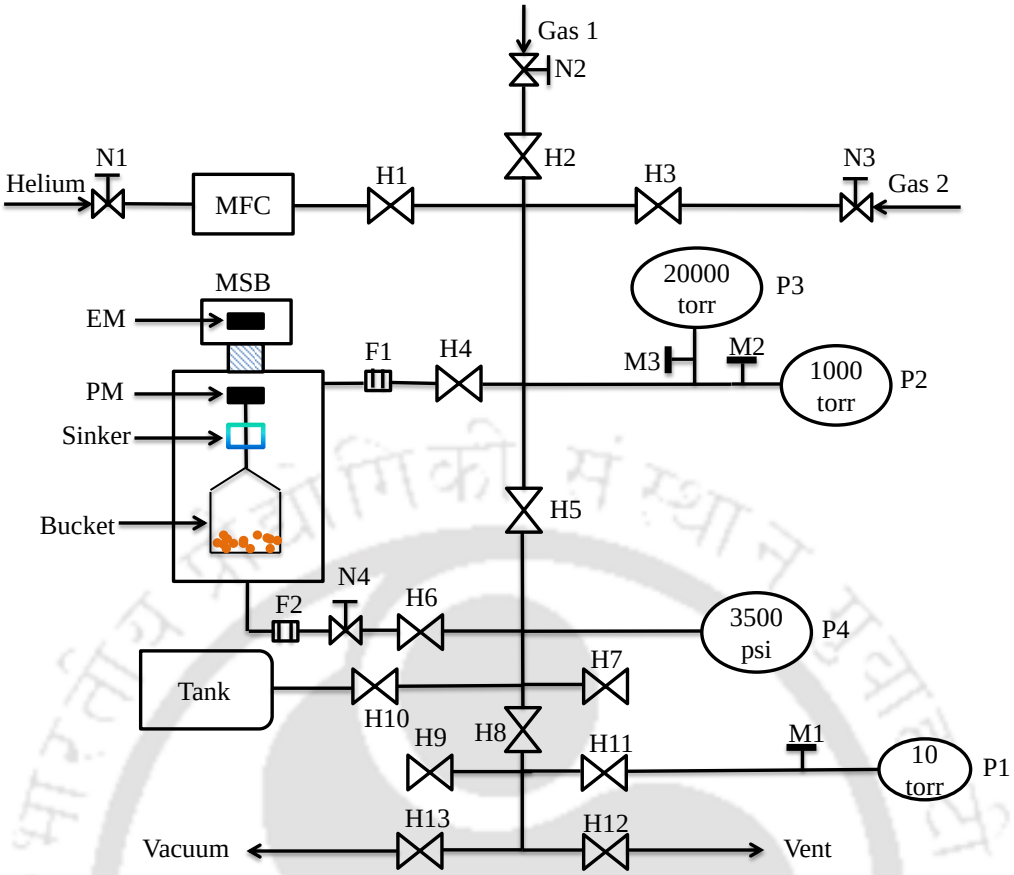

Figure 3.5: The Schematic of Experimental Setup for Gas Adsorption Measurement.

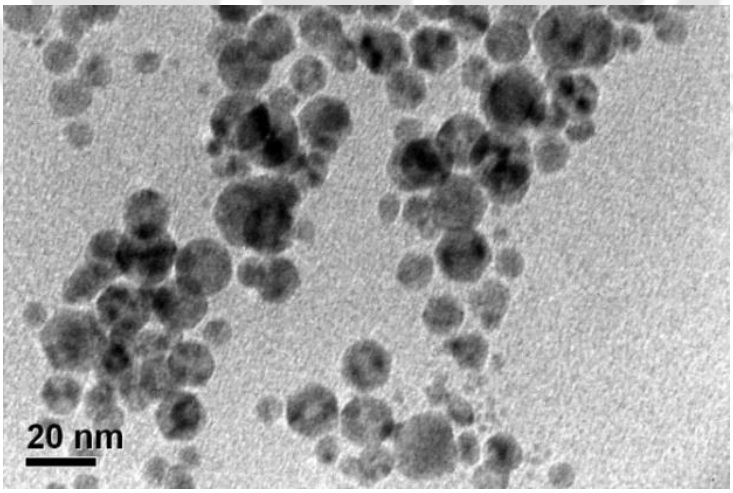

Figure 3.6: TEM image of Pd Nanoparticle Synthesized in 9 hours

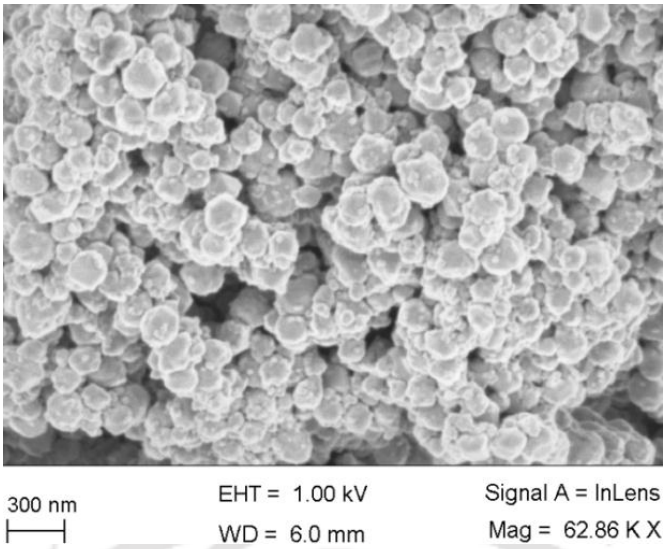

Figure 3.7: FESEM image of Pd Nanoparticle Synthesized in 18 hours

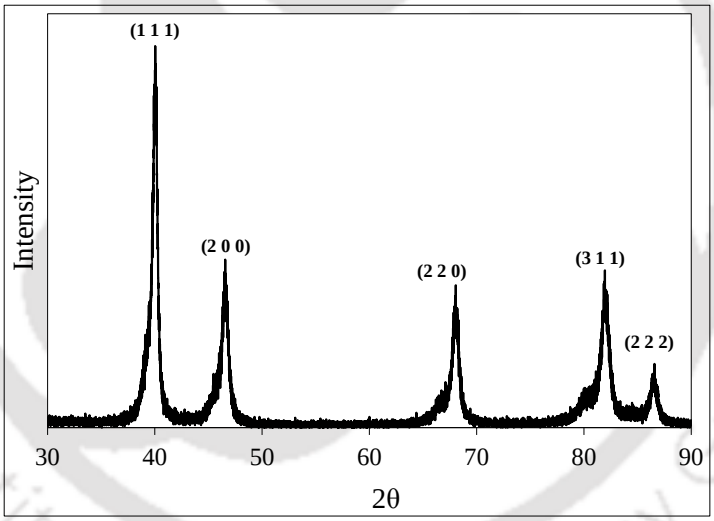

Figure 3.8: Powder XRD Pattern of Palladium Nanoparticle; Intensity in Arbitrary Units Plotted Against 2θ

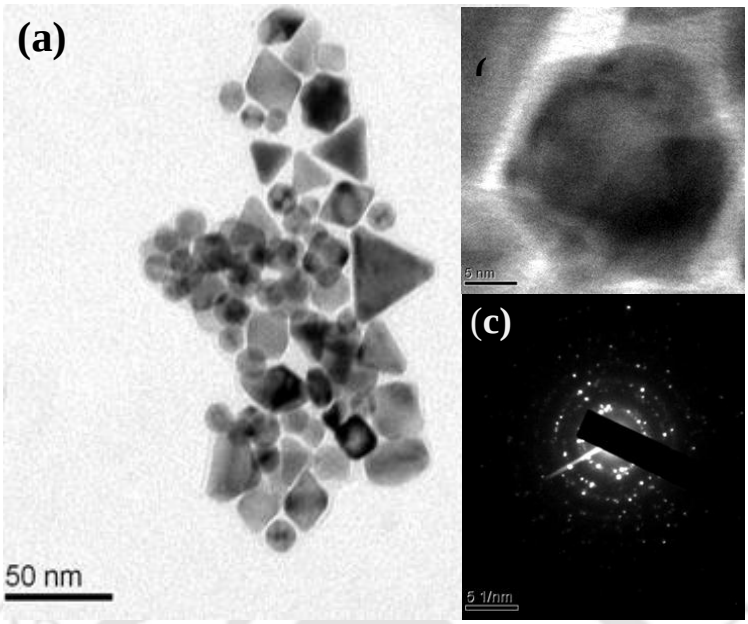

Figure 3.9: (a) TEM Image of Nanoparticles, (B) An Icosahedrons Particle detected by HRTEM (C) SAED shows Diffraction from 5 Reflection Planes Surrounding the Core

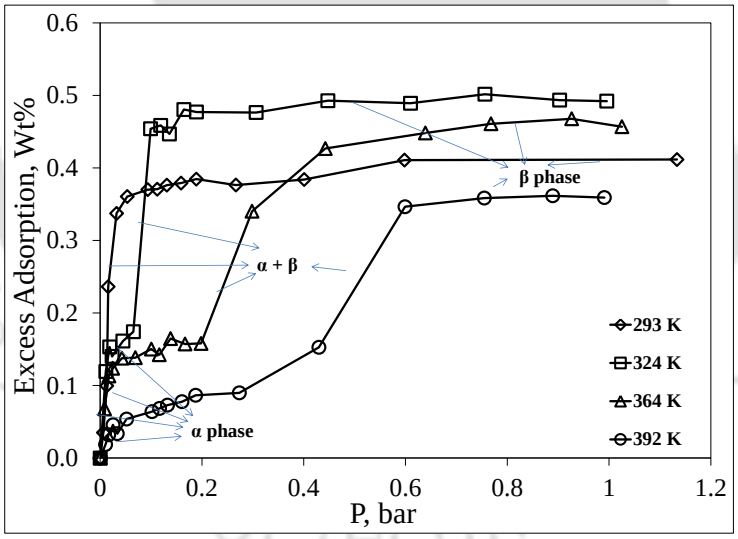

Figure 3.10. Hydrogen Uptake on Palladium Nanoparticles at Low Pressure; Lines are drawn as a Guide to the Eye

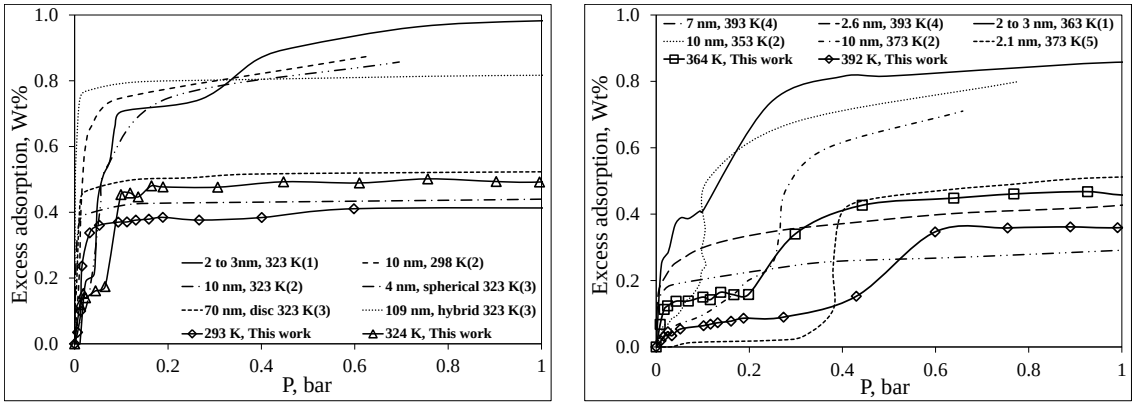

(a) **(b)**

Figure 3.11: Pressure composition isotherm on palladium nanoparticles compared to work reported in the literature; (1) Narehood *et al*., [2009]; (2) Kuji *et al*., [2002]; (3) Kishore *et al*., [2005]; (4) Yamauchi *et al*., [2008]; (5) Harinouchi *et al*., [2006]

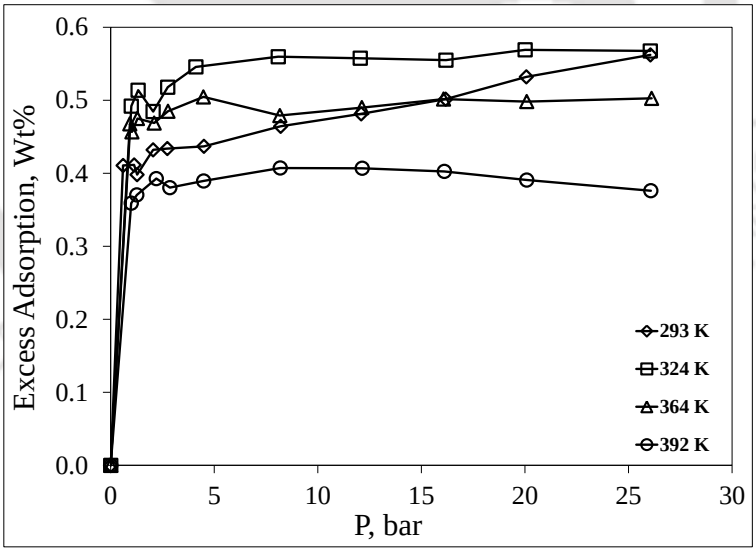

Figure 3.12: Hydrogen Uptake on Palladium Nanoparticles at High Pressure; Lines are drawn As a Guide to the Eye

Tables

Table 3.1: Colour of Flame for different Alkali Metals [Amrita Virtual Laboratory]

Element Emission	**Wavelength, nm**	**Flame Colour**
Sodium (Na)	589	Yellow
Potassium (K)	766	Violet
Barium (Ba)	554	Lime Green
Lithium (Li)	670	Red

Table 3.2: Packing Densities for Adsorbents

Adsorbent	**Density, g cc^{-1}**	**Adsorbent**	**Density, g cc^{-1}**	**Adsorbent**	**Density, g cc^{-1}**
MCM 41	0.195	Cr-BDC	0.290	Cr-BDC/Li	0.227
Zn-BDC	0.545	Mg-DOBDC	0.347	-	-
Ni-DABCO	0.310	Co-DOBDC	0.441	-	-
MOF-205	0.221	Cu-BTC	0.431	Cu-BTC/Li	0.360

Table 3.3: Constants Associated with the Equation of State (EoS) Proposed by Lemmon *et al.* [2008]

i	**a_i**	**b_i**	**c_i**
1	0.058885	1.325	1.00
2	-0.061360	1.870	1.00
3	-0.002650	2.500	2.00
4	0.002731	2.800	2.00
5	0.001802	2.938	2.42
6	-0.001150	3.140	2.63
7	9.59E-05	3.370	3.00
8	1.11E-07	3.750	4.00
9	1.26E-10	4.000	5.00

Table 3.4: Details of Major Instruments in the Gravimetric Adsorption Measurement Unit

Component	**Model**	**Manufacturer**	**Range**	**Accuracy**	**Resolution**
Gravimetric Balance	3-position Magnetic suspension balance	Rubotherm	0-25 g	±20 µg	10 µg
Mass flow controller	GFC-17	Diegler Aalborg	0-200 cc min-1 of N2	2% of full scale	1 cc min-1
Pressure transducers	627B11TDCAB	MKS Instruments	0-10 torr	±0.12% of full scale	0.001 torr
	627D18TBC1B		0-100 torr		0.1 torr
	627B24TBC1B		0-20000 torr		1 torr
	PX41C0-3500PSIA	Omegadyne	0-3500 psi	±0.5% of full scale	1psi
Thermocouples	K Type		73-1623 K	±3K	1 K
Temperature indicators		Masibus			
Heated and refrigerated circulator	RW-2025 G	Jeio Tech	248 - 423 K	±0.05 K	0.1 K
Isothermal bath	N/A	Home made	90 to 194 K	N/A	N/A
Heating mantle	800 W	Sigma Instruments	333 to 573 K	N/A	N/A
Vacuum pump	DUO 2.5	Pfeiffer Vacuum	<1.5 m torr	N/A	N/A
Compressor	HS-WP-1	High speed appliances	0–100 psi	N/A	N/A

Table 3.5: Experimental Conditions for Adsorbent Samples

Material	**Experimental Measurement Conditions**		**Material**	**Experimental Measurement Conditions**	
	T, K	**P, bar**		**T, K**	**P, bar**
Pd-NP	293, 324, 364, 392	0-26	Cu-BTC/1.2AC	91, 295	0-100
MCM 41	92, 296	0-104	Cu-BTC/1.2Pt-AC	91, 297	0-98
Zn-BDC	101, 136, 169, 297	0-102	Cu-BTC/3.3Pt-AC	92, 296	0-101
Cr-BDC	92, 136, 165, 297	0-103	Cu-BTC/7.1Pt-AC	90, 296	0-101
Ni-DABCO	90, 145, 194, 297	0-94	Cu-BTC/11Pt-AC	92, 297	0-100
MOF-205	91, 140, 193, 296	0-104	Cu-BTC/31Pt-AC	101, 298	0-102
Mg-DOBDC	101, 133, 192, 298	0-85	Cu-BTC/3.7Pd-GO	90, 296	0-101
Co-DOBDC	91, 297	0-104	Cu-BTC/3.3IGO	97, 297	0-101
Cu-BTC	101, 192, 297	0-113	Cu-BTC/3.7Pd-IGO	106, 297	0-102
Cr-BDC/Li	92, 138, 189, 298	0-105	Cu-BTC/8Pd-IGO	102, 295	0-104
Cu-BTC/Li	91, 188, 296	0-104	Cu-BTC/10Pd-IGO	113, 297	0-100
Cr-BDC/1.9Pd-IGO	92, 297	0-99	Cu-BTC/37Pd-IGO	91, 297	0-97
Cr-BDC/4.6Pd-IGO	107, 297	0-98	Cu-BTC/1.2Pt-AC/Li	92, 297	0-102
Cr-BDC/6.4Pd-IGO	101, 296	0-103	Cu-BTC/3.3Pt-AC/Li	100, 297	0-99
Cr-BDC/21Pd-IGO	95, 297	0-100	Cu-BTC/7.1Pt-AC/Li	99, 297	0-103
Cr-BDC/1.9Pt-AC	90, 298	0-102	Cu-BTC/11Pt-AC/Li	99, 297	0-100
Cr-BDC/1.4IGO	90, 296	0-100	Cu-BTC/3.7Pd-GO/Li	100, 297	0-101
Cr-BDC/1.9Pt-AC/Li	91, 298	0-102	Cu-BTC/3.7Pd-IGO/Li	97, 298	0-101
Cr-BDC/1.9Pd-IGO/Li	104, 298	0-100	Cu-BTC/8Pd-IGO/Li	98, 296	0-93
Cr-BDC/6.4Pd-IGO/Li	96, 296	0-97	Cu-BTC/10Pd-IGO/Li	95, 296	0-94
Cr-BDC/21Pd-IGO/Li	103, 295	0-90	MOF-205/2.3Pt-AC	93, 298	0-102

Description of Sample Labels	
MOF	Pure MOF
MOF/Li	Washed with 1 M LiCl solution for 10 days followed by pure solvent for another 3 days
MOF/XPd-IGO	MOF synthesized in a reaction mixture containing X wt% (dry pure MOF basis) 3.2% Pd loaded on improved graphene oxide. The improved graphene oxide was synthesized using improved Hummers method and Pd is loaded onto this material by reducing a Pd salt solution onto dispersed graphene oxide.
MOF/XPd-GO	MOF synthesized in a reaction mixture containing X wt% (dry pure MOF basis) 3.2% Pd loaded on graphene oxide. The graphene oxide was synthesized using modified Hummers' method and Pd is loaded onto this material by reducing a Pd salt solution onto dispersed graphene oxide.

MOF/XPt-AC	MOF synthesized in a reaction mixture containing X wt% (dry pure MOF basis) Pt loaded on activated carbon. The Pt loaded activated carbon is purchased from Sigma Aldrich and contains ~5 wt% Pt.
MOF/XIGO	MOF synthesized in a reaction mixture containing X wt% (dry pure MOF basis) improved graphene oxide synthesized from improved Hummers' method
MOF/XAC	MOF synthesized in a reaction mixture containing X wt% (dry pure MOF basis) activated carbon purchased from Sigma Aldrich

CHAPTER 4

Hydrogen Adsorption on Selected Metal Organic Frameworks

4.1. Background

Literature review presented in Chapter 2, gives a detailed report about hydrogen adsorption on several porous materials, like zeolites, allotropes of carbon and metal organic frameworks (MOFs). MOFs are the 3D porous networks made up of metal atoms and organic ligands. These materials have gained the attention of a large number of researchers due to their known characteristics such as high surface area / pore volume [Furukawa *et al*. 2010], and tunable structure [Mishra *et al*. 2013]. They are also known as hybrid materials due to involvement of both organic (linkers) and inorganic (metal atoms). Both the organic linker as well as the constituent metal atom plays an important role on the physical properties of MOFs. Several MOFs are reported to perform better than other porous adsorbents for hydrogen storage [Czaja *et al*., 2009]. Hydrogen uptake capacity on MOFs generally depends on the variety of parameters such as pore size, surface area, pore volume, presence of coordinatively unsaturated metal sites, metal constituent of the MOF etc. However, in some instances slight variation in the hydrogen uptake capacity is reported for the same MOF in the literature due to differences in synthesis procedure and adsorption measurements [Saha and Deng, 2009, Saha et al., 2009]. Post-synthetic modification leaves a scope for enhanced uptake at times [Yang *et al*.; 2013] for the reported MOFs.

Some MOFs with large surface area such as MOF-210 adsorbs more than 8 wt% hydrogen at 77 K. But none of the MOFs satisfy DOE targets for 2017 as hydrogen

storage of 5.5 wt% in gravimetric scale and 40 g L^{-1} in volumetric scale at an operating temperature of 233 K to 333 K under a maximum delivery pressure of 100 bar [US DOE website]. As already mentioned, since H_2 adsorption in MOFs is through physisorption, and the van der Waals interactions between H_2 and surface of MOFs are weak, lower uptakes at room temperature are realized. The H_2 uptake capacity at room temperatures falls down to less than 1/10 of the saturation uptake at cryogenic temperatures. In order to enhance the H_2 uptake at ambient temperature, strong adsorption sites should be incorporated into the pores [Ghoufi *et al*., 2012]. In addition, the adsorbent surface/pore channel should be optimized for efficient adsorbate packing [Ryan *et al*., 2006].

A large volume of literature is available on adsorption of hydrogen on materials such as allotropes of carbon, zeolites, and MOFs at liquid nitrogen temperature 77 K and at room temperature. Isotherms on MOFs at cryogenic intermediate temperatures are rather limited. An alternative to very low temperature storage/adsorption of hydrogen (and physically realizable target in near future) is to store it at an intermediate temperature. Moreover, study of hydrogen adsorption properties at the intermediate temperatures help in understanding the effect of various characteristics of porous solids and in the design and development of "tuned" materials to enhance hydrogen storage capacity. This chapter focuses on measurement and analysis of hydrogen adsorption on MOFs at temperatures between 77 – 298 K. Multi temperature high pressure hydrogen adsorption isotherms are obtained on various MOFs namely Zn-BDC, Ni-DABCO, MOF-205, Cu-BTC, Cr-BDC, Mg-DOBDC and Co-DOBDC. These MOFs are chosen carefully to cover variations in pore size, surface area, pore volume, *cus* metal sites etc. (Table 4.1) to understand the effect of these parameters on the hydrogen adsorption characteristics of MOFs.

Different combinations of metal atom, geometry of SBUs and organic linkers have resulted in the formation of a different of MOF structures. Cambridge Structure Database (CSD) has recorded more than 11,000 MOF compounds in their repository. A brief summary of the structures of various MOFs studied in this chapter are described below.

4.2. Structures of Adsorbents Studied

4.2.1. Zn-BDC

Zn-BDC MOF ($Zn_4O[(O_2C)C_6H_4(CO_2)]_3$, formula weight 790 g mol^{-1}) structure is represented in Figure 4.1. Here octahedral $Zn_4O(CO)_6$ SBUs are connected to each other through benzene links. This yields a cubic network in which octahedral SBUs act as "nodes' and benzene links as "strut". SBUs as well as linkers are large, the resultant structure has shown substantial pore volume. The cationic cluster has a truncated tetrahedral envelop and the rigidly planar H_2BDC linkers have a planar slat envelop. Cubic shape unit cell dimensions can be represented as a = b = c = 25.832 Å (with respect to primary secondary and tertiary axes) [Calvo *et al*., 2008].

4.2.2. Ni-DABCO

Zn-DABCO structure is reported by Dybtsev et al., which was followed by Arstad et al. [Arstad *et al*., 2008] to synthesize Ni-DABCO (isostructure is reconstructed by replacing Zn with Ni). Ni-DABCO structure is represented in Figure 4.2. In this MOF, DABCO molecule acts as a pillar to a two-dimensional layer of metal dicarboxylate (Figure 4.2). There are two distinct pore sizes (7.5 Å × 7.5 Å along the *tertiary* axis and 4.8 Å × 3.2 Å along *primary* and *secondary* axes) [Lee *et al*., 2007]. The mass and the volume of a unit cell of Ni-DABCO MOF are 9.48 $\times 10^{-22}$ g and 1147.6 $Å^3$ respectively [Dybtsev *et al*., 2004], which correspond to a crystal density of 0.826 g cc^{-1}.

4.2.3. MOF-205

MOF-205 (C_{48} H_{26} O_{13} Zn_4) structure is first reported by Yaghi's group [Furukawa *et al*., 2010] and has a formula weight of 1072.17 g mol^{-1}. Zinc coordinates with H_3BTB to build the octahedral network and the second linker NDC bridges two parallel network and the structure grows in three dimension like honey comb structure (Figure 4.3). Cubic shape unit cell dimensions can be represented as a = b = c = 30.353 Å. The mass and the volume of a unit cell of MOF 205 are 10.68 $\times 10^{-21}$ g and 27964 $Å^3$ respectively, which correspond to a crystal density of 0.382 g cc^{-1}. The pore size and pore volume of this MOF are considerably large thereby it exhibits significant hydrogen uptake capacity at saturation conditions.

4.2.4. Cu-BTC

Cu-BTC ($Cu_3(C_9H_3O_6)_2.(H_2O)_3.XH_2O$, also known as HKUST-1) is assembled by the coordinate bond between Cu ions and trimesic acid (H_3BTC) (Figure 4.4). Cu-BTC was first reported by Williams et al. [Chui *et al*., 1999] Structure of Cu-BTC possesses cubic shape unit cell [Li *et al*., 1999]. One unit cell dimension of Cu-BTC can be represented as a = b = c = 26.343 Å. Cubic shape unit cell reported to have square channels of 9 Å × 9 Å [Yaghi *et al*., 2006]. Cu-BTC has sufficient open metal sites when activated at high temperature at inert condition [Chowdhury *et al*., 2009]. Once exposed to air, Cu-BTC gets rehydrated.

4.2.5. Cr-BDC

Cr-BDC ($Cr_3F(H_2O)_2O[(O_2C)C_6H_4.(CO_2)]_3.XH_2O$, formula weight 989 g mol^{-1}) has a complex structure [Latroche *et al*., 2006]. Cr-BDC is made from the linkage of terephthalic acid (H_2BDC) anions and inorganic trimer as represented in Figure 4.5. This

trimer [$Cr_3(\mu_3\text{-}O)\text{-}(COO)_6$] consist of three chromium atoms in an octahedral environment with four oxygen atoms of the bidentate dicarboxylate, one μ_3O and one oxygen atom from the terminal water (OH) or fluorine group (OF). Unit cell dimensions can be represented as a = b= c = 88.869 Å, volume is 701860.3 $Å^3$ Unsaturated Cr metal sites are available once the MOF is desolvated [Hong *et al*., 2009]. Cubic structure of Cr-BDC exhibits a mesoporous zeotype architecture with a large free aperture (1.2 nm for pentagonal channel and 1.6 nm×1.45 nm for hexagonal channel), mesoporous cages (2.9 and 3.4 nm) [Ferey *et al*., 2005]. Hydroxyl groups at some Cr(III) sites (unsaturated) are available once the MOF is desolvated [Hong *et al*., 2009]. Cubic structure of Cr-BDC exhibits several unique features: high specific surface area (BET, 4100 m^2g^{-1} and Langmuir, 5500 m^2g^{-1}), and numerous unsaturated chromium sites [Ferey *et al*., 2005].

4.2.6. Mg-DOBDC and Co-DOBDC

In DOBDC MOFs, metal atoms are coordinatively bonded to the oxygen atoms of the carboxylate and hydroxylate groups of the 2,5-dihydroxy terephthalic acid ligand (Figure 4.6). This coordination happens when five coordination positions of metal atom are occupied by oxygen atoms. The sixth position is occupied by water (solvent) molecule which can be removed by desolvation at higher temperature at inert condition. Metal sites of framework become coordinatively unsaturated [Dietzel *et al*., 2006]. The structure of these MOFs is hexagonal cage with large one-dimensional channel of 11–12 Å diameter [Dietzel *et al*., 2009]. Unit cell dimensions of Mg-DOBDC ($C_{72}H_{18}O_{54}Mg_{18}$, formula weight 2184.7) framework can be represented as a = b = 26.026 Å, c = 6.7587 Å and cell angles, $\alpha = \beta = 90^o$, $\gamma = 120^o$. Unit cell volume is 3964.7 $Å^3$. Similarly, Unit cell dimensions of Co-DOBDC ($C_{72}H_{18}O_{54}Co_{18}$, formula weight 2808) framework can be represented as a = b = 25.885 Å, c = 6.8058 Å and cell angles, $\alpha = \beta = 90^o$, $\gamma = 120^o$. Unit cell volume is 3949 $Å^3$.

Reported surface area of these type of MOFs are ~1200 m^2 g^{-1} only but crystal density of Mg-DOBDC is 0.915 g cm^{-3} whereas for Co-DOBDC even heavier (1.18 g cm^{-3}).

In addition, one mesoporous adsorbent (MCM-41) is also considered for this study. This traditional porous material exhibits surface area at par with MOFs, narrow pore size distributions and a variety of tunable pore systems in terms of pore size (typically 3−10 nm), pore volume (typically 0.5−1.5 cm^3g^{-1}), and pore connectivity.

4.3. Material Synthesis

4.3.1. Synthesis of MCM-41

MCM-41 is synthesized as per procedure suggested in the literature [Loganathan *et al*., 2013]. 2 g Cetrimide (Alkyltrimethyl ammonium bromide, Merck) is added to a 250 cm^3 beaker filled with 120 cm^3 of distilled water. The cetrimide−water mixture is stirred for 30 min using a magnetic stirrer. Once cetrimide is homogeneously dispersed, 10 cm^3 of TEOS (Tetraethyl orthosilicate, Merck) is added and stirred for 5 min, followed by the addition of 1 cm^3 of 25% aqueous ammonia, and again stirred for 5 min. The gel mixture is then stirred for 12 h. The beaker containing the gel mixture was kept airtight throughout the reaction period to prevent loss of aqueous ammonia. The as-synthesized white precipitate is filtered and washed with ethanol and distilled water. Then obtained white product is subjected to 12 h of drying to remove moisture. Finally, the dried sample is calcined at 823 K for 5 h to obtain as synthesized MCM-41.

4.3.2. Synthesis of Zn-BDC

Zn-BDC also known as IRMOF-1 is synthesized as per procedure suggested in the literature [Luzan *et al*., 2009]. 2.4 g of zinc nitrate hexahydrate ($Zn(NO_3)_2.6H_2O$, Sigma–Aldrich) and 0.668 g of terephthalic acid (H_2BDC, Merck) are dissolved in 80 cm^3 of

N,N-dimethyl formamide (DMF, Merck) under mild stirring. After few minutes, 4.4 cm^3 of triethyl amine (TEA, Merck) is slowly added to the solution under continuous stirring. After 2 h of stirring the solution is filtered off, washed thrice with DMF, and dried in the oven at 378 K for 20 h to obtain IRMOF-1 crystals.

4.3.3 Synthesis of Ni-DABCO

Ni-DABCO is synthesized as reported earlier [Song *et al*., 2011]. A mixture of 0.872 g nickel nitrate hexahydrate ($Ni(NO_3)_2 \cdot 6H_2O$, Merck), 0.499 g H_2BDC, (Merck), 0.279 g 1,4-diazabicyclo 2,2,2-octane (DABCO, Alfa Aesar) and 60 cm^3 DMF, is taken in a conical flask at room temperature and stirred for about 10 min. This mixture is then transferred into an autoclave. The autoclave is placed inside oven at 383 K and held for 24 h. Then it is cooled to room temperature; the obtained green color solid product is filtered and washed thoroughly with DMF followed by drying at ambient temperature (290–303 K) under vacuum.

4.3.4 Synthesis of MOF-205

MOF-205 is synthesized following the procedure reported in the literature [Furukawa *et al*. 2010] with slight modifications. First H_3BTB is synthesized as per the procedure described below [Furukawa *et al*. 2010].

4.3.4.1. Synthesis of H_3BTB

2 g TPB (1,3,5-Triphenyl benzene, Alfa Aesar) is dissolved in 40 cm^3 dichloromethane in a conical flask; in another flask 6.6 g $AlCl_3$ (Merck) is dissolved in 36 cm^3 acetyl chloride (Merck) at 273 K. The contents of the first flask are slowly added to that in the second one; the mixture is stirred for 2 h at room temperature. The resultant

red slurry is taken in a separating funnel and 500 cm^3 ice cold water is added; a light-yellow colored precipitate is formed. Stirring is continued for further 12 h followed by addition of CH_2Cl_2 to extract the precipitate (about 3 x 40 cm^3). The aqueous layer after the three washes is discarded. The organic layer is further washed with (3 × 50 cm^3) 5% NaOH solution and stirred with dry $MgSO_4$ to remove water from organic layer. The CH_2Cl_2 in the organic layer is evaporated inside a fume hood to get a yellowish white solid. This solid is boiled with ethanol until the precipitate becomes white. The solution is filtered when hot and the solid is dried in vacuum at room temperature to obtain acetyl phenyl benzene.

2 g acetyl phenyl benzene is dissolved in 1,4-di-Oxane in a conical flask. In another flask, 7.8 g NaOH is dissolved in 52 cm^3 water and chilled; 3.2 cm^3 bromine is added to the cold NaOH solution to obtain NaOBr. The NaOBr is added to di-Oxane and acetyl phenyl benzene slurry and the solution is held at 333 K for 2h. The clear solution thus obtained is cooled to room temperature, quenched with $Na_2S_2O_3.5H_2O$ solution (1 g in 20 cm^3) and acidified with 10 cm^3 HCl (35%, pH<2). The resultant solid is washed with water (4 × 250 cm^3), filtered and dried in vacuum oven at 333 K for 24 h to obtain H_3BTB.

4.3.4.2. Synthesis of MOF-205

For the synthesis of MOF-205, 868 mg H_3BTB, 698 mg NDC (Naphthalene 2,6-dicarboxylic acid, Alfa Aesar) and 2.85 g $Zn(NO_3)_2.6H_2O$ are added to a solution containing 200 cm^3 DMF and 20 cm^3 ethanol. The solution is kept in hot air oven in a 250 cm^3 PP bottle for 24 h at 371 K. The obtained brown crystals are washed with DMF thrice and then left for 4-5 days in chlorobenzene. Thereafter, the material was boiled in

chlorobenzene for three days. The solution is filtered and solid is dried in vacuum at room temperature to obtain white crystals of MOF-205.

4.3.5. Synthesis of Cu-BTC

Cu-BTC is synthesized using procedure reported earlier [Liu *et al*., 2007]. 1,3,5-benzene tricarboxylic acid (H_3BTC) (1.0 g) is dissolved in 30 cm^3 of a 1:1 mixture of ethanol/N,N-dimethyl formamide (DMF) then added to a 15 cm^3 aqueous solution of $Cu(NO_3)_2.3H_2O$ (2.077 g) in a 60 cm^3 capped polypropylene bottle. The mixture is sonicated for 10 min and then heated in an oven at 373 K for 10 h. The resulting blue precipitate is isolated by filtration and washed with methanol.

4.3.6 Synthesis of Cr-BDC

Cr-BDC also known as MIL-101 is synthesized as per reported literature [Chowdhury *et al*., 2009]. 4 g of chromium nitrate nonahydrate ($Cr(NO_3)_3 \cdot 9H_2O$, Loba Chemie) is dissolved in 48 cm^3 deionized water followed by addition of 1.64 g H_2BDC. After stirring this solution for some time 0.5 cm^3 hydrofluoric acid is added drop wise while stirring continued for another 15 minutes. The complete solution is transferred to teflon-lined stainless steel reactors (autoclave) and sealed. The reactors are placed inside a hot air oven at 493 K and held for 8 h. A fine green colored powder is obtained; excess H_2BDC are still present in the form of needle-shaped crystals. To remove this H_2BDC, DMF is added incrementally with continuous stirring. Filtered product is dried at 423 K overnight. As in case of Cu-BTC to remove H_2BDC further, an additional ethanol rinse is performed because ethanol has solubility parameter [24.9 $(J\ ml^{-1})^{1/2}$] closer to solubility parameter of DMF [24 $(J\ ml^{-1})^{1/2}$]. About 200 mg of the dried product is mixed with 15 cm^3 ethanol

and kept at 373 K for 20 h. After cooling, the resulting product is filtered and washed with ethanol. The product is finally dried at 423 K overnight.

In order to fully activate the crystal structure, it is essential that all the solvents including those coordinatively bonded with the metal centers are removed. For Cu-BTC methanol is used in a soxhalet extractor to remove the excess DMF. Similarly, Cr-BDC is boiled with ethanol to remove DMF. Both methanol and ethanol has solubility parameter of 28.5 and 24.9 $(J\ ml^{-1})^{1/2}$ respectively which is closer to solubility parameter of DMF which is 24 $(J\ ml^{-1})^{1/2}$. While boiling with ethanol or methanol, the highly polar solvents preferentially bind to the open metal sites as compared to other solvents with lower polarity thus resulting in release of the coordinated DMF from the structure [Yang *et al*., 2013]. Unused organic linkers like BTC/ BDC may block the pores of as synthesized MOF and thus should be removed to get the maximum accessibility of the pores. Trung et al. washed the MIL-53(Al) samples in boiling DMF followed by calcination at 553 K to remove the excess BDC molecules [Trung *et al*., 2008]. Significant improvement (almost 2 times) in surface area was observed for Cr-BDC by Llewellyn and co-workers when they washed the material with NH_4F [Latroche *et al*., 2006].

4.3.7. Synthesis of Mg-DOBDC

Mg-DOBDC also known as Mg-MOF-74 is synthesized as per procedure suggested in the literature [Sumida *et al*., 2011]. A solid mixture of 0.793 g 2,5 dihydroxy benzene dicarboxilic acid (H_4DOBDC, Sigma-Aldrich) and 3.3915 g magnesium nitrate hexahydrate ($Mg(NO_3)_2.6H_2O$, Merck) is added to 357 cm^3 solution of DMF, Ethanol and Water of 15:1:1 volumetric ratio and mixed by sonication for about 15-20 minutes. This mixture is transferred to twelve 60 cm^3 vials, sealed properly and then kept at 398 K in a hot air oven for 20 h. The yellowish product is decanted slowly and added with 30 cm^3 of

methanol in each vial. Entire solution is collected in one reagent bottle and methanol is replaced with fresh methanol after every 12 hours in next two days. Finally, the yellow precipitate is dried in vacuum before it was transferred into inert atmosphere.

4.3.8. Synthesis of Co-DOBDC

Co-DOBDC was synthesized as per procedure suggested in the literature [Caskey *et al.*, 2008]. A solid mixture of 0.482 g 2,5 dihydroxy benzene dicarboxilic acid and 2.377 g cobalt nitrate hexahydrate ($Co(NO_3)_2.6H_2O$, Merck) is added to 200 cm^3 solution of DMF, ethanol and water of 1:1:1 volumetric ratio and mixed by sonication for 15 to 20 minutes. This mixture is transferred to a 250 cm^3 pp bottle, sealed properly and then kept at 378 K in a hot air oven for 24 h. Obtained reddish product is decanted slowly and added with 100 cm^3 of methanol. Entire solution is collected in one reagent bottle and methanol is replaced with fresh methanol after every 12 hours in next two days. Finally, the red precipitate is dried in vacuum before it was transferred into inert atmosphere.

4.4. Characterization of the Adsorbents

4.4.1. Thermogravimetric Analysis

The thermogravimetric analysis (TGA) of synthesized samples (Figure 4.7a) is performed to study the stability of the samples. The corresponding derivative thermograms (DTG) are shown in Fig 4.7 b. The outgassing (activation) temperature during hydrogen adsorption measurements and BET surface area analysis is also fixed just accordingly. The first weight loss for the samples corresponds to the moisture/solvent removal. Thereafter they are stable upto a certain temperature after which a sharp decrease in weight indicates the collapses of crystal structure. However, in the case of DOBDC compounds weight reduction even up to 500 K due to detachment of

coordinatively bonded water molecules [Dietzel *et al*., 2006]. In fact it is necessary to expose the DOBDC samples to temperature in excess of 520 K to obtain coordinatively unsaturated metal centers [Dietzel *et al*., 2006]. While, Co-DOBDC is stable upto 540 K and all other MOFs are stable up to at least 600 K. The degassing temperatures are kept below 540 K in order to avoid structural decomposition of MOF. MCM-41 loses moisture within a temperature of 373 K and there after it remains stable beyond 800 K [Loganathan *et al*., 2013]. Saturated MOFs Zn-BDC, Ni-DABCO and MOF-205 are also stable beyond 700 K [Luzan *et al*., 2009, Song *et al*., 2011, Furakawa *et al*., 2010]. Ni-DABCO and Zn-BDC release solvent within 443 K whereas MOF-205 takes it upto 491 K because it was stored in chlorobenzene (which has boiling point 404 K). In case of Cr-BDC the initial moisture removal is fast but as the temperature increases to 473 K it starts releasing DMF, therefore a slow decline is observed. Heating up beyond 640 K, Cr-BDC structure decomposes [Yang *et al*., 2009]. Table 4.2 shows the activation conditions used for various adsorbents studied in this work.

From derivative thermogram (DTG) it is clear that Cu-BTC and Ni-DABCO MOF has the highest decomposition rate occurring at 617 K and 693 K respectively (Figure 4.7b). For Cr-BDC and Mg-DOBDC this peak appear at 650 K and 600 K respectively though the weight change curve (see Figure 4.7a and Figure 4.7b) for these two material does not turn sharp at decomposition. MOF-205 takes a high temperature for solvent removal, 425 K however decomposes at 756 K. Though Zn-BDC has the ultimate decomposition temperature of 770 K, its marginal decomposition at 631 K is also noticeable from DTG plot. On the other hand, MCM-41 does not decompose in the range of our measurement hence does not show any peak either.

4.4.2. XRD Analysis

Dry powder samples (approximately 40-80 mg) were loaded for analysis at atmospheric condition. Following the reported pattern in literature, most of the MOFs are scanned between 1° to 35° (Cu-BTC and Zn-BDC MOFs are scanned between 5 to 35°). The XRD patterns of these materials are shown in Figures 4.8a - 4.8b. The results conform to earlier reports in literature. XRD pattern of Zn-BDC can be characterized by peaks at 6.64° (1 1 0), 9.64° (2 1 0), 13.64° (2 2 0), 15.28°, 20.4° (3 2 1) and at 22.4° (1 3 1) respectively [Saha *et al*., 2009]. Ni-DABCO shows Bragg's peak at 8.1°, 9.4°, 11.35°, 12.4° and at 16.15° respectively [Song *et al*., 2009]. MOF-205 shows Bragg's peak at 4.05° (1 1 0), 6.4° (2 1 0), 10° (3 1 0) and at 11.6° (2 2 2) respectively [Furukawa *et al*., 2010]. MCM-41 was scanned between 1 to 10° (Only one low-angle peak for [1 0 0] plane corresponding to the mesophase is observed in MCM-41 [Loganathan *et al*., 2013].

Isostructural Co-DOBDC and Mg-DOBDC have almost similar XRD patterns with peaks at 6.6° and at 11.55° respectively. The XRD patterns obtained for these DOBDC MOFs in this work are compared with that available in the literature to confirm the synthesis of the samples [Caskey *et al*., 2008]. Cr-BDC has mesopores, most peaks for this material are observed in a small angle region (0° - 12°) which is characteristic of the mesoporous MOF [Latroche *et al*., 2007, Vimont *et al*., 2006]. Pure Cu-BTC consists of a face-centered cubic (FCC) crystal lattice, with reflections of (200), (220), (222), (400), (331), (420), (422), (511), and (440) planes at 2θ of 9.50°, 11.66°, 13.46°, 14.68°, 16.48°, 17.48°, and 19.06°, respectively [Liu *et al*., 2012]. The XRD results for all the eight samples presented here indicate good match with the earlier reports in literature.

4.4.3. Surface Area and Pore Volume Analysis

The BET surface area and pore volume of the adsorbents studied in this work are calculated by performing N_2 physisorption at 77 K (Figure 4.9). Prior to measurement of N_2 isotherms, all samples were out-gassed under vacuum at higher temperatures for sufficient time; the temperature chosen was dependent on the adsorbent as discussed earlier (see Table 4.2 for details). MOF-205 has larger surface area (~4590 m^2 g^{-1}) than other adsorbents. Most of the studied MOFs are having better surface area than the porous silica material MCM-41 (919 m^2g^{-1}). However, due to a large degree of mesoporosity, MCM-41 exhibits high pore volume of 1.48 cm^3 g^{-1}. The obtained surface area of the materials synthesized in this work compares well with earlier reports in literature (Table 4.1).

4.5. Excess Adsorption Isotherms

Excess adsorption isotherms of hydrogen are measured at different temperatures on several adsorbents studied in this work. Isotherms of all the adsorbents show saturation at 90-100 K within our experimental pressure range. At room temperature, the isotherms were within the Henry region throughout the entire measurement. However, for intermediate temperature range (133 – 194 K) even though saturation was not achieved, significant adsorption capacities were observed. For all the eight samples studied, equilibrium between the bulk gas and adsorbent was established within a few minutes after each pressure increment during the isotherm measurement experiments. The obtained hydrogen adsorption uptakes are compared with the available literature. Isotherms are suitably modeled to calculate important properties such as Henry's constant and enthalpy of adsorption.

4.5.1. Hydrogen Uptakes on Various Adsorbents

Saturation loading of hydrogen on mesoporous silica material MCM-41 is 1.4 wt% at 52 bar and 92 K (Figure 4.10). This value is similar to the loading reported in literature [Sheppard *et al*., 2005]. Mesopores present in MCM-41 result in higher pore volume but they are large and the huge voids do not offer enough potential for hydrogen adsorption. This adsorption uptake is much lower than that on Cr-BDC (3.8 wt%) even though pore volume of both MCM-41 (1.48 cc g^{-1}) and Cr-BDC (1.52 cc g^{-1}) are comparable. These results highlight the importance of having microporosity in the sample for achieving better hydrogen adsorption uptakes. However, this uptake is better than graphene (1.2 wt% at 77 K, 10 bar) [Srinivas *et al*., 2010], expensive zeolites like CsX (1.32 wt%, 77 K, 15 bar), RbX (1.46 wt%, 77 K, 15 bar) etc. [Langmi *et al*., 2005]. Hydrogen uptake on MCM-41 is also extremely low (only ~0.22 wt%) at room temperature and 100 bar.

Saturation hydrogen uptake on Zn-BDC is 0.85 wt% (at ~ 20 bar) and 101 K (Figure 4.11). This value is five times less compared to the loading reported by Yaghi's group [Rosi *et al*., 2003]; this difference in the loading is mainly due to the difference in the surface area and pore volume (see Table 4.1) which is not uncommon for Zn-BDC [Panella *et al*., 2005]. Saha et al. reported two entirely different surface areas for Zn-BDC in two different literatures [Saha and Deng, 2009, Saha *et al*., 2009]. For Zn-BDC, the hydrogen loading increases from 0.47 wt% to 0.84 wt% at 50 bar when temperature changes from 169 K to 136 K (Figure 4.11). Saturation is not achieved at 100 bar for either of these temperatures. Hydrogen uptake on Zn-BDC is comparable with uptake on graphene (1.2 wt% at 77 K, 10 bar) [Srinivas *et al.* 2010] and Cerium based heterometallic MOF (1.34 wt% at 77 K, 34 bar) [Wang *et al*., 2010].

In case of Ni-DABCO the adsorption isotherm saturates at 3.65 wt% at 25 bar and 90 K. This material performs better than Ce-based heterometallic MOF as reported by Wang

et al. [Wang *et al*., 2010]. Ni-DABCO also adsorbs more hydrogen than MCM-41 (1.6 wt% at 77K, 35 bar) [Sheppard *et al*., 2005], graphene (1.2 wt% at 77 K, 10 bar) [Srinivas et al., 2010] and zeolite CaX (2.19 wt%, 77 K, 15 bar) [Langmi *et al*., 2005]. However, Ni-DABCO exhibits lesser uptake than any large pore MOF like MOF-200 (7.33 wt% at 77 K, 46 bar), NOTT-112 (7 wt% at 77 K, 40 bar) etc [Furukawa *et al*., 2010]. At intermediate temperature a noticeable increment needs to be mentioned (0.9 wt% to 2.1 wt%) at ~40 bar when temperature decreases from 194 K to 145 K (Figure 4.12).

At low temperature (91 K) maximum excess loading of 5.86 wt% at 32 bar was obtained for MOF-205 (Figure 4.13) due to its high pore volume compared to other MOFs. This material has uptake capacity better than many MOFs including Mn-BTT (5.1 wt% at 77 K, 90 bar) [Dinca and Long, 2008] and has similar uptake as PCN-61 (6.24 wt% at, 77 K, 33 bar) [Yuan *et al*., 2010]. However, MOF-205 has less capacity when compared to MOF with even larger linker like MOF-210 (8.73 wt% at 77 K, 65 bar) [Furukawa *et al*., 2010]. At intermediate temperature, once the temperature is raised to 140 K then the uptake capacity decreases to 3.47 wt% at 100 bar. At room temperature and 100 bar hydrogen loading on MOF-205 is 0.63 wt% whereas at 193 K its 1.52 wt% at 100 bar.

The adsorption isotherms on MOFs containing unsaturated metal sites like, Cu-BTC, Cr-BDC, Co-DOBDC and Mg-DOBDC are shown in Figures 4.14 -4.17 respectively. For pure Cu-BTC, the adsorption isotherm saturates with 3.38 wt% loading at 20 bar and 101 K (Figure 4.14). Hydrogen uptake on Cu-BTC has better uptake capacity than zeolites like CaX [Langmi *et al*., 2005] and MOF like Ni-DOBDC (2.5 wt% at 77 K, 15 bar) [Zhou *et al*., 2008]. Hydrogen uptake of MOF like MIL-53 (3.8 wt% at 77 K, 16 bar) [Ferey *et al*., 2003], SNU-4 (3.7 wt% at 77 K, 50 bar) [Lee et al., 2008] are comparable with the uptake of Cu-BTC. On the other hand, it is still less than that on MOFs in the

similar category like PCN-10, (4.33 wt%, 77 K, 20 bar) and PCN-11 (5.05 wt%, 77 K, 20 bar) [Wang *et al*., 2008]. At room temperature Cu-BTC has a loading of 0.59 wt% at 100 bar which is better than many MOFs hence post synthetic modifications are tried on this MOF in next chapter for enhancement.

For Cr-BDC the saturation is 3.8 wt% at 45 bar and 92 K (Figure 4.15). Cr-BDC saturates at higher pressure compared to other samples due to its bigger pore sizes which reduces the affinity between adsorbate and adsorbent as the kinetic diameter of H_2 is small and the narrower the pore size, higher is the preference [Dinca *and Long*, 2005]. However, saturation loading on Cr-BDC is better due to its higher pore volume compared to other unsaturated MOFs studied in this work. Though large pore MOF like MOF 205 has better uptake (5.86 wt% at 91 K, 32 bar), Cr-BDC performs better than MIL-100(Cr) (3.28 wt%, 77 K, 26.5 bar) as well as MIL- 53 (Cr) (3.1 wt% at 77 K, 16 bar) [Ferey *et al*., 2003]. Hydrogen uptake of Cr-BDC in this work can be compared with that of MIL-101a (as synthesized Cr-BDC reported by Latroche *et al*. [2006]). However, their MIL-101b (washed with NH_4F) has better hydrogen uptake of 6.1 wt% at 77 K, 80 bar. As intermediate temperature measurement implies Cr-BDC change in hydrogen uptake from 1.2 wt% to 1.8 wt% at ~40 bar when temperature changes from 165 K to 136 K (Figure 4.15).

DOBDC series of MOFs are popular for its high binding sites for hydrogen [Liu *et al*., 2008]. As observed in the pressure composition isotherms, Co-DOBDC saturate with 2.97 wt% hydrogen at 91 K, 20 bar (Figure 4.16). This uptake is better than zeolites like CaX [Langmi *et al*., 2008], silica based material like MCM-41 and Ce based heterometallic MOF [Wang *et al*. 2010]. Zhou et al. reported saturation uptake of Ni-DOBDC (3 wt% at 77 K, 15 bar) is better than all other DOBDC MOFs including Co-DOBDC [Zhou *et al*.,

2008], interestingly hydrogen uptake on Co-DOBDC in this work is better than their reported value (~2.5 wt%, 77 K, 15 bar). Co-DOBDC has also a high room temperature loading of 0.57 wt% at 100 bar.

In the DOBDC series if Mg is used it will adsorb even more hydrogen than Zn/Co [Zhou *et al*., 2008]. For Mg-DOBDC the adsorption isotherm saturates with 3.2 wt% loading at 25 bar and 101 K (Figure 4.17). Hydrogen uptake of MOF like MIL-53 (3.8 wt% at 77 K, 16 bar) [Ferey *et al*., 2003] is comparable with the uptake of Mg-DOBDC. Noticeable changes in hydrogen uptake (1.6 wt% to 2.7 wt%) at ~40 bar are observed for Mg-DOBDC when temperature is reduced from 192 K to 133 K (Figure 4.17). Hydrogen uptake on Mg/DOBDC is ~2.3 wt% at 192 K and 80 bar which is far better than that on all other MOFs discussed here. While, Cu-BTC has an uptake capacity of ~1.5 wt%, MOF-205 has a uptake capacity of 1.4 wt% at similar condition.

4.5.2. Henry's Constant

The variation in Henry's constant with temperature is shown in Figure 4.18. For better accuracy Henry's constants were obtained from the intercept of virial domain plot (log (P/N) vs. N) [Sun *et al*., 1998]. Henry's constants of Mg-DOBDC and Co-DOBDC at cryogenic temperature are slightly higher than that of other MOFs; this could be possibly due to the presence of electrostatic interactions in Mg-DOBDC and Co-DOBDC as these MOFs contain *cus* metal sites. As temperature increases from 90 K to 297 K, the difference between Henry's constants of all the MOFs gradually decreases. The enthalpies of adsorption at zero coverage (Table 4.3) were obtained from the change in Henry's constants with temperature (Eq. 3.17). This is in good agreement with known trends observed for materials which store hydrogen by physisorption [Bae and Snurr, 2010].

Henry's constants for various MOFs at 298 K are shown in Figure 4.19. Clearly the mesorporous material MCM-41 has the lowest value while all other MOFs considered have more or less similar values of Henry's constants between ~0.04- 0.05 mol kg^{-1} bar^{-1}, well within the experimental uncertainty (estimated ~ 20 % of the calculated value of Henry's constants). On the other hand, the Henry's constants of various MOFs at low temperature (towards the right edge of Fig. 4.18) are significantly different. MOFs such as Co-DOBDC, Mg-DOBDC, Cu-BTC and Cr-BDC have higher Henry's constants due to availability of saturated metal centers. While both, Cr-BDC and Cu-BTC have unsaturated metal centers, Cu-BTC which has less number of open metal sites (compared to Cr-BDC) but its pore size is also smaller. As a result, the Henry's constant on Cu-BTC is slightly higher. Zhou *et al*. [2008] reported that relative H_2 binding strength of different metals, where they show that Ni and Co-DOBDC compounds have greater affinity for hydrogen.

4.5.3. Enthalpy of Adsorption

As in case of Henry's constant, the enthalpies of adsorption at zero coverage (Figure 4.20) for closed metal center MOFs such as Ni-DABCOand MOFs with large pore sizes such as Cr-BDC, MOF-205 and mesoporous silica material MCM-41 are low (~6 kJ mol^{-1}). Zn-BDC has relatively narrow pores hence higher enthalpy of adsorption is noticed. MOFs with open metal centers and with relatively narrow pores (Mg-DOBDC, Co-DOBDC and Cu-BTC) have enthalpies ranging between 8-10 kJ mol^{-1}. Among the MOFs studied here, Co-DOBDC has highest enthalpy of adsorption at zero coverage. This is in line with the observation by Zhou *et al*. who report high enthalpies of adsorption on Ni and Co-DOBDC MOFs at ~10 kJ mol^{-1}.

Snurr and coworkers have shown that the H_2 uptake capacity at ambient temperature (298 K) of a MOF can be considerably increased at high pressures [Frost and Snurr, 2006]. In other work, Snurr and coworkers reported H_2 storage and delivery at 15-20 bar in different MOFs. By using GCMC simulations, they estimated the optimal Q_{st} (ΔH_{des}) value for maximum H_2 desorption (delivery) is close to 20 kJ mol^{-1} [Bae and Snurr, 2010]. The deliverable capacity is the difference between the adsorbed amount of H_2 at high pressure and the adsorbed amount of H_2 at the discharge pressure 1.5 bar (according to DOE target). However, according to Bhatia and Myers, the enthalpy of adsorption for hydrogen on most porous MOFs is in the range 5-9 kJ mol^{-1} [Bhatia *et al*., 2006, Frost and Snurr, 2006] and the results in this work for a variety of MOFs seem to corroborate this finding.

At high loading (near saturation) the loading capacity is mainly governed by the pore volume available [Petit and Bandosz, 2009]. While saturation is not achieved at ambient temperatures, at cryogenic temperatures, hydrogen adsorption reaches saturation. The saturation adsorption capacity is well correlated with the pore volume as shown in Figure 4.21. A simple Langmuir equation was used to model the experimental excess adsorption isotherms obtained in this work. The model parameters for this isotherm are given in Table 4.4.

4.6. Net Adsorption

Net adsorption is a direct measure of the enhancement of hydrogen storage due presence of adsorbent in the storage vessel, as already discussed. All the raw experimental measurements are directly converted into net adsorption isotherms, applying the buoyancy correction term for the bucket alone (Eq. 3.9) [Gumma and Talu, 2010]. The net adsorption isotherms for various adsorbents considered are shown in Figs 4.22 –

4.29. At room temperature, net adsorption for MCM-41 is less than zero (Fig. 4.22 and 4.23), indicating that at any given pressure, a tank containing this material will store less amount of hydrogen compared to a tank without the adsorbent.

The net adsorption amounts for Ni-DABCO (Figure 4.24), MOF-205 (Figure 4.25) and Cr-BDC (Figure 4.26) are close to zero, indicating that no significant benefit exists in using adsorbent for storage. A tank with or without an adsorbent contains almost the same amount of hydrogen. It must be emphasized that excess amounts adsorbed on these materials are higher than 0.4 wt% at 297 K and 90 bar (Figs. 4.12, 4.13 and 4.15); however reasonable excess amounts do not translate into enhanced hydrogen storage due to the presence of adsorbent. Net adsorption on the other hand directly accounts for loss in the volume of the tank due to impenetrable solid and can be readily used to understand the effectiveness of an adsorbent [Gumma and Talu, 2010] in hydrogen storage applications.

In case of Cu-BTC net adsorption at (Figure 4.27) room temperature is slightly higher (0.18 wt% at 297 K, 100 bar). The MOFs containing open metal sites such as Co-DOBDC and Mg-DOBDC exhibit significant net adsorption capacities (~ 0.32 wt% at 298 K and 80 bar, Figure 4.28 and 4.29). The presence of metal sites thus plays an important role. The highest net loading at intermediate temperatures was observed for Mg-DOBDC as 1.9 wt% at 192 K and 75 bar (Figure 4.29). This value is almost twice than that for other MOFs thereby highlights the usefulness of open metal sites on hydrogen adsorption. All MOFs in this study with exception of MOF-5, exhibit a maximum net adsorption uptake of about 3 wt% at the lowest experimental temperature.

Due to large pore volume, MOF 205 shows a net uptake capacity of 5.4 wt% at 91 K and 32 bar.

4.7. Volume of Hydrogen Storage Vessels containing Adsorbents

The tank volumes needed to store 1 kg of H_2 at different temperatures and at 100 bar using different adsorbents studied in this work are calculated to illustrate gas storage capacity/enhancement using the adsorbents (Figure 4.30). These calculations were made using the net adsorption isotherms and procedure outlined in Section 3.5. The volume of the tank containing MCM-41 or Zn-BDC adsorbents is higher than that without these adsorbents (the points lie above the solid line). Thus, they actually reduce the hydrogen storage capacity of the tank as already discussed (since their net adsorption capacities are negative). Even at cryogenic temperature of 101 K, the volume of the tank required to store 1 kg of hydrogen 46 litres when it is filled with Zn-BDC (compared to 41 liters if it is stored as compressed gas without the adsorbent).

On the other hand, if the tank is filled with MOFs such as Cr-BDC, Ni-DABCO, MOF-205 or Mg/Co-DOBDC the tank volume necessary to store 1 kg of hydrogen decreases. The smallest volume required would be for the tank using Mg-DOBDC as adsorbent; at 298 K and 100 bar the volume required to store 1 kg of hydrogen is 97 liters for tank filled with Mg/DOBDC (a compressed gas tank at similar conditions needs a volume of 122 liters). Thus, about 20 % less storage volume is necessary. The volume decreases further at lower temperatures. At 101 K, the volume of a compressed gas tank is about 41 liters while that containing Mg-DOBDC as adsorbent is only 31 liters (a benefit of about 25 %).

Volume gain for MOF-205 is similar to DOBDC compound (though the surface area is 5 times higher). Similarly the tank volume reduces to 27 L when filled with MOF-205

at 91 K instead of 37 L if no adsorbent is used. These calculations at various temperatures for the adsorbents studied in this work are shown in Figs. 4.31 – 4.38. It is observed that over the temperature range of our measurements, the volume of the tank for hydrogen storage is reduced by about 20-30% by using MOF-205 or Mg/Co-DOBDC as an adsorbent. However none of these are close to the DoE target outlined in Chapter 1.

4.8. Summary

Several MOFs namely Zn-BDC, Ni-DABCO MOF-205, Cu-BTC, Cr-BDC, Co-DOBDC and Mg-DOBDC (in addition to mesoporous MCM 41) have been synthesized in our laboratory for hydrogen adsorption studies. Gravimetric adsorption measurement has been carried out between 90 and 298 K. Structures, properties and possible applications of MOFs as hydrogen storage media were studied. Effect of coordinatively unsaturated metal sites on the hydrogen adsorption characteristics was demonstrated with respect to temperature; it was observed that for experimental conditions where isotherms are not saturated, these unsaturated metal sites play a major role during adsorption. On the other hand, saturation loadings are governed by pore volume.

Net adsorption framework is used to readily calculate the benefits of adsorptive storage; it avoids unnecessary confusion in determination of impenetrable solid volume and the pore volumes; it directly highlights the actual advantage of storing hydrogen in a tank containing adsorbent as compared to that in a tank without adsorbent. Except Zn-BDC and MCM-41 net adsorption is positive in most of the cases and thus using those MOFs will lead to a volume gain (even if it small and do not meet the DoE targets). At room temperature tank filled with unsaturated MOFs such as Mg-DOBDC will store more

hydrogen than a tank storing hydrogen as compressed gas at similar conditions but without the adsorbent (enhancement of ~ 20 %).

Figures

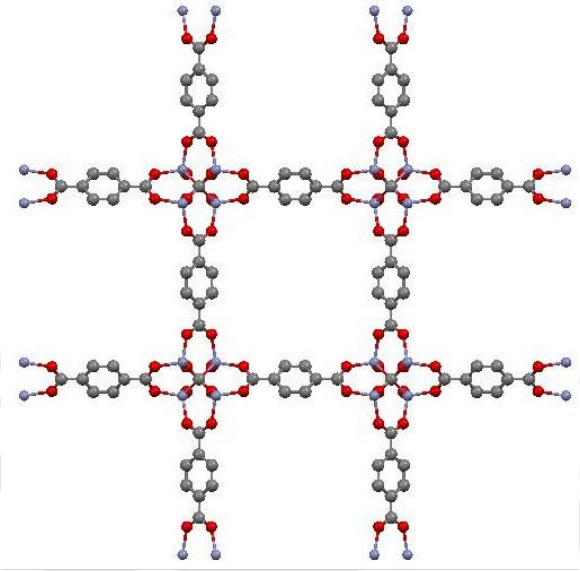

Figure 4.1: Crystal Structure of Zn-BDC: Zinc, blue; Oxygen, red and Carbon, black [Yaghi *et al*. 2003].

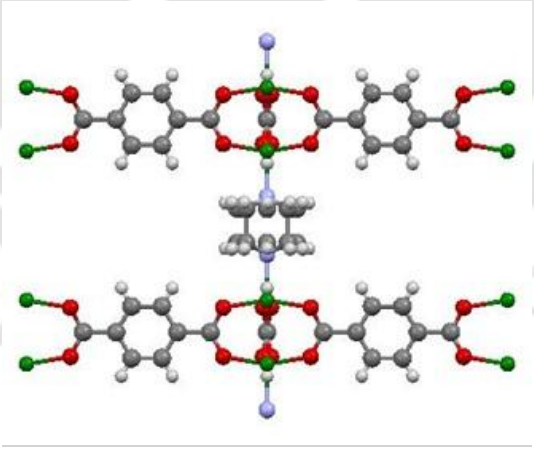

Figure 4.2: Crystal Structure of Ni-DABCO MOF (Oxygen, red; Carbon, grey; Hydrogen, blue; Nitrogen, blue; Nickel, green) [Dybsev *et al*., 2004].

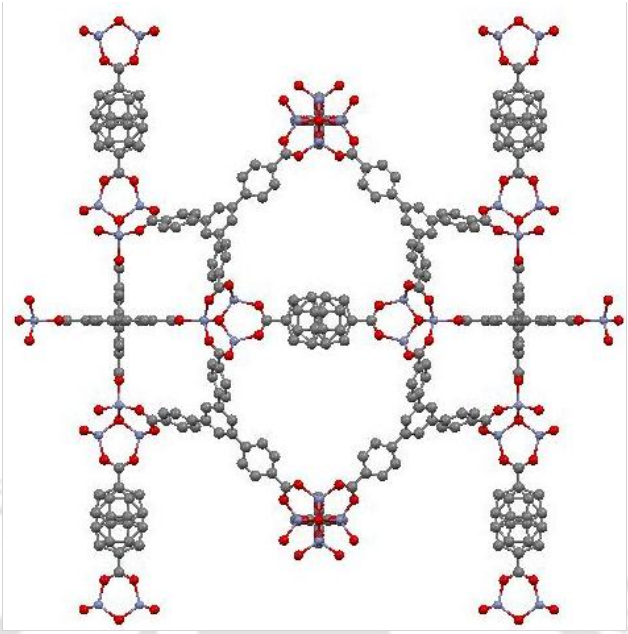

Figure 4.3: Crystal Structure of MOF-205: Zinc, blue, Oxygen, red and Carbon, black [Furukawa *et al*., 2010].

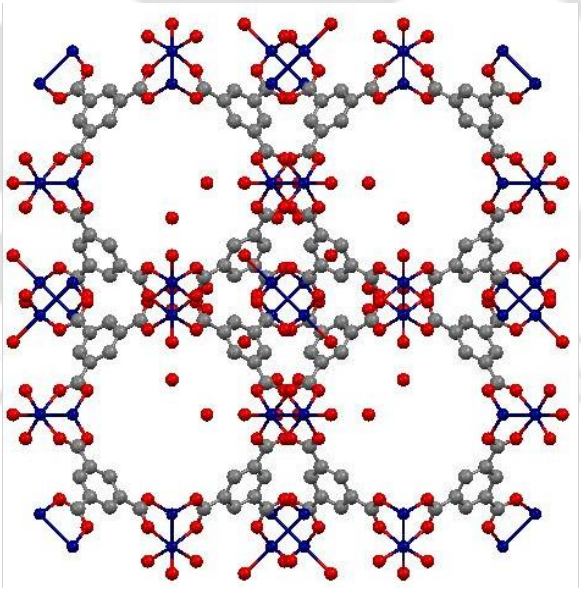

Figure 4.4: Crystal Structure for Cu-BTC MOF. Copper, blue, Oxygen, Red, Carbon, gray [Krungleviciute *et al*., 2007].

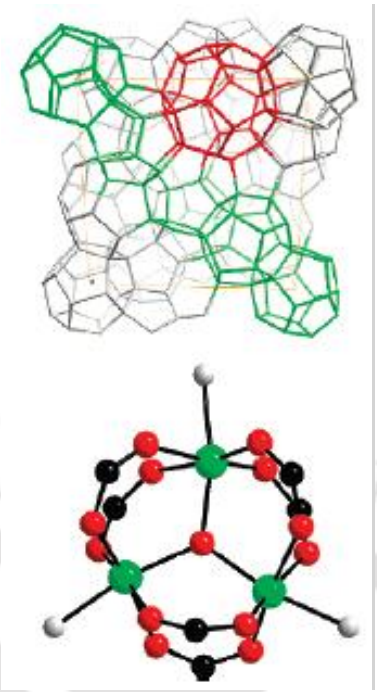

Figure 4.5: View of the Structure of Cr-BDC; green, Chromium; red, oxygen; black, carbon; white, water [Hamon *et al*., 2009].

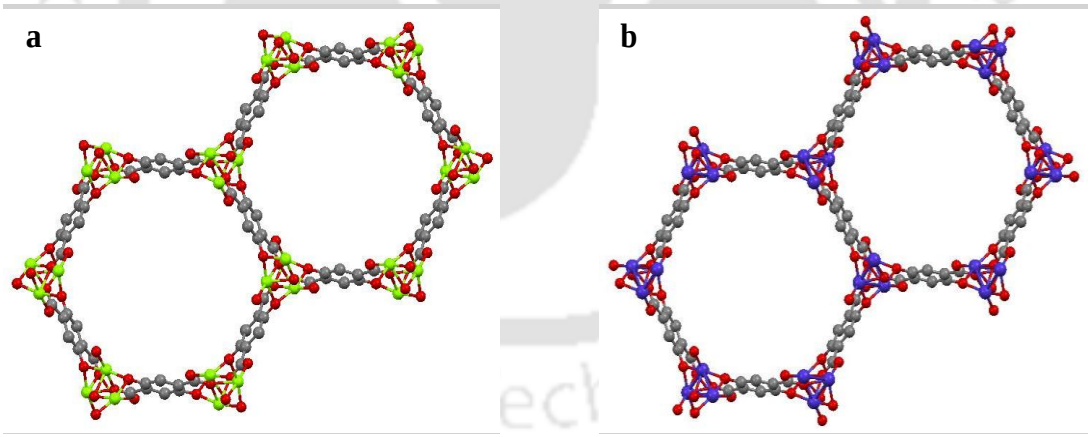

Figure 4.6: Crystal Structure of (a) Mg-DOBDC [Dietzel *et al*., 2006], (b) Co-DOBDC [Dietzel *et al*., 2009] MOFs (Oxygen, red; Carbon, grey; Magnesium, bright green; Cobalt, violet).

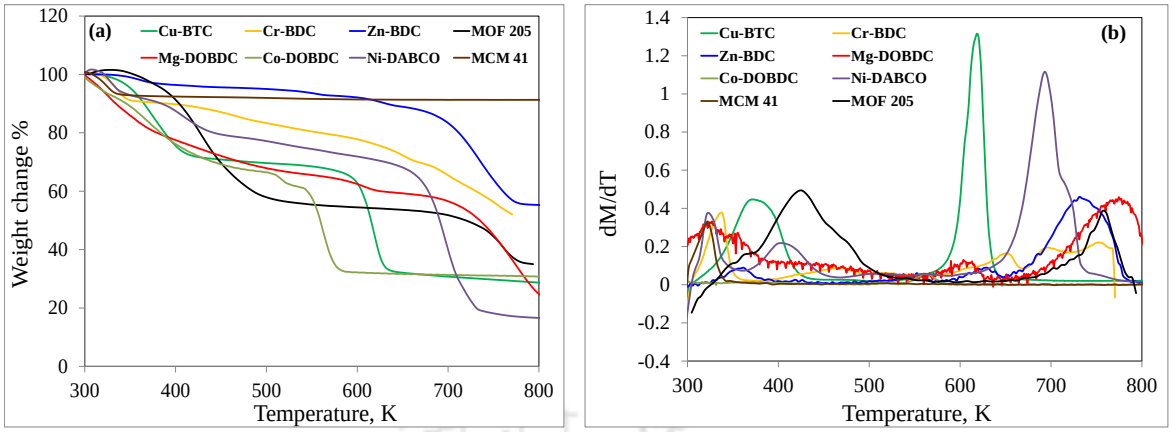

Figure 4.7: Thermograms of Adsorbents Studied.

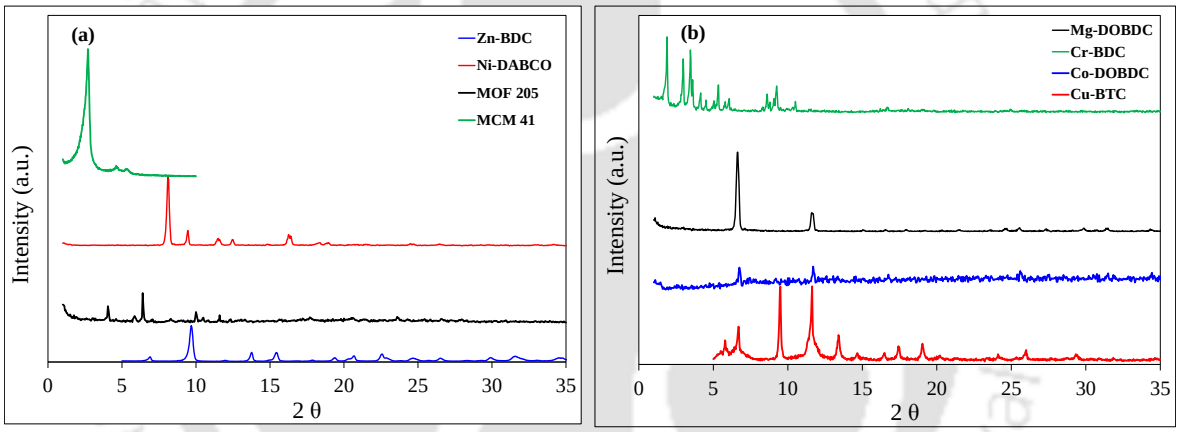

Figure 4.8: Powder XRD Patterns of Adsorbents Studied.

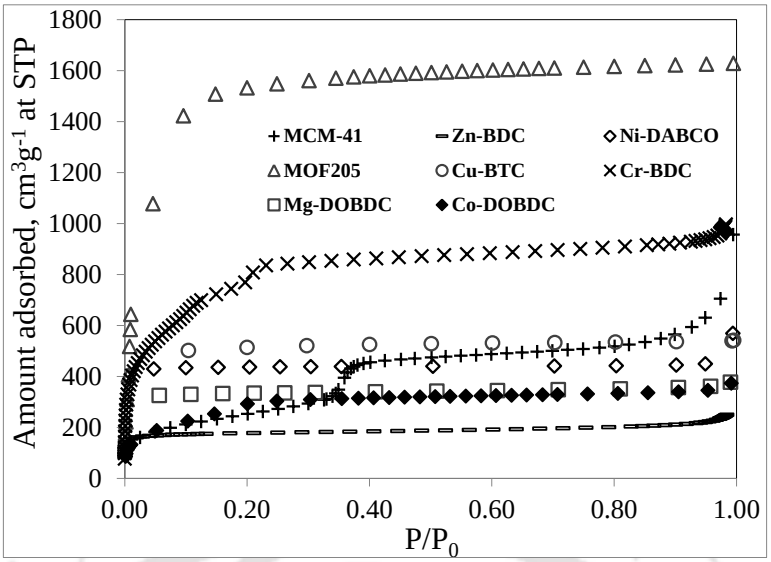

Figure 4.9: N_2 Adsorption Isotherms at 77 K for Various Adsorbents Studied.

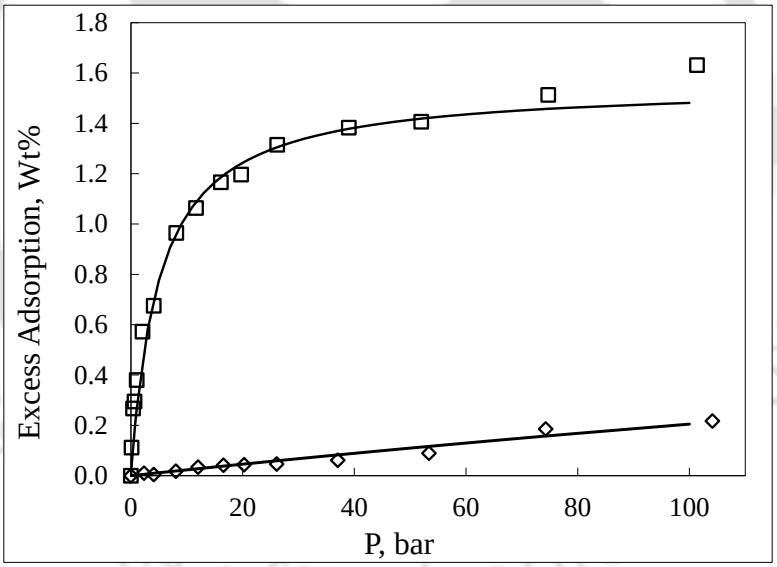

Figure 4.10: H_2 Adsorption Isotherms of MCM-41. Symbols are experimental data at 92 K (square) and 296 K (diamond); Lines are fits from Langmuir Isotherm Model.

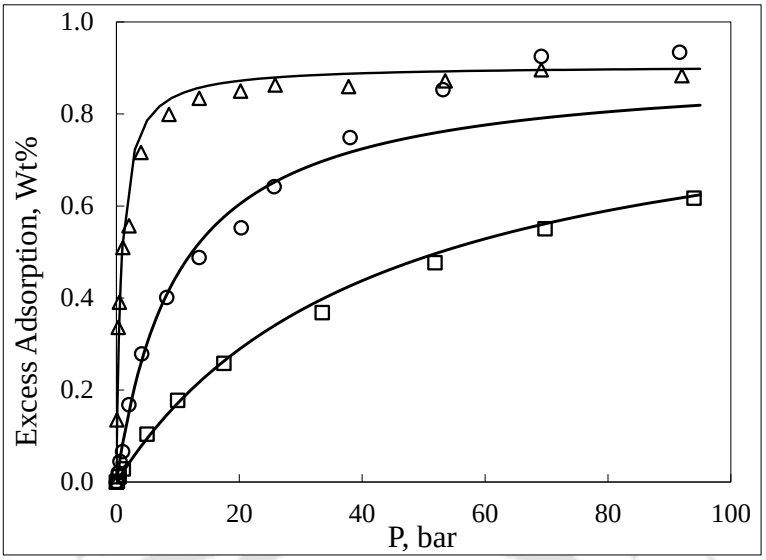

Figure 4.11: H_2 Adsorption Isotherms of Zn-BDC. Symbols are experimental data at 101 K (triangle), 136 K (circle), 169 K (square); Lines are fits from Langmuir Isotherm Model.

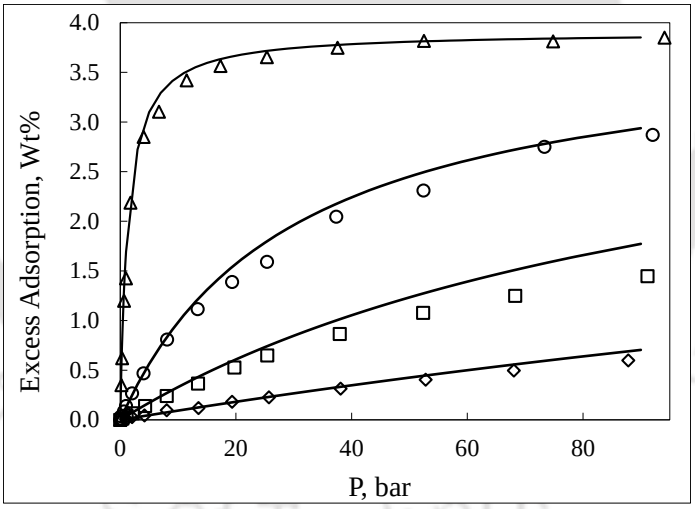

Figure 4.12: H_2 Adsorption Isotherms of Ni-DABCO. Symbols are experimental at 90 K (triangle), 145 K (circle), 194 K (square) and 297 K (diamond); Lines are fits from Langmuir Isotherm Model.

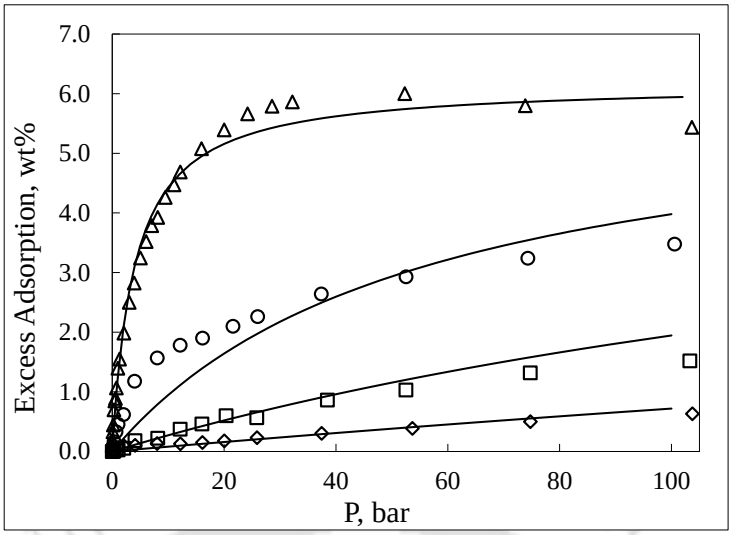

Figure 4.13: H_2 Adsorption Isotherms of MOF-205. Symbols are experimental at 91 K (triangle), 140 K (circle), 193 K (square) and 296 K (diamond); Lines are fits from Langmuir Isotherm Model.

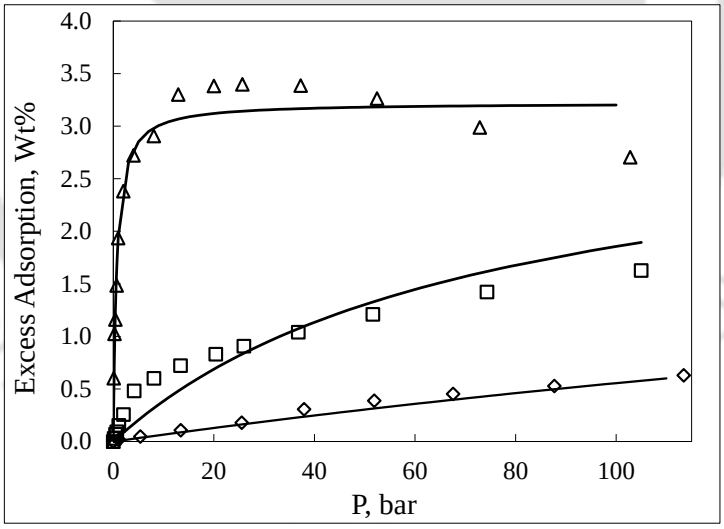

Figure 4.14: H_2 Adsorption Isotherms of Cu-BTC. Symbols are experimental at 101 K (triangle); 192 K (square); 297 K (diamond); Lines are fits from Langmuir Isotherm Model.

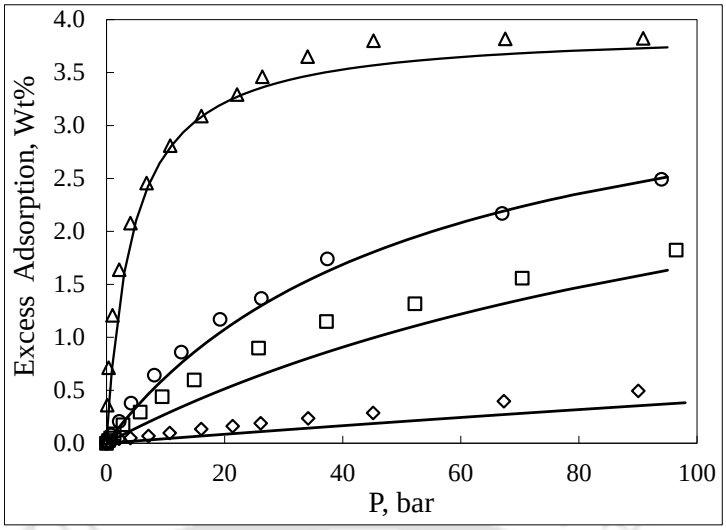

Figure 4.15: H_2 Adsorption Isotherms of Cr-BDC. Symbols are experimental at 92 K (triangle), 136 K (circle), 165 K (square) and 297 K (diamond); Lines are fits from Langmuir Isotherm Model.

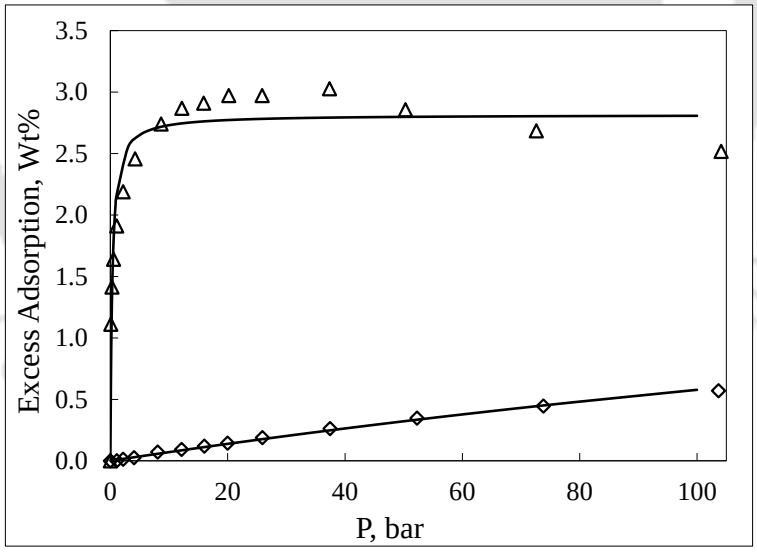

Figure 4.16: H_2 Adsorption Isotherms of Co-DOBDC. Symbols are experimental at 91 K (triangle) and 297 K (diamond); Lines are fits from Langmuir Isotherm Model.

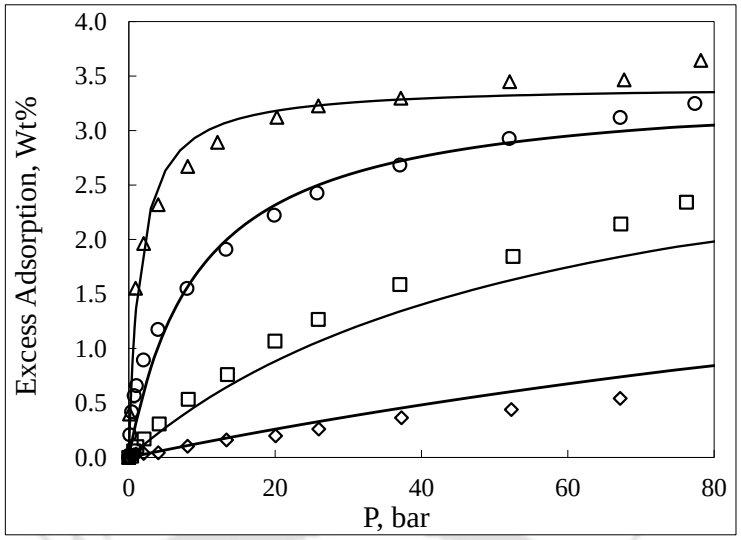

Figure 4.17: H_2 Adsorption Isotherms of Mg-DOBDC. Symbols are experimental at 101 K (triangle), 133 K (circle), 192 K (square) and 298 K (diamond); Lines are fits from Langmuir Isotherm Model.

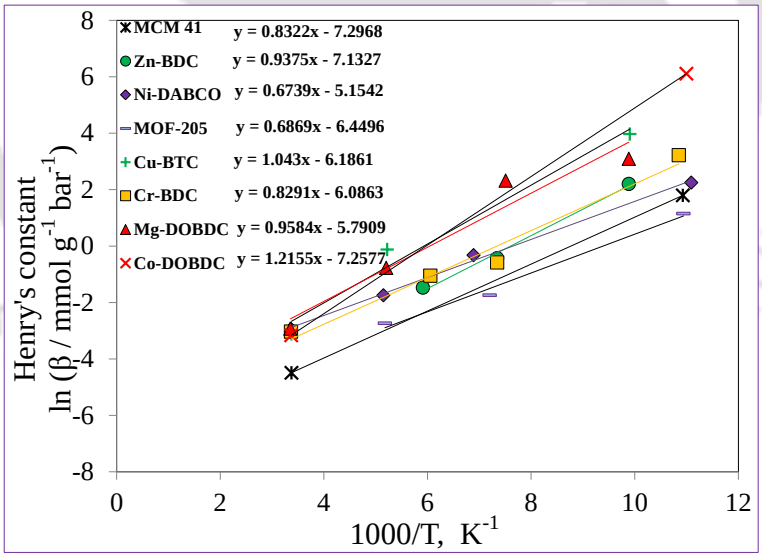

Figure 4.18: Variation of Henry's Constants with Temperature; Best fit Straight Lines are also shown.

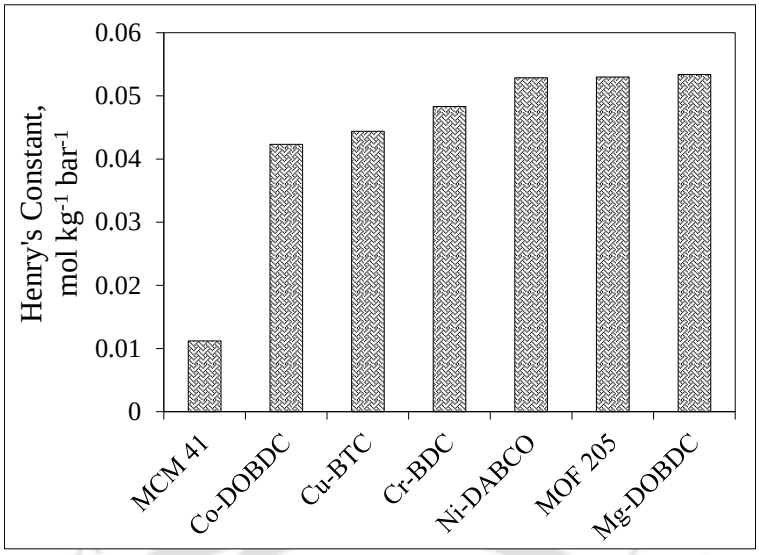

Figure 4.19: Henry's Constant for H_2 adsorption at Room Temperature for Studied MOFs and MCM-41.

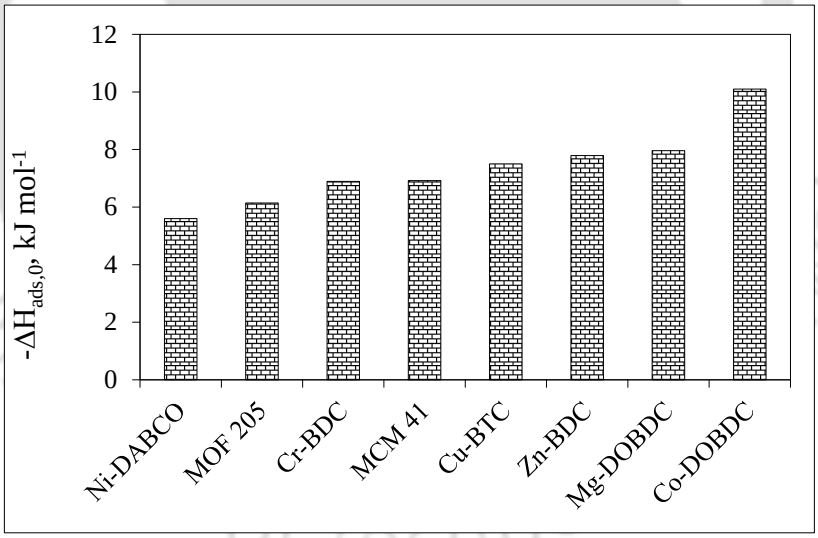

Figure 4.20: Enthalpy of Adsorption for H_2 at Zero Coverage for Studied MOFs and MCM-41.

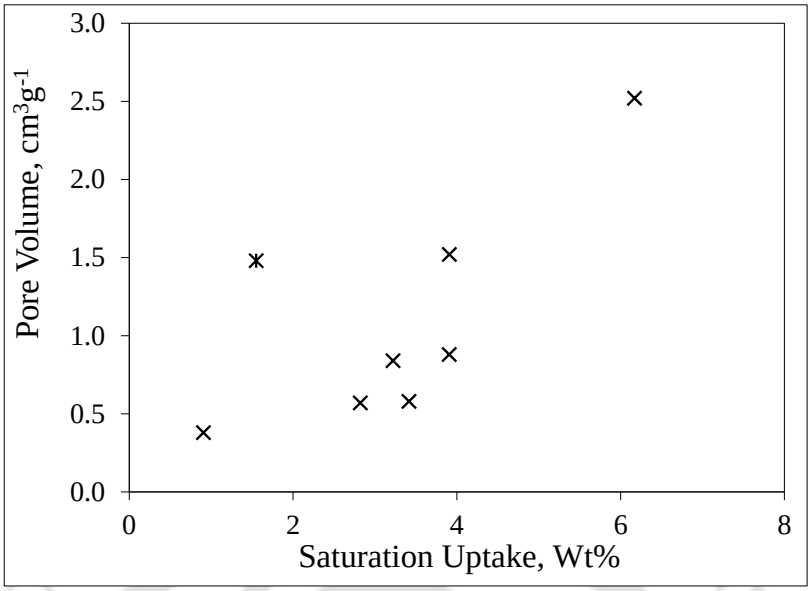

Figure 4.21: Variation of Hydrogen Saturation Uptake Capacity with Pore Volume for Adsorbents Studied.

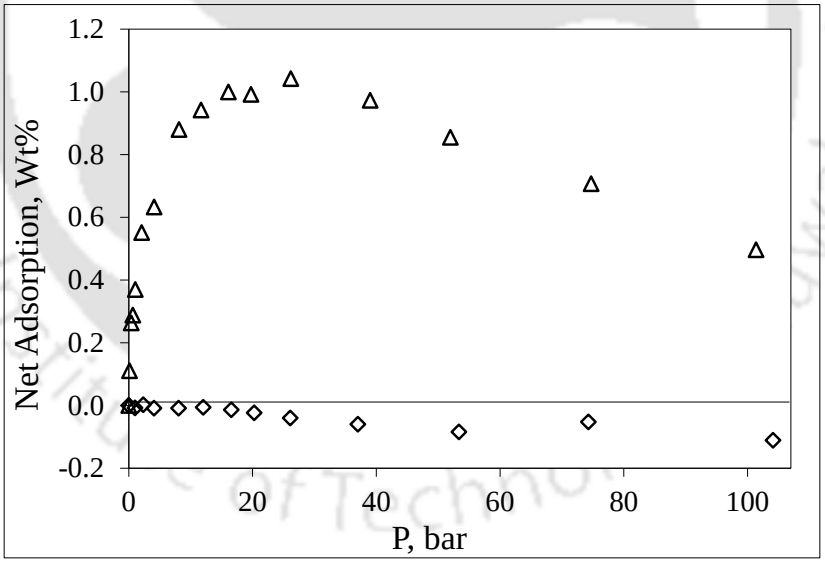

Figure 4.22: Net Adsorption Isotherms of MCM-41 at 92 K (triangle) and 296 K (diamond).

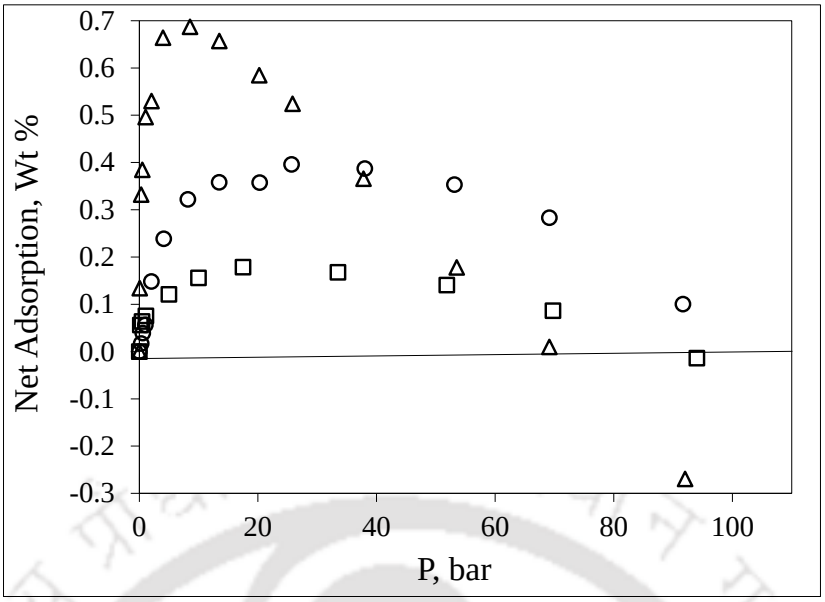

Figure 4.23: Net Adsorption Isotherms of Zn-BDC at 101 K (triangle), 136 K (circle), and 169 K (square).

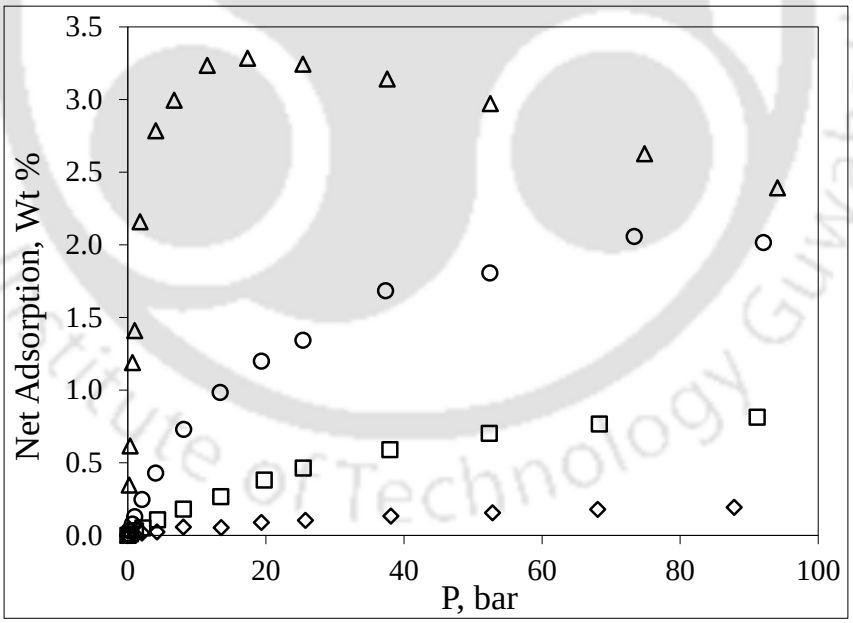

Figure 4.24: Net Adsorption Isotherms of Ni-DABCO at 90 K (triangle), 145 K (circle), 194 K (square) and 297K (diamond).

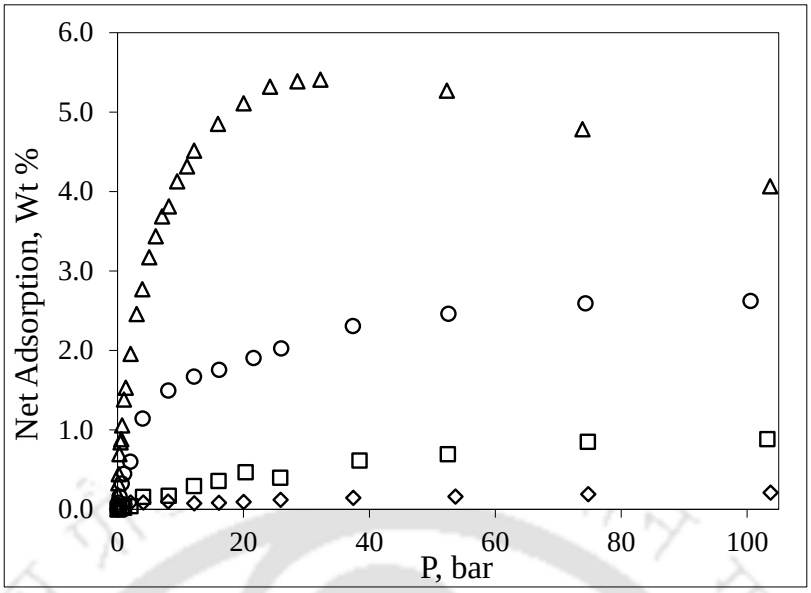

Figure 4.25: Net Adsorption Isotherms of MOF-205 at 91 K (triangle), 140 K (circle), 193 K (square) and 296 K (diamond).

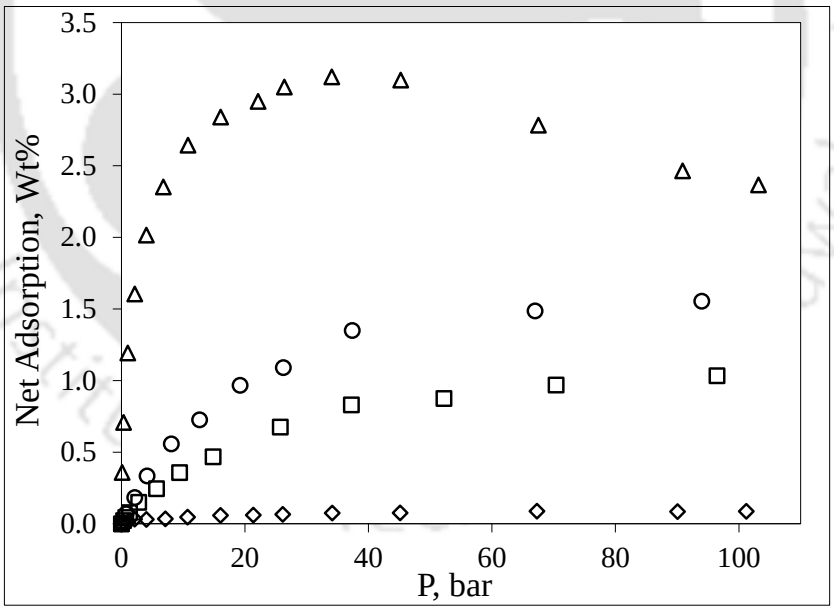

Figure 4.26: Net Adsorption Isotherms of Cr-BDC at 92 K (triangle), 136 K (circle), 165 K (square) and 297 K (diamond).

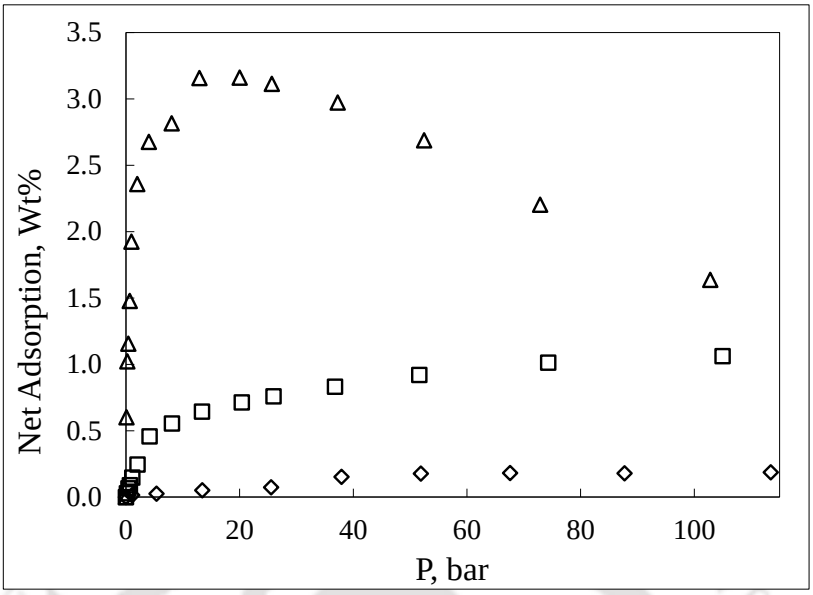

Figure 4.27: Net Adsorption Isotherms of Cu-BTC at 101 K (triangle), 192 K (square) and 297 K (diamond).

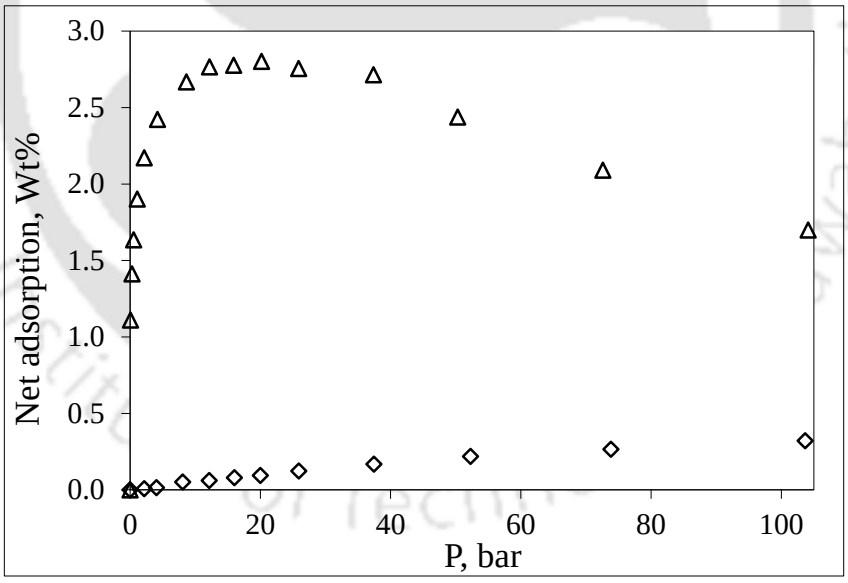

Figure 4.28: Net Adsorption Isotherms of Co-DOBDC at 91 K (triangle) and 297 K (diamond).

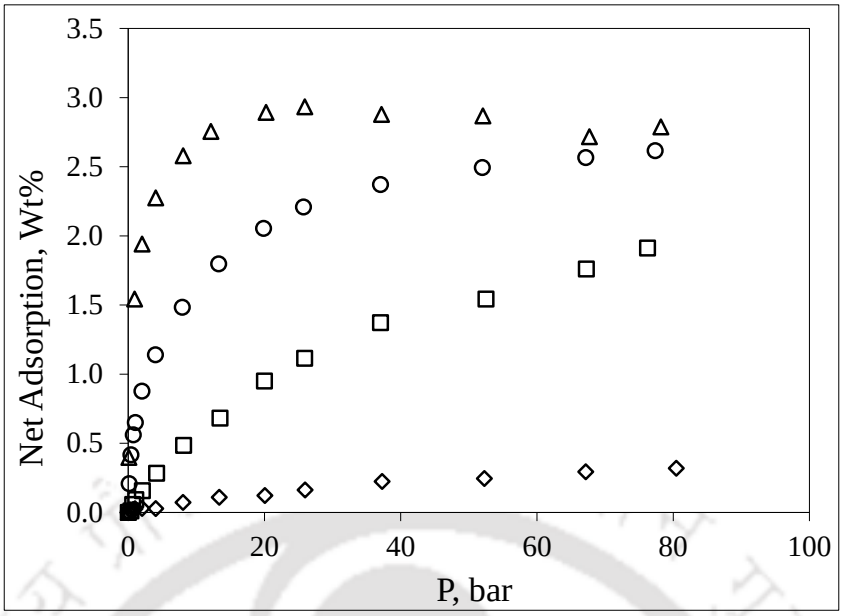

Figure 4.29: Net Adsorption Isotherms of Mg-DOBDC at 101 K (triangle), 133 K (circle), 192 K (square) and 298 K (diamond).

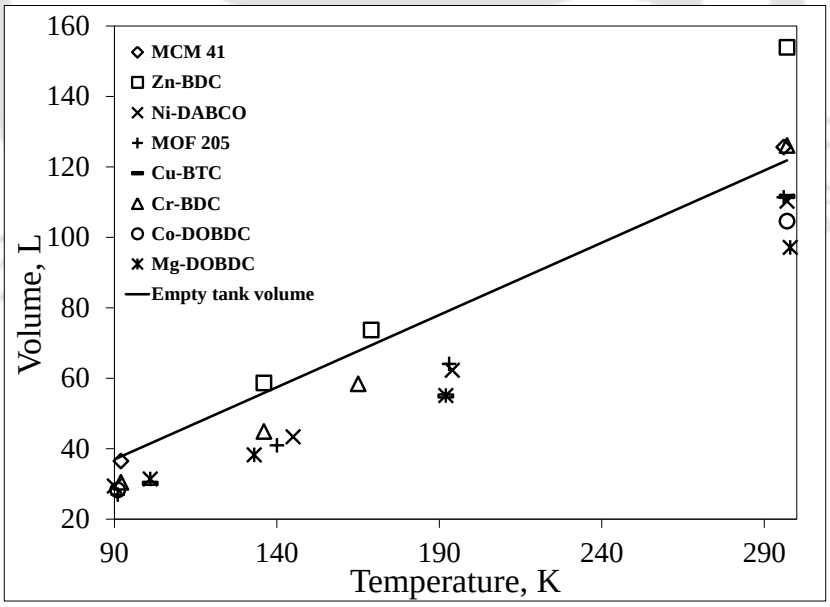

Figure 4.30: Tank volumes required to store 1 kg of H_2 with different Adsorbents. The solid line indicates volume of Tank necessary to store 1 kg H_2 as a Compressed gas at 100 bar and the Temperature of Interest.

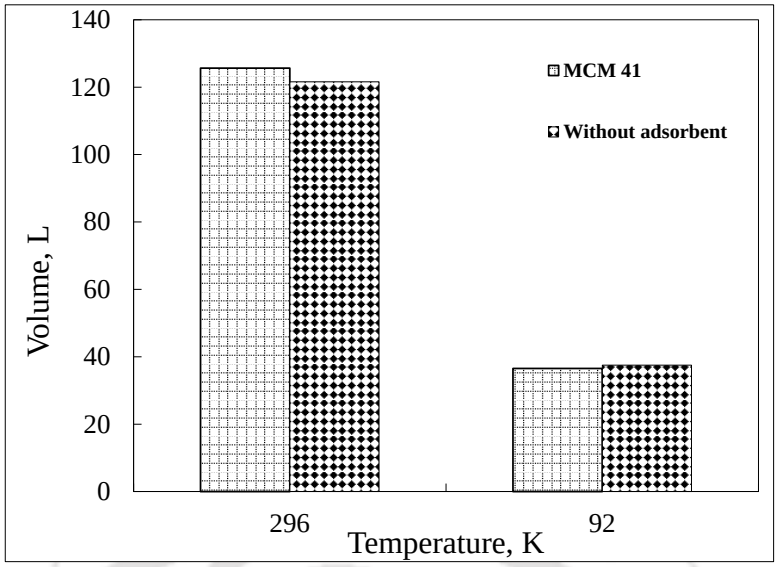

Figure 4.31: Tank volume required to store 1 kg of H_2 with MCM-41 as Adsorbent

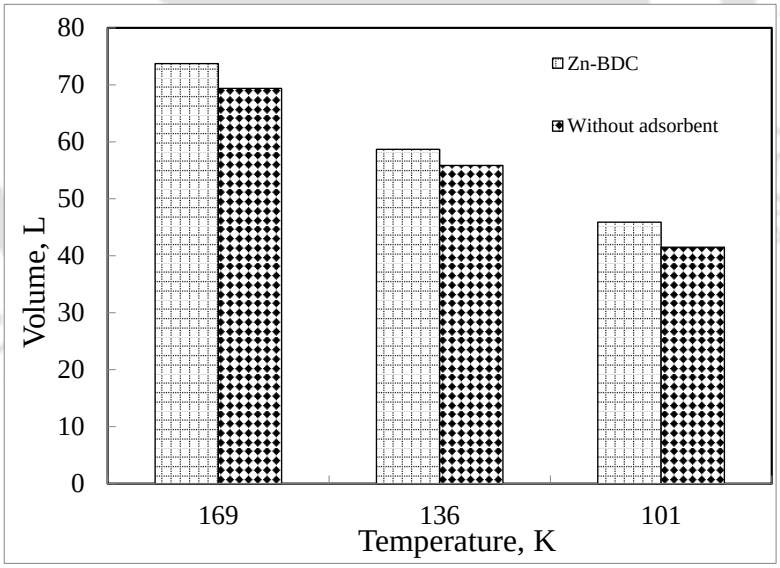

Figure 4.32: Tank volume required to store 1 kg of H_2 with Zn-BDC as Adsorbent

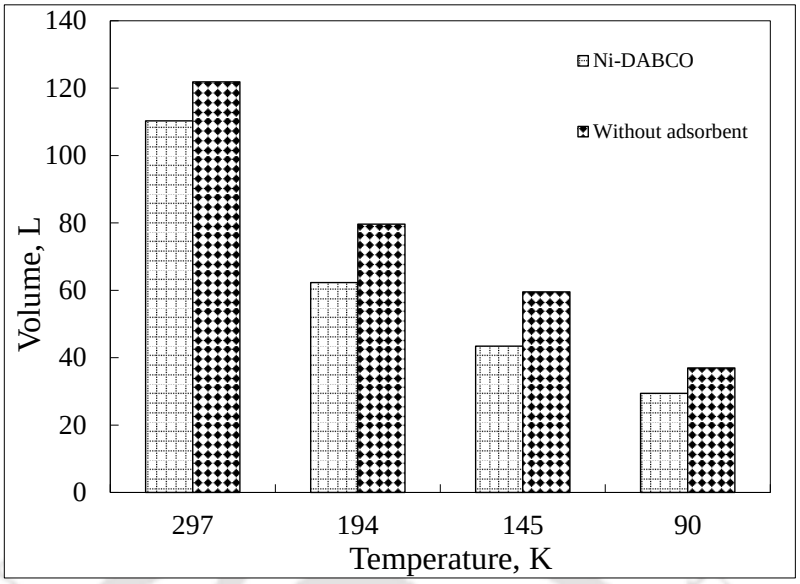

Figure 4.33: Tank volume required to store 1 kg of H_2 with Ni-DABCO as Adsorbent

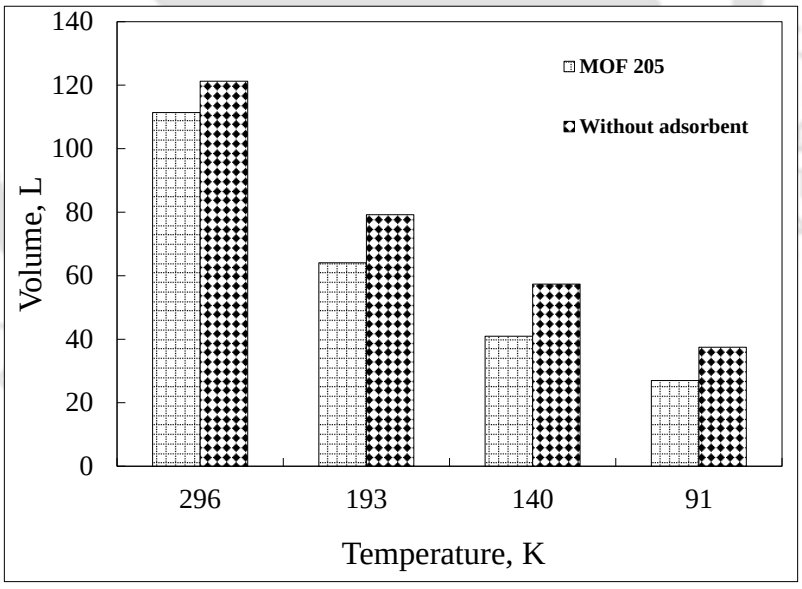

Figure 4.34: Tank volume required to store 1 kg of H_2 with MOF-205 as Adsorbent

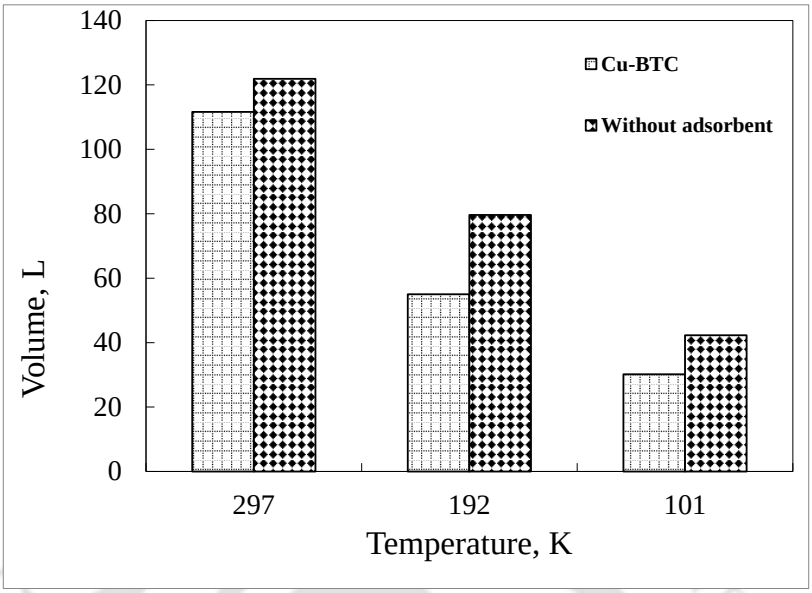

Figure 4.35: Tank volume required to store 1 kg of H_2 with Cu-BTC as Adsorbent

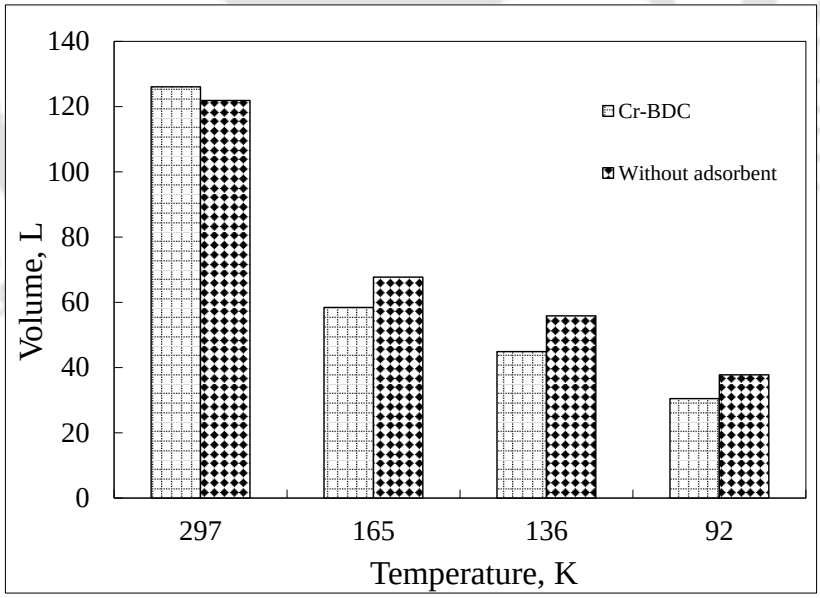

Figure 4.36: Tank volume required to store 1 kg of H_2 with Cr-BDC as Adsorbent

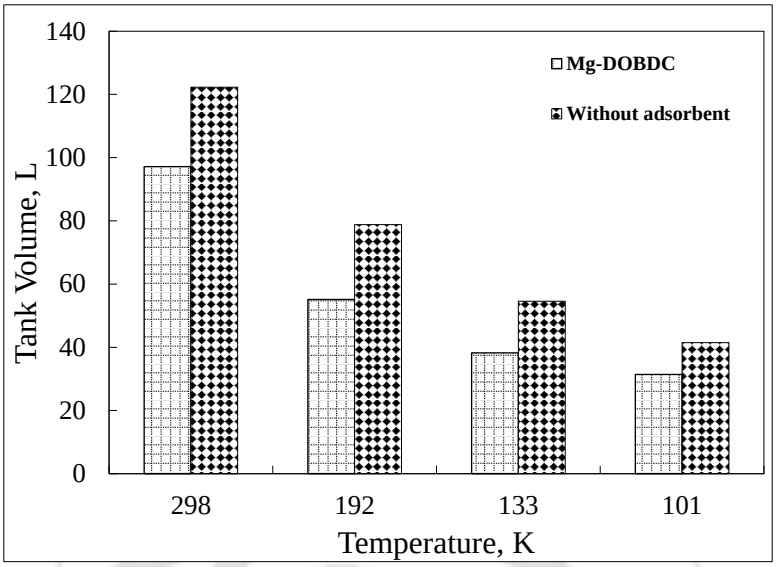

Figure 4.37: Tank volume required to store 1 kg of H_2 with Mg-DOBDC as Adsorbent

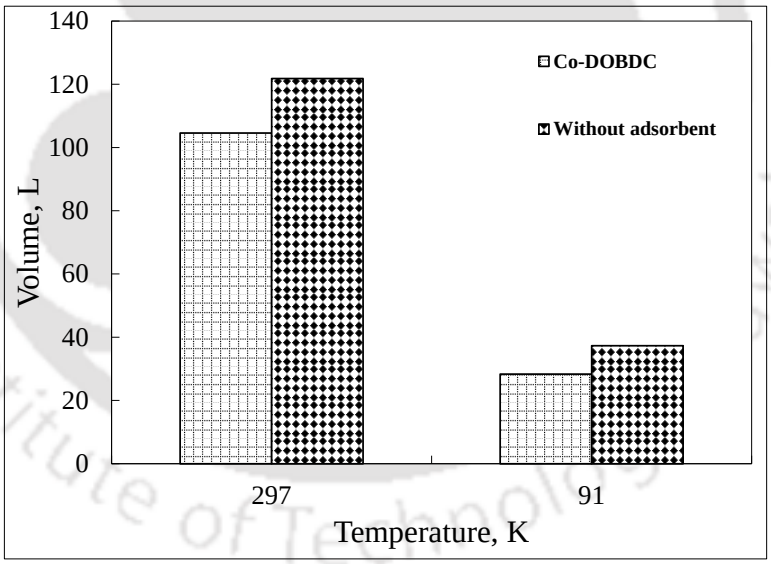

Figure 4.38: Tank volume required to store 1 kg of H_2 with Co-DOBDC as Adsorbent

Tables

Table 4.1: Physical Properties of Adsorbents Studied.

Compound	**Open metal sites**	**Surface area, $m^2\ g^{-1}$**	**Pore volume, $cc\ g^{-1}$**	**Reference**
Zn-BDC or MOF-5	No	2833	1.13	[Andrew *et al*., 2005]
		832	0.3	[Luzan *et al*., 2010]
		572	0.28	[Hirsher and Panella, 2005]
		623	0.38	This work, [Sahu *et al*., 2013]
MOF-205	No	4590	2.52	This work
Ni-DABCO	No	1306	0.88	This work
Cr-BDC or MIL-101 (Cr)	Yes	2927 2931	1.52 1.45	This work, [Sahu *et al*., 2013] [Li *et al*., 2007]
Mg-DOBDC or MOF-74 (Mg)	Yes	1332 1048	0.61 0.58	[Wu *et al*., 2009] This work, [Sahu *et al*., 2013]
Co-DOBDC or MOF-74 (Co)	Yes	1001 1056	0.57 0.48	This work [Wu *et al*., 2009]
Cu-BTC or HKUST-1	Yes	1494 1482	0.84 0.83	This work [Liu *et al*., 2007]
MCM-41	No	919 1017	1.48 0.73	This work [Sheppard *et al*., 2005]

Table 4.2: Activation Conditions for Adsorbents Studied

Adsorbent	**Solvent (to store)**	**Activation**		**Adsorbent**	**Solvent (to store)**	**Activation**	
		T, K	Time, h			T, K	Time, h
MCM-41	NA	473	3	Cr-BDC	Methanol	467	3
Zn-BDC	Methanol	393	6	Mg-DOBDC	Methanol	523	3
Ni-DABCO	DMF	443	3	Co-DOBDC	Methanol	520	5
MOF-205	Chloro-benzene	493	3	Cu-BTC	Methanol	473	3

Table 4.3: Maximum H_2 Uptake, Henry's Constants and Enthalpy of Adsorption for Adsorbents Studied

Adsobent	**Maximum H_2 uptake**	**Henry's constant at cryogenic temperature**		**Henry's constant at room temperature**	**Adsorption Enthalpy at zero coverage**
	$W_{max,}$ Wt%	T, K	mol kg^{-1} bar^{-1}	mol kg^{-1} bar^{-1}	kJ mol^{-1}
MCM-41	1.63	92	6.0	0.011	6.9
Zn-BDC	0.89	101	9.0	-	7.8
Ni-DABCO	3.81	90	9.5	0.053	5.6
MOF-205	6	91	13.2	0.053	6.1
Cu-BTC	3.39	101	53.0	0.044	8.7
Cr-BDC	3.88	92	25.0	0.048	6.9
Mg-DOBDC	3.64	101	22.1	0.053	8.0
Co-DOBDC	3.02	91	> 450*	0.042	10.1

* Due to experimental limitations and heavy adsorption this number could not be determined with more certainty

Table 4.4; Langmuir Isotherm Model Parameters for H_2 Adsorption on Adsorbents Studied

MOF	**Maximum loading**	**Affinity Constant**	
	W_{max} (Wt%)	**b_0 x 10^4** (bar^{-1})	**b_1** (K)
MCM 41	1.55	1.62	661
Zn-BDC	0.905	0.584	1014
Ni-DABCO	3.907	1.665	744
MOF 205	6.17	1.25	696
Cu-BTC	3.22	0.7	1010
Cr-BDC	3.908	1.245	714
Co-DOBDC	2.82	1.11	934
Mg-DOBDC	3.416	3.369	780

CHAPETR 5

Effect of Lithium Doping on MOFs on their Hydrogen Adsorption Characteristics

5.1. Background

In order to enhance the H_2 uptake capacity on an adsorbent, the H_2 affinity with the surface should be increased. A review of literature for enhancement of hydrogen sorption in MOFs has been presented earlier in Chapter 2 (Section 2.3.4). Several strategies that have been studied include generation of coordinatively unsaturated metal sites [Sumida *et al*., 2008], doping of metal ions with light alkali metals such as Li^+ in the structure [Yang *et al*., 2009], incorporation of metal nanoparticles [Zlotea *et al*., 2010] and functionalization of the ligands that are exposed to the pores [Weston *et al*., 2011].

Cu-BTC and Cr-BDC MOFs are well studied MOFs in literature and have reasonable surface area and pore volume. In addition, Cr-BDC has good thermal and structural stability [Sumida *et al*., 2012]. As already discussed in the previous chapter, the hydrogen storage capacity of both these MOFs do not meet the DOE target and methods to enhance their hydrogen uptake capacity are to be explored. While the attempt here is to enhance the uptake capacity of these two MOFs in particular the method adopted should be applicable suitably to other MOFs as well, in addition to providing some insight into the methodology itself.

Lithium has well documented affinity towards hydrogen [Xiang *et al*., 2012]. To investigate the influence of lithium doping in Cu-BTC and Cr-BDC on hydrogen adsorption ability of these MOFs, we have used the cation (lithium) exchange technique

to introduce lithium into MOFs [Yang *et al*., 2009]. Few other reported techniques are reported for incorporation Li by lithium naphthalenide using solvents like tetrahydrofuran and lithium *t*-butoxide [Xiang *et al*., 2012, Mulfort *et al*., 2009].

5.2. Material Synthesis

Synthesis of Cu-BTC and Cr-BDC MOFs is detailed in Sections 4.2.4 and 4.2.5 respectively. The MOFs were first synthesized using this procedure; they were then subjected to Lithium doping. Li doping was achieved by soaking approximately 1 g MOF in 35 cm^3 1 M LiCl (Anhydrous, Spectrochem) solution in methanol (HPLC grade, Spectrochem) for 10 days, (replacing the salt solution every 8 h). These samples are then washed with pure methanol for another three days (replacing methanol every 8 h) to remove weakly attached lithium. The obtained compounds were lighter in color compared to the original MOFs (light blue for Cu-BTC and light green for Cr-BDC). We call these samples as Cu-BTC/Li and Cr-BDC/Li, respectively. The samples are stored in pure methanol for further analysis.

5.3. Material Characterization

5.3.1. Elemental Analysis

In a typical analysis, 2 mg dry sample was dissolved in 0.6 ml concentrated HCl and then diluted with water to make about 25 ml clear solution. The MOF solution was analyzed in flame photometer for Li concentration, while atomic absorption spectroscopy (AAS) was used to determine the concentration of Cu (or Cr) in the MOF samples. In case of flame photometry experiments, 2 ppm $LiCO_3$ solution is used for calibration and 1 ppm $LiCO_3$ solution is used to cross check the calibration. The results indicate that Li/Cu ratio in Cu-BTC/Li is about 0.01, while Li/Cr ratio in Cr-BDC/Li is about 0.07. This type

of Li doping into the frameworks is not unusual and is earlier reported for DO-MOF (MOF synthesized from diol containing strut with Zn-salt as metal source), where Li is doped into the MOF using Li *t*-butoxide to a Li/Zn_2 ratio of 0.2. However, the parent MOF considered in that study has lower surface area (and hydrogen loading); slight improvement in surface area, pore volume and hydrogen loading were observed after doping [Mulfort *et al*, 2009 a]. In another computational study, Han et al. demonstrated that Li atoms prefer to bind at the centers of the hexagonal aromatic rings, but Li atoms at the adjacent rings are located exactly on the opposite sides [Han *et al*, 2007].

5.3.2. TGA Analysis

Thermo-gravimetric analysis (TGA) of synthesized samples (Figure 5.1) was performed to study the thermal stability of the products. The initial weight loss (below ~ 400 K) for all of the samples corresponds to the solvent removal. Yang and coworkers showed if Cu-BTC is washed with different solvents it takes different shape in TGA curve [Yang *et al*., 2013]. The following observations can be made by comparing the TGA profiles of Cu-BTC and Cu-BTC/Li.

(a) The first weight loss step (~ 30 % of the mass) for Cu-BTC completes by about 430 K whereas for Cu-BTC/Li this step lasts until about 480 K although the weight loss is slightly lower (~ 26 %). The rate of weight loss is also slower in case of Li-doped sample indicating that the solvent may be more strongly bound to the framework in case of Cu-BTC/Li.

(b) The second weight loss step for both the samples starts between 575 and 590 K and completes before 660 K. The final weight of the sample in case of Cu-BTC/Li is higher about 10 wt %. One possible reason for lower weight loss might be more efficient removal of unreacted organic linker and/or other solvent molecules from

the pores of the framework during the doping procedure, when the framework is in contact with excess LiCl/methanol for prolonged time period (more than 10 days). Yang *et al*. report similar weight loss after washing the Cu-BTC framework with methanol for 2 days [Yang *et al*., 2013].

The profiles of Cr-BDC and Cr-BDC/Li can also be compared in a similar fashion.

(a) The first weight loss step (~ 10 % of the mass) for Cr-BDC completes by about 350 K whereas for Cr-BDC/Li this step lasts until about 400 K although the weight loss is slightly lower (~ 8 %). The rate of weight loss is also slower in case of Li-doped sample indicating that the solvent may be more strongly bound to the framework in case of Cr-BDC/Li.

(b) In between 420 and 550 K, the mass of Cr-BDC/Li is relatively stable whereas Cr-BDC loses about 10 wt% indicating removal of solvent and/or other impurities in the sample.

(c) The final weight loss step starts between 580 and 630 K in both cases. However, the mass of Cr-BDC/Li at 700 K is about 10 wt % higher than that of Cr-BDC. As in case of Cu-BTC, the reason for this lower weight loss in the Li doped sample may be attributed to more efficient removal of unreacted organic linker and/or solvent molecules from the framework. Llewellyn *et al*. [2008] have earlier used an ammonium salt (NH_4F) for removal of unreacted terephthalic acid from the pores and thus realizing more effective activation of the Cr-BDC sample. The LiCl/MeOH solution used for Li doping in this work may also have played a similar role for removal of unreacted terephthalic acid.

5.3.3. XRD Analysis

Powder X-ray diffraction measurements were carried out on synthesized materials. Dry powder samples were loaded for analysis at atmospheric condition. Specimens were scanned between 1^{o} to 35^{o}. It was observed that XRD patterns obtained in this work (Figure 5.2) match well with undoped Cr-BDC and Cu-BTC samples as well as with those reported in literature earlier [Latroche *et al*., 2007, Liu *et al*., 2012]. The results broadly indicate that the structure of MOF samples is unaltered due to the Li doping procedure. Xiang *et al*. [2011] reported that incorporation of Li into Cu-BTC in low concentration (Li/Cu 0.07 and 0.12) does not change the XRD pattern whereas excessive Li loading (Li/Cu 16 and 73.9) will alter the pattern.

5.3.4. IR Analysis

Infrared spectroscopy was performed on the pure and doped MOF samples using IRAffinity-1 (Shimadzu) spectrometer at room temperature in the wave number range of 400 to 4000 cm^{-1}; samples were pelletized with KBr for analysis. The FTIR spectra of as synthesized Cu-BTC and Cu-BTC/Li (Figure 5.3a) are identical indicating that the structure is preserved after doping. No difference is observed in the broad band around 3500 cm^{-1}. Xiang et al. showed that purification of Cr-BDC MOF leads to elimination of peak at 2926 cm^{-1} consequent to the saturated carboxylate formation [Xiang *et al*., 2012]. Both Cr-BDC and Cr-BDC/Li samples synthesized in this work seem to show very weak peaks at 2926 cm^{-1} (Figure 5.3b). However, pure Cu-BTC shows a sharp peak at 2926 cm^{-1} whereas Cu-BTC/Li has a weak peak at 2926 cm^{-1} might be consequent to saturated carboxylate formation. Both Cu-BTC and Cu-BTC/Li show wide peaks at 1645, 1616 and at 1453 cm^{-1} respectively, whereas the pure and doped Cr-BDC samples show broad peak at 3435 cm^{-1}, wide peak at 1260, 1160, 1090, 926 and 876 cm^{-1}, medium peaks at 1510

and 1020 cm^{-1}, small peaks at 746 and 580 cm^{-1}, very small peak at 1660, 1540 and 1410 cm^{-1}.

5.3.5. Surface Area and Pore Volume

The surface area and pore volume of the doped Cu-BTC and Cr-BDC samples were determined from nitrogen adsorption isotherms at 77 K (Figure 5.4). Prior to the measurements, outgassing of the samples was performed at a temperature of about 500 K.

These nitrogen isotherms indicate that the surface area and pore volume of Cu-BTC/Li and Cr-BDC/Li (Table 5.1) improve significantly compared to that of the parent MOFs. As already indicated in the discussion on TGA analysis, it is possible that the Li doping process additionally removes unreacted organic linkers (trimesic acid in case of Cu-BTC and terephthalic acid in case of Cr-BDC) as well as solvent molecules used during synthesis due to extended contact with methanol. This removal allows for more access to the surface of the MOF thereby increasing its surface area as well as pore volume. In addition, the "measured" mass of the sample also decreases (and approaches its "true" value) when the unwanted impurities are removed. Both the above factors result in effective increase in specific surface area and pore volume of the MOF samples. It is worth mentioning that the amount of lithium doped (and hence its contribution to additional mass of the sample) is negligible and is thus unlikely to have any negative impact on the "specific" surface area. As given in Table 5.1, the increase in surface area as well as pore volume is in excess of 40 % (the increase in pore volume for Cu-BTC to Cu-BTC/Li is slightly lower at about 27 %).

Yang *et al*. [2013] report an extensive methanol wash procedure to improve the surface area and pore volume of Cu-BTC to 2042 m^2g^{-1} and 0.823 $cm^3\ g^{-1}$ respectively.

The values reported for Cu-BTC in this work are even higher and are close to the accessible surface area calculated theoretically according to the procedure suggested by Duren et al., [Duren *et al*., 2007]. It is important to mention here that an additional attempt was made in this work to subject as synthesized Cu-BTC to extensive washing procedure using methanol alone (instead of 1M LiCl in methanol solution as used in Li doping). However, no improvement was seen in the surface area and pore volume of the MOF, thus highlighting the role of LiCl. Similar results were obtained in the case of Cr-BDC also. The best reported surface area and pore volume so far for Cr-BDC were 4230 m^2g^{-1} and 2.15 cm^3g^{-1} using a wash procedure with NH_4F [Llewellyn *et al*., 2008] and thus the results obtained in this work are better than all the earlier reports to the best of our knowledge.

5.4. Hydrogen Adsorption Measurements

5.4.1. Excess Adsorption Isotherm

The excess adsorption isotherms of hydrogen at different temperatures are shown in Figures 5.5 - 5.6. Hydrogen loading on Cu-BTC/Li saturates at 91 K within 20 bar. At room temperature there is no apparent saturation even at 100 bar and the isotherm is linear. The loading improves from 0.6 wt% to 1.76 wt% at 100 bar when temperature changes from 296 K to 188 K (Figure 5.5). Similarly, isotherm of Cr-BDC/Li saturates at 92 K at about 51 bar. The hydrogen loading on Cr-BDC/Li changes from 0.54 wt% to 1.94 wt% at ~100 bar when temperature changes from 298 K to 189 K (Figure 5.6). If the temperature drops further to 138 K then loading improves to about 3 wt% at 100 bar.

Isotherms of Cu-BTC/Li and Cu-BTC are compared in Figure 5.7a - 5.7b The maximum hydrogen uptake is 4.27 wt% (at 25 bar and 91 K) in case of Cu-BTC/Li; it is

~25 % higher than that on Cu-BTC (3.39 wt% at 25 bar and 101 K). This enhancement is attributed to the presence of Li metal as well as higher surface area / pore volume of Cu-BTC/Li. At about 0.01 Li atoms per Cu in the Cu-BTC framework (as mentioned earlier), the additional uptake translates to about 3.4 molecules per added Li. The comparison of isotherms around 1 bar on Cu-BTC and Cu-BTC/Li (although at slightly different temperatures of 101 and 91 K respectively) indicates that additional uptake is about 1.9 hydrogen molecules per added Li. Mulfort *et al*. reported an enhancement of about 2 molecules per added Li (at 77 K and 1 bar) [Mulfort *et al*, 2009]. They indicate that post-synthesis alkoxide formation of Li with the framework to be possible reason for enhanced hydrogen uptake. These results are also in line with earlier computational study by Lochan and Gordon indicating that a Li ion can bind with six hydrogen molecules [Lochan and Gordon, 2006].

On the other hand, at ambient temperature the difference in uptake of Cu-BTC/Li and Cu-BTC is almost negligible. Such a behavior has been reported earlier on light weight metal atom functionalized carbons; the adsorption enhancement was mainly attributed to charge induced dipole interactions. In these cases, it was concluded that such adsorption energies rapidly decrease with temperature and the effect on room temperature adsorption of hydrogen is negligible. Thus, the negligible difference between room temperature uptakes of hydrogen between parent Cu-BTC and Cu-BTC/Li is not surprising.

An earlier work by Snurr and coworkers [Frost *et al*., 2006] demonstrates that hydrogen uptake correlates well with surface area at intermediate loadings and pore volume at higher loadings. However, at low loadings isosteric heat which is a measure of strength of vertical interactions (between the adsorbate and adsorbent surface) determines the uptake capacity [Deng *et al*., 2004, Zhu *et al*., 2004]. Since at ambient temperature, the hydrogen uptake is linear and is in the Henry's law region, a mere increase in surface

area and/or pore volume will not be sufficient to enhance the hydrogen uptake; comparison of enthalpy of adsorption between the doped and parent MOF will be necessary and is presented later.

Isotherms of doped MOF Cr-BDC/Li and parent Cr-BDC are compared in Figures 5.8a - 5.8c. The maximum hydrogen uptake is 6.02 wt% (at ~ 74 bar and 92 K) in case of Cu-BTC/Li which is ~58 % higher than that on parent Cr-BDC (3.82 wt% at ~91 bar and 92 K). Furthermore, these excess hydrogen adsorption values are comparable to MOF-205 which has similar surface area and pore volume (Figure 4.13). This enhancement is attributed to the presence of Li metal as well as higher surface area / pore volume of Cr-BDC/Li. At about 0.07 Li atoms per Cr in the Cr-BDC framework (as mentioned earlier), the additional uptake translates to about 1.44 molecules per added Li. While this increase (on per Li added basis) is lower than that observed in case of Cu-BTC/Li it is well within the ranges of other theoretical and experimental reports [Lochan and Gordon, 2006, Mulfort *et al*, 2009]. As in case of Cu-BTC, a reasonable increase in hydrogen uptake after doping is obtained at intermediate loadings (at about 95 bar and 136 the increase in hydrogen is about 25 %) and negligible change is seen at ambient temperature.

For sake of comparison the best known reports for hydrogen uptake based on these parent MOFs are also included in Figures 5.7 and 5.8. As mentioned earlier, room temperature uptake on doped Cu-BTC (or Cr-BDC) is not different from undoped samples in this work or from reports in literature. However, at low temperatures, the hydrogen uptake obtained in this work for a material based on Cu-BTC MOF is best known till date. On the other hand, the values for the maximum uptake on Cr-BDC are comparable to those reported by Latroche *et al*. [2006] who adopt an improved washing procedure using NH_4F to obtain enhanced surface area and pore volume. Even in this case it is worth noting that the Li doped sample exhibits comparable loadings to that of

Latroche *et al*. even though the H_2 isotherm temperature in this work is significantly higher (92 K for in this work against 77 K Latroche *et al*). Our experimental limitations currently do not allow us to perform measurements at 77 K.

A good correlation can be readily seen between the pore volumes and saturation uptake capacity on various Cu-BTC (Figure 5.9a) and Cr-BDC (Figure 5.9b) sample reported in literature including those synthesized in this work. Hydrogen uptake on Li doped MOFs also shown in the same figure which emphasizes that enhancement in hydrogen uptake is proportional to the pore volume.

The variation in Henry's constant with temperature is shown in Figure 5.10. As in case of pure MOFs these values were calculated from the intercept of isotherm in the virial domain. As temperature drops from 298 K to 92 K, the difference between Henry's constants of all the MOFs gradually increases. Henry's constant at cryogenic temperature as well as at room temperature is given in Table 5.2. For, ease in comparison the values are adjusted to those at 100 K and at 298 K from the trend lines in Figure 5.10. All the values indicate that the results are within experimental uncertainties and there is very marginal difference between the Henry constants of Li doped Cu-BTC and Cr-BDC compared to the parent MOFs.

The enthalpies of adsorption at zero coverage (Table 5.2 and Figure 5.12) were obtained from the change in Henry's constants with temperature. Li doping slightly enhances the isosteric heat values (0.3 to 0.7 kJ mol^{-1}) and the value for enthalpy of adsorption are close to those on other Li doped MOFs reported in literature [Nouar *et al*., 2009, Mulfort *et al*., 2009 a; Dinca *et al*. 2007]. Similar enhancement of adsorption enthalpy due to Li doping is reported in some of the earlier works also. For example, Himsl *et al*. reported enhanced enthalpy of adsorption for Li doped MIL-53 (Al)

framework and explained that initial adsorption takes place at high hydrogen affinity regions *i.e.* near to Li cations followed by less favorable sites [Himsl *et al*., 2009]. Yang *et al*. showed Li doping improves the enthalpy of adsorption of NOTT-200 though it increased the pore volume after doping (see Chapter 2) [Yang *et al*., 2009]. Although increase in enthalpy should manifest in enhanced hydrogen uptake at low loadings as discussed by Snurr and coworkers [Frost *et al*. 2006], such increase probably is small enough that its influence on the hydrogen adsorption at ambient temperature (which is very low to begin with) could not be captured with our experimental measurements. On the other hand, the Henry's constants at the experimental temperatures are almost similar, indicating that the strength of interaction with the "active" sites at low coverage is not significantly different (Figure 5.10).

5.4.2. Net Adsorption

As explained in the previous chapter net adsorption framework is more suitable for comparison of adsorbents used in gas storage applications. Net adsorption isotherms for Cu-BTC/Li and Cr-BDC/Li are given in Figures 5.13 - 5.14. At room temperature, net adsorption for both Cu-BTC/Li and Cr-BDC/Li is close to zero, indicating no significant benefit in using these adsorbents for hydrogen storage; the density enhancement due to adsorption is approximately negated by loss in tank volume due to impenetrable solid.

The net adsorption isotherms can also be used to calculate the volume of hydrogen storage vessel as indicated earlier. As an illustration, the volume of the vessel necessary to store 1 kg hydrogen at 100 bar is shown in Figure 5.15. The volume of the storage vessel significantly decreases when Cr-BDC/Li is used at 92 K (~10% lesser volume required than using pure Cr-BDC). On the other hand, as mentioned in the previous chapter using pure Cr-BDC at room temperature actually resulted in a larger storage vessel volume compared to one with no adsorbent; however, with Cr-BDC/Li as an

adsorbent about 10 % lesser volume is required (122 liters for compressed gas tank and 111 liters for adsorptive storage vessel).

5.5. Summary

The parent Cu-BTC and Cr-BDC MOFs were soaked in 1 M LiCl/methanol solutions for about 10 days with frequent replacement of the solution. The analysis of the samples show Li/Cu ratio of 0.01 and Li/Cr ratio of about 0.07 in Cu-BTC/LI and Cr-BDC/Li samples. The resultant "doped" MOFs also exhibit significant improvement in surface area and pore volume, better than all known reports in literature. As a result, significant enhancement in saturation gravimetric loading is observed at low temperatures (about 3.4 and 1.44 additional hydrogen molecules per Li added for Cu-BTC and Cr-BDC respectively). The hydrogen uptake obtained in this work for material based on Cu-BTC MOF are best known till date; on the other hand the values for the maximum uptake on Cr-BDC are comparable to those reported by Latroche *et al*. [2006] who adopt an improved washing procedure using NH_4F to obtain enhanced surface area and pore volume. The hydrogen uptake on Cr-BDC/Li matches with uptake measured on MOF-205 (Chapter 4) which contains a large organic ligand (and thereby possess greater pore volume).

However, as in case of earlier reports in literature on other MOFs, at ambient temperature negligible increase in hydrogen uptake is observed due to Li doping. This is to be expected since adsorption energies for interaction of hydrogen with light weight metals are known to rapidly fall down with temperature. The enthalpy of adsorption also increases marginally due to Li doping. In general, the increase in hydrogen uptake and enthalpy match with the trends reported for the effect of Li doping on MOFs in previous

theoretical and experimental works reported in the literature. While Li doping seems to be an effective method to enhance the saturation uptake of MOFs, its effect at ambient conditions is negligible.

Encouraged by the results on these well studied MOFs attempts were made to dope Li using a similar procedure on other MOFs synthesized in this work. However, the structures of weakly stable MOFs such as Mg-DOBDC, MOF-205, and Zn-BDC quickly collapsed when samples were soaked in LiCl/methanol solution. On the other hand, the soaking process did not result in any enhancement of surface area, pore volume or hydrogen uptake capacity of MOFs such as Ni/DABCO and Co-DOBDC.

Figures

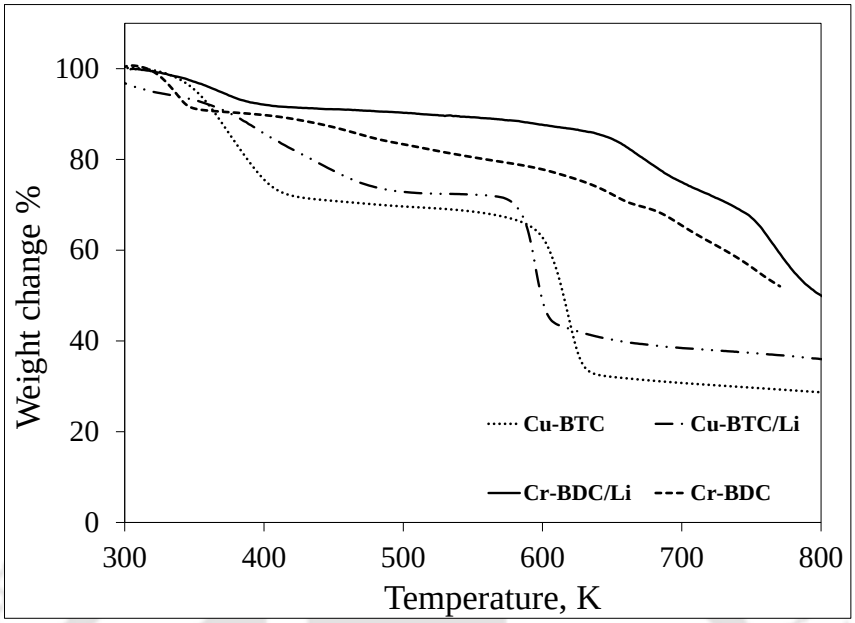

Figure 5.1: Thermograms of Cu-BTC/Li and Cr-BDC/Li compared to Parent MOFs (at a Heating rate of 5 K min^{-1} under a flow of 40 cm^3 min^{-1} of N_2).

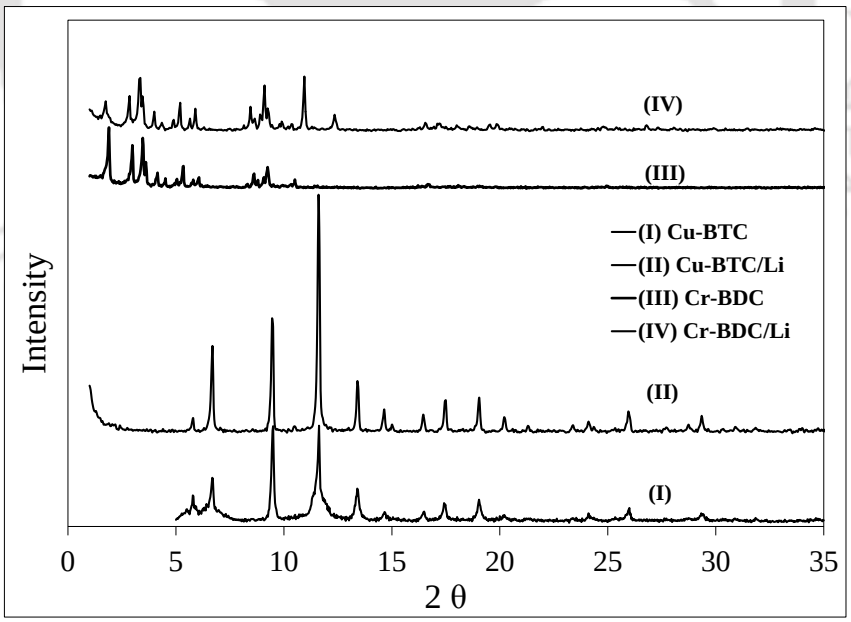

Figure 5.2: X-ray Diffractogram of Cu-BTC/Li and Cr-BDC/Li compared to Parent MOFs.

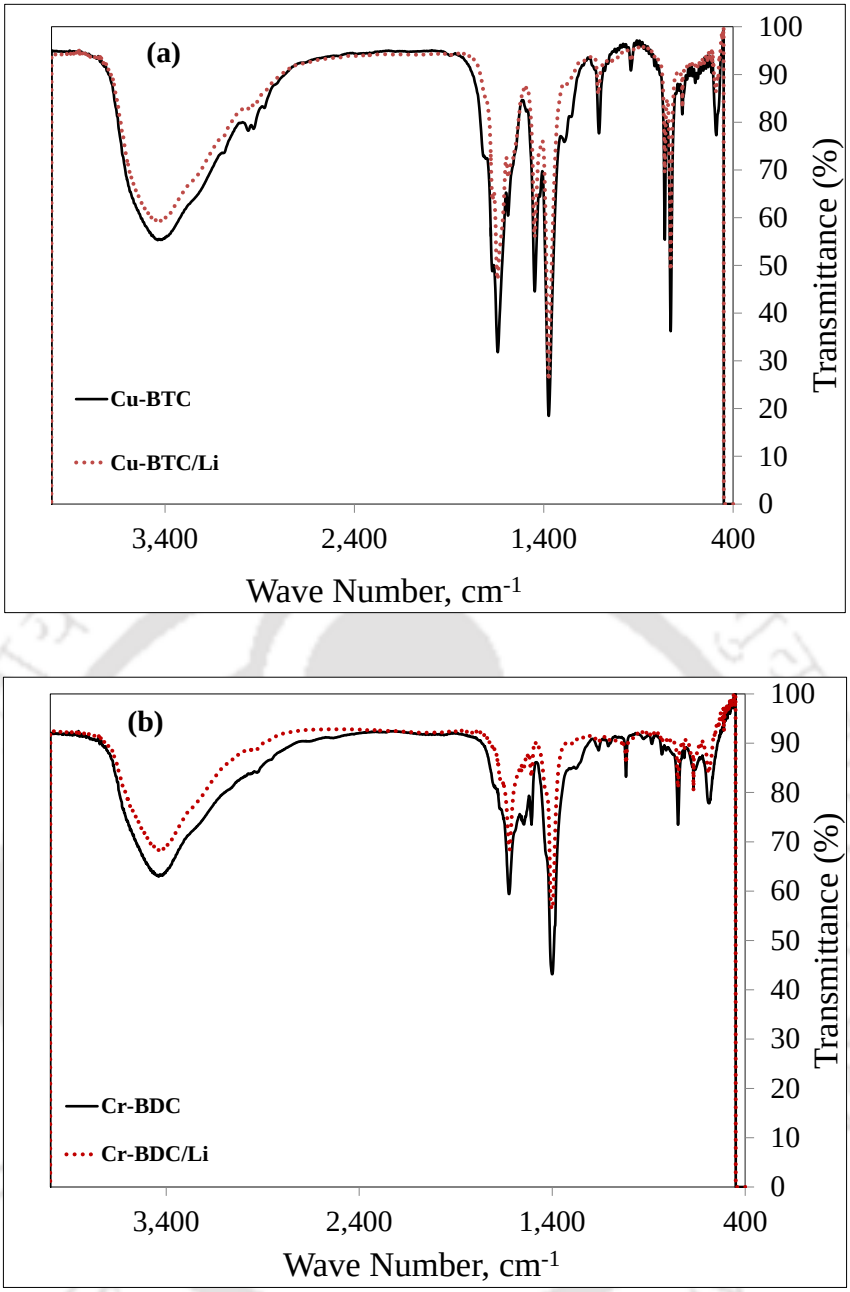

Figure 5.3: IR Patterns of (a) Cu-BTC and (b) Cr-BDC MOFs.

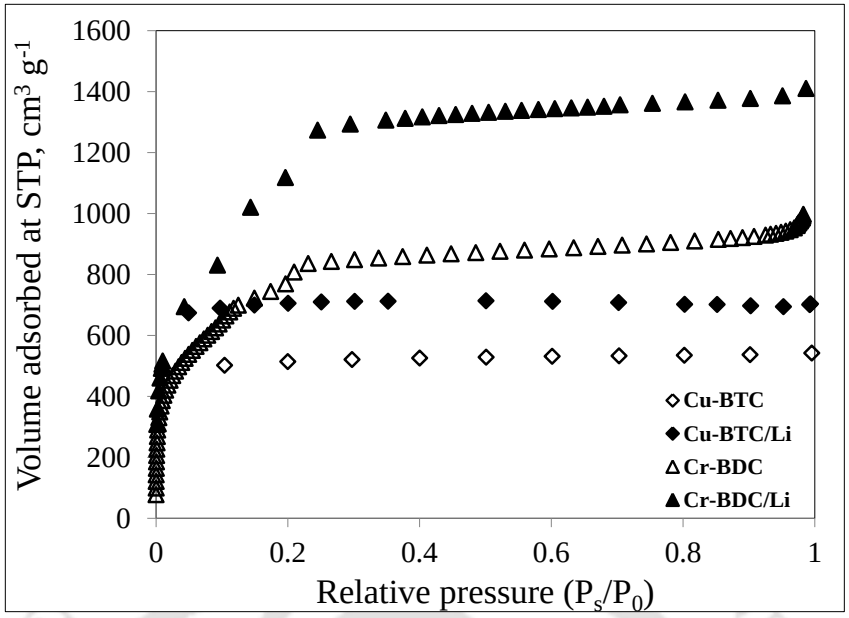

Figure 5.4: N_2 Adsorption Isotherms at 77 K on Cu-BTC/Li and Cr-BDC/Li Samples compared to Parent MOFs.

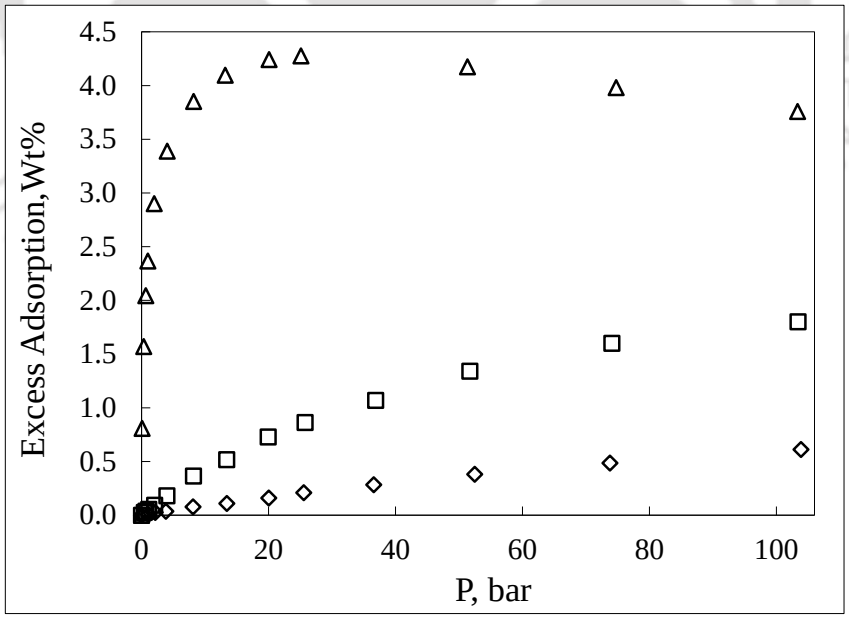

Figure 5.5: H_2 Adsorption Isotherms of Cu-BTC/Li. Symbols represent: triangle, 91 K; square, 188 K; diamond, 296 K.

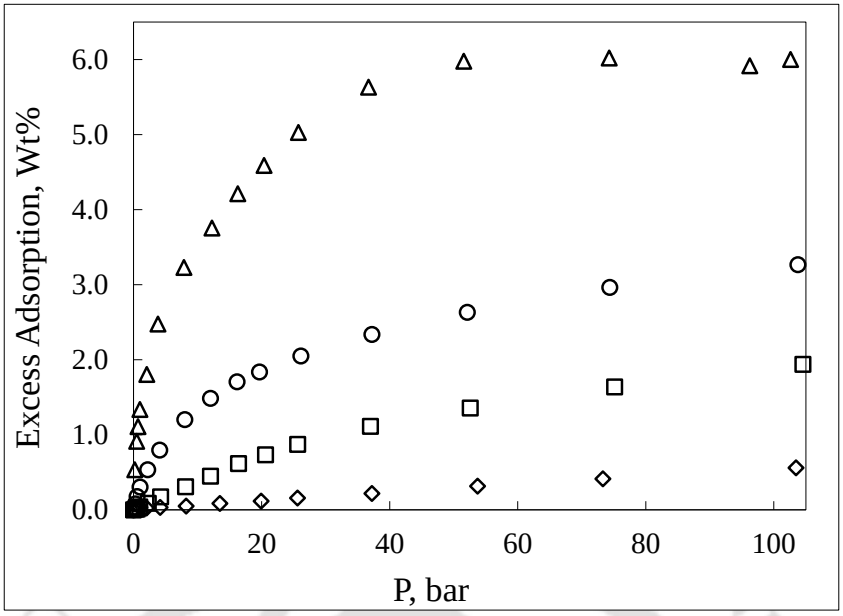

Figure 5.6: H_2 Adsorption Isotherms of Cr-BDC/Li. Symbols represent: triangle, 92 K; circle, 138 K; square, 189 K; diamond, 298 K.

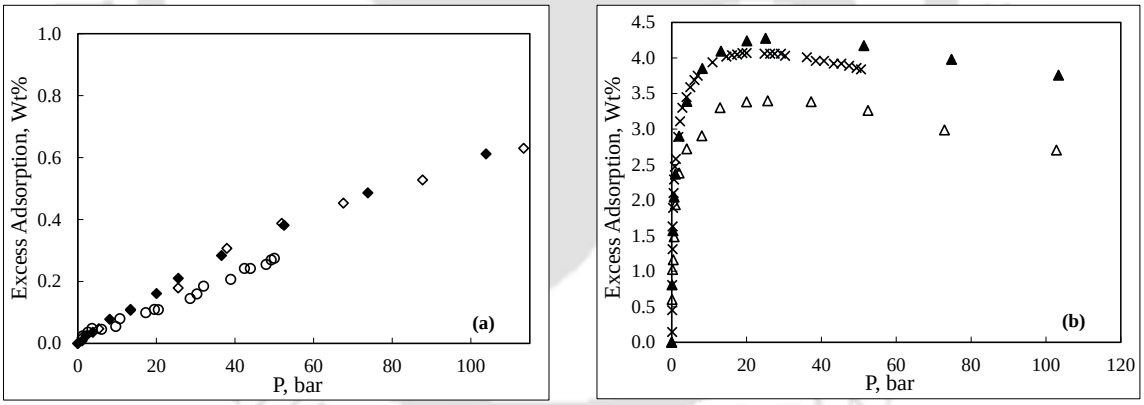

Figure 5.7: Comparative Excess Adsorption Isotherms of (a) Cu-BTC at 297 K (diamond), 298 K (circle) reported value from Liu *et al*. [2007], Cu-BTC/Li at 296 K (filled diamond); (b) Cu-BTC at 101 K (triangle), 77 K (cross) reported value from Liu *et al*. [2007], Cu-BTC/Li at 91 K (filled triangle).

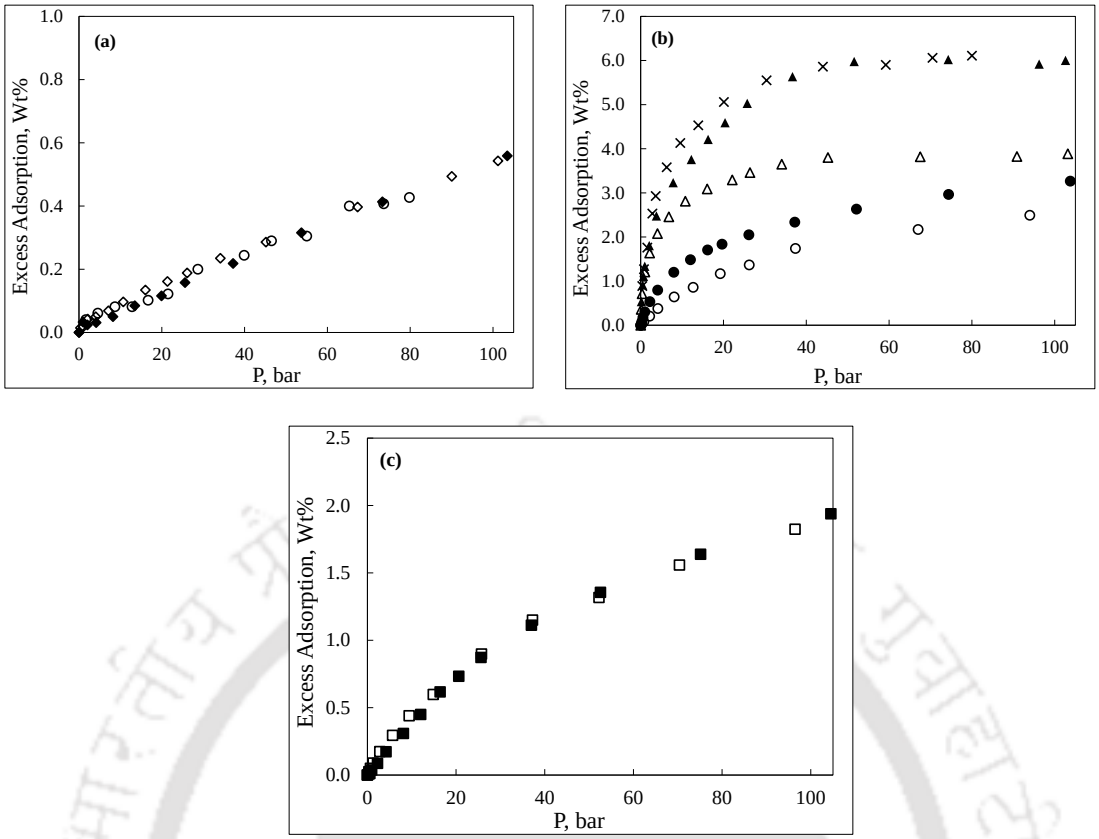

Figure 5.8: Comparative Excess Adsorption Isotherms: (a): Cr-BDC at 297 K (diamond), Cr-BDC at 298 K (circle) reported value from Latroche *et al*., [2006], Cr-BDC/Li at 298 K (filled diamond); (b): Cr-BDC at 92 K (triangle), Cr-BDC at 77 K (cross) reported value from Latroche *et al*., [2006], Cr-BDC at 136 K (circle); Cr-BDC/Li at 92 K (filled triangle), 138 K (filled circle); (c): Cr-BDC at 165 K (square), Cr-BDC/Li at 189 K (filled square).

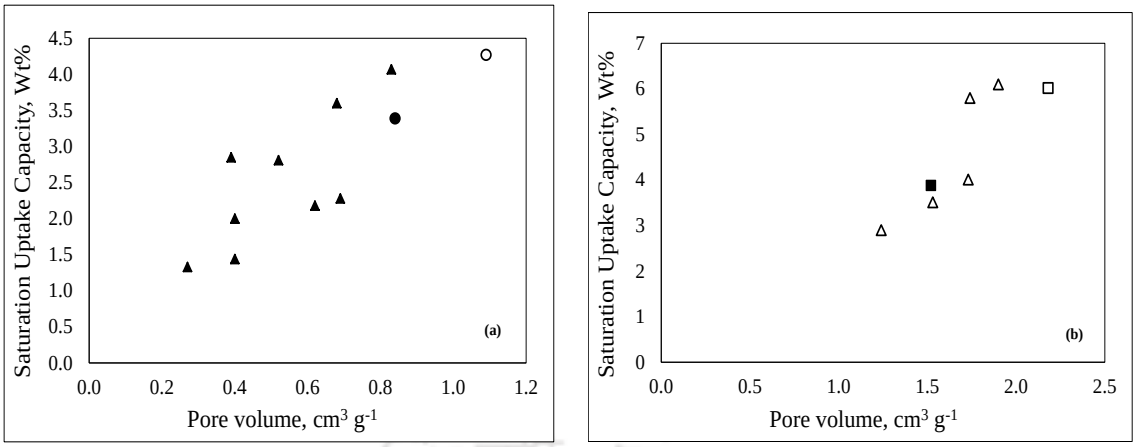

Figure 5.9: Variation of Saturation loading with Pore volume: (a): Cu-BTC-This work (filled circle); Cu-BTC (filled triangle) are from Lee *et al*., [2005], Liu *et al*., [2007], Xiao *et al*., [2007], Yang *et al*., [2008], Krawiec *et al*., [2006], Prestipino *et al*., [2006], Peterson *et al*., [2007], Liu *et al*., [2013]; Cu-BTC/Li-This work (circle). (b): Cr-BDC-This work (filled square); Cr-BDC (triangle) are from Latroche *et al*., [2006], Ardelean *et al*., 2006, Liu *et al*., [2007], Yang *et al*., [2010], ; Cr-BDC/Li-This work (square).

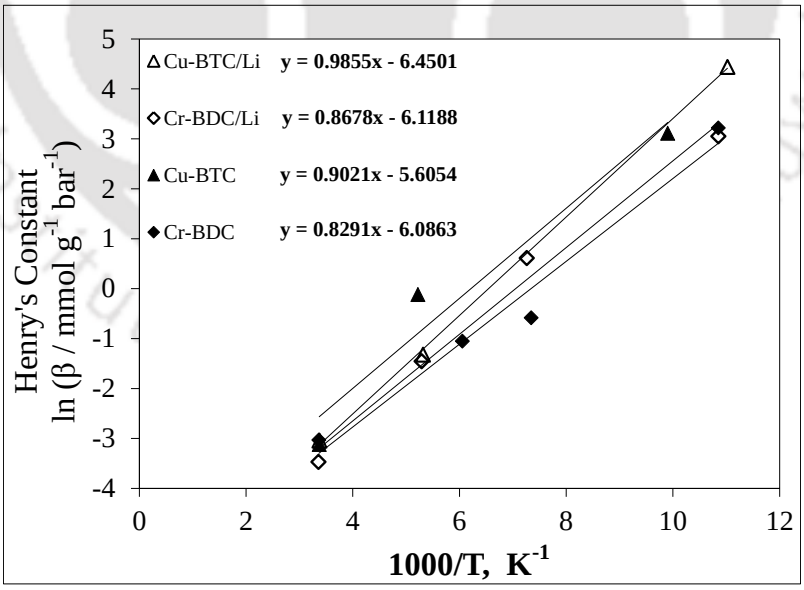

Figure 5.10: Henry's constants for Cu-BTC/Li and Cr-BDC/Li Compared to Parent MOFs. Filled triangle, Cu-BTC ; triangle, Cu-BTC/Li; filled diamond, Cr-BDC and diamond, Cr-BDC/Li.

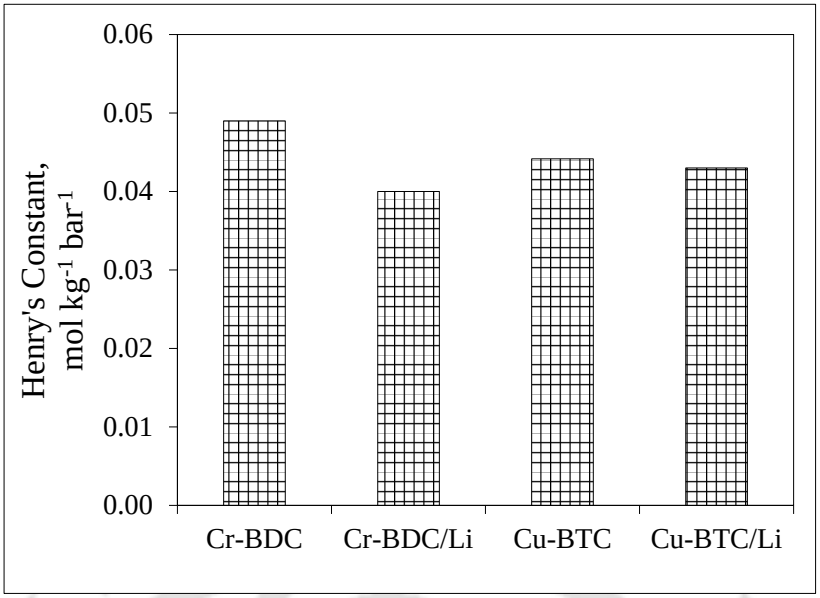

Figure 5.11: Henry's constant at Room Temperature for Cu-BTC/Li and Cr-BDC/Li compared to Parent MOFs

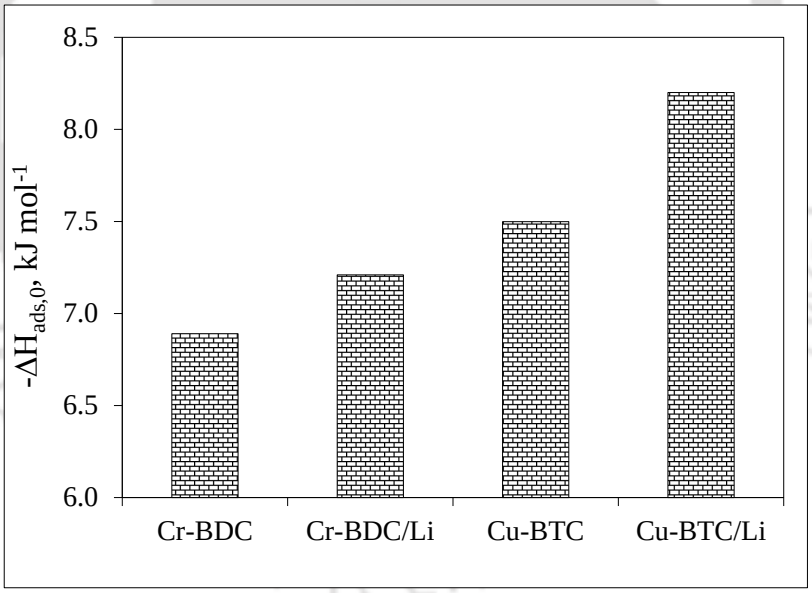

Figure 5.12: Enthalpy of Adsorption at Zero Coverage for Cu-BTC/Li and Cr-BDC/Li compared to Parent MOFs

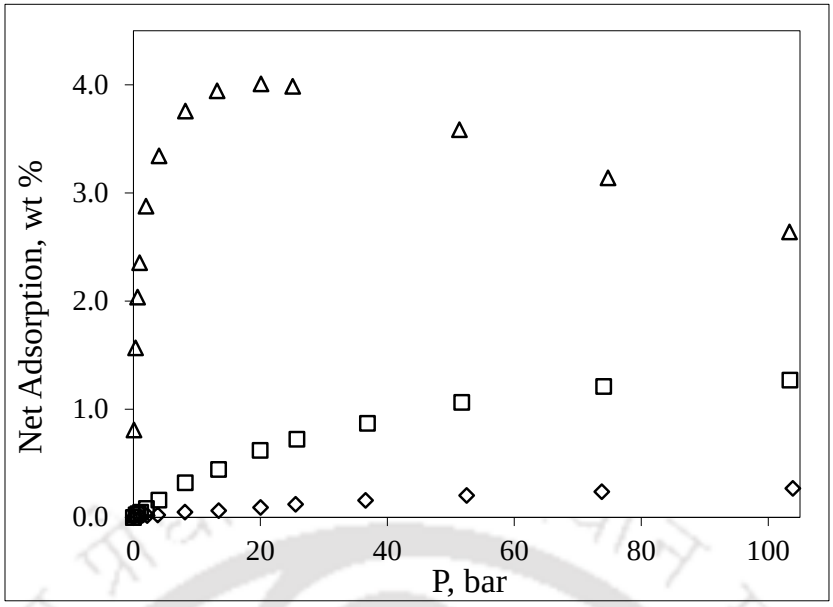

Figure 5.13: Net Adsorption Isotherms of Cu-BTC/Li at triangle, 91 K; square, 188 K and diamond, 296 K.

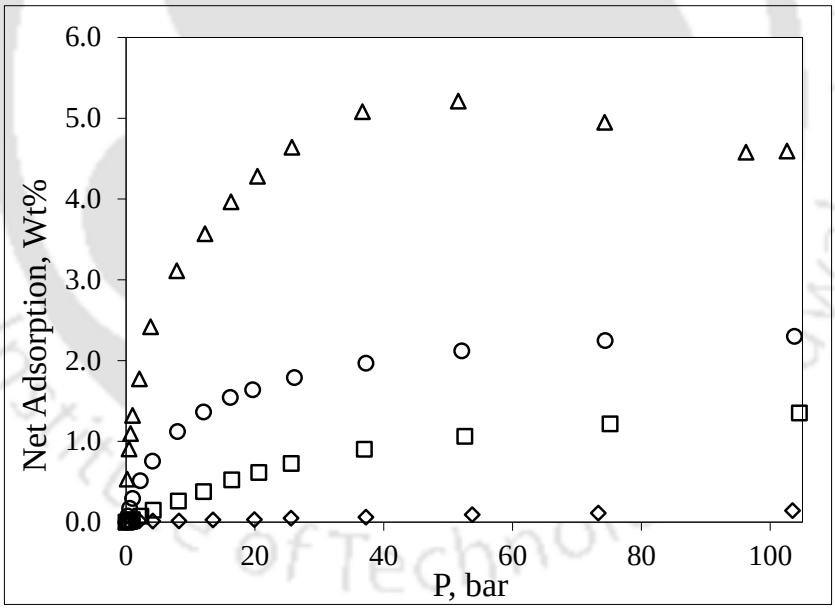

Figure 5.14: Net Adsorption Isotherms of Cr-BDC/Li: triangle, 92 K; circle, 138 K; square, 189 K; and diamond, 298 K.

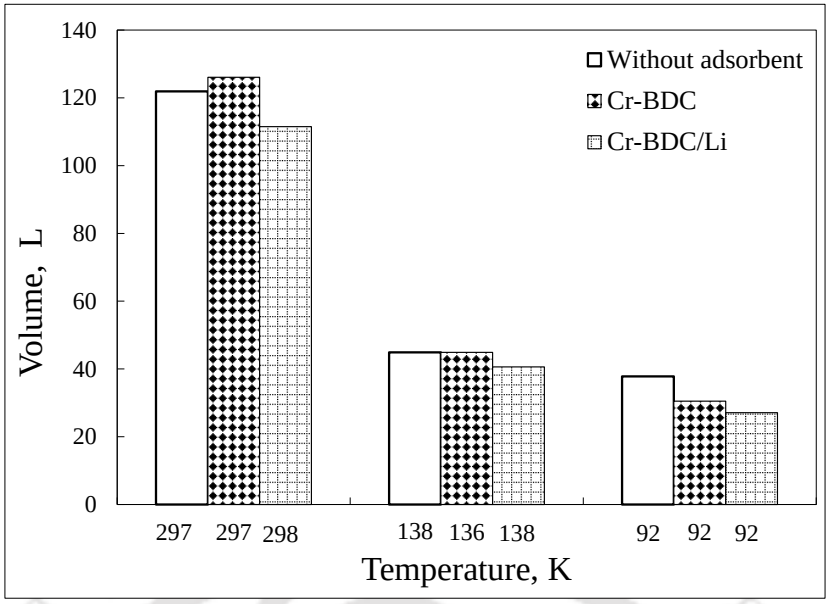

Figure 5.15: Volume of Vessel Required to Store 1 kg of H_2 at 100 bar using Cr-BDC/Li and Cr-BDC

Tables

Table 5.1: Surface area and Pore volume of various Cu-BTC and Cr-BDC MOFs.

Compound	**BET surface area** (m^2g^{-1})	**Pore volume** (cm^3g^{-1})	**References**
Cu-BTC	1482	0.83	[Liu *et al*., 2006]
	2042	0.82	[Yang *et al*., 2013]
	1494	0.84	This work
	2153*	-	[Duren *et al*., 2007]
Cu-BTC/Li	795	0.51	[Xiang *et al*., 2012]
Cu-BTC/Li	2132	1.09	This work
Cr-BDC	4100	2	[Ferey *et al*., 2005]
	5500#	1.9	[Latroche *et al*., 2006]
	3223	1.57	[Khan *et al*., 2011]
	2927	1.52	This work
Cr-BDC/Li	4310	2.18	This work
Cr-BDC/Li	1840	1.38	[Xiang *et al*., 2012]

*Accessible Surface area calculated reported by Duren *et al*. [2007], #Langmuir Surface Area

Table 5.2: H_2 Uptake at Saturation, Henry's constant and Enthalpy of Adsorption for Cu-BTC/Li and Cr-BDC/Li compared to Parent MOFs.

Adsobent	**Saturation H_2 uptake**		**Henry's constant at 100 K**	**Henry's constant at 298 K**	**Adsorption enthalpy at zero coverage**
	W_{max}, Wt%	T, K	mol kg^{-1} bar^{-1}	mol kg^{-1} bar^{-1}	kJ mol^{-1}
Cu-BTC	3.39	101	30.4	0.044	7.5
Cu-BTC/Li	4.27	91	30.1	0.043	8.2
Cr-BDC	3.88	92	9.1	0.049	6.9
Cr-BDC/Li	6.02	92	12.9	0.040	7.2

CHAPTER 6

Effect of Heavy Metal Doping on Hydrogen Adsorption in Selected Metal Organic Frameworks

6.1. Background

Functionalization of MOFs has been demonstrated to be an effective approach to enhance the performance of MOFs for targeted applications [Suh *et al*., 2012]., Different approaches to improve the hydrogen uptake in MOFs such as catenation, linker modification and inclusion of metal sites, have been discussed in the literature survey (Chapter 2). One of the approaches for pore-size and hydrogen volumetric density optimization is the partial pore filling of MOFs by another adsorbent [Rowsell *et al*., 2006]. This can be achieved by impregnation with a non-volatile guest material [Yang *et al*., 2009]. In addition to the reduction of the pore diameter, such guest molecules may provide extra adsorptive sites for hydrogen; since metal like Pt/Pd are known to have preference for hydrogen attempts were made to incorporate these materials into the pores of various MOFs. In addition, successful synthesis procedures are reported in the literature describing the formation of MOF composites with Pt/Pd supported on another substrate. The substrate varies depending on the MOF selected and the application targeted [Petit and Bandosz, 2009, Petit *et al*., 2010]. Most commonly used materials are polymers, [O'Neil *et al*., 2010, Rowe *et al*., 2009] alumina, [Arnold *et al*., 2007] carbon nanotubes, [Yang et al., 2009] functionalized graphite, [Jahan *et al*., 2010] or graphene oxide (GO). [Petit *et al*., 2010] The substrate is used to enhance the adsorbate-adsorbent interaction at appropriate condition.

Structure of Cu-BTC as reported by Yaghi and coworkers; possesses cubic shape unit cell [Li *et al*., 1999]. Coordination sites to the metal are comprised within parallel planes (if we consider parallel faces of the cubic cell) or perpendicular planes (if we consider perpendicular faces of the cubic cell). This type of structure may favor the attachment of the graphene layers to the MOF units and the subsequent growth of the crystal [Petit and Bandosz, 2010]. The synthesis and characterizations of hybrid composites of several MOF and graphene oxide composites are documented in the literature [Kumar *et al*., 2013, Petit and Bandosz, 2011]. In case of Cr-BDC, the geometry of the MOF unit differs greatly since the pores are within the cages (spheres) rather than in cubes as for Cu-BTC. As a result, the coordination sites of the metals are located in various planes that are not necessarily parallel or perpendicular to each other. Consequently, a disordered structure can be anticipated from the formation of Cr-BDC and GO composites [Zhou *et al*., 2013]. Literature reports have shown that Pd immobilized on MOFs (e.g., Cr-BDC) could be employed as highly efficient heterogeneous catalysts for a variety of transformations, such as carbon–carbon coupling, oxidization, and hydrogenation of aromatic compounds [Hermes *et al*., 2005].

In addition to the reports cited as above, Cu-BTC and Cr-BDC are among the MOFs that have been widely studied in literature and due to well established synthesis procedures the results amongst different batches are reproducible. Moreover, in the previous chapter of this work a methodology has been outlined to enhance the hydrogen storage capacity of Cu-BTC and Cr-BDC MOFs. In this chapter, attempts made to incorporate transition (heavy) metals such as Pd or Pt into these two MOFs will be discussed and the results would be compared to those of Li-doped samples.

In order to investigate the effect of Pt/Pd doping on MOF, composites can be prepared with a support such as activated carbon or graphene oxide; formation of composites is rather easier way to incorporate heavy metal without altering its porous nature. In this work, a variety of substrates such as activated carbon (AC), grapheme oxide (GO), Pt doped activated carbon (Pt-AC) and palladium doped improved grapheme oxide (Pd-IGO) were used in synthesis of Cu-BTC and Cr-BDC to obtain MOF composites. More details on various composites synthesized are given in Table 6.1. A systematic study on hydrogen adsorption characteristics of these composites should shed some light on development of hydrogen storage materials.

6.2. Material Synthesis

6.2.1. Graphene Oxide

Graphene oxide was prepared from the natural graphite powder (Loba Chemie, 99.9% purity) according to a modified Hummers method [Hummers, 1958]. In a typical synthesis, graphite (2.0 g) was added to cold (273 K) concentrated H_2SO_4 (80 cm^3) in an ice bath. $NaNO_3$ (4.0 g) and $KMnO_4$ (8.0 g) were then added to this mixture gradually, under stirring and the temperature of the mixture was kept below 283 K. The reaction mixture was stirred within a cold bath (below 283 K) for another 4 h. The mixture was stirred at 308 K for 4 h, and then diluted with deionized (DI) water (200 cm^3) in an ice bath to keep the temperature below 373 K. After adding water, the mixture was stirred for 1 h. The contents were then quenched by adding 30% H_2O_2 solution (15 cm^3). The solid product was separated by centrifugation, washed repeatedly with 5% HCl solution until sulfate could not be detected with $BaCl_2$. For further purification, the resulting solid was dispersed in DI water and then was dialyzed for 3 days to remove residual salts and

acids. The suspension was dried in a vacuum oven at 333 K for 24 h to obtain graphene oxide (GO).

6.2.2. Improved Graphene Oxide

Hummers' method was used with slight improvements for the synthesis of graphene oxide [Marcano *et al*., 2010]. A 9:1 mixture of concentrated H_2SO_4/H_3PO_4 (360:40 cm^3) was added to a mixture of graphite flakes (3.0 g, 1 wt. equiv) and $KMnO_4$ (18.0 g). The reaction mixture was then heated to 323 K and stirred for 12 h. The contents were cooled to room temperature and poured onto ice (400 cm^3) with 30% H_2O_2 (3 cm^3). Then the colloid is filtered through a polyester cloth. The filtrate was centrifuged (4000 rpm for 1 h), and the supernatant was decanted away. The remaining solid material was then washed in succession with 200 cm^3 of water, 200 cm^3 of 30% HCl, and 200 cm^3 of ethanol; for each wash, the mixture was sifted through polyester fiber with the filtrate being centrifuged (4000 rpm for 1 h) and the supernatant decanted away. The solid obtained on the filter was vacuum-dried overnight at room temperature. The product so obtained is named as IGO.

6.2.3. Palladium Supported Graphene Oxide and Palladium Supported Improved Graphene Oxide

Pd particles were introduced onto the GO (or IGO) surface using a polyol process (glycol reduction method) [Xu *et al*., 2008]. The details of Pd nanoparticles synthesis was similar to the method presented in Section 3.10.2. To obtain Pd nanoparticles on graphene oxide, as-synthesized GO (50 mg) was dispersed in DI water (50 cm^3) by sonication for 30 mins to form stable GO colloid. Ethylene glycol (100 cm^3) and DI water solution (2.5 cm^3) of H_2PdCl_4 (0.01

M) were added to the solution under magnetic stirring for 30 mins. Then the mixture was put in an oil bath and heated at 373 K for 6 h with magnetic stirring. The products were separated from the ethylene glycol solution in the centrifuge, washed with DI water three times, and dried in a vacuum oven at 333 K for 12 h. The Pd-loaded GO sample was named as Pd-GO. Palladium supported Improved Graphene Oxide (Pd-IGO) is obtained by replacing GO with IGO in the above method.

The size of Pd nanoparticle synthesized by a polylol process depends on the duration of reaction as well as temperature (Chapter 3). Here the duration is 6 h and temperature is 373 K was chosen to obtain Pd nanoparticles of approximately 10 nm.

6.2.4. Composites of Cu-BTC

The composites were prepared in the same procedure as that of pure Cu-BTC (Section 4.3.5), except for the addition of an appropriate substrate i.e. AC, Pt-AC, IGO, Pd-GO or Pd-IGO. The IGO, Pd-GO and Pd-IGO were synthesized in our laboratory as outlined in the previous sections (6.2.1 – 6.2.3). AC was obtained from M/s Merck Chemicals. Pt-AC (5 wt% Pt loaded activated carbon) was obtained directly from M/s Sigma Aldrich.

In the labeling of composite Cu-BTC/XPd-IGO, X indicates the mass % of the Pd-IGO used during synthesis based on the yield of final product. For example, Cu-BTC/3.3Pd-IGO indicates that it is a composite of Cu-BTC and Pd loaded improved graphene oxide, Pd-IGO and that the mass fraction of Pd-IGO used in synthesis is about 0.033 of the final yield. The synthesis was done by adding appropriate amount of Pd-IGO to the original reactant solution for Cu-BTC (Section 4.3.5). The amount of Pd-IGO is calculated by estimating the yield of Cu-BTC that

would be obtained for the quantity of reactants used (from prior experience during synthesis of pure BTC, 1g of BTC and 2.077 g of $Cu(NO_3)_2.3H_2O$ when reacted, yield ~1.68 g of Cu-BTC). For example, Cu-BTC/3.3Pd-IGO is prepared as follows.

1,3,5-benzene tricarboxylic acid (H_3BTC) (1.0 g) is dissolved in 30 cm^3 of a 1:1 mixture of ethanol/N,N-dimethyl formamide (DMF) then added to a 15 cm^3 aqueous solution of $Cu(NO_3)_2.3H_2O$ (2.077 g) in a 60 cm^3 capped polypropylene bottle. 46.2 mg of Pd-IGO is then added to this mixture. The mixture is sonicated for 10 min and then heated in an oven at 373 K for 8 h. The resulting blue precipitate is isolated by filtration and washed with methanol. To remove the solvated DMF, blue solid is placed in a Soxhlet extractor and extracted with methanol overnight. The yield of the final product is ~1.24 g (and contains ~ 46.2 mg Pd-IGO i.e. ~ 3.7 wt %).

The labeling convention and synthesis procedures for other Cu-BTC composites AC, Pt-AC, IGO and Pd-GO are similar; only the amount of AC, Pt-AC, IGO or, Pd-GO is changed to achieve different mass fractions in the composites (see Table 6.1).

6.2.5. Cr-BDC Composites

The composites were prepared in the same procedure as that of pure Cr-BDC (Section 4.3.6), except, for the addition of IGO, Pd-IGO or Pt-AC. The IGO and Pd-IGO were synthesized in our laboratory as outlined in the previous section 6.2.2-6.2.3. Pt-AC (5 wt % Pt loaded activated carbon) was obtained directly from M/s Sigma Aldrich.

In the labeling of composite Cr-BDC/XPd-IGO, X indicates the mass % of the Pd-IGO used during synthesis based on the yield of final product. For example, Cr-BDC/4.6Pd-IGO indicates

that it is a composite of Cr-BDC and Pd loaded improved graphene oxide, Pd-IGO and that the mass fraction of Pd-IGO used in synthesis to the final yield in the composite is about 0.046. The synthesis was done by adding appropriate amount of Pd-IGO to the original reactant solution for Cr-BDC (Section 4.3.6). For example, Cr-BDC/4.6Pd-IGO is prepared as follows.

4 g of chromium nitrate nonahydrate ($Cr(NO_3)_3 \cdot 9H_2O$, Loba Chemie) is dissolved in 48 cm^3 deionized water followed by addition of 1.64 g H_2BDC. To this mixture 25 mg of Pd-IGO is added. After stirring this solution for some time 0.5 cm^3 hydrofluoric acid is added drop wise while stirring continued for another 15 minutes. The complete solution is transferred to teflon-lined stainless steel reactors (autoclave) and sealed. The reactors are placed inside a hot air oven at 493 K and held for 8 h. A fine green colored powder is obtained; excess H_2BDC are still present in the form of needle-shaped crystals. To remove this H_2BDC, DMF is added incrementally with continuous stirring. Filtered product is dried at 423 K overnight. To remove H_2BDC further, an additional ethanol rinse is performed. About 200 mg of the dried product is mixed with 15 cm^3 ethanol in a 60 cm^3 vial and kept at 373 K for 20 h. After cooling, the resulting product is filtered and washed with ethanol. The product is finally dried at 423 K overnight. The yield of final product is about 0.54 g (thus Pd-IGO used corresponds to 4.6 % of this yield).

The labeling convention and synthesis procedures for other Cr-BDC composites Cr-BDC/XIGO and Cr-BDC/XPt-AC are similar; only the amount of IGO or Pt-AC is changed to achieve different mass fractions in the composites (see Table 6.1).

6.2.6. MOF-205/Pt-AC Composite

For the synthesis of MOF-205/2.3Pt-AC, 868 mg H_3BTB (synthesized according to procedure outlined in section 4.2.4.1), 698 mg NDC (Napthalene 2,6-dicarboxylic acid, Alfa Aesar) and 2.85 g $Zn(NO_3)_2.6H_2O$ (Merck) along with 18.5 mg Pt-AC (5 wt % Pt on activated carbon, Sigma Aldrich) are added to a solution containing 200 cm^3 DMF and 20 cm^3 ethanol. The solution is kept in hot air oven in a 250 cm^3 PP bottle for 24 h at 371 K. Obtained brown crystals are washed with DMF thrice and then left for 4-5 days in chlorobenzene. Thereafter, the material was boiled in chlorobenzene for three days. Filter and dry in vacuum at RT result into 0.81 g grey white crystals of Zn-BTB. The product is labeled as MOF-205/2.3Pt-AC.

6.2.7. Doping of Li into the MOF Composites

The MOF composites (Cu-BTC/XPt-AC, Cu-BTC/XPd-GO, Cu-BTC/XPd-IGO, Cr-BDC/XPd-IGO, Cr-BDC/XPt-AC) synthesized by the methods described in the previous sections were further subjected to Li doping process. Li doping was achieved as in case of the pure MOF analogues (section 5.2) by soaking approximately 1 g MOF in 35 cm^3 1 M LiCl (Anhydrous, Spectrochem) solution in methanol (HPLC grade, Spectrochem) for 7 days, (replacing the salt solution every 8 h). These samples are then washed with pure methanol for another 3 days (replacing methanol every 8 h) to remove weakly attached lithium. We call these samples with a prefix "/Li" (for example Cu-BTC/XPt-AC/Li) to indicate that the samples were subjected to Lithium doping. Details of all the samples subjected to Li doping are given in Tables 6.2 and 6.3.

6.3. Material Characterization

6.3.1. TEM Imaging

TEM is carried out on well dispersed improved grapheme oxide, IGO sample to analyze the morphology. The wrinkled graphene oxide layers are shown in Figure 6.1 is similar to that of GO layers reported elsewhere in literature [Petit and Bandosz, 2010].

Figures 6.2.a and 6.2.b are taken on the same spots at different magnifications for graphene oxide sample impregnated with palladium. The images clearly show nanoparticles (~ 10-20 nm in size) deposited on the graphene oxide. Usually, the epoxy groups on the GO layers act as seed sites for Pd NP crystallization [Gao *et al*., 2014].

The morphology of MOF composites and their images will be interesting, but studying the morphology of a GO-MOF composite by dispersing it in a solvent is extremely difficult [Zhou *et al*., 2014] because both MOF ligand and graphene oxide has complex carbon-oxygen linking. It is also reported in the literature that few minutes of high energy beam (TEM) may damage the MOF linker and the metal particle encapsulated in the pores show a larger image than MOF pore [Houk *et al*., 2009]. No attempts were made to image the MOF composites due to these reasons.

6.3.2. AAS Analysis

50 mg of Pd-IGO sample was leached into 5 ml, 10 ml and 20 ml conc. HCl (27%) for 1 day and then filtered. Filtrate was added with water to dilute and make the samples A, B, C. Standard solution of 10, 20, 30, 40, 50 ppm was prepared from a stock solution (15 mg $PdCl_2$ in 1 ml conc. HCl and diluted further with water). Calibrating with absorptance of standard solutions Pd

quantity was approximated to 3.2% maximum in the Pd-IGO compound. The results match reasonable with our initial estimates; the reaction conditions and the amount of H_2PdCl_4 for synthesis of Pd-IGO (section 6.2.3) were chosen to yield about 5 wt % of Pd-IGO.

6.3.3. XRD Analysis

The XRD patterns for various Cu-BTC composites are shown in Figure 6.3. As can be seen in these patterns the structure of the original Cu-BTC MOF seems to have been preserved in all the cases. The addition of AC, IGO, Pd-GO, Pd-IGO or Pt-AC did not seem to prevent the formation of Cu-BTC (although at higher concentrations the intensity of the Cu-BTC peaks seems to have somewhat diminished). Petit *et al.* reported that MOF "blocks" attach to a graphene layer by the interaction between metal sites of MOFs and epoxy groups on GO [Petit and Bandosz., 2009, Petit *et al*., 2011]. A similar mechanism occurring here might explain formation of Cu-BTC in the presence of various substrates considered. At higher concentration of Pt-AC (10 and 25 %), however the intensity of Cu-BTC peaks is almost negligible (Fig 6. 3) and possibly the formation of MOF might have been significantly effected due to presence of Pt-AC. In contrast, even higher concentrations of Pd-IGO do not seem to adversely affect the formation of Cu-BTC.

Figure 6.4 presents the X-ray diffraction patterns of various Cr-BDC composites. Due to the mesoporous character of Cr-BDC, most peaks are observed in a small angle region (0^o -12^o) and are characteristic of the structure of this MOF [Latroche *et al*., 2007, Vimont *et al*., 2006]. Even in case of the Cr-BDC composites, most peaks from this low angle region are preserved, (2 Theta ~2.75, 3.25, 4, 5.2, 6, and 9°), suggesting that the MOF structure is intact; and the graphene layers from GO only induced slight distortion. No additional peak of Pd-IGO is observed on this

materials. Pd-IGO yields a weak peak at ~8^{o} which is masked when the composite is formed. Rallapalli *et al*. [2013] synthesized Cr-BDC/XAC composites and found 2θ at ~1.75^{o} to disappear at higher concentration of AC and a similar trend is visible here which indicates the distortion in the structure. Again, the intensity significantly reduces as the mass% of Pd-IGO increases and the peaks at small angles in particular become broader (at 4.6, 6.4 and 21 wt% Pd-IGO) suggesting some deterioration in the quality of Cr-BDC present in these composites.

The XRD patterns for MOF-205, pure Pt-AC and MOF-205/2.3Pt-AC are shown in Figure 6.5. Clearly, in case of MOF-205, presence of even 2.3 % Pt-AC seems to have significantly effected its formation. The surface area analysis of these composites should give further clues on the formation pattern and effect of the presence of impurities/dopants in the mother solution used in synthesis of these MOFs.

6.3.4. Specific Surface Area and Pore Volume of MOF Composites

To evaluate the porosity of the materials, nitrogen adsorption isotherms of the composites and substrates were measured at 77 K, and are shown in Figures 6. 6 - 6.14. The specific surface area and pore volume of the samples are listed in Tables 6.2 and 6.3. First, before evaluation of the properties for composites the surface area and pore volume of the substrates used in the MOF reaction mixture were analyzed. The nitrogen uptake capacity at 77 K on pure graphene oxide (GO), and IGO (and hence their surface area and pore volume) are negligible. In addition, the isotherms for pure activated carbon (AC) and 5 wt% Pt loaded activated carbon (Pt-AC) are shown in Figures 6. 6.

In case of composites the nitrogen uptake isotherms at 77 K are shown in Figures 6. 6 – 6. 10., while the isotherms of composites after subjecting them to Li doping procedure are shown in Figures 6. 11 – 6. 14. While some difference is observed in the uptake, it is rather difficult to relate the differences to the composition of the composites.

The surface area and pore volume of MOF-205/2.3Pt-AC composite reduces considerably compared to that of the parent MOF-205 (Table 6.4). Similarly, the surface area and pore volume of Cu-BTC/1.2AC (compared to Cu-BTC/1.2Pt-AC), Cu-BTC/3.7Pd-GO (compared to Cu-BTC/3.7Pd-IGO), Cu-BTC/3.3IGO (compared to Cu-BTC/3.7Pd-IGO), Cr-BDC/1.9Pt-AC (compared to Cr-BDC/1.9Pd-IGO) and Cr-BDC/1.4IGO (compared to Cr-BDC/1.9Pd-IGO) were significantly lower and further variation in concentrations of these composites is not considered. For sake of comparison between Pt-AC and Pd-IGO composites, both Cu-BTC/XPt-AC and Cu-BTC/XPd-IGO were studied with varying values of X. However, since Pd-IGO composite seemed to have better hydrogen loading capacity compared to that of the Pt-AC composite of Cu-BTC, only Cr-BDC/XPd-IGO composites with varying X were considered for hydrogen adsorption measurements (Table 6.3).

The effect of composite concentration on the surface area and pore volume are shown in Figures 6.-15 – 6.-17. Several interesting observations can be made from these figures. In all the cases, the surface area and pore volume increase marginally (compared to that of a pure parent MOF) as transition metal containing substrate is initially doped into the MOF. This increase is typically between 10 and 20 %, much lower than the effect observed in case of Li doped MOF samples (discussed in Chapter 5). A similar increase in surface area and pore volume of the composites has been reported earlier in literature also. This has been attributed to the well

dispersed MOF crystallites which improve the porosity and accessibility of the MOF network for the adsorbate. In addition, some new pores may also be created at the interface between the MOF units and the graphene layers owing to the coordination of the oxygen groups of IGO with the metallic centers of the MOF [Petit and Bandosz, 2011].

However, as this loading is increased further, a decrease is seen in the surface area and pore volume. At high loadings (X > 10) in case of Cu-BTC/XPt-AC the specific surface area and pore volume seem to level off (Figure 6.2.15) to a value close to that of Pt-AC itself (737 m^2g^{-1}, 0.69 cm^3 g^{-1}). However, in case of Pd-IGO since IGO itself has negligible surface area as concentration of Pd-IGO is increased from 10 to 37 % (Fig 6.2.16) a sharp decrease (> 50%) in these values (instead of the leveling off seen in earlier case) is observed between Cu-BTC/10Pd-IGO and Cu-BTC/37Pd-IGO. In contrast, the difference between surface area and pore volume of Cr-BDC/6.4Pd-IGO and Cr-BDC/21Pd-IGO is less than 10%; due to large pore size and pore volume of Cr-BDC additional Pd-IGO substrate is readily accommodated into the pores of Cr-BDC MOF and does not block the pores and active surface as it does in case of Cu-BTC which has much smaller pores. This difference contributes to somewhat less drastic decrease in surface area and pore volume of Cr-BDC composites compared to that of Cu-BTC composites especially at higher Pd-IGO loadings.

Lithium doping of the composite in most cases improves the surface area and pore volume somewhat compared to the corresponding composite (without Li doping) as shown by filled columns in Figures 6. 15- 6. 17. However, it is interesting to note that in all the cases, even after doping the composites with Li, none of them achieve the surface area and pore volume comparable to that of Li doped MOF samples discussed in chapter 5. Thus, Li doped MOF

samples (Cu-BTC/Li and Cr-BDC/Li) exhibit maximum surface area and pore volume compared to all other composites made from the corresponding parent MOF. As an example, Cr-BDC/Li has better surface area and pore volume (4310 m^2-g^{-1} and 2.18 cm^3 g^{-1}); the composite Cr-BDC/1.9Pd-IGO/Li exhibits maximum values of surface area and pore volume (3687 m^2 g^{-1} and 1.92 cm^3 g^{-1}), all other composites of Cr-BDC have even lower surface area and pore volume. While these values for Cr-BDC/1.9Pd-IGO/Li are certainly better than Cr-BDC and Cr-BDC/1.9Pd-IGO, they are significantly lower than Cr-BDC/Li (pure Cr-BDC doped with Li).

6.4. Hydrogen Adsorption on MOF Composites

6.4.1. Isotherms on MOF-205 Composite

At low temperature (93 K) maximum excess loading of 4 wt% was observed for MOF-205/2.3Pt-AC (Table 6.4) whereas as already discussed in Chapter 4 (Figure 4.13), pure MOF-205 has a hydrogen adsorption capacity (Figure 6.18) of about 6 wt% at saturation. At room temperature and at 100 bar loading is 0.42 wt% which is less compared to 0.63 wt% loading on pure MOF-205 (Figure 6.19). Thus, addition of Pt-AC shows a substantial reduction in surface area and pore volume of the MOF (and hence in hydrogen adsorption uptakes). Due to this reason, other composites of this MOF were not considered. This MOF is highly unstable and sensitive upon exposure to ambient conditions [Sumida *et al*., 2012]. Even during synthesis and characterization of pure MOF-205 careful handling is necessary to prevent unwanted exposure to atmosphere. This is another reason for not considering MOF-205 composites any further.

6.4.2. Hydrogen Adsorption on Cu-BTC/Pt-AC and Cu-BTC/AC Composites

The hydrogen adsorption isotherms on some composites and that of pure Cu-BTC MOF are shown in Figure 6.20 and 6.21 at cryogenic and ambient temperatures. The isotherms at cryogenic temperatures are shown in Figure 6.20. As already discussed, the surface area and pore volume of Cu-BTC/1.2AC is low compared to that of pure MOF; accordingly the hydrogen uptake on this composite is also significantly lower. However, the composite with Pt-AC of similar doping i.e. Cu-BTC/1.2 Pt-AC exhibits significantly higher hydrogen adsorption than Cu-BTC/1.2AC alone. Due to this reason, composites of Cu-BTC/AC with varying AC dope% are not considered further. In addition, while gravimetric uptake on Cu-BTC/1.2Pt-AC is slightly lower than that of pure Cu-BTC, it improves significantly after performing the Li doping procedure on the composite. Although, hydrogen uptake on Cu-BTC/1.2Pt-AC/Li is marginally higher than that on pure Cu-BTC, but significantly lower than pure Cu-BTC doped with Li i.e. Cu-BTC/Li. The maximum uptake capacity for hydrogen varies between ~2 wt% for Cu-BTC/1.2AC to about 3.6 wt% for Cu-BTC/1.2Pt-AC/Li almost in accordance with the increasing pore volume of the samples. The isotherms at room temperature are shown in Figure 6.21. While the loading on Cu-BTC/1.2AC is significantly lower, loading on other samples is almost comparable.

Hydrogen isotherms at cryogenic temperature on various Cu-BTC/Pt-AC composites along with that on Pure Cu-BTC MOF are shown in Figure 6.22. With increasing doping the hydrogen uptake capacity seems to be decreasing in general. However, when doping is in excess of 10 wt% (Cu-BTC/11Pt-AC and Cu-BTC/31Pt-AC samples) the hydrogen uptake is substantially lower, while the uptake on other three samples Cu-BTC/1.2Pt-AC, Cu-BTC/3.3Pt-AC and Cu-

BTC/7.1Pt-AC are much closer to one another. It is interesting to note that Pt/Cu ratio in Cu-BTC/3.3Pt-AC is about 0.008 (about the same as Li/Cu ratio in Cu-BTC/Li discussed in chapter 5). Nevertheless, even in these samples, the uptake is about slightly lower (about 6% at maximum loading) than that on pure Cu-BTC MOF. This may be partially due to the additional weight of "heavy" mass and larger size of Pt. Since the adsorption is significantly lower and isotherms do not exhibit saturation uptake at ambient temperature with in the experimental pressure range (Figure 6.23), the differences between various samples are less prominent than in case of isotherms at cryogenic temperature.

The isotherms on Li doped composites are shown in Figures 6.24 and 6.25. There is almost no difference between the isotherms on these samples, except in case of Cu-BTC/Li which exhibits higher loadings at both temperatures. It is interesting to note that after Li doping, composite containing low Pt-AC content (Cu-BTC/1.2Pt-AC/Li) exhibits an uptake from 3.52 wt% around 25 bar (about 15% enhancement compared to the parent Cu-BTC/1.2Pt-AC composite) at cryogenic temperature; in contrast composite with high Pt-AC content (Cu-BTC/11Pt-AC) exhibits an enhancement in excess of 50% after Li doping. A similar trend is observed in case of hydrogen adsorption at ambient temperature. At around 100 bar, the hydrogen adsorption on Cu-BTC/11Pt-AC is 0.32 wt%, while its Li doped composite (Cu-BTC/11Pt-AC/Li) has an uptake of about 0.52 wt% (an increase of about 60%, although temperatures are slightly different). It is possible that the Li doping process is synergistically modifying the surface characteristics of the Pt-AC in the composite thereby affecting its hydrogen adsorption characteristics; as a result the effect of Li on hydrogen adsorption is more significant in composites containing higher content of Pt-AC. The low pressure adsorption characteristics might also reveal some interesting phenomenon.

The Henry's constant for hydrogen adsorption is estimated form the virial domain plot ln (P/N) vs. N plot [Sun *et al*., 1998]. Since there was a variation of experimental temperature between the samples, the Henry's constants were suitably calculated at two temperatures (100 K and 298 K) from experimental data for each sample by interpolating appropriately. Figure 6.26 shows the variation of Henrys constants for various Cu-BTC/XPt-AC composites. With increase in doping, the Henrys constant of Cu-BTC/XPt-AC composites seem to be decreasing at cryogenic temperatures. However, after doping these composites with Li, the Henry's constants significantly improve to levels better than that of even Li doped pure Cu-BTC MOF (Figure 6.27). While the general trend discussed above exits, it proved rather difficult to estimate the accurate values of Henrys' constant at cryogenic temperatures (as indicated by the error bars in the figures) due to our experimental limitations.

While the uptake on some of the MOF composites shown here are better than that of pure MOF, none of them show results similar to that reported by Yang's group [Li and Yang, 2008] where hydrogen adsorption is significantly enhanced due to spillover effect. Due to the intimate contact of the MOF with doped Pt-AC (as needed for observing spillover effect) we have expected results comparable to that of Yang's group. However, addition of Pt-AC during the synthesis of Cu-BTC MOF (below doping levels of about 10% Pt-AC) seems to improve the hydrogen adsorption slightly in the low pressure region; in contrast Luzan and Talyzin reported that hydrogen adsorption capacity of MOF-5 goes down after bridging or physically mixing of the MOF sample with Pt-AC [Luzan and Talyzin, 2010, Luzan and Talyzin, 2011].

The enthalpy of adsorption at zero coverage is calculated from the change of Henry's constant with temperature. The variation of enthalpy of adsorption with dope % in composites is

shown in Figure 6.28. In case of composites, the adsorption enthalpy at zero coverage is largely around 7.5 kJ mol^{-1} and increases to about 9 kJ mol^{-1} only for Cu-BTC/31 Pt-AC. In contrast, for the Li doped samples as Pt-AC content of the composites increases a gradual increase in adsorption enthalpy is observed. This indicates that Li doping procedure is possibly providing "active" sites for adsorption on the Pt-AC surface; the hydrogen molecules initially occupy these active sites and the strength of adsorbate interactions with these sites govern the adsorption enthalpy at zero coverage.

6.4.3. Hydrogen Adsorption on Cu-BTC/IGO Cu-BTC/Pd-GO and Cu-BTC/Pd-IGO Composites

The isotherms of some Cu-BTC composites with various graphene oxide dopes are shown in Figure 6.29. Cu-BTC/3.3 IGO composite does not contain the transition metal (Pd) nanoparticles doped on graphene oxide; as already discussed earlier it possess lower surface area and pore volume compared to composites that contain graphene oxide doped with Pd (Cu-BTC/3.7Pd-IGO for example). The presence of transition metal enhances the adsorption characteristics of MOF composite. Petit and Bandosz reported that GO component itself does not adsorb hydrogen as epoxy/hydroxyl groups block entry of non-polar hydrogen [Petit *et al*., 2011]. Therefore MOF composite consisting of only GO does not prove to be beneficial.

Similarly, improved graphene oxide (IGO) instead of "regular" graphene oxide yields composites with better adsorption characteristics (comparing isotherms for Cu-BTC/3.7Pd-GO and Cu-BTC/3.7Pd-IGO in Figure 6.29). Finally, the adsorption characteristics of Cu-BTC/3.7Pd-IGO are comparable to that of pure Cu-BTC MOF itself. The composites doped with Li (Cu-BTC/3.7Pd-GO/Li and Cu-BTC/3.7Pd-GO/Li) exhibit better adsorption capacities

compared to the respective parent composites not subjected to Li doping. However, none of the composites exhibit hydrogen adsorption characteristics close to that of Cu-BTC/Li i.e. pure Cu-BTC doped with Li; this scenario is similar to the one seen in case of Cu-BTC/Pt-AC composites. The results at ambient temperature closely follow almost a similar trend but differences between the various samples are much smaller (Figure 6.30).

The hydrogen isotherms on various Cu-BTC/Pd-IGO composites are shown in Figure 6.31 and 6.32. As the amount of Pd-IGO in the composite increases, the hydrogen uptake at cryogenic temperature increases initially compared to the parent Cu-BTC MOF; however at higher Pd-IGO content the hydrogen adsorption capacity of the composites decreases (in case of Cu-BTC/10Pd-IGO and Cu-BTC 37Pd-IGO). It is worth noting that ratio of Pd/Cu in Cu-BTC/3.7Pd-IGO is about 0.01 (about the same as Li/Cu ratio in Cu-BTC/Li pure Cu-BTC doped with Li). The differences between hydrogen adsorption capacities of the composite samples at ambient temperature are lower (Figure 6.32), nevertheless Cu-BTC/37Pd-IGO still exhibits lowest uptake.

Zhou *et al.* [2013] synthesized few Cu-BTC/XPt-GO composites and documented enhanced hydrogen uptake at room temperature due to spillover effect. Interestingly their best composite Cu-BTC/5Pt-GO has a room temperature hydrogen uptake of 0.8 wt% and it saturates at 60 bar; whereas the pure MOF adsorbs 0.4 wt% at similar condition. Its noteworthy, the pure Cu-BTC in this work has room temperature uptake of 0.59 wt% at 100 bar which is one among the best reported value in the literature.

As in case of Cu-BTC/Pt-AC composites, Cu-BTC/Pd-IGO samples were also subjected to a Li doping procedure. The hydrogen adsorption isotherms on Li doped Cu-BTC/Pd-IGO

composites are shown in Figure 6.33 and 6.34. In general, the effect of Li doping on hydrogen adsorption was more prominent at higher Pd-IGO contents in the composite. For example, the hydrogen adsorption at cryogenic conditions and around 20 bar increases by about 8% when Cu-BTC/3.7Pd-IGO is doped with Li. In contrast, the capacity of Cu-BTC/10Pd-IGO/Li increases to 3.59 wt% from 2.54 wt% for Cu-BTC/10Pd-IGO (an increase of about 40 %). At ambient temperature this increase is more modest (at about 15 %). Thus, Li doping seems to be more effective in increasing hydrogen adsorption capacity in composites containing higher Pd-IGO contents, similar to what has been observed for Cu-BTC/Pt-AC samples. Cu-BTC/Pd-IGO composites with low Pd-IGO contents do not show significant changes in their adsorption characteristics when doped with Li.

The Henry's constant variation with amount of Pd-IGO content is shown in Figures 6.35 and 6.36; significant changes occur in Henry's constant only when the Pd-IGO content in the composite is in excess of 10 wt%. Even in case of Henry's constant, the effect of Li doping on the composites is significant only for Cu-BTC/10Pd-IGO/Li. In any case, the capacities as well as Henry's constants of both Cu-BTC/Pd-IGO and Cu-BTC/Pd-IGO/Li at similar doping levels are almost identical.

Enthalpy of adsorption value for Cu-BTC MOF composites is highest for Cu-BTC/8Pd-IGO (~ 9.26 kJ mol^{-1} compared to 7.5 kJ mol^{-1} for pure Cu-BTC) and the value decreases with further loading of dopant (Table 6.2, Figure 6.37). Better adsorbate-adsorbent interaction may be the reason for this improvement. Suh *et al.,* [2009] impregnated ~3 nm Pd NP into SNU-3 MOF (hydrogen uptake increases at 77 K) and to check with the spillover effect calculated enthalpy of adsorption. SNU-3/Pd has less enthalpy of adsorption 6.62 kJ mol^{-1} than pure SNU-3 (8.11 kJ

mol^{-1}). However, it is interesting to note that unlike in the case of Cu-BTC composites with Pt-AC, the Cu-BTC/XPd-IGO composites do not exhibit enhanced adsorption enthalpies after Li doping. Mulfort *et al*. reported that Li doping may not always improve the ΔH_{ads} if there is adsorption site heterogeneity in the structure [Mulfort *et al*., 2009]. This is another reason to hypothesize that Li doping in case of Cu-BTC/Pt-AC creates active sites inside the pores of Pt-AC thereby exhibiting enhanced adsorption enthalpies.

On the other hand, Pt-AC particles themselves are larger (compared to sheet like graphene oxide layers) and hence it is possible that they partially block the pores of the MOF upon doping. This leads to a decrease in pore volume and surface area thereby the maximum uptake on Cu-BTC/Pt-AC composites are lower compared to that on Cu-BTC/Pd-IGO composites.

6.4.4. Hydrogen Adsorption on Cr-BDC/IGO, Cr-BDC/Pt-AC and Cr-BDC/Pd-IGO Composites

The hydrogen adsorption isotherms on some Cr-BDC composites with IGO, Pt-AC and Pd-IGO materials are shown in Figures 6.38 and 6.39. The adsorption capacity of Cr-BDC/1.9PtAC composite is slightly lower than that of the parent Cr-BDC MOF at cryogenic temperature; on the other hand, after Li doping i.e. for Cr-BTC/1.9Pt-AC/Li the hydrogen adsorption capacity improves and in fact betters the parent Cr-BDC MOF. The capacity for Cr-BDC/1.4IGO is comparable to that of parent Cr-BDC MOF; addition of transition metal into the graphene oxide used in the composite improves adsorption capacity as described in case of Cu-BTC MOF. Thus Cr-BDC/1.9Pd-IGO exhibits slightly better hydrogen adsorption uptake than parent Cr-BDC MOF. Li doping of this composite further improves its uptake capacity by about 2-3 %.

Ralapalli *et al*. [2011] synthesized Cr-BDC composites with addition of AC to improve the porosity in Cr-BDC. With very low concentration they were able to increase the pore volume from 1.45 to 1.75 cc g^{-1} and absolute adsorption of H_2 improved from 6.36 to 10.1 wt% which is very close to best reported loading of ~9 wt% (6.1 wt% on excess) on pure Cr-BDC by Latroche *et al*., [2006]. They claimed AC added smaller pores in the resultant composite.

Hydrogen adsorption isotherms on Cr-BDC/Pd-IGO composites are shown in Figures 6.40 and 6.41. In contrast to observation in Cu-BTC composites, the composites of Cr-BDC have enhanced hydrogen adsorption capacities compared to that of the parent MOF and in general it increases with increase in the content of Pd-IGO in the composite. Thus, although a low surface area material (Pd-IGO) is added to Cr-BDC with a surface area of about 3000 m^2 g^{-1} in excess of 20 wt %, the loss in gravimetric adsorption capacity is more than compensated; For example, Cr-BDC/21Pd-IGO at about 50 bar and cryogenic temperature has an uptake of 4.48 wt % compared to parent Cr-BDC which has an uptake capacity of about 3.68 wt% at similar conditions (an enhancement of about 20 %). The large pores of Cr-BDC possibly accommodate the Pd-IGO better without adversely affecting the characteristics of the parent MOF; in case of Cu-BTC the pores are smaller. At ambient temperature however, the difference between uptakes on the composites considered are much smaller and only the composite with highest Pd-IGO content considered (Cr-BDC/21Pd-IGO) exhibits better capacity than the parent Cr-BDC MOF. Li doping enhances the uptake on the composites by about 5-10 % at cryogenic temperatures (Figure 6.42). At ambient conditions, all Li doped samples exhibit almost similar uptake capacities for hydrogen and are in general about 5-10 % higher than the parent composites not doped with Li (Figure 6.43). These values are also comparable to that of pure Cr-BDC doped with Li (Cr-BDC/Li). However, at cryogenic conditions and high pressures none of the

composites exhibit uptake capacities offered by Cr-BDC/Li, which is more than 20 % higher than the any of the Cr-BDC/Pd-IGO composites doped with Li.

Figures 6.44 and 6.45 show the variation of Henry's constant with the Pd-IGO amount in the composite. Significant increase in Henry's constant is observed only in samples having high dopant. Clearly, Li doped samples exhibit a gradual increase in the Henry's constant; such a trend strongly points to the possibility of Li acting synergistically along with the Pd-IGO substrate to enhance the hydrogen adsorption. As the amount of Pd-IGO in the composite increases, the effect of Li doping is larger.

Enthalpy of adsorption value for Cr-BDC MOF composites is highest for Cr-BDC/4.6Pd-IGO (~ 9 kJ mol^{-1} compared to 6.89 kJ mol^{-1} for pure Cr-BDC) and the value decreases with further loading of dopant (Table 6.3, Figure 6.46). Yang *et al*. calculated (Clausius Clapeyron equation) Cr-BDC bridged with 5% Pt-AC to have ΔH_{ads} ~12.5 kJ mol^{-1} and the room temperature loading of such material is 1.5 wt% at 100 bar. According to their study ΔH_{ads} for bridged Cr-BDC is even greater than bridged Cu-BTC (~8.5 kJ mol^{-1}). However they did not report saturation loading of such materials. As in other cases so far, the Li doped Cr-BDC/Pd-IGO composites exhibit a gradual increase in the adsorption enthalpy as the content of Pd-IGO increases attaining ~9.6 kJ mol^{-1} for Cr-BDC/21Pd-IGO/Li sample. The effect of Li doping is significant at higher Pd-IGO content. Nevertheless, maximum gravimetric uptake is exhibited by the Li doped pure Cr-BDC sample.

6.4.5. Correlation between Pore Volume and Maximum Hydrogen Uptake Capacity

As already discussed well in literature, the maximum excess hydrogen capacity on MOFs is proportional to its pore volume in general [Petit *et al*., 2009, Liu *et al*., 2013]. The plot is shown in Figure 6.47 for all the Cu-BTC, Cr-BDC, and MOF-205 composites discussed in previous sections 6.4.2 – 6.4.4. The two quantities seem to be well correlated, although the plot includes various MOFs with a largely different doping levels in the composite(s). Li and Yang described that spillover effect improves the hydrogen adsorption by surface diffusion which cannot be correlated with the pore volume. In this work this relationship is rather linear. Liu et al., reported that MOF composite consisting of GO will have better pore volume hence improvement in hydrogen loading is linear [Liu *et al*., 2013].

6.5. Summary

The composites of Cr-BDC and Cu-BTC were prepared with varying ratios of the Pt-AC, Pd-IGO catalysts. The prepared samples were characterized by various techniques and hydrogen adsorption isotherms on these samples were measured. The presence of transition metal Pd or Pt is necessary for observing better hydrogen adsorption capacities. Pure activated carbons (AC) or improved graphene oxide (IGO) do not enhance hydrogen adsorption characteristics to the same extent.

Cu-BTC/Pt-AC composites exhibit somewhat lower gravimetric uptake capacity for hydrogen due to presence of Pt-AC, but after Li doping all samples with varying amounts of Pt-AC in the composite (between 1.2 to 11 wt%) exhibit almost similar uptake behavior for hydrogen equaling that of pure Cu-BTC. However, these values are still lower than that of Cu-

BTC/Li (pure Cu-BTC doped with Li). The Cu-BTC/Pd-IGO samples exhibit better hydrogen uptakes than the corresponding Pt-AC counterparts. In fact, some of the composites exhibit better uptake capacities than pure Cu-BTC itself. Li of Cu-BTC/Pd-IGO doping further enhances the uptakes on some of these composites. In case of Cr-BDC/Pd-IGO composites the effect of substrate (Pd-IGO) on gravimetric uptake even at high amounts (21 wt% in the composite) is marginal. This is in contrast to Cu-BTC composites where, the hydrogen uptake capacity at high substrate contents decreases significantly. As in case of Cu-BTC composites, Li doping of the composites significantly improves the hydrogen uptakes; the saturation uptake capacity of Cr-BDC/6.4Pd-IGO is ~ 4.2 wt%, while its Li doped sample Cr-BDC/6.4Pd-IGO/Li has a saturation capacity of 4.6 wt %. Nevertheless this value is still lower than that of Cr-BDC/Li (6.02 wt%).

The improvement in enthalpy of adsorption at zero coverage for both Cu-BTC and Cr-BDC composites is marginal at low substrate contents; however, at high amount of Pd-IGO or Pt-AC in the composites, the enthalpies reach about to values greater than 9 kJ mol^{-1}. This is contrast to Li doped samples where the changes in enthalpies are more modest (< 8.2 kJ mol^{-1}). This is to be expected, since the transition metals such as Pd or Pt are more likely to provide strong adsorption sites compared to Li which is likely to exist as a complex. However, higher adsorption enthalpies do not necessarily translate into better gravimetric adsorption capacities; the additional mass of the framework due to presence of substrates offsets the advantage gained by doping in most cases. Thus, Li doped pure Cu-BTC and Cr-BDC MOFs still outperform all heir composites in terms of gravimetric storage capacities.

Figures

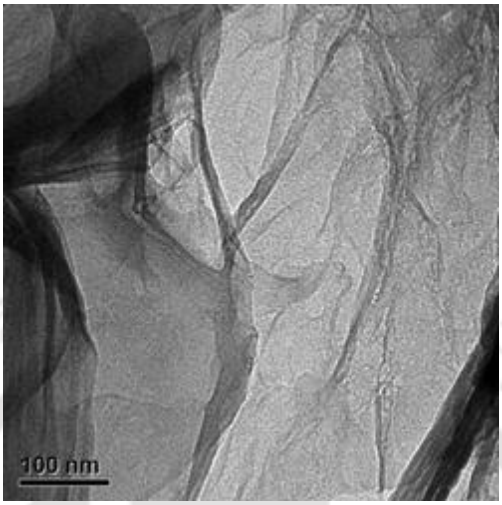

Figure 6.1: TEM Image of Improved Graphene Oxide.

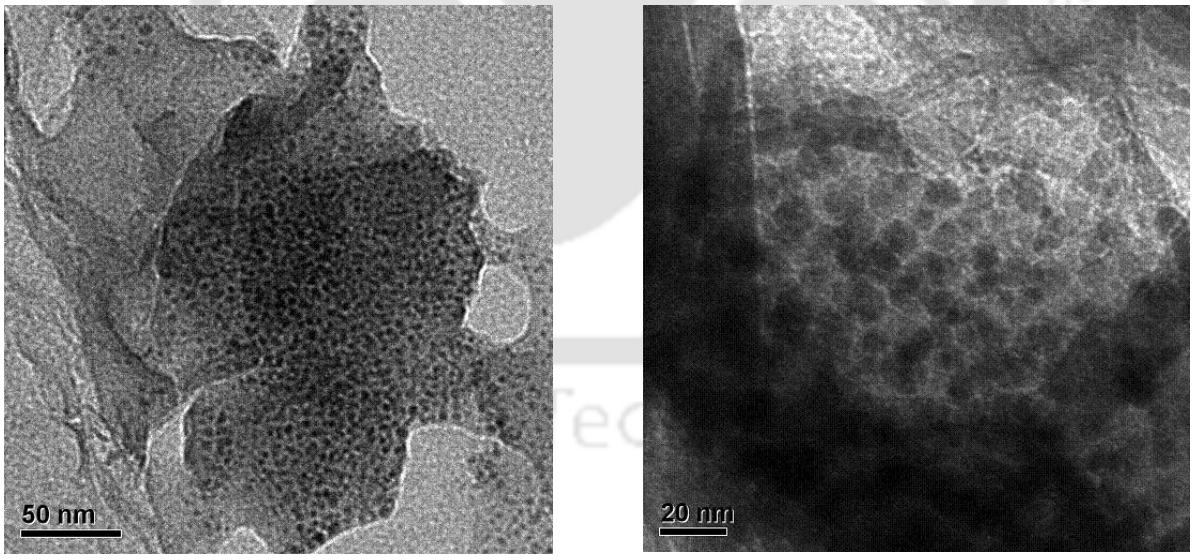

(a) **(b)**

Figure 6.2: TEM Image of Pd nanoparticles deposited on Improved Graphene Oxide.

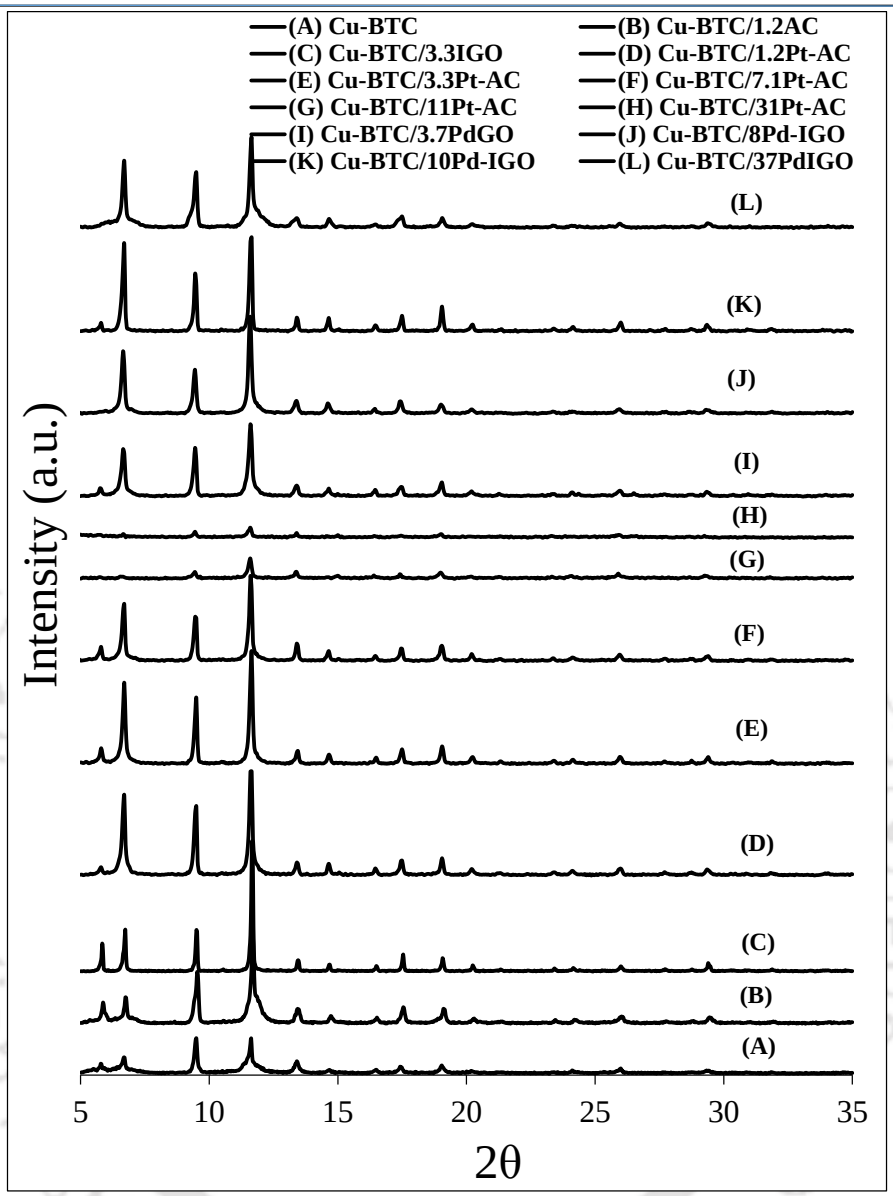

Figure 6.3: Powder XRD Pattern for Cu-BTC composites.

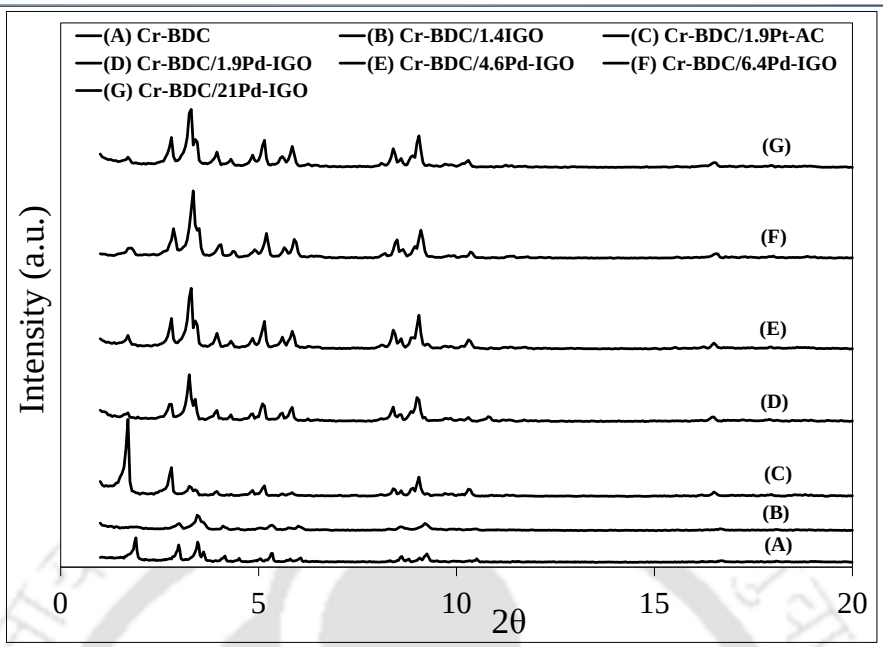

Figure 6.4: Powder XRD Pattern for Cr-BDC composites.

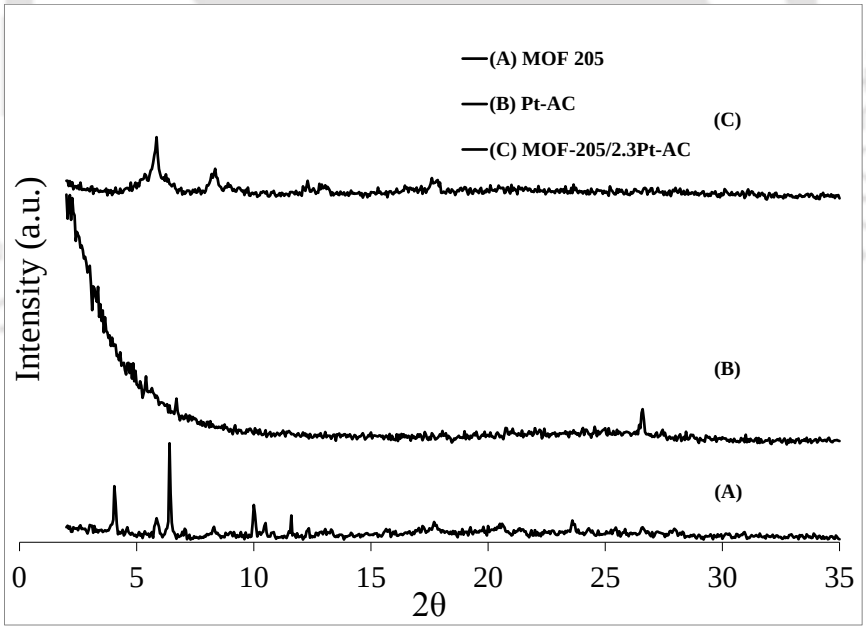

Figure 6.5: Powder XRD Pattern for MOF-205 Composite.

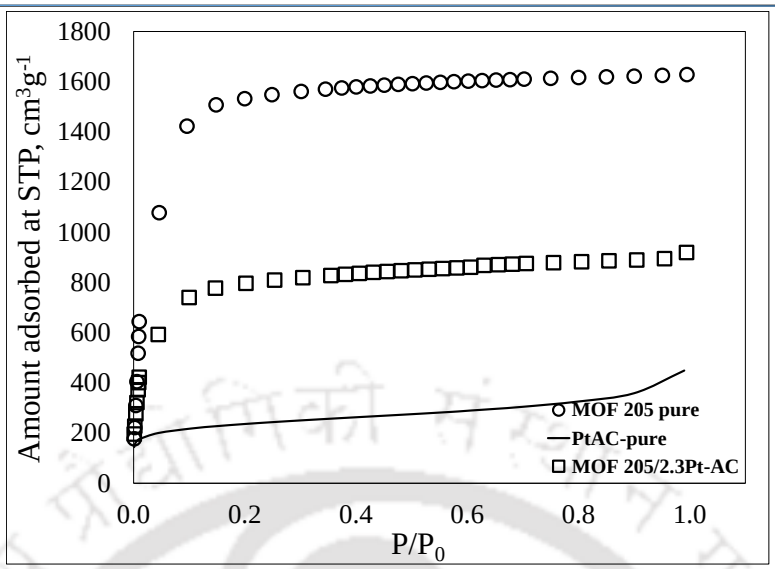

Figure 6.6: N_2 Adsorption Isotherm at 77 K on Pt-AC, MOF-205 and MOF-205/2.3Pt-AC Composite

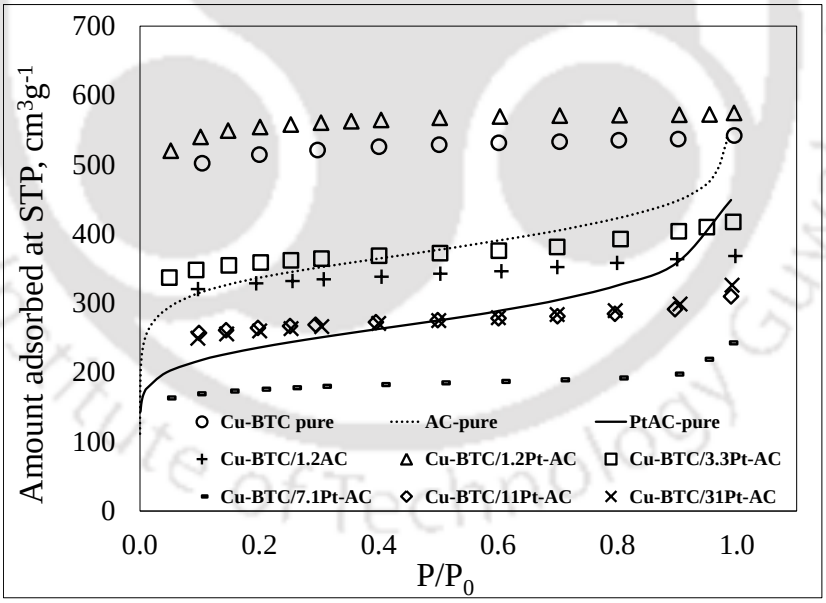

Figure 6.7: N_2 Adsorption Isotherm at 77 K on AC, Pt-AC, Cu-BTC and Cu-BTC/XPt-AC Composites

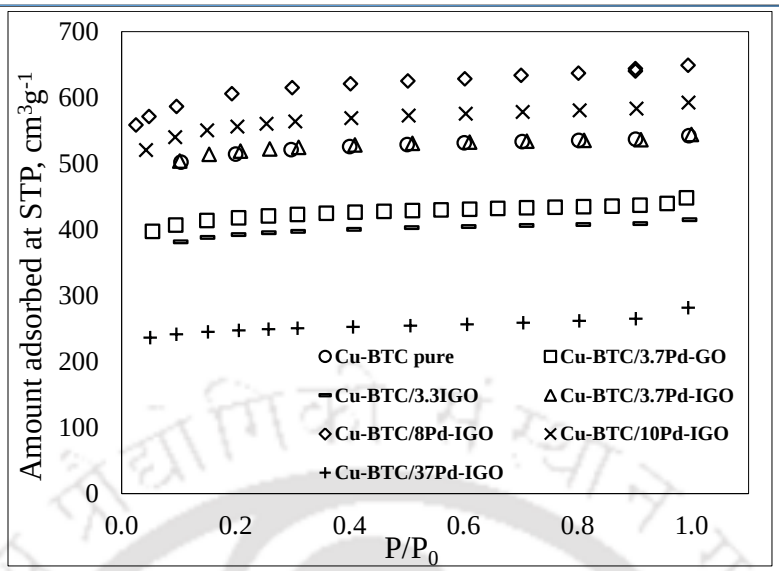

Figure 6.8: N_2 Adsorption Isotherm at 77 K on Cu-BTC and Cu-BTC/3.7Pd-GO, Cu-BTC/3.3IGO, Cu-BTC/XPd-IGO Composites

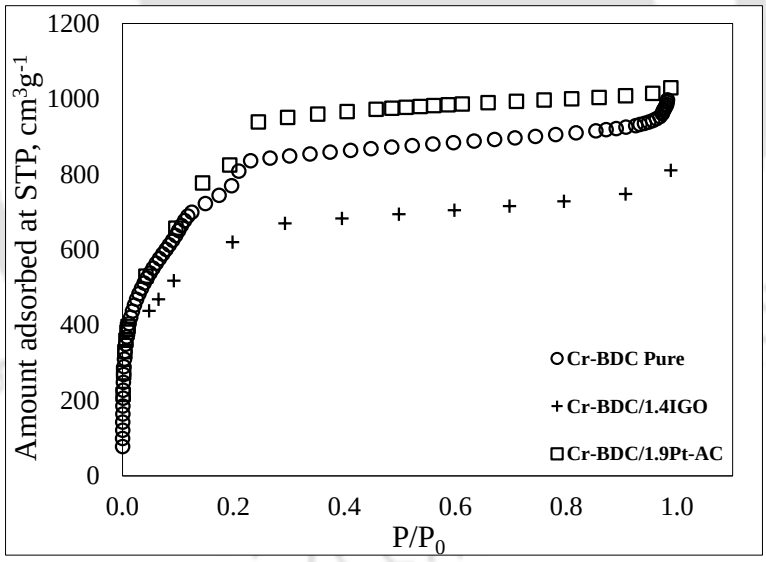

Figure 6.9: N_2 Adsorption Isotherm at 77 K on Cr-BDC, Cr-BDC/1.4IGO, Cr-BDC/1.9Pt-AC Composites.

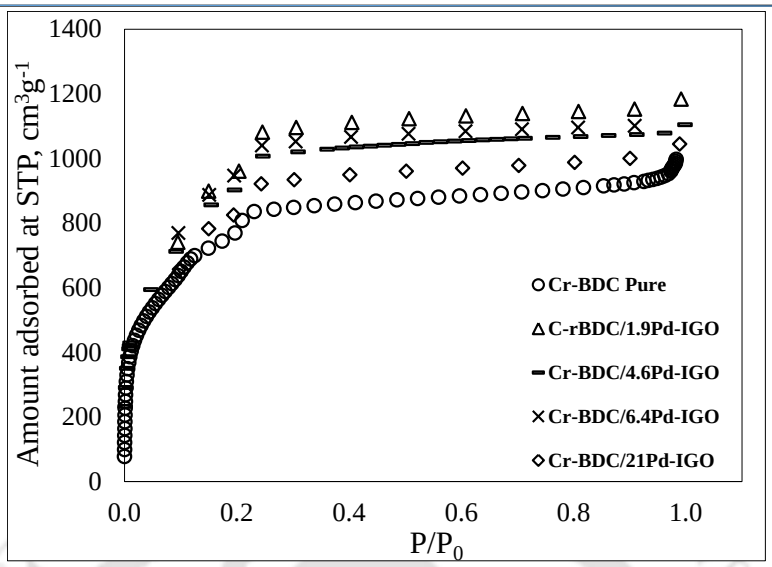

Figure 6.10: N_2 Adsorption Isotherm at 77 K on Cr-BDC and Cr-BDC/XPd-IGO Composites.

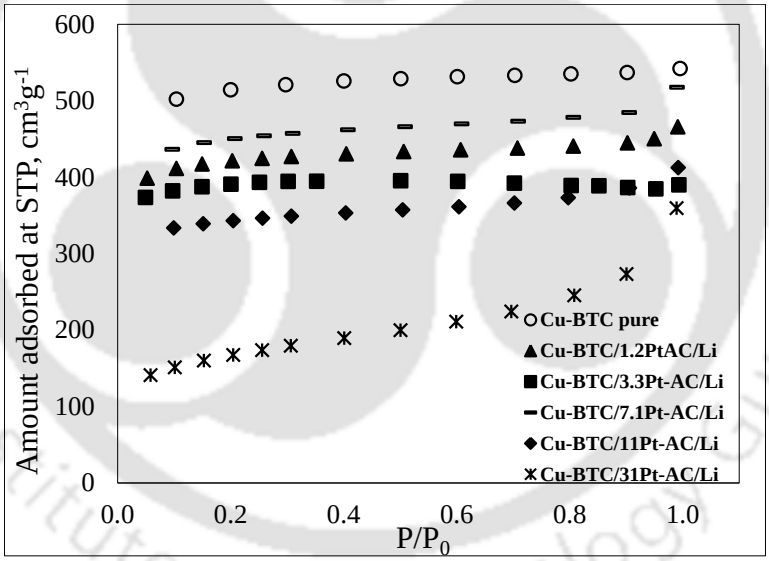

Figure 6.11: N_2 Adsorption Isotherm at 77 K on Cu-BTC and Cu-BTC/XPt-AC/Li Composites.

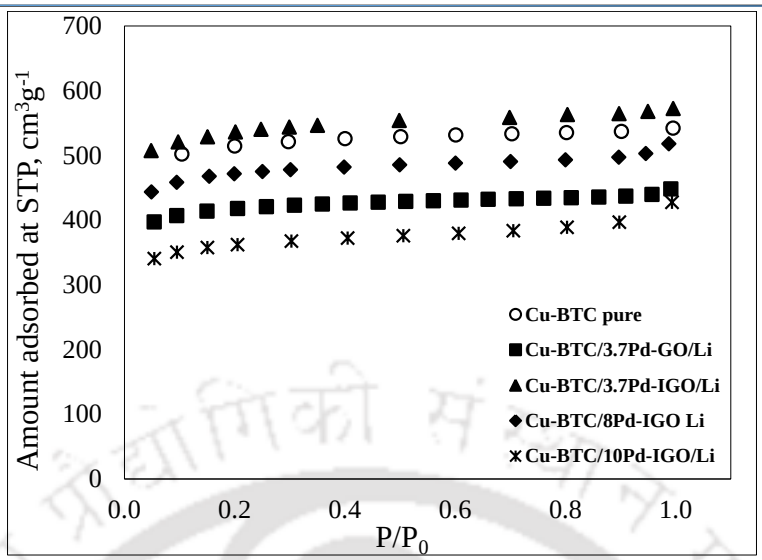

Figure 6.12: N_2 Adsorption Isotherm at 77 K on Cu-BTC, Cu-BTC/3.7Pd-GO/Li, Cu-BTC/XPd-IGO/Li Composites.

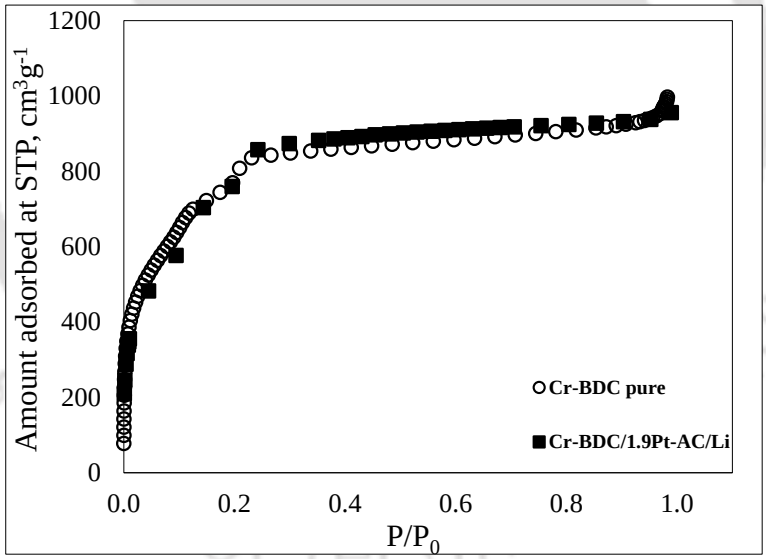

Figure 6.13: N_2 Adsorption Isotherm at 77 K on Cr-BDC, Cr-BDC/1.9Pt-AC/Li Composite.

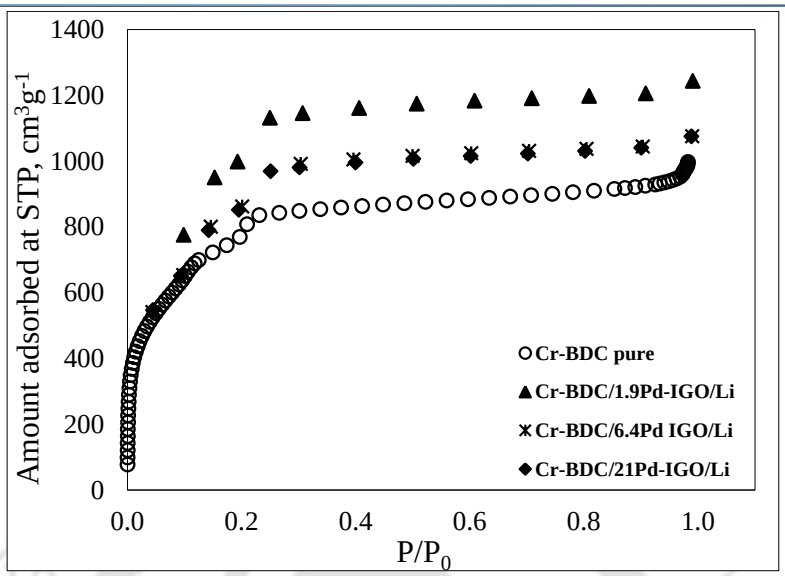

Figure 6.14: N_2 Adsorption Isotherm at 77 K on Cr-BDC and Cr-BDC/XPd-IGO/Li Composites.

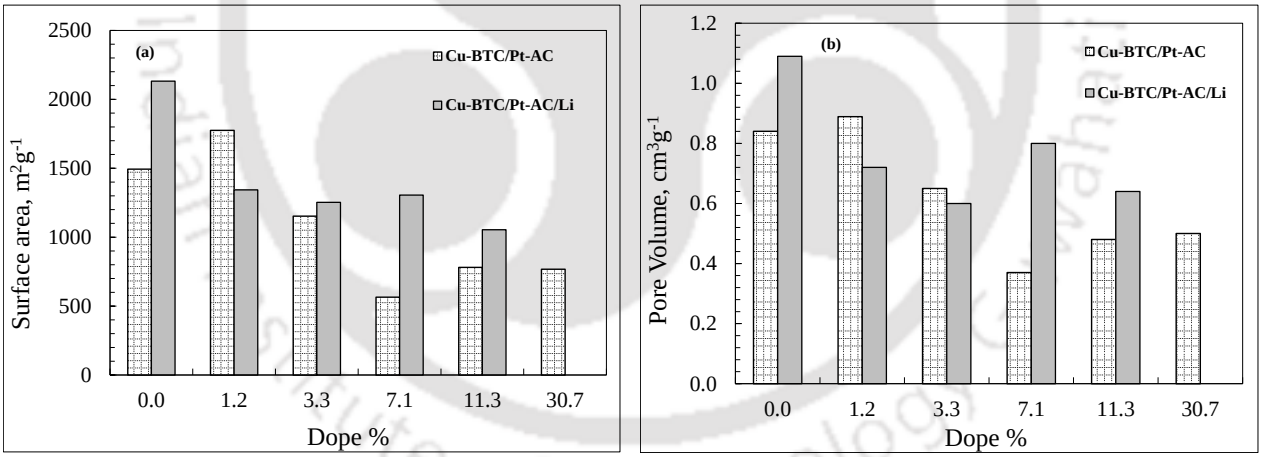

Figure 6.15: Variation of Surface Area and Pore Volume with Doping for Cu-BTC/XPt-AC and Cu-BTC/XPt-AC/Li Composites.

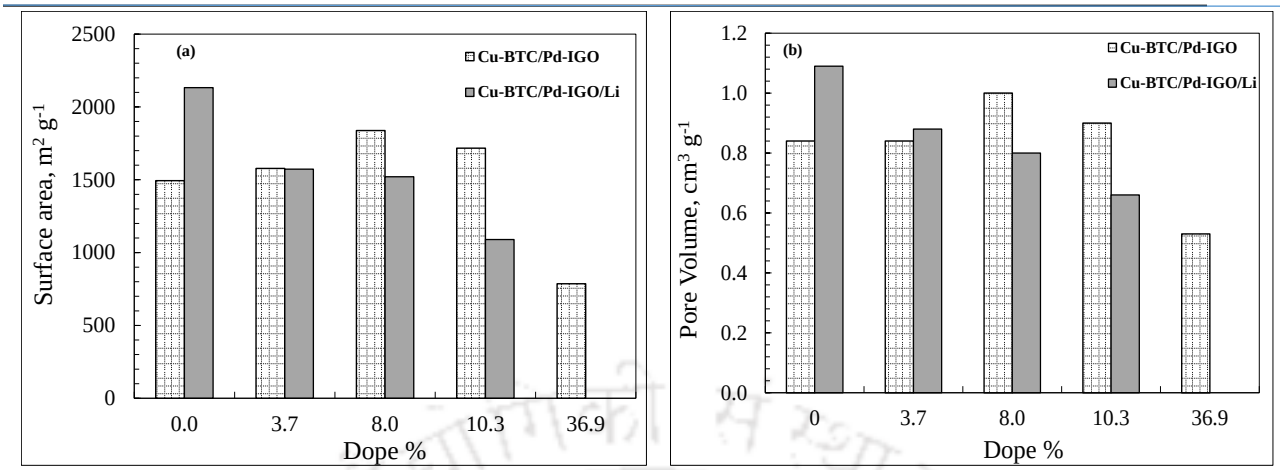

Figure 6.16: Variation of Surface Area and Pore Volume with Doping for Cu-BTC/XPd-IGO and Cu-BTC/XPd-IGO/Li Composites.

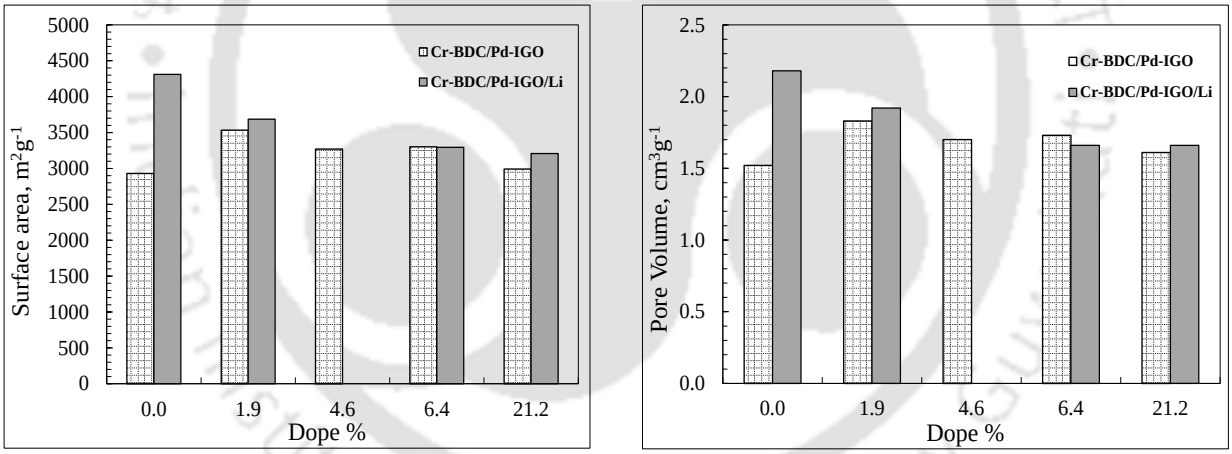

Figure 6.17: Variation of Surface Area and Pore Volume with Doping for Cr-BDC/XPd-IGO and Cr-BDC/XPd-IGO/Li Composites.

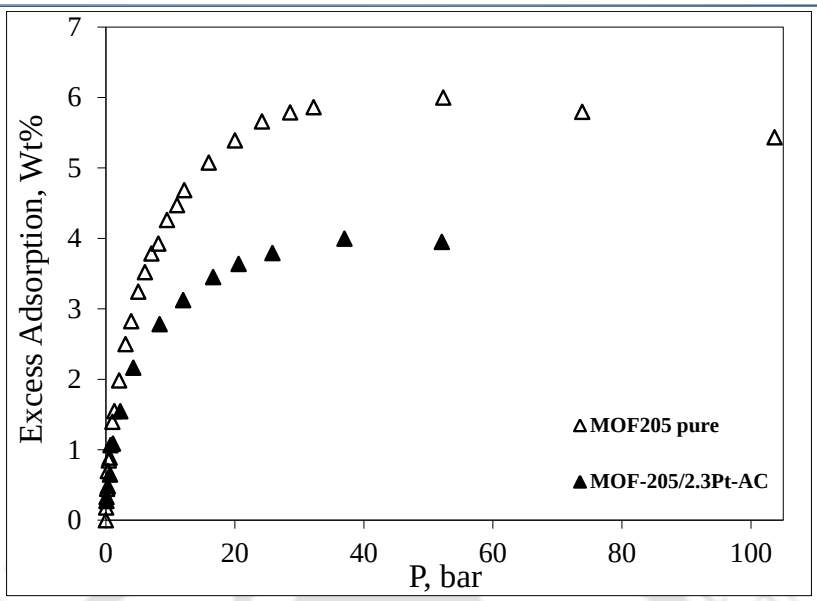

Figure 6.18: H_2 Adsorption Isotherms of MOF-205 (91 K, triangle), MOF-205/2.3Pt-AC (93 K, filled triangle).

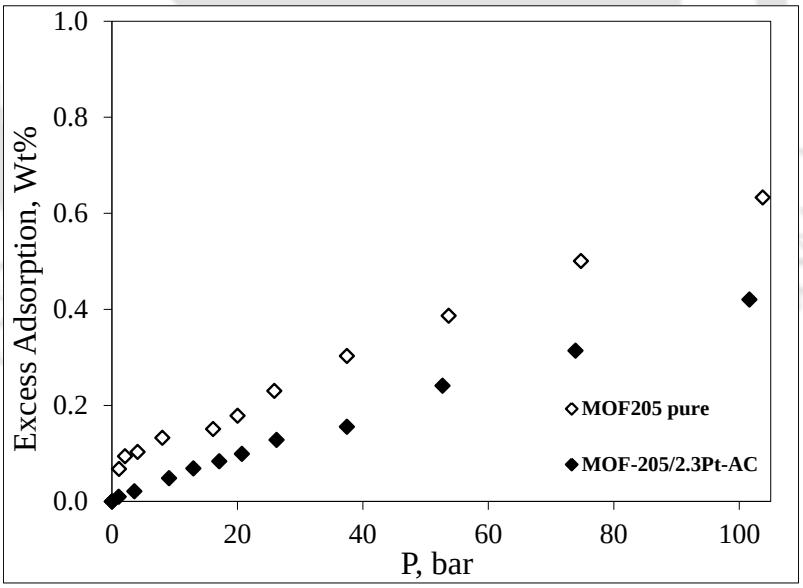

Figure 6.19: H_2 Adsorption Isotherms of MOF-205(296 K, diamond), MOF-205/2.3Pt-AC (298 K, filled diamond).

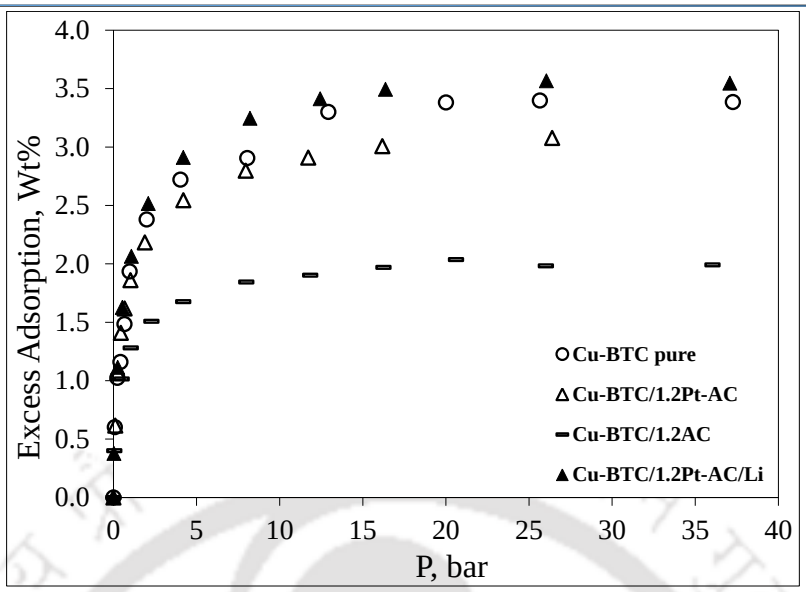

Figure 6.20: H_2 Adsorption Isotherms of Cu-BTC (101 K, circle), Cu-BTC/1.2Pt-AC (91 K, open triangle), Cu-BTC/1.2AC (91 K, dash), Cu-BTC/1.2Pt-AC/Li (92 K, filled triangle).

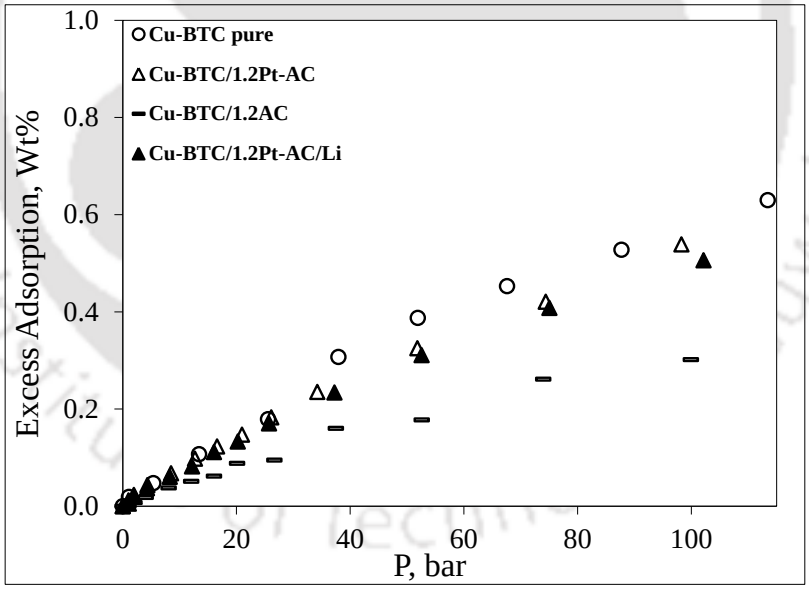

Figure 6.21: H_2 Adsorption Isotherms of Cu-BTC (297 K, circle), Cu-BTC/1.2Pt-AC (297 K, triangle), Cu-BTC/1.2AC (296 K, dash), Cu-BTC/1.2Pt-AC/Li (297 K, filled triangle).

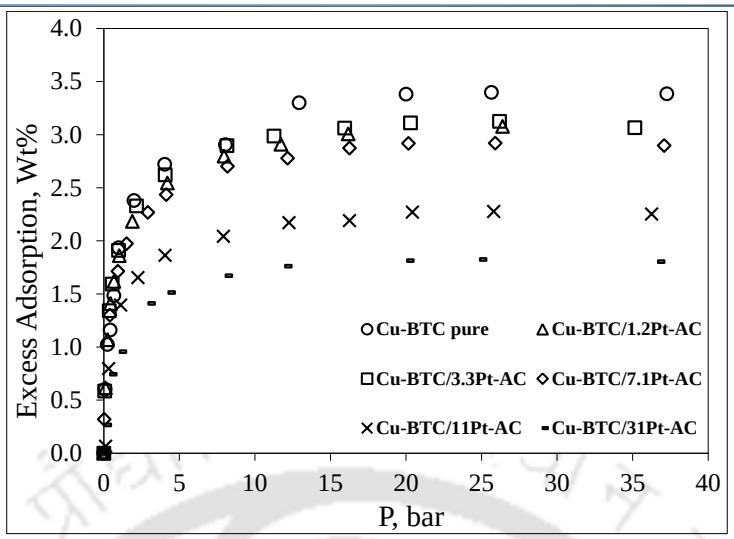

Figure 6.22: H_2 Adsorption Isotherms of Cu-BTC (101 K, circle), Cu-BTC/1.2Pt-AC (91 K, triangle), Cu-BTC/3.3Pt-AC (91 K, square), Cu-BTC/7.1Pt-AC (90 K, diamond), Cu-BTC/11Pt-AC (92 K, cross), Cu-BTC/31Pt-AC (101 K, dot).

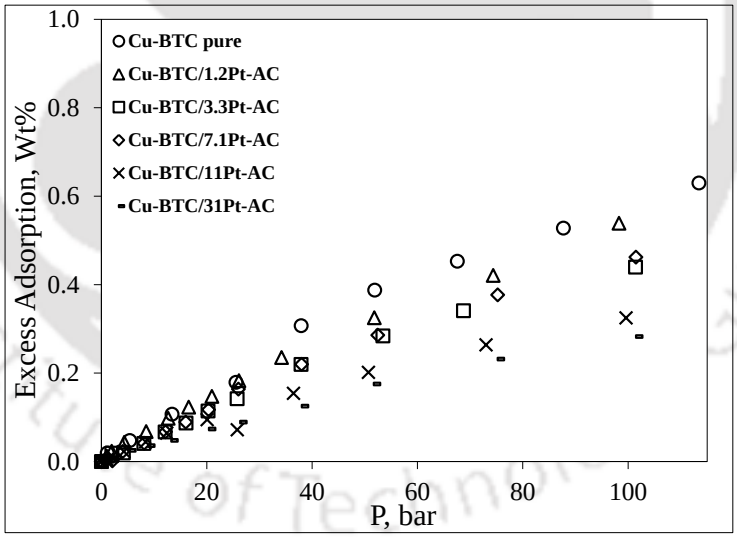

Figure 6.23: H_2 Adsorption Isotherms of Cu-BTC (297 K, circle), Cu-BTC/1.2Pt-AC (297 K, triangle), Cu-BTC/3.3Pt-AC (296 K, square), Cu-BTC/7.1Pt-AC (296 K, diamond), Cu-BTC/11Pt-AC (296 K, cross), Cu-BTC/31Pt-AC (298 K, dot).

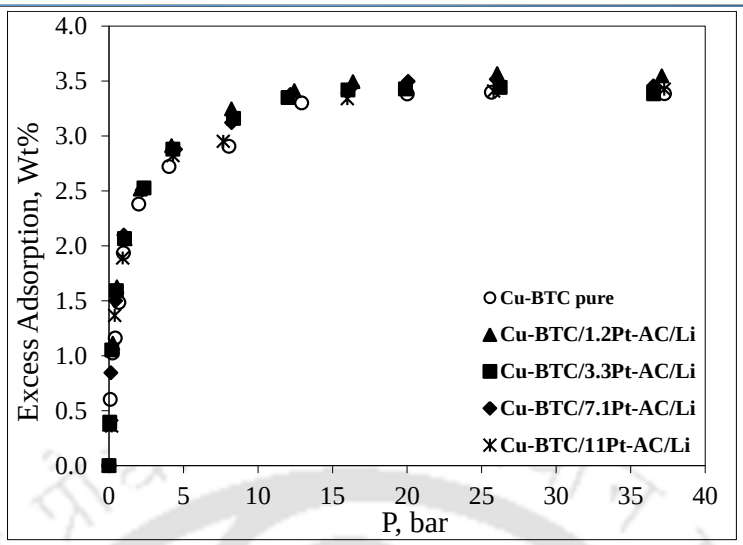

Figure 6.24: H_2 Adsorption Isotherms of Cu-BTC (101 K, circle), Cu-BTC/1.2Pt-AC/Li, (92 K, filled triangle), Cu-BTC/3.3Pt-AC/Li (100 K, filled square), Cu-BTC/7.1Pt-AC/Li (99 K, filled diamond), Cu-BTC/11Pt-AC/Li (99 K, star).

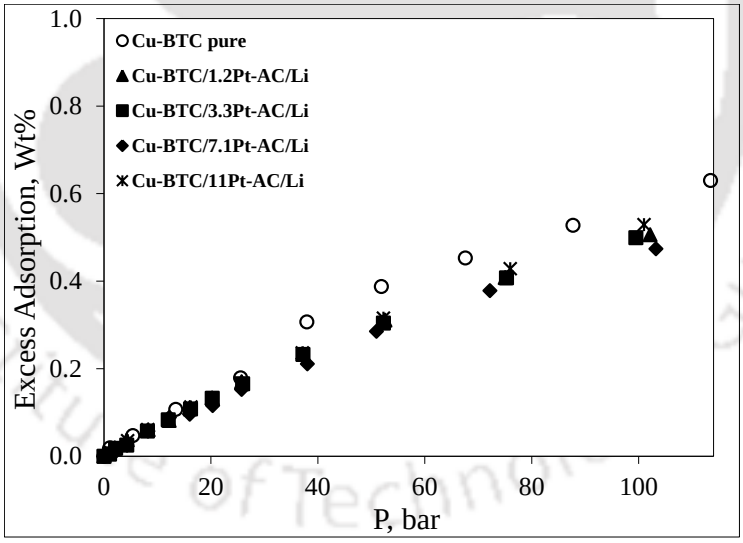

Figure 6.25: H_2 Adsorption Isotherms of Cu-BTC (297 K, circle), Cu-BTC/1.2Pt-AC/Li (297 K, filled triangle), Cu-BTC/3.3Pt-AC/Li (297 K, filled square), Cu-BTC/7.1Pt-AC/Li, (297 K, filled diamond), Cu-BTC/11Pt-AC/Li (297 K, star).

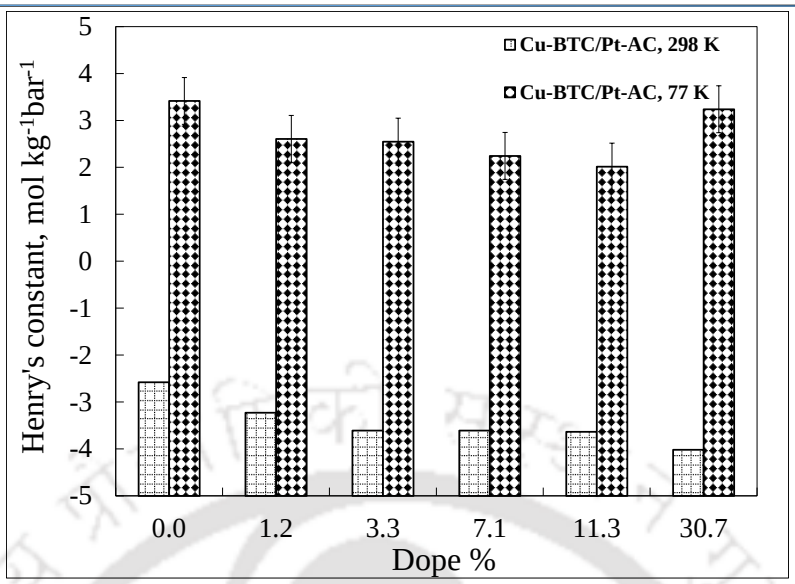

Figure 6.26: Variation of Henry's constants for Hydrogen Adsorption with Dope % for Cu-BTC/XPt-AC composites.

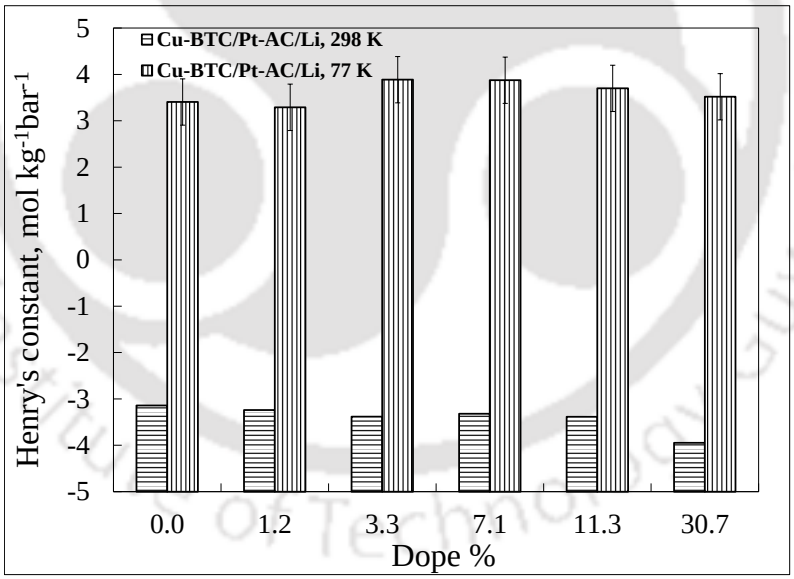

Figure 6.27: Variation of Henry's constants for Hydrogen Adsorption with Dope % for Cu-BTC/XPt-AC/Li Composites.

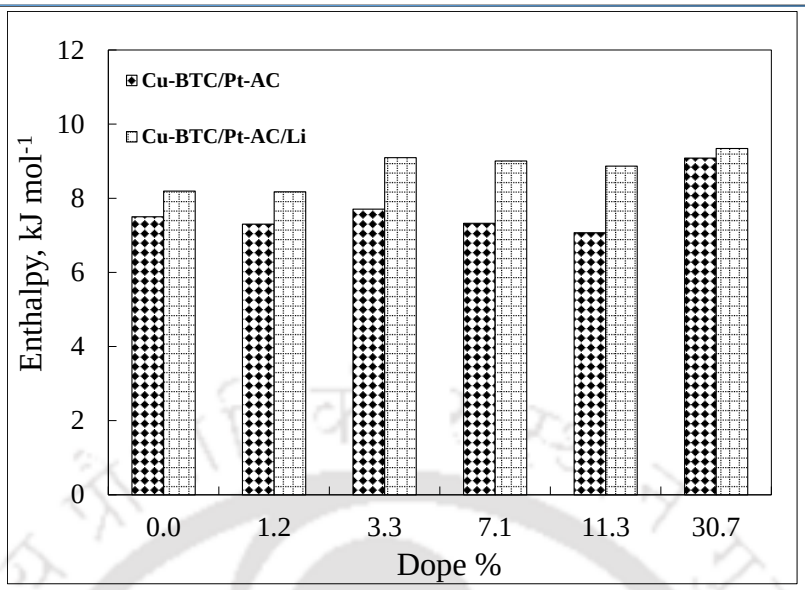

Figure 6.28: Variation of Adsorption Enthalpy for Hydrogen with Dope % for Cu-BTC/XPt-AC Composites.

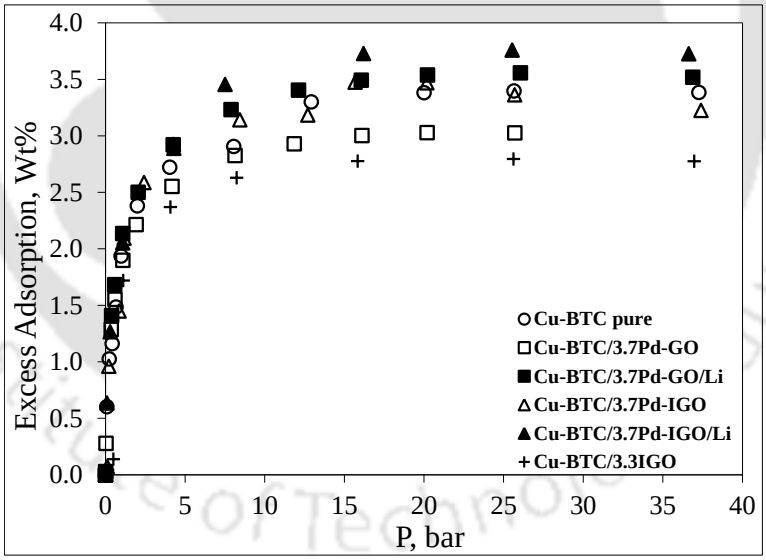

Figure 6.29: H_2 Adsorption Isotherms of Cu-BTC (101 K, circle), Cu-BTC/3.7Pd-GO (90 K, square), Cu-BTC/3.7Pd-GO/Li (297 K, filled square), Cu-BTC/3.7Pd-IGO (106 K, triangle), Cu-BTC/3.7Pd-IGO/Li (97 K, filled triangle), Cu-BTC/3.3IGO (97 K, plus).

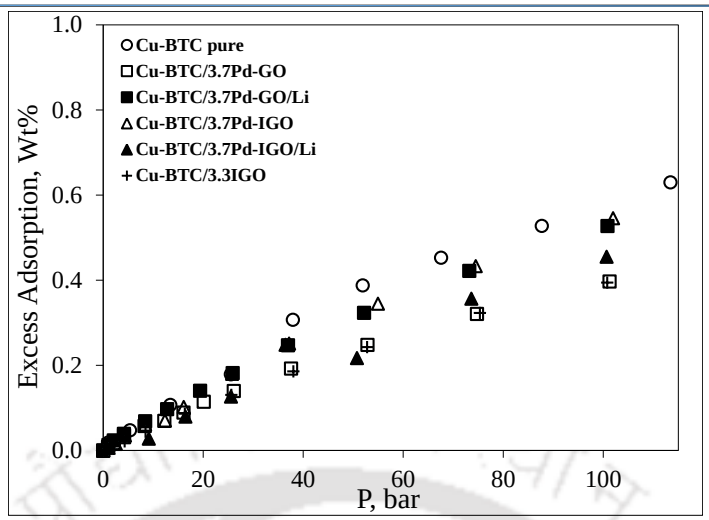

Figure 6.30: H_2 Adsorption Isotherms of Cu-BTC (297 K, circle), Cu-BTC/3.7Pd-GO (296 K, square), Cu-BTC/3.7Pd-/GO/Li (297 K, filled square), Cu-BTC/3.7Pd-IGO (297 K, triangle), Cu-BTC/3.7Pd-IGO/Li (298 K, filled triangle), Cu-BTC/3.3IGO (297 K, plus).

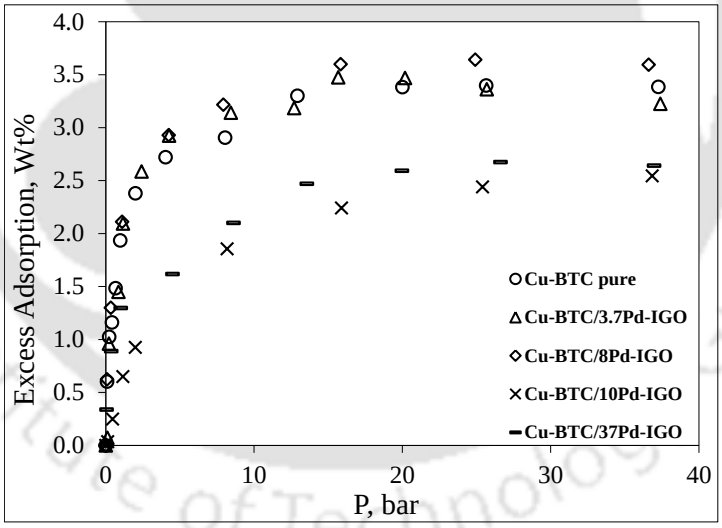

Figure 6.31: H_2 Adsorption Isotherms of Cu-BTC (101 K, circle), Cu-BTC/3.7Pd-IGO (106 K, triangle), Cu-BTC/8Pd-IGO (102 K, diamond), Cu-BTC/10Pd-IGO (113 K, cross), Cu-BTC/37Pd-IGO (91 K, dash).

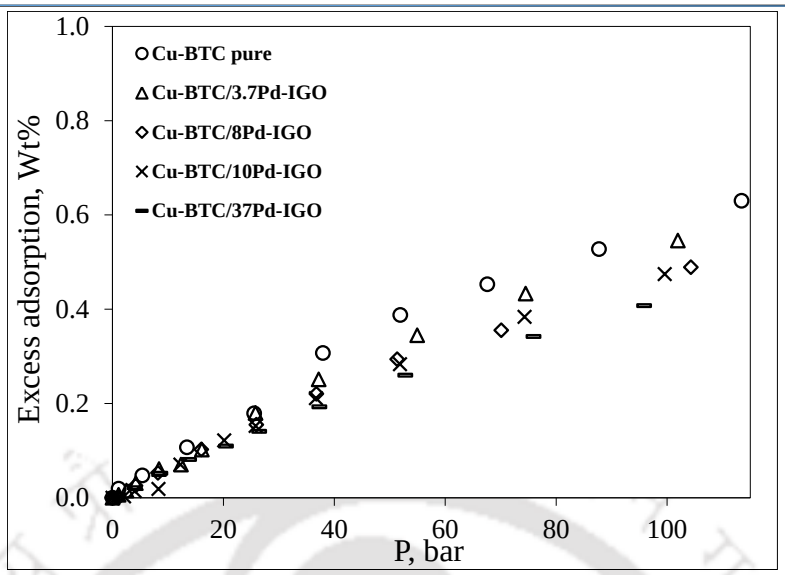

Figure 6.32: H_2 Adsorption Isotherms of Cu-BTC (297 K, circle), Cu-BTC/3.7Pd-IGO (297 K, triangle), Cu-BTC/8Pd-IGO (295 K, diamond), Cu-BTC/10Pd-IGO (297 K, cross), Cu-BTC/37Pd-IGO (297 K, dash).

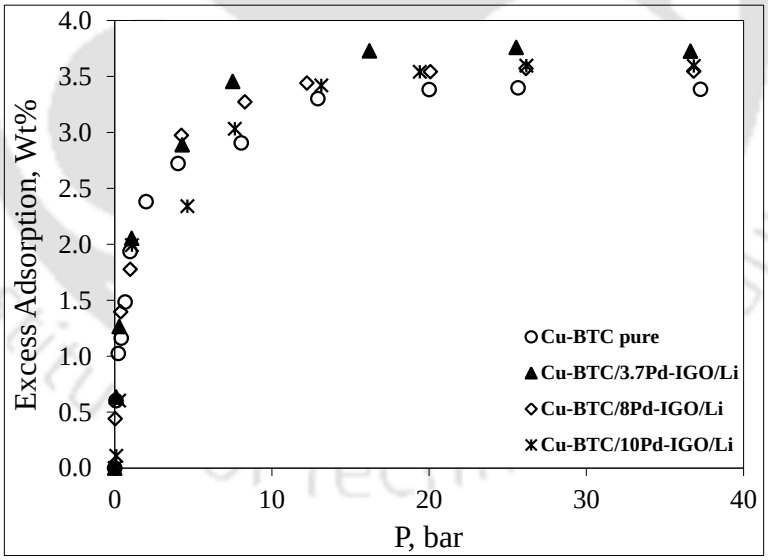

Figure 6.33: H_2 Adsorption Isotherms of Cu-BTC (101 K, circle), Cu-BTC/3.7Pd-IGO/Li (97 K, filled triangle), Cu-BTC/8Pd-IGO/Li (98 K, diamond), Cu-BTC/10Pd-IGO/Li (95 K, star).

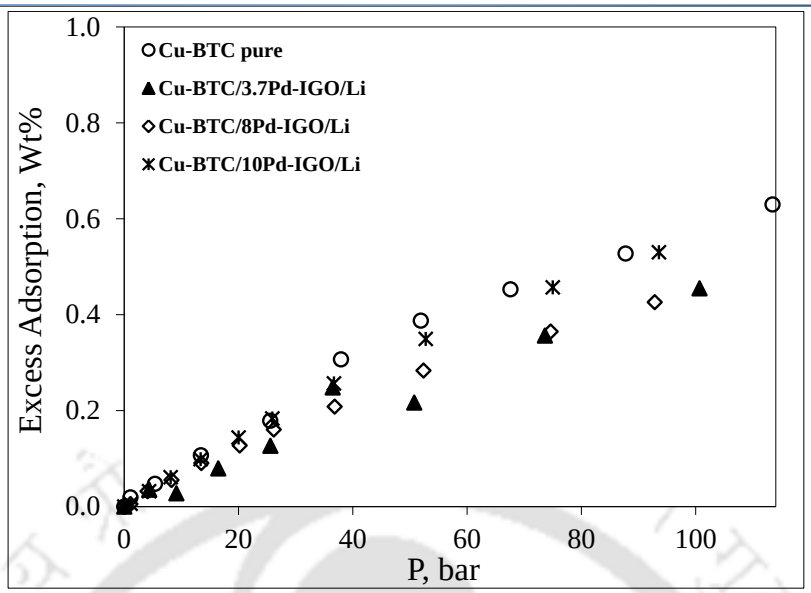

Figure 6.34: H_2 Adsorption Isotherms of Cu-BTC (297 K, circle), Cu-BTC/3.7Pd-IGO/Li (298 K, filled triangle), Cu-BTC/8Pd-IGO/Li (296 K, diamond), Cu-BTC/10Pd-IGO/Li. (296 K, star).

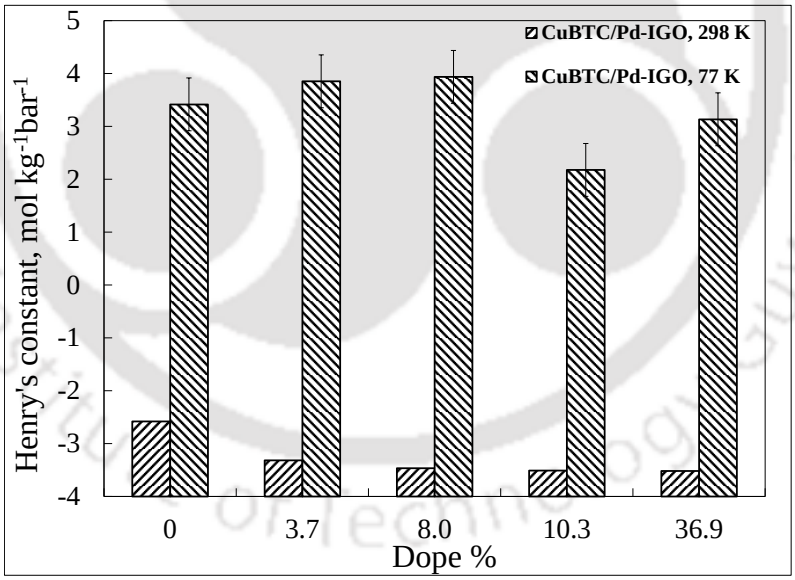

Figure 6.35: Variation of Henry's Constants for Hydrogen Adsorption with Dope % for Cu-BTC/XPd-IGO Composites.

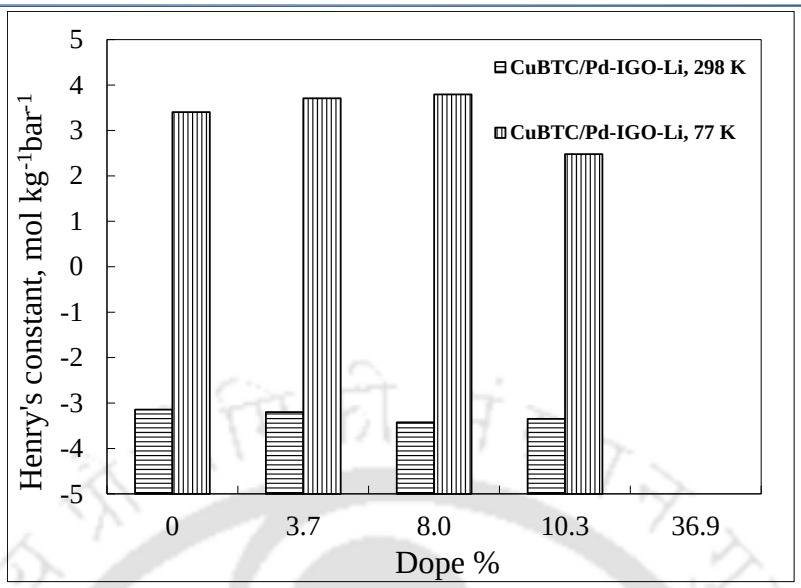

Figure 6.36: Variation of Henry's Constants for Hydrogen Adsorption with Dope % for Cu-BTC/XPd-IGO/Li Composites.

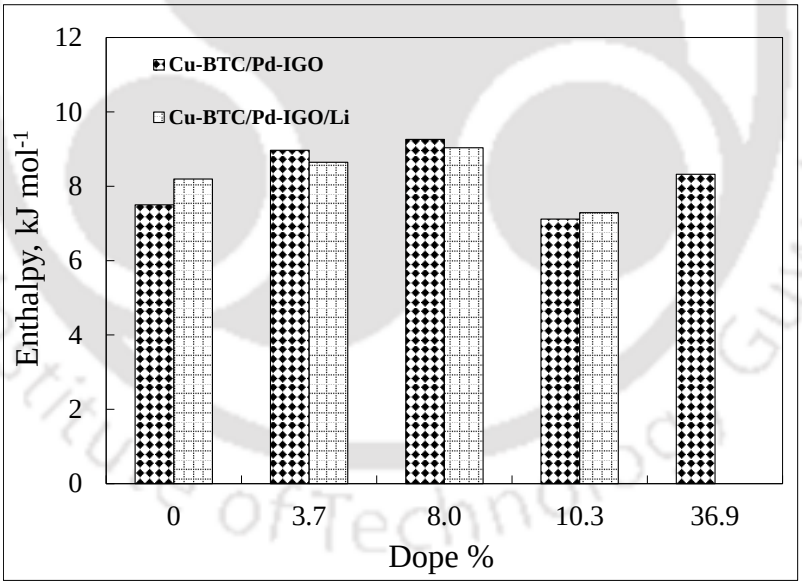

Figure 6.37: Variation of Adsorption Enthalpy for Hydrogen with Dope % for Cu-BTC/XPd-IGO Composites.

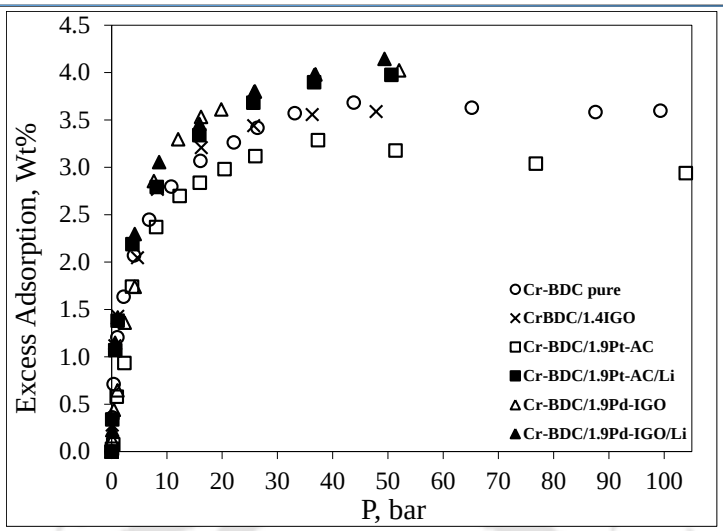

Figure 6.38: H_2 Adsorption Isotherms Cr-BDC (92 K, circle), Cr-BDC/1.4IGO (90 K, cross), Cr-BDC/1.9Pt-AC (90 K, square), Cr-BDC/1.9Pt-AC/Li (91 K, filled square), Cr-BDC/1.9Pd-IGO (92 K, triangle), Cr-BDC/1.9Pd-IGO/Li (104 K, filled triangle).

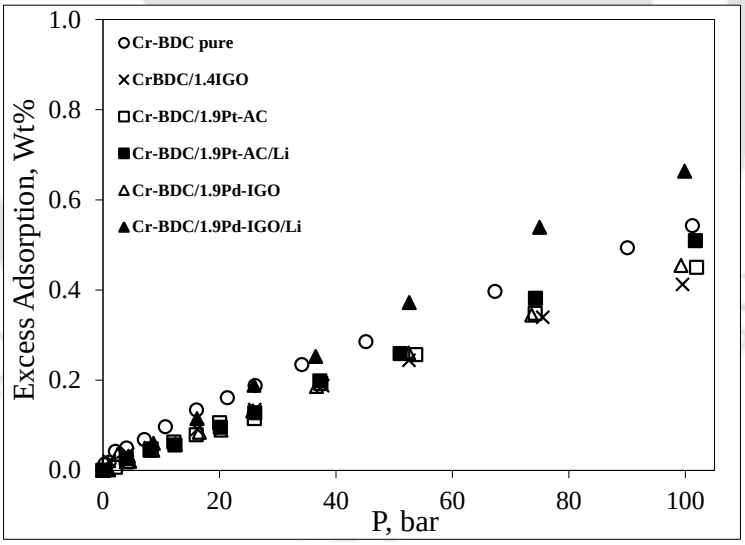

Figure 6.39: H_2 Adsorption Isotherms Cr-BDC (297 K, circle), Cr-BDC/1.9Pt-AC (298 K, square), Cr-BDC/1.9Pt-AC/Li (298 K, filled square), Cr-BDC/1.9Pd-IGO (297 K, (triangle), Cr-BDC/1.9Pd-IGO/Li (298 K, filled triangle).

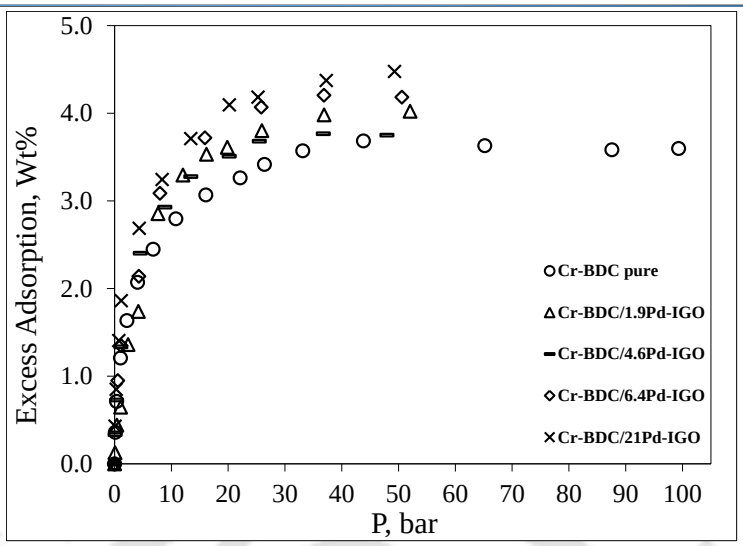

Figure 6.40: H_2 Adsorption Isotherms of Cr-BDC (92 K, circle), Cr-BDC/1.9Pd-IGO (92 K, triangle), Cr-BDC/4.6Pd-IGO (107 K, dash), Cr-BDC/6.4Pd-IGO (101 K, diamond), Cr-BDC/21Pd-IGO (95 K, cross).

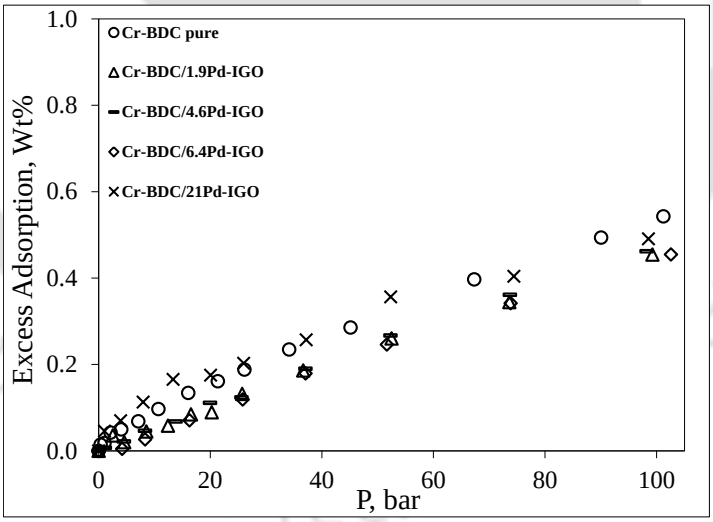

Figure 6.41: H_2 Adsorption Isotherms of Cr-BDC (297 K, circle), Cr-BDC/1.9Pd-IGO (297 K, triangle), Cr-BDC/4.6Pd-IGO (297 K, dash), Cr-BDC/6.4Pd-IGO (296 K, diamond), Cr-BDC/21Pd-IGO (297 K, cross).

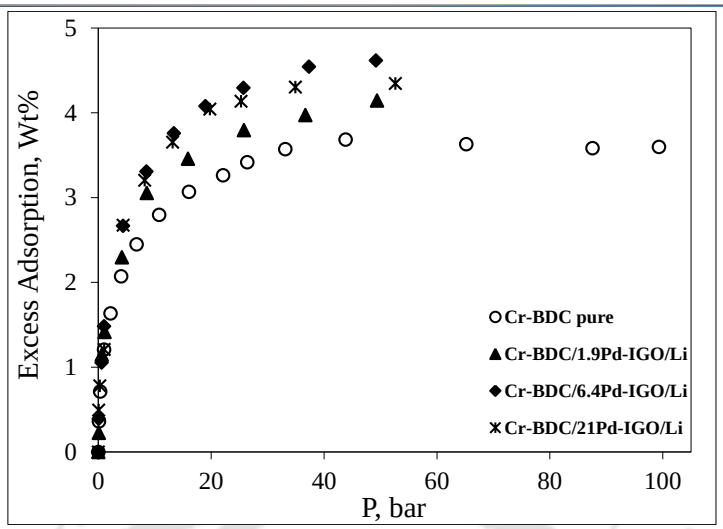

Figure 6.42: H_2 Adsorption Isotherms of Cr-BDC (92 K, circle), Cr-BDC/1.9Pd-IGO/Li (104 K, filled triangle), Cr-BDC/6.4Pd-IGO/Li (96 K, filled diamond), Cr-BDC/21Pd-IGO/Li (103 K, star).

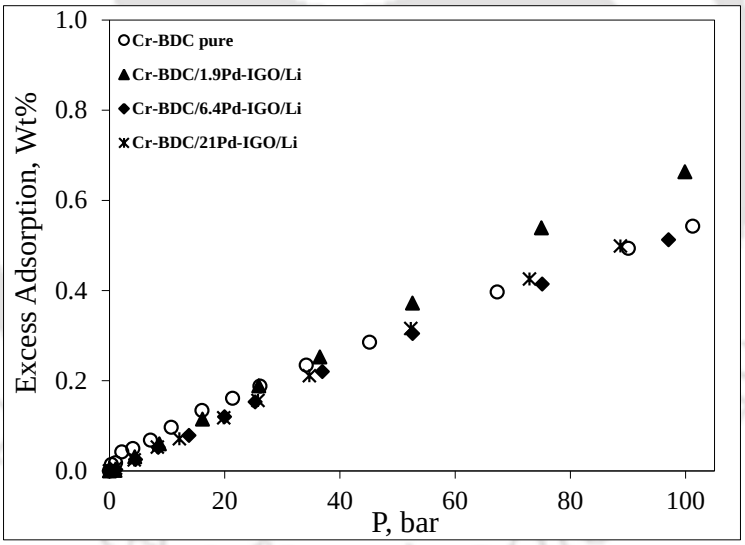

Figure 6.43: H_2 Adsorption Isotherms of Cr-BDC (297 K, circle), Cr-BDC/1.9Pd-IGO/Li (298 K, filled triangle), Cr-BDC/6.4Pd-IGO/Li (296 K, filled diamond), Cr-BDC/21Pd-IGO/Li (295 K, star).

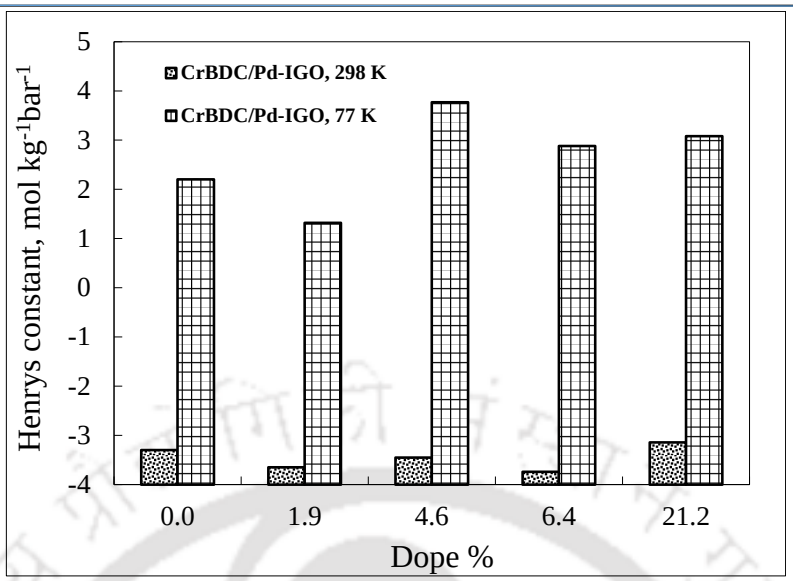

Figure 6.44: Variation of Henry's Constants for Hydrogen Adsorption with Dope % for Cr-BDC/XPd-IGO Composites

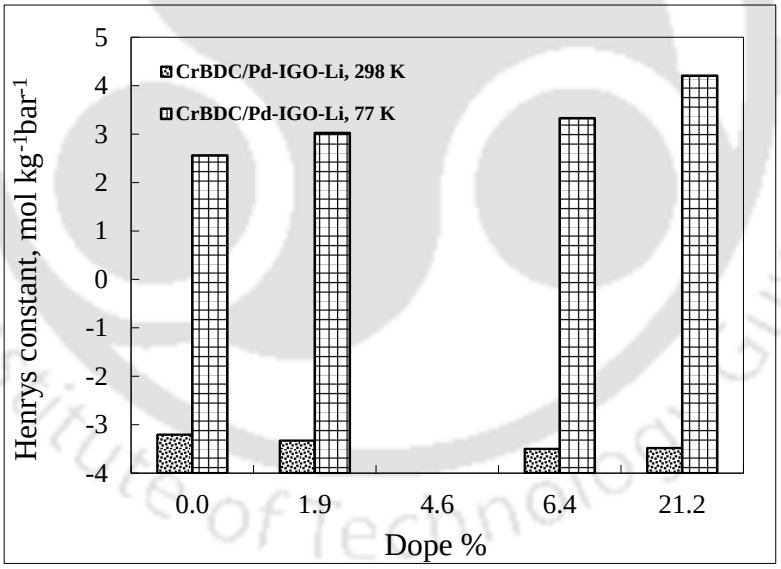

Figure 6.45: Variation of Henry's Constants for Hydrogen Adsorption with Dope % for Cr-BDC/XPd-IGO/Li Composites

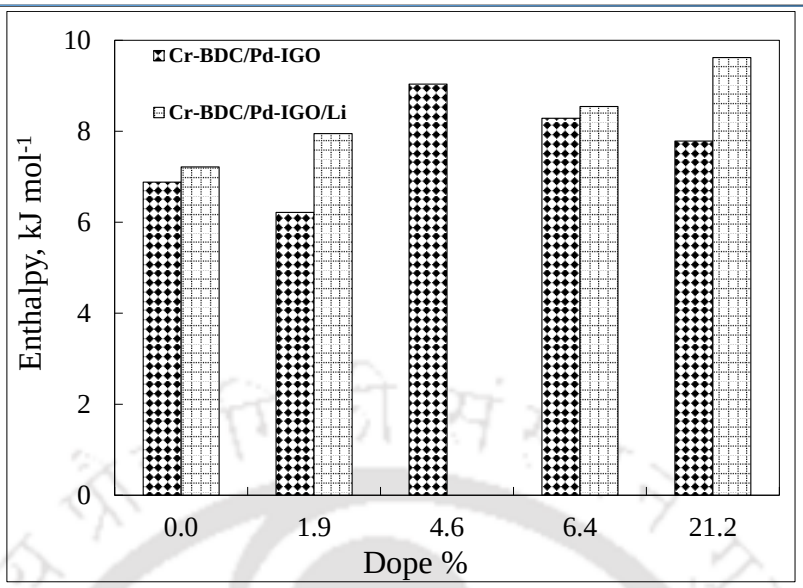

Figure 6.46: Variation of Adsorption Enthalpy for Hydrogen with Dope % for Cr-BDC/XPd-IGO Composites

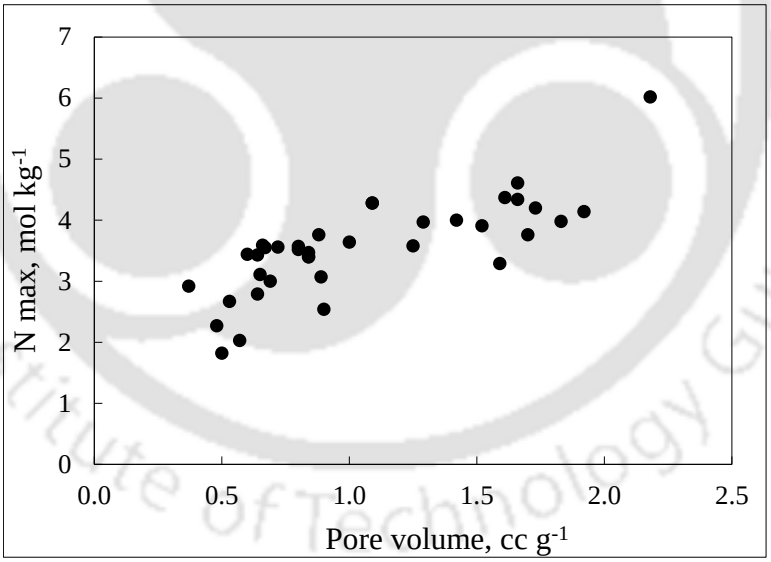

Figure 6.47: Variation of Saturation Loading of Hydrogen with Pore Volume for Various Adsorbents Considered.

Tables

Table 6.1: Composition and Doping Levels of different MOF composites

MOF/dopant	**BDC 1.6 g, Cr-salt 4 g**		**MOF/dopant**	**BTC 1g, Cu-salt 2.078 g**	
	Catalyst, mg	**Final yield, g**		**Catalyst, mg**	**Final yield, g**
Cr-BDC/1.9Pd-IGO	10	0.54	Cu-BTC/1.2AC	18.4	1.5
Cr-BDC/4.6Pd-IGO	25	0.54	Cu-BTC/1.2Pt-AC	18.4	1.57
Cr-BDC/6.4Pd-IGO	50	0.78	Cu-BTC/3.3Pt-AC	46.2	1.38
Cr-BDC/21Pd-IGO	125	0.59	Cu-BTC/7.1Pt-AC	97	1.37
Cr-BDC/1.9Pt-AC	10	0.53	Cu-BTC/11Pt-AC	153.8	1.36
Cr-BDC/1.4IGO	10	0.71	Cu-BTC/31Pt-AC	384	1.25
MOF/dopant	**BTB 854 mg, NDC 700 mg Zn-salt 2.85 g**		Cu-BTC/3.7Pd-GO	18.4	1.24
	Catalyst, mg	**Final yield, g**	Cu-BTC/3.3IGO	46.2	1.39
MOF 205/2.3PtAC	18.46	0.81	Cu-BTC/3.7Pd-IGO	46.2	1.24
			Cu-BTC/8Pd-IGO	97	1.21
			Cu-BTC/10Pd-IGO	153.8	1.5
			Cu-BTC/37Pd-IGO	384	1.04

Table 6.2: Surface area, Pore volume, Saturation uptake, Henry's Constant and Enthalpy of Adsorption for Hydrogen Uptake on Various Cu-BTC Composites

Cu-BTC Composite	**Surface area**	**Pore volume**	**N_{max}**	**Henry's Constant, 298 K**	**Henry's Constant, 100 K**	**H_{ads},**	**Surface area,**	**Pore volume,**	**N_{max},**	**Henry's Constant, 298 K**	**Henry's Constant, 100 K**	**H_{ads},**
	$m^2\ g^{-1}$	$cc\ g^{-1}$	Wt%	mol bar^{-1} K^{-1}	mol bar^{-1} K^{-1}	kJ mol^{-1}	$m^2\ g^{-1}$	$cc\ g^{-1}$	Wt%	mol bar^{-1} K^{-1}	mol bar^{-1} K^{-1}	kJ mol^{-1}
As synthesized composite							After Li doping					
Cu-BTC	1494	0.84	3.22	0.044	30.4	7.5	2132	1.09	4.13	0.043	30.1	8.2
CuBTC/1.2AC	1017	0.57	2.03	0.020	22.7	8.8	N/A	N/A	N/A	N/A	N/A	N/A
CuBTC/1.2Pt-AC	1775	0.89	3.07	0.040	13.6	7.3	1343	0.72	3.56	0.039	26.9	8.2
CuBTC/3.3Pt-AC	1153	0.65	3.11	0.027	12.8	7.7	1253	0.6	3.44	0.034	48.7	9.1
CuBTC/7.1Pt-AC	565	0.37	2.92	0.027	9.4	7.3	1305	0.8	3.52	0.036	48.2	9
CuBTC/11Pt-AC	781	0.48	2.27	0.027	7.5	7.1	1054	0.64	3.43	0.034	40.4	8.9
CuBTC/31Pt-AC	768	0.5	1.82	0.018	25.5	9.1	N/A	N/A	3.52	0.019	33.7	9.3
CuBTC/3.7Pd-GO	1252	0.69	3	0.028	20.5	8.3	1310	0.67	3.55	0.042	25	8
CuBTC/3.3IGO	1195	0.64	2.79	0.025	12.2	7.8	N/A	N/A	N/A	N/A	N/A	N/A
CuBTC/3.7Pd-IGO	1578	0.84	3.47	0.036	47.1	9	1573	0.88	3.76	0.041	40.8	8.6
CuBTC/8Pd-IGO	1838	1	3.64	0.031	51.2	9.3	1521	0.8	3.57	0.033	44.5	9
CuBTC/10Pd-IGO	1717	0.9	2.54	0.03	8.8	7.1	1090	0.66	3.59	0.035	11.9	7.3
CuBTC/37Pd-IGO	786	0.53	2.67	0.03	22.9	8.3	N/A	#N/A	N/A	N/A	N/A	#N/A

Table 6.3: Surface area, Pore volume, Saturation uptake, Henry's Constant and Enthalpy of Adsorption for Hydrogen Uptake on Various Cr-BDC Composites

Cr-BDC Composites	**Surface area**	**Pore volume**	**N_{max}**	**Henry's Constant, 298 K**	**Henry's Constant, 100 K**	**H_{ads},**	**Surface area,**	**Pore volume,**	**N_{max},**	**Henry's Constant, 298 K**	**Henry's Constant, 100 K**	**H_{ads},**
	$m^2\ g^{-1}$	$cc\ g^{-1}$	Wt%	$mol\ bar^{-1}\ K^{-1}$	$mol\ bar^{-1}\ K^{-1}$	$kJ\ mol^{-1}$	$m^2\ g^{-1}$	$cc\ g^{-1}$	Wt%	$mol\ bar^{-1}\ K^{-1}$	$mol\ bar^{-1}\ K^{-1}$	$kJ\ mol^{-1}$
As synthesized composite							After Li doping					
Cr-BDC	2927	1.52	3.91	0.049	9.1	6.89	4310	2.18	6.18	0.04	12.9	7.2
CrBDC/1.4IGO	2112	1.25	3.58	0.030	7.6	6.91	N/A	N/A	N/A	N/A	N/A	N/A
CrBDC/1.9Pt-AC	3096	1.59	3.29	0.028	1.8	5.26	2500	1.29	3.97	0.027	9.3	7.3
CrBDC/1.9Pd-IGO	3533	1.83	3.98	0.026	3.7	6.22	3687	1.92	4.14	0.036	20.6	8
CrBDC/4.6Pd-IGO	3270	1.7	3.76	0.032	43.4	9.04	N/A	N/A	N/A	N/A	N/A	N/A
CrBDC/6.4Pd-IGO	3301	1.73	4.2	0.024	17.9	8.28	3294	1.66	4.61	0.030	27.9	8.54
CrBDC/21Pd-IGO	2991	1.61	4.37	0.043	21.8	7.79	3207	1.66	4.34	0.031	67	9.6

Table 6.4: Surface Area, Pore volume, Saturation uptake, Henry's Constant and enthalpy of Adsorption for Hydrogen Uptake on MOF-205 Composite

MOF-205 Composite	**Surface area,** $m^2\ g^{-1}$	**Pore volume,** $cc\ g^{-1}$	N_{max}, Wt%	**Henry's Constant, 298 K,** $mol\ bar^{-1}\ K^{-1}$	**Henry's Constant, 100 K** $mol\ bar^{-1}\ K^{-1}$	H_{ads}, $kJ\ mol^{-1}$
MOF-205	4590	2.52	6.17	0.053	13.2	6.1
MOF-205/2.3Pt-AC	2512	1.42	4	0.029	12.8	6.9

CHAPTER 7

Conclusions and Future Scope

7.1. Conclusions

The aim of this study is to systematically investigate various metal organic frameworks (MOFs) for their hydrogen adsorption characteristics. Adsorption measurements for hydrogen have been performed for a wide range of temperature and pressure on selected MOF materials and MOF composites. The hybrid porous materials like MOFs were modified with metals such as Li, Pt, Pd in order to enhance their hydrogen adsorption capacities. We believe the results in this work provide useful insights into hydrogen adsorption in modified metal organic frameworks and can serve as a useful reference for development and modification of porous materials for hydrogen adsorption.

A variety of MOFs viz. Zn-BDC (IRMOF-1), Ni-DABCO, Mg/Co-DOBDC (MOF 74), MOF-205, Cu-BTC (or, HKUST-1) and Cr-BDC (or, MIL-101) were successfully synthesized. Zn-BDC, MOF-205 and Ni-DABCO contain coordinatively saturated metal sites and have a large variation in surface areas (623 m^2g^{-1} for Zn-BDC to 4590 m^2g^{-1} for MOF-205). The other series of MOFs contain coordinatively unsaturated metal sites (Cu-BTC, Cr-BDC, Mg-DOBDC, Co-DOBDC), while their surface areas vary between ~1000 m^2g^{-1} for DOBDC series to 2927 m^2g^{-1} for Cr-BDC. These MOFs were carefully chosen to cover a wide range of pore sizes, surface area and pore volumes in addition to differences in their surface properties. For sake of comparison a mesoporous silica material MCM-41 (surface area 919 m^2 g^{-1}) was also investigated for its hydrogen adsorption characteristics. H_2 adsorption isotherms were measured gravimetrically using a

magnetic suspension balance (Rubotherm) in a series of experiments on these adsorbents. The following is a summary of major findings in this work.

1) Initially, the experimental protocol is validated by successful measurement of hydrogen adsorption on Pd nanoparticles at 293 K, 324 K, 364 K and 392 K in the pressure range of 0-26 bar. Pd is a model material for hydrogen sorption; in addition, the experience obtained in synthesis procedure for Pd nanoparticles was be utilized later for doping Pd on graphene oxide. Maximum adsorption of 0.58 wt% was observed at 324 K and 20 bar. Results are within the range of other reports in literature.

2) Multi temperature adsorption measurements (at various temperatures between ~ 90 K and 298 K) have been carried out between 0 and 100 bar. Saturation loading of hydrogen on except Zn-BDC and MOF 205 showed saturation capacity of 3-4 wt% at 90-100 K. Zn-BDC gets saturated with <1 wt%; whereas, MOF-205 saturates at ~6 wt% at largely depending on the difference of their pore volume. At saturation conditions pore volume plays a crucial role.

3) The enthalpies of adsorption at zero coverage (Δh_{ads}) for the adsorbents studied vary between 5.6 kJ mol^{-1} (Ni-DABCO) and 10.1 kJ mol^{-1} (Co-DOBDC). Whereas Henry's constant at 91 K for Co-DOBDC was >450 mol bar^{-1} kg^{-1}. Ni-DABCO seems to have least enthalpy of adsorption because of saturated metal sites. This is similar to silica based material MCM-41. MOFs with unsaturated metal sites such as DOBDC series have better enthalpies of adsorption. While very small number of such adsorption sites are also present in case of Cu-BTC and Cr-BDC frameworks, either they are occupied well below our experimental limits or not fully accessible and may be hindered due to presence of

left over solvent molecules from the synthesis procedure. Presence of larger number of open metal sites tend to enhance adsorption enthalpy incase for H_2 on Co-DOBDC.

4) At room temperature, MOF-205 has the highest value of Henry's constant than other saturated MOFs. This is to be expected due to large porosity in this framework (thereby the framework density is very small); low framework densities translate into better specific adsorption uptake capacities although on volumetric basis the capacities tend to be poor. In case of unsaturated MOFs, Mg-DOBDC has highest Henry's constant at room temperature; again although Co-DOBDC has better affinity for hydrogen (as evident from enthalpies), the framework density is lower for Mg-DOBDC due to lower framework density; the contribution of Mg to the mass of the framework is significantly lower than that of Co. However, if one compares the Henry's constant on molecules adsorbed per unit cell basis, both frameworks compare well with one another.

5) At low to intermediate loadings well below the saturation limit, coordinatively unsaturated metal sites play a significant role; MOFs with such sites exhibit better adsorption characteristics. This consideration will be important ion design of adsorbents for hydrogen storage at cryogenic temperatures; pore volume (and hence saturation hydrogen uptake) will not be governing criteria at these conditions.

6) The net adsorption framework which is better suited to evaluate the actual adsorption capacity of a storage vessel filled with solid adsorbent since the loss of tank volume due to impenetrable solid adsorbent is readily accounted. A positive net adsorption value indicates enhancement of hydrogen storage capacity of the vessel. A 30 % enhancement is observed with Mg-DOBDC as adsorbent for storing hydrogen at ~ 190 K, while this reduces to ~ 20 % at room temperature. The volume of the tank containing Mg-DOBDC

adsorbent necessary to store 1 kg H2 at 100 bar is about 55 liters at 190 K (compared to about 80 liters without the adsorbent).

7) Cu-BTC and Cr-BDC are some of the well-studied MOFs in literature. Cr-BDC has large pore volume and relatively stable than most other MOFs. Cu-BTC has relatively small pores which result in better interactions with adsorbate molecules. As a result, these two MOFs were chosen for post synthesis modifications to enhance hydrogen adsorption capacity. First, these MOFs were subjected to doping with light weight metals (Li in this case) to enhance hydrogen sorption. Li doping on the Cu-BTC and Cr-BDC MOFs was achieved by soaking the as synthesized MOF in a methanol solution of LiCl salt for prolonged period. Characterization indicates Li/Cu ratio of ~ 0.01 in case of doped MOF Cu-BTC/Li and a Li/Cr ratio of ~ 0.07 for Cr-BDC/Li. The surface area and pore volume of both these MOFs is the best reported till date. Although attempts were made in literature to dope Li in both Cu-BTC and Cr-BDC frameworks, such results for significantly enhanced surface area, pore volume and hydrogen uptake are not reported. The hydrogen adsorption uptakes at saturation increase from 3.4 to 4.27 wt% for Cu-BTC and 3.91 to 6.02 wt% for Cr-BDC (~ 90 K). The saturation hydrogen uptake on Cu-BTC/Li even exceeds that of undoped Cr-BDC (which has a much higher pore volume) and to the best of our knowledge highest reported till date on a MOF based on Cu-BTC. Similarly, the Cr-BDC/Li exhibits comparable pore volume and hence saturation uptake to best reported one so far in literature (obtained via an NH_4F wash of the sample).

8) Li doped u-BTC and Cr-BDC MOFs exhibit improved enthalpies of adsorption at zero loading by about 0.3-0.7 kJ mol^{-1}, which matches well with results from Li doping in other frameworks reported in literature. It is widely reported in literature that although Li binding energies with hydrogen are much higher, the binding energies significantly fall

when Li complexes with other atoms in the framework. As a result, it probably only enhances the induced dipole interactions of the hydrogen molecules inside the pores resulting in modest increase of adsorption enthalpies. The marginal increase in the adsorption enthalpies observed for the Li doped samples indicate that Li probably forms a complex with organic linkers in the framework.

9) The Cu-BTC and Cr-BDC MOF composites consisting of Palladium supported on Graphene Oxide (Pd-IGO) or Platinum on Activated Carbon (Pt-AC) were synthesized by dispersing a pre-determined quantity (typically between 1 and 30 wt%) of the dopant in the reaction mixture used for regular MOF synthesis. While 5 wt% Pt on AC is procured directly, Pd-IGO (~ 3.2 wt % Pt on IGO) was synthesized in our laboratory. The composites of MOFs consisting of transition metals doped on carbonaceous materials (Cu-BTC/Pt-AC, Cr-BDC/Pd-IGO etc.) perform better than composites of MOFs with carbonaceous materials alone (Cu-BTC/AC or Cr-BDC/IGO).

10) In the case of Cu-BTC/Pt-AC composites, the hydrogen uptake on composites is lower than that on pure Cu-BTC and falls off rapidly at higher amounts of Pt-AC in the composites (more than 45 % loss of capacity in case of Cu-BTC/31Pt-AC). However, after doping these composites with Li i.e. in case of Cu-BTC/Pt-AC/Li samples, the hydrogen loadings at different levels of Pt-AC content in the composites are comparable. However the loadings of Cu-BTC/Pt-AC/Li composites were still lower than that on Cu-BTC/Li.

11) The composites of Cu-BTC/Pd-IGO perform better at comparable levels of doping in the composites. In fact some of the Cu-BTC /Pd-IGO composites have marginally higher (5-10%) hydrogen uptake than that of pure Cu-BTC. Li doping of these composites

further enhances the hydrogen sorption. The enhancement in adsorption enthalpy at zero coverage is about 1.5 kJ mol^{-1}, observed in samples with higher contents of Pd-IGO (Cu-BTC/37 Pd-IGO for example) in the composite. At low concentrations of Pd-IGO, the number of Pd sites is probably too small (Pd/Cu ratio in Cu-BTC/3.7 Pd-IGO is ~0.01 and ~ 0.1 for Cu-BTC/37 Pd-IGO).

12) Due to larger pore volume in Cr-BDC, the additional mass of the substrate does not significantly decrease the gravimetric uptake in Cr-BDC/Pd-IGO composites (even at high Pd-IGO contents in the composites) as opposed to the results in Cu-BTC/Pd-IGO composites. Even in this case, the increase in adsorption enthalpies at zero coverage are comparable ~ 1- 1.5 kJ mol^{-1}, especially at high Pd-IGO content in the composites.

14) None of the results for hydrogen uptake on MOF composites containing Pd or Pt result in enhanced hydrogen sorption at room temperature to the levels indicated due to the so-called 'spillover' phenomenon. At best, in some composites, the enhancement at room temperature was only marginal. Spillover effect although well documented in literature is poorly reproducible, and several groups indicated failure to reproduce it in their laboratories.

15) The increase in enthalpies of adsorption due to transition metal doping are much higher than those due to Li doping; however, the gravimetric hydrogen uptake capacities of Li doped samples are superior partially due to negative effect of additional mass of the substrate in the composites. Li doping of most composites although improves their hydrogen sorption, none of them match the capacities obtained by pure MOFs doped with Li.

7.2. Future Scope

There are several areas which merit attention of scientific community for understanding the hydrogen adsorption behavior in these interesting materials. At room temperature or above Pd nanoparticle seems useful whereas MOFs seem to be promising for their role in hydrogen storage at cryogenic/low temperature.

[A] Synthesis conditions and post-synthesis activation methods are directly related to the physical properties of the MOFs, most importantly their specific surface area, thermal and chemical stability. The role of various solvents during activation of MOF samples needs to be thoroughly understood to effectively increase their surface area, pore volume and hence the hydrogen adsorption capacity.

[B] The Li doping levels reported in this work are within the range of other reports in literature based on different MOFs. However, the effect of Li doping on hydrogen adsorption capacity is not close to some of the theoretical reports; effective Li doping techniques to enhance hydrogen uptake in MOFs to levels predicted from theory /simulations still remains elusive.

[C] While some of the MOF composites exhibit better hydrogen uptake capacities compared to pure MOFs, additional mass of the substrates greatly offsets the advantage offered by doping, thereby significant enhancements in gravimetric uptake capacity is not seen. This may probably be overcome, if composites are made from MOFs with larger pore volumes (in excess of 2 cm^3 mol^{-1}) such as MOF-205. While attempts in this work to make composites of MOF-205 were unsuccessful, even pure MOF-205 is quite sensitive and degrades upon exposure to atmosphere for a short time. Attempts should be made to synthesize composites of other MOFs with large pore volumes, where the effect of heavy

metal incorporation into the framework on their hydrogen sorption capacities is likely to be better.

[D] In addition to the metals (Li, Pt and Pd considered in this work) it would be interesting to see the effect of similar techniques using other metals. A careful analysis on the optimum temperature range for hydrogen storage for each of the dopants is needed. Only two extreme temperatures were considered in this work (~ 90 K and room temperature).

[E] While a systematic study was carried out in this work on hydrogen uptake of various composites, by varying type and amount of the substrate, such studies are very few and limited. The actual mechanism and reasons for enhanced surface area, pore volume and uptake capacity are not understood. It would be interesting if spillover effect can be observed in these materials on a consistent basis across different laboratories; it would greatly improve the chances for success of MOFs in hydrogen storage applications.

[F] While none of the existing adsorbents reach the DoE targets, considerable progress is being made in the right direction although in incremental steps. Eventually, the adsorbent materials need to be evaluated for actual storage processes; stability of these materials (especially at high pressures), cyclability and deterioration in hydrogen uptake capacities need to be carefully evaluated. Development of storage and delivery systems at cryogenic conditions is another area which needs focus.

RFERENCES

Web addresses

1. DOE (2007a) DOE Hydrogen Program 2007 Annual Report on www.hydrogen.energy.gov/annual_progress07.html
2. DOE (2007b) article NREL/MP-150–42220 on www.nrel.gov/docs/gen/fy08/42220.pdf
3. International Energy Agency (IEA), Hydrogen Implementing Agreement, Paris http://www.iea.org/publications/freepublications/publication/hydrogen.pdf
4. Alternative Fuels Data Centre (AFDC), U.S. Department of Energy http://www.afdc.energy.gov/
5. Energy Efficiency and Renewable Energy (EERE), U.S. Department of Energy http://www1.eere.energy.gov/hydrogenandfuelcells/pdfs/fct_h2_production.pdf
6. Toyota Motor Corporation http://www.toyota-global.com/innovation/environmental_technology/fuelcell_vehicle/
7. Dyntek Solutions, Prince Edward Island, Canada http://www.gov.pe.ca/photos/original/dev_solutions.pdf
8. Thermo Physical Properties, National Institute of Standards and Technology http://webbook.nist.gov
9. Amrita Virtual Laboratory, Amrita Vishwa Vidyapeetham, Coimbatore, India http://amrita.vlab.co.in
10. Rubotherm, Germany http://www.rubotherm.com/rubotherm-gmbh-en.html

Journals, Book Chapters and Presentations are in Alphabetical Order

A

1. Andrew, R. M.; Yaghi, O. M. *Metal-Organic Frameworks with Exceptionally High Capacity for Storage of Carbon Dioxide at Room Temperature*. J. Am. Chem. Soc., **2005**,127, 17998.

2. Arnold, M.; Kortunov, P.; Jones, D. J.; Nedellec, Y.; Kärger, J.; Caro, J. *Oriented Crystallisation on Supports and Anisotropic Mass Transport of the Metal-Organic Framework Manganese Formate*. Eur. J. Inorg. Chem., **2007**, 2007, 60.

3. Acatrinei, A. I.; Hartl, M. A.; Eckert, J.; Falcao, E. H. L.; Chertkov, G.; Daemen, L. L. *Hydrogen Adsorption in the Ti-Doped Mesoporous Silicate SBA-15*. J. Phys. Chem. C, **2009**, 113, 15634.

4. Attfield, M. P. *Microporous materials*. Science Progress, **2002**, 85, 319.

5. Arstad, B.; Fjellvåg, H.; Kongshaug, K.; Swang, O.; Blom, R. *Amine functionalized metal organic frameworks (MOFs) as adsorbents for carbon dioxide.* Adsorption, **2008,** *14,* 755.

B

1. Bae, Y. S.; Snurr, R. Q. *Molecular simulations of very high pressure hydrogen storage using metal–organic frameworks*. Microporous Mesoporous Mater., **2010**, 135, 178.

2. Bisson, L.; Boissiere, C.; Nicole, L.; Grosso, D.; Jolivet, J. P.; Thomazeau, C.; Uzio, D.; Berhault, G.; Sanchez, C. *Formation of Palladium Nanostructures in a Seed-Mediated*

Synthesis through an Oriented-Attachment-Directed Aggregation. Chem. Mater., **2009**, 21 2668.

3. Barrett, E. P.; Joyner, L. G.; Halenda, P. P. *The determination of pore volume and area distributions in porous substances; computations from nitrogen isotherms*. J Am. Chem. Soc., **1951,** 73, 373.

4. Bhatia, S. K.; Myers, A. L. *Optimum Conditions for Adsorptive Storage.* Langmuir, **2006**, 22, 1688.

5. Bogdanovic, B.; Schwickardi, M. *Ti-doped alkali metal aluminium hydride as potential novel reversible hydrogen storage materials.* J. Alloys Comp., **1995**, 253-254, 1.

6. Budd, P.; Butler, A., Selbie, J., Mahmood, K.; McKeown, N. B.; Ghanem, B.; Msayib, K.; Book, D.; Walton, A. *The potential of organic polymer-based hydrogen storage materials.* Phys. Chem. Chem. Phys., **2007**, 9, 1802.

C

1. Cai, D. Y.; Song, M. *Preparation of fully exfoliated graphite oxide nanoplatelets in organic solvents*. J. Mater. Chem., **2007**, 17, 3678.

2. Caskey, S.R.; Wong-Foy, A. G.; Matzger, A. J. *Dramatic Tuning of Carbon Dioxide Uptake via Metal Substitution in a Coordination Polymer with Cylindrical Pores.* J. Am. Chem. Soc., **2008**, 130, 10870.

3. Chun, H.; Jung, H.; Koo, G.; Jeong, H.; Kim, D. K. *Efficient hydrogen sorption in 8-connected MOFs based on trinuclear pinwheel motifs.* Inorg. Chem., **2008**, 47, 5355.

4. Chen, B.; Eddaoudi, M.; Hyde, S. T.; Keefe, M. O.; Yaghi, O. M. *Inter woven metal-organic framework on a periodic minimal surface with extra-large pores*. Science, **2001**, 291, 1021.

5. Chowdhury, P.; Bikkina, C.; Meister, D.; Dreisbach, F.; Gumma, S. *Comparison of adsorption isotherms on Cu-BTC metal organic frameworks synthesized from different routes*. Microporous Mesoporous Mater., **2009**, 117, 406.

6. Chowdhury, P.; Bikkina, C.; Gumma, S. *Adsorption properties of the chromium based metal organic framework MIL-101*. J. Phys. Chem. C., **2009**, 113, 6616.

7. Chowdhury, P. *Gas Adsorption on Cu-BTC and Cr-BDC Metal Organic Frameworks (MOFs), PhD Dissertation*, **2010**, Indian Institute of Technology Guwahati, India

8. Calvo, A. M.; Perez, E. G.; Castillo, J. M.; Calero, S. *Molecular simulations for adsorption and separation of natural gas in IRMOF-1 and Cu-BTC metal-organic frameworks*. Phys. Chem. Chem. Phys., **2008**, 10, 7085.

9. Chui, S. S. Y.; Lo, S. M. F.; Charmant, J. P. H.; Orpen, A. G.; Williams, I. D. *A chemically functionalizable nanoporous material [$Cu_3(TMA)_2(H2O)_3$]n.* Science, **1999**, 283, 1148.

10. Cheng, L. S.; Yang, R. T. *Improved Horvath-Kawazoe equations including spherical pore models for calculating micropore size distribution*. Chem. Eng. Science, **1994,** 49, 2599.

11. Cheon, Y. E.; Suh, M. P. *Selective gas adsorption in a microporous metal–organic framework constructed of* $Co^{II}{}_4$ *clusters*. Chem. Commun., **2009**, 45, 2296.

12. Campesi, R.; Cuevas, F.; Leroy, E.; Hirscher, M.; Gadiou, R.; Vix-Guterl, C.; Latroche, M. *In situ synthesis and hydrogen storage properties of PdNi alloy nanoparticles*

in an ordered mesoporous carbon template. Microporous Mesoporous Mater., **2009**, 117, 511.

13. Campesi, R.; Cuevas, F.; Latroche, M.; Hirscher, M. *Hydrogen spillover measurements of unbridged and bridged metalorganic frameworks - revisited.* Phys. Chem. Chem. Phys., **2010**, 12, 10457.

14. Cheon, Y. E.; Suh, M. P. *Enhanced hydrogen storage by palladium nanoparticles fabricated in a redox-active metal–organic framework.* Angew. Chem., Int. Ed. **2009**, 48, 2899.

15. Conner, W. C.; Falconer J. L. *Spillover in heterogeneous catalysis.* Chem. Rev., **1995**, 95, 759.

16. Czaja, A. U.; Trukhan, N.; Muller, U. *Industrial applications of Metal organic Frameworks*. Chem. Soc. Rev., **2009**, 38, 1284.

D

1. Deng, W. Q; Xu, X; Goddard, W. A. *New Alkali Doped Pillared Carbon Materials Designed to Achieve Practical Reversible Hydrogen Storage for Transportation*. Phys. Rev. Lett., **2004**, 92, 166103.

2. Dinca, M.; Long, J. R. *Strong H_2 Binding and Selective Gas Adsorption within the Microporous Coordination Solid $Mg_3(O_2C\text{-}C_{10}H_6\text{-}CO_2)_3$* J. Am. Chem. Soc., **2005**, 127, 9376.

3. Dinca, M.; Dailly, A.; Liu, Y.; Brown, C. M.; Neumann, D. A.; Long, J. R. *Hydrogen Storage in a Microporous Metal-Organic Framework with Exposed Mn^{2+} Coordination Sites.* J. Am. Chem. Soc., **2006**, 128, 16876

4. Dinca, M.; Long, J. R.; *Hydrogen Storage in Microporous Metal–Organic Frameworks with Exposed Metal Sites.* Angew. Chem. Int. Ed. **2008**, 47, 6766.

5. Dinca, M.; Long, J. R.; *High-Enthalpy Hydrogen Adsorption in Cation-Exchanged Variants of the Microporous Metal-Organic Framework* $Mn_3[(Mn_4Cl)_3(BTT)_8(CH_3OH)_{10}]_2$. J. Am. Chem. Soc., **2007,** 129, 11172.

6. Dietzel, P. D. C.; Panella, B.; Hirscher, M.; Blom, R.; Fjellvag, H. *Hydrogen adsorption in a nickel based coordination polymer with open metal sites in the cylindrical cavities of the desolvated framework.* Chem. Commun., **2006,** 2006, 959.

7. Dietzel, P. D. C.; Besikiotis, V.; Blom, R. *Application of metal–organic frameworks with coordinatively unsaturated metal sites in storage and separation of methane and carbon dioxide*. J. Mater. Chem., **2009,** *19*, 7362.

8. Do, D. D. *Adsorption Analysis: Equilibria and Kinetics*, Imperial College Press, London, **1998**.

9. Dubinin, M. M., *The potential theory of adsorption of gases and vapors for adsorbents with energetically nonuniform surfaces*. Chem. Rev., **1960,** 60, 235.

10. Duren, T., Millange, F.; Fe´rey, G.; Walton, K. S., Snurr, R. Q. *Calculating Geometric Surface Areas as a Characterization Tool for Metal-Organic Frameworks*. J. Phys. Chem. C., **2007**, 111, 15350.

11. Dybtsev, D. N.; Chun, H.; Kim, K. Rigid and Flexible: *A Highly Porous Metal–Organic Framework with Unusual Guest-Dependent Dynamic Behavior*. *Angew. Chem., Int. Ed.,* **2004,** *43,* 5033.

E

1. Eddaoudi, M.; Li, H.; Yaghi, O. M. *Highly porous and stable metal organic frameworks: structure design and sorption properties*. J. Am. Chem. Soc., **2000**, 122, 1391.

2. Egerton, R. F. *Physical principles of electron microscopy*, Springer, Germany, **2005**.

F

1. Farha, O. K.; Yazaydin, A. O.; Eryazici, I.; Malliakas, C. D.; Hauser, B. G.; Kanatzidis, M. G.; Nguyen, S. T.; Snurr, R. Q.; Hupp, J. T. *De novo synthesis of a metal–organic framework material featuring ultrahigh surface area and gas storage capacities.* Nat. Chem., **2010**, 2, 944.

2. Fletcher, A. J.; Thomas, K. M.; Rosseinsky, M. J. *Flexibility in metal organic framework materials: Impact on sorption properties*. J. Solid State Chem., **2005**, 178, 2491.

3. Ferey, G.; Latroche, M.; Serre, C.; Millange, F.; Loiseau, T.; Guégan, A. P. *Hydrogen adsorption in the nanoporous metal-benzenedicarboxylate M(OH)(O_2C–C_6H_4–CO_2) (M = Al^{3+}, Cr^{3+}), MIL-53*. Chem. Commun., **2003**, 2003, 2976.

4. Ferey, G.; Mellot-Draznieks, C.; Serre, C.; Millange, F.; Dutour, J.; Surble, S.; Margiolaki, I. *A Chromium Terephthalate–Based Solid with Unusually Large Pore Volumes and Surface Area.* Science, **2005**, 309, 2040

5. Fe´rey, G. *Hybrid porous solids: past, present, future.* Chem. Soc. Rev., **2008**, 37, 191.

6. Forster, P. M.; Eckert, J.; Chang, J. S.; Park, S. E.; Ferey, G.; Cheetham, A. K. *Hydrogen adsorption in nanoporous nickel(II) phosphates*. J. Am. Chem. Soc., **2003**, 125, 1309.

7. Frost, H.; Duren, T.; Snurr, R. Q. *Effects of Surface Area, Free Volume, and Heat of Adsorption on Hydrogen Uptake in Metal-Organic Frameworks.* J. Phys. Chem. B, **2006**, 110, 9565.

8. Frost, H.; Snurr, R. Q. *Design Requirements for Metal-Organic Frameworks as Hydrogen Storage Materials.* J. Phys. Chem. C, **2007**, 111 (50), 18794.

9. Furukawa, H.; Ko, N.; Go, Y. B.; Aratani, N.; Choi, S. B.; Choi, E.; Yazaydin, A. O.; Snurr, R. Q.; Keeffe, M. O.; Kim, J.; Yaghi O. M. *Ultrahigh porosity in metal-organic frameworks*. Science, **2010**, 329, 424.

G

1. Gao, L.; Yue, W.; Tao, S.; Fan, L. *A novel strategy for preparation of graphene-Pd, Pt composite and its enhanced electrocatalytic activity for alcohol oxidation,* Langmuir, **2013**, 29, 957.

2. Guisnet, M.; Gilson, J. P. *Zeolites for Cleaner Technologies*. Imperial College Press, London, **2002**.

3. Gutierrez, I.; Dıaz, E.; Ordonez S. *Consequences of cavity size and palladium addition on the selective hydrogen adsorption in isoreticular metal-organic frameworks.* Thermochim. Acta., **2013**, 567, 79.

4. Gascon, J.; Aguado, S.; Kapteijn, F. *Manufacture of dense coatings of $Cu_3(BTC)_2$ (HKUST-1) on a-alumina.* Microporous Mesoporous Mater., **2008**, 113, 132.

5. Geim, A. K.; Novoselov, K. S. *The rise of graphene*. Nature Materials, **2007**, 6, 183.

6. Gao, S.; Zhao, N.; Shu, M.; Che, S. *Palladium nanoparticles supported on MOF-5: A highly active catalyst for a ligand- and copper-free Sonogashira coupling reaction*. Applied Catalysis A: General; **2010**, 388; 196

7. Gumma, S.; Talu, O. *Net Adsorption: A Thermodynamic Framework for Supercritical Gas Adsorption and Storage in Porous Solids.* Langmuir, **2010**, 26, 17013.

8. Ghoufi, A.; Deschamps, J.; Maurin, G. *Theoretical hydrogen cryostorage in doped MIL-101(Cr) metal−organic frameworks.* J. Phys. Chem. C, **2012**, 116, 10504.

H

1. Hamon, L.; Serre, C,; Devic, T.; Loiseau, T.; Millange, F.; Fe rey, G.; Weireld G.D. *Comparative Study of Hydrogen Sulfide Adsorption in the MIL-53(Al, Cr, Fe), MIL-47(V), MIL-100(Cr), and MIL-101(Cr) Metal-Organic Frameworks at Room Temperature,* J. Am. Chem. Soc., **2009**, 131, 8775.

2. Huot, J.; Enoki, H.; Akiba, E. *Synthesis, phase transformation, and hydrogen storage properties of ball-milled* $TiV_{0.9}Mn_{1.1}$. J. Alloys comp., **2008**, 453, 203.

3. Himsl, D.; Wallacher, D.; Hartmann, M. *Improving the Hydrogen-Adsorption Properties of a Hydroxy-Modified MIL-53(Al) Structural Analogue by Lithium Doping.* Angew. Chem., Int. Ed., **2009**, 48, 4639.

4. Han, S. S.; Goddard, W. A. *Lithium-Doped Metal-Organic Frameworks for Reversible* H_2 *Storage at Ambient Temperature.* J. Am. Chem. Soc., **2007**, 129, 8422.

5. Han, S. S.; Goddard, W. A. High H_2 *Storage of Hexagonal Metal -Organic Frameworks from First-Principles-Based Grand Canonical Monte Carlo Simulations.* J. Phys. Chem. C., **2008**, 112, 13431.

6. Hirsher, M.; Panella, B. *Hydrogen physisorption in metal organic porous crystals.* Adv. Mater., **2005**, 17, 538

7. Hong, D. Y.; Hwanag, Y. K.; Serre, C.; Ferey, G.; Chang, J. S. *Porous chromium terephthalate MIL-101 with coordinatively unsaturated sites: surface functionalization, encapsulation, sorption and catalysis.* Adv. Funct. Mater., **2009**, 19, 1537.

8. Higuchi, K.; Yamamoto, K.; Kajioka, H.; Toiyama, K.; Honda, M.; Orimoc, S.; Fujii, H. *Remarkable hydrogen storage properties in three-layered Pd/Mg/Pd thin Films.* J. Alloys Comp. **2002**, 330–332, 526.

9. Himsl, D.; Wallacher, D.; Hartmann, M. *Improving the Hydrogen-Adsorption Properties of a Hydroxy-Modified MIL-53(Al) Structural Analogue by Lithium Doping.* Angew. Chem., Int. Ed. **2009**, 48, 4639.

10. Horvath, G.; Kawazoe, K. *Method for the Calculation of Effective Pore-Size Distribution in Molecular-Sieve Carbon*. J. Chem. Eng. Japan, **1983,** 16(6), 470.

11. Houk R. J. T.; Jacobs, B. W.; Gabaly, F. E.; Chang, N. N,.; Talin, A. A.; Graham, D. D.; House, S. D.; Robertson, I. M.; Allendorf, M. D. *Silver cluster formation, dynamics, and chemistry in metal-organic frameworks*. Nano Lett., **2009**, 9, 3413.

12. Hermes, S.; Schroter, M. K.; Schmid, R.; Khodeir, L.; Muhler, M.; Tissler, A.; Fischer, R. W.; Fischer, R. A. *Metal@MOF: Loading of Highly Porous Coordination Polymers Host Lattices by Metal Organic Chemical Vapor Deposition.* Angew. Chem., Int. Ed., **2005**, 44, 6237.

13. Hummers, W. S.; Offeman, R. E. *Preparation of Graphitic Oxide.* J. Am. Chem. Soc., **1958**, 80, 1339.

14. Hermes, S.; Zacher, D.; Baunemann, A.; Wöll, C.; Fischer, R. A. *Selective Growth and MOCVD Loading of Small Single Crystals of MOF-5 at Alumina and Silica Surfaces Modified with Organic Self-Assembled Monolayers.* Chem. Mater., **2007**, 19, 2168.

15. Horinouchi, S.; Yamanoi, Y.; Yonezawa, T.; Mouri, T.; Nishihara, H. *Hydrogen Storage Properties of Isocyanide-Stabilized Palladium Nanoparticles.* Langmuir, **2006**, 22 1880-1884.

J

1. Jahan, M.; Bao, Q.; Yang, J.-X.; Loh, K. P. *Structure-Directing Role of Graphene in the Synthesis of Metal-Organic Framework Nanowire.* J. Am. Chem. Soc., **2010**, 132, 14487.

2. Janot, R.; Darok, X.; Rougier, A.; Aymard, L.; Nazri, G. A.; Tarascon, J. M.; *Hydrogen sorption properties for surface treated MgH_2 and Mg_2Ni alloys.* J. Alloys Comp., **2005**, 404–406, 293.

3. *de*-Jongh, P. E.; Adelhelm, P. *Nanoparticles and 3D supported nanomaterials*, WILEY-VCH, **2009**, 293.

4. Jhung, S. H.; Yoon, J. W.; Kim, H. K.; Chang J. S. *Low temperature adsorption of hydrogen on nanoporous materials.* Bull. Korean Chem. Soc., **2005**, 26, 1075.

K

1. Kazansky. V. B.; Borovkov. V.; Yu, Serich. A; Karge, H. G.; *'Low temperature hydrogen adsorption on sodium forms of faujasites: barometric measurements and drift spectra'*. Microporous Mesoporous Mater., **1998**, 22, 251.

2. Koh, K.; Wong-Foy, A. G.; Matzger, A. J. *A Crystalline Mesoporous Coordination Copolymer with High Microporosity.* Angew. Chem., Int. Ed., **2008**, 47, 677.

3. Koh, K.; Wong-Foy, A. G.; Matzger, A. J. *Coordination Copolymerization Mediated by $Zn_4O(CO_2R)_6$ Metal Clusters: a Balancing Act between Statistics and Geometry.* J. Am. Chem. Soc., **2010**, 132, 15005.

4. Krungleviciute, V.; Lask, K.; Heroux, L.; Migone, A. D.; Lee, J. Y.; Li, J.; Skoulidas, A. *Argon Adsorption on Cu_3(Benzene-1,3,5-tricarboxylate)$_2(H_2O)_3$ Metal-Organic Framework*, Langmuir, **2007**, **23**, 3106.

5. Kim, J.; Chen, B.; Reineke, T. M.; Li, H.; Eddaoudi, M.; Moler D. B.; O'Keeffe, M.; Yaghi, O. M. *Assembly of metal-organic frameworks from large organic and inorganic secondary building units: new examples and simplifying principles for complex structures. J. Am. Chem. Soc.* **2001,** *123,* 8239.

6. Kitagawa, S.; Kitaura R.; Noro, S. *Functional porous coordination polymers*. Angew. Chem., Int. Ed., **2004**, 43, 2334.

7. Kaye, S. S.; Long, J. R. *Matrix Isolation Chemistry in a Porous Metal-Organic Framework: Photochemical Substitutions of N_2 and H_2 in Zn_4O[(η6-1,4-Benzenedicarboxylate)$Cr(CO)_3]_3$* . J. Am. Chem. Soc., **2008**, 130, 806.

8. Klontzas, E.; Mavrandonakis, A.; Tylianakis, E.; Froudakis, G. E. *Improving Hydrogen Storage Capacity of MOF by Functionalization of the Organic Linker with Lithium Atoms.* Nano Lett., **2008**, 8, 1572.

9. Kumar, R.; Jayaramulu, K.; Maji, T. K.; Rao, C. N. R. *Hybrid nanocomposites of ZIF-8 with graphene oxide exhibiting tunable morphology, significant CO_2 uptake and other novel properties.* Chem. Commun., **2013**, 49, 4947

10. Kishore, S.; Nelson, J. A.; Adair, J. H.; Eklund, P. C. *Hydrogen storage in spherical and platelet palladium nanoparticles.* J. Alloys Comp., **2005**, 389, 234.

11. Kuji, T.; Mastumura, Y.; Uchida, H,; Aizawa, T. *Hydrogen absorption of nanocrystalline palladium.* J. Alloys Comp., **2002**, 330–332, 718.

12. Krawiec, P.; Kramer, M.; Sabo, M.; Kunschke, R.; Frode, H.; Kaskel, S. *Improved Hydrogen Storage in the Metal-Organic Framework* $Cu_3(BTC)_2$. Adv. Eng. Mater., **2006**, 8, 293.

L

1. Langmi, H. W.; Book, D.; Walton, A.; Johnson, S. R.; Al-Mamouri, M. M.; Speight, J. D.; Edwards, P. P.; Harris, I. R.; Anderson, P. A. *Hydrogen storage in ion exchanged zeolites.* J. Alloys Comp., **2005**, 404–406, 637.

2. Latroche, M.; Suble, S.; Serre, C.; Mellot-Draznieks, C.; Llewellyn, P. L.; Lee, J. H.; Chang, J. S.; Jhung, S. H.; Ferey, G. *Hydrogen Storage in the Giant-Pore Metal–Organic Frameworks MIL-100 and MIL-101*. Angew. Chem., Int. Ed., **2006**, 45, 8227.

3. Lemmon, E. W.; Huber, M. L.; Lechman, J. W. *Revised Standardized Equation for Hydrogen Gas Densities for Fuel Consumption Applications.* J. Res. Natl. Inst. Stand. Technol., **2008**, 113, 341.

4. Lee, Y.G.; Moon, H. R.; Cheon, Y. E.; Suh, M. P. *A Comparison of the* H_2 *Sorption Capacities of Isostructural Metal–Organic Frameworks with and without Accessible Metal Sites:*$[\{Zn_2(abtc)(dmf)_2\}_3]$ *and* $[\{Cu_2(abtc)(dmf)_2\}_3]$ *versus* $[\{Cu_2(abtc)\}_3]$. Angew. Chem., Int. Ed., **2008**, 47, 7741.

5. Lee, J. Y.; Olson, D. H.; Pan, L.; Emge, T. J.; Li, J. *Microporous metal–organic frameworks with high gas sorption and separation capacity.* Ad. Funct. Mater., **2007,** 17, 1255.

6. Li, H.; Eddaoudi, M.; O'Keeffe, M.; Yaghi, O. M. *Design and synthesis of an exceptionally stable and highly porous metal-organic framework.* Nature. **1999**, *402***,** 276–279.

7. Li, Y. W.; Yang, R. T.; *Gas adsorption and storage in metal-organic framework MOF-177.* Langmuir, **2007**, 23, 12937.

8. Li, Y. W.; Yang, R. T. *Significantly enhanced hydrogen storage in metal-organic frameworks via spillover.* J. Am. Chem. Soc., **2006**, 128, 726.

9. Li, Y. W., Yang, R. T. *Hydrogen storage in metal-organic and covalent-organic frameworks by spillover.* AJChE J., **2008**, 54:269

10. Li, H.; Eddaoudi, M.; Keeffe, M. O.; Yaghi, O. M. *Design and synthesis of an exceptionally stable and highly porous metal-organic framework*. Nature, **1999**, 402, 276.

11. Lin, K-S; Adhikari, A. K.; Chang, K-C.; Chiang, C-L.; Wang, C-H. *Synthesis, Characterization, and Hydrogen Storage Enhancement of $M_2(BDC)_2$dabco with Palladium-Doped Activated Carbon.* J. Nanosci. Nanotech., **2014**,14, 2700.

12. Lin, X.; Jia, J.; Zhao, X.; Thomas, K. M.; Blake, A. J.; Walker, G. S.; Champness, N. R.; *Hubberstey, P.; Schroder, M. High H_2 Adsorption by Coordination-Framework Materials.* Angew. Chem., Int. Ed. **2006**, 45, 7358.

13. Liu, Y. Y.; Zeng, J. L.; Zhang, J.; Xu, F.; Sun, L. X. *Improved hydrogen storage in the modified metal-organic frameworks by hydrogen spillover effect*. Int. J. Hydrogen Energy, **2007**, 32, 4005.

14. Liu, J.; Culp, J. T.; Natesakhawat, S.; Bockrath, B. C.; Zande, B.; Sankar, S. G.; Garberoglio, G.; Johnson, J. K. *Experimental and Theoretical Studies of Gas Adsorption in $Cu_3(BTC)_2$: An Effective Activation Procedure.* J. Phys. Chem. C., **2007**, 111, 9305.

15. Liu, Y.; Kravtsov, V. Ch.; Larsen, R.; Eddaoudi, M. *Molecular building blocks approach to the assembly of zeolite-like metal–organic frameworks (ZMOFs) with extra-large cavities.* Chem. Commun., **2006**, 1488.

16. Liu, Y.; Kabbour, H.; Brown, C. M.; Neumann, D. A.; Ahn, C. C. *Increasing the Density of Adsorbed Hydrogen with Coordinatively Unsaturated Metal Centers in Metal-Organic Frameworks.* Langmuir, **2008**, 24, 4772.

17. Liu S.; Sun, L. X.; Xu, F.; Zhang J.; Jiao, C. L.; Li, F.; Li, Z. B.; Wang, S.; Wang, Z. Q.; Jiang, X.; Zhou, H. Y.; Yang, L. N.; Schick, C. *Nanosized Cu-MOFs induced by graphene oxide and enhanced gas storage capacity.* Energy Environ. Sci., **2013**, 6, 818.

18. Liu, Y.; Ng, Z.; Khan, E. A.; Jeong, H.-K.; Ching, C.-B.; Lai, Z. *Synthesis of continuous MOF-5 membranes on porous a-alumina substrates.* Microporous Mesoporous Mater., **2009**, 118, 296.

19. Liu, X. M.; Rather, S.; Li, Q.; Lueking, A.; Zhao, Y.; Li, J. *Hydrogenation of CuBTC Framework with the Introduction of a PtC Hydrogen Spillover Catalyst*. J. Phys. Chem. C., **2012**, 116, 3477.

20. Llewellyn, P. L.; Bourrelly, S., Serre, C.; Vimont, A.; Daturi, M.; Hamon, L.; Weireld, G. D.; Chang, J. S.; Hong, D. Y.; Hwang, Y. K.; Jhung S. H.; Ferey, G. *High Uptakes of CO_2 and CH_4 in Mesoporous Metal Organic Frameworks MIL-100 and MIL-101*. Langmuir, **2008**, 24, 7245.

21. Lochan, R. C.; Gordon, M. H. *Computational studies of molecular hydrogen binding affinities: The role of dispersion forces, electrostatics, and orbital interactions. Phys.* Chem. Chem. Phys., **2006**, 8, 1357.

22. Loganathan, S.; Tikmani, M.; Ghosal, A. K. *Novel Pore-Expanded MCM-41 for CO2 Capture: Synthesis and Characterization.* Langmuir, **2013**, 29, 3491.

23. Luzan, S. M.; Talyzin, A. V. *Hydrogen adsorption in Pt catalyst/ MOF-5 materials*. Microporous Mesoporous Mater., **2010**, 135, 201.

24. Luzan S. M.; Talyzin A. V. *Comment to the "Response to "Hydrogen adsorption in Pt catalyst/MOF-5 materials" by Li et al [1]".*Microporous Mesoporous Mater., **2011**, *139*, 216.

25. Luzan, S. M.; Jung, H.; Chun, G.; Talyzin, A. V. *Hydrogen storage in Co-and Zn-based metal-organic frameworks at ambient temperature.* Int. J. Hydrogen Energy, **2009**, 34, 9754.

26. Luzan. S. M. *Materials for Hydrogen Storage and Synthesis of New Materials by Hydrogenation*, Doctoral thesis, **2012**, Umea University http://www.diva-portal.org/smash/get/diva2:549550/FULLTEXT01.pdf

M

1. Ma, S.; Sun, D.; Ambrogio, M.; Fillinger, J. A.; Parkin, S.; Zhou, H.-C. *Framework-Catenation Isomerism in Metal-Organic Frameworks and Its Impact on Hydrogen Uptake.* J. Am. Chem. Soc., **2007**, 129, 1858.

2. Ma, S.; Eckert, J.; Forster, P. M.; Yoon, J. W.; Hwang, Y. K.; Chang, J.-S.; Collier, C. D.; Parise, J. B.; Zhou, H.-C. *Further Investigation of the Effect of Framework Catenation on Hydrogen Uptake in Metal Organic Frameworks.* J. Am. Chem. Soc., **2008**, 130, 15896.

3. Marcano, D. C.; Kosynkin, D. V.; Berlin, J. M.; Sinitskii, A.; Sun, Z. Z.; Slesarev, A.; Alemany, L. B.; Lu W.; Tour, J. M. *Improved Synthesis of Graphene Oxide.* ACS Nano, **2010**, 4, 4806.

4. Makarova, M. A.; Zholobenko, V. L.; Al-Ghefalli, K. M.; Thompson, N. E.; Dewing, J.; Dwyer J. *Brønsted acid sites in zeolites*, J. Chem. Soc., Faraday Trans., **1994**, 90, 1047.

5. Mavrandonakis, A.; Klonzas, E.; Tylianakis, E.; Froudakis, G. E. *Enhancement of hydrogen adsorption in metal-organic frameworks by the incorporation of the sulfonate group and Li cations. A multiscale computational study*. J. Am. Chem. Soc., **2009**, 131, 13410.

6. Miller, M. A.; Wang, C. Y.; Merrill G. N. *Experimental and Theoretical Investigation Into Hydrogen Storage via Spillover in IRMOF-8.* J. Phys. Chem. C., **2009**, 113, 3222.

7. Mishra, P.; Edubilli, S.; Uppara, H.; Mandal, B.; Gumma S. *Effect of Adsorbent History on Adsorption Characteristics of MIL-53(Al) Metal Organic Framework*. Langmuir, **2013**, 29, 12162.

8. Mishra, P.; Edubilli, S.; Mandal, B.; Gumma S. *Adsorption of CO_2, CO, CH_4 and N_2 on DABCO based metal organic frameworks*. Microporous Mesoporous Mater., **2013**, 169, 75.

9. Mulfort, K. L.; Hupp. *Chemical Reduction of Metal-Organic Framework Materials as a Method to Enhance Gas Uptake and Binding.* J. Am. Chem. Soc., **2007**, 129, 9604.

10. Mulfort, K. L.; Hupp, J. T. *Alkali Metal Cation Effects on Hydrogen Uptake and Binding in Metal-Organic Frameworks*. Inorg. Chem., **2008,** 47, 7936.

11. Mulfort, K. L.; Wilson, T. M, Wasielewski, M. R.; Hupp, J. T. *Framework reduction and alkali-metal doping of a triply catenating metal-organic framework enhances and then diminishes H2 uptake*. Langmuir, **2009**, 25, 503.

12. Mulfort, K. L.; Farha, O. K.; Stern, C. L.; Sarjeant, A. A.; Hupp, J. T. *Post-Synthesis Alkoxide Formation Within Metal-Organic Framework Materials: A Strategy for Incorporating Highly Coordinatively Unsaturated Metal Ions.* J. Am. Chem. Soc., **2009**, 131, 3866.

N

1. Narayanan, R.; El-Sayed, M. *Effect of Catalysis on the Stability of Metallic Nanoparticles: Suzuki Reaction Catalyzed by PVP-Palladium Nanoparticles*. J. Am. Chem. Soc., **2003,**125, 8340.

2. Narayanan, R.; El-Sayed, M. *Effect of Colloidal Catalysis on the Nanoparticle Size Distribution: Dendrimer-Pd vs PVP-Pd Nanoparticles Catalyzing the Suzuki Coupling Reaction*. J. Phys. Chem. B, **2004,**108, 8572.

3. Narehood, D. G.; Kishore, S.; Goto, H.; Adair, J. H.; Nelson, J.A.; Gutierrez, H. R.; Eklund, P. C. *X-ray diffraction and H-storage in ultra-small palladium particles*. Int. J. Hydrogen Energy, **2009,** 34,952.

4. Narayanan, R.; Laine, R. M. *Synthesis and Characterization of Precursors for Group II Metal Aluminates*. Appl. Organomet. Chem., **1997**, 11, 919.

5. Nijkamp, M. G.; Raaymakers, J. E. M. J.; *van*-Dillen, A. J.; de Jong, K. P. '*Hydrogen storage using physisorption – materials demand'*. Appl. Phys. A, **2001,** 72, 619.

6. Nouar, F.; Eckert, J.; Eubank, J. F.; Forster, P.; Eddaoudi, M. *Zeolite-like Metal-Organic Frameworks (ZMOFs) as Hydrogen Storage Platform: Lithium and Magnesium Ion-Exchange and H2-(rho-ZMOF) Interaction Studies.* J. Am. Chem. Soc., **2009**, 131, 2864.

O

1. O'Neill, L. D.; Zhang, H.; Bradshaw, D. *Macro-/microporous MOF composite beads.* J. Mater. Chem., **2010**, 20, 5720.

P

1. Park, T. H.; Hickman, A. J.; Koh, K.; Martin, S.; Wong-Foy, A. G.; Sanford, M. S.; Matzger, J. A. *Highly Dispersed Palladium(II) in a Defective Metal-Organic Framework: Application to C-H Activation and Functionalization.* J. Am. Chem. Soc., **2011**, 133, 20138.

2. Paranthaman, S.; Coudert F. X.; Fuchs, A. H.; *Water adsorption in hydrophobic MOF channels.* Phys. Chem. Chem. Phys., **2010**, 12, 8123.

3. Peterson, V. K.; Liu, Y.; Brown, C. M.; Kepert, C. J. *Neutron Powder Diffraction Study of D2 Sorption in* Cu_3*(1,3,5-benzenetricarboxylate)*$_2$. J. Am. Chem. Soc., **2006**, 128, 15578.

4. Petit, C.; Bandosz, T. J. *MOF-graphite oxide composites: combining the uniqueness of graphene layers and metalorganic frameworks.* Adv. Mater., **2009**, 21, 4753.

5. Petit, C.; Burress, J.; Bandosz, T. J. *The synthesis and characterization of copper-based metal-organic framework/graphite oxide composites.* Carbon, **2011**, 49,563.

6. Petit, C.; Bandosz, T. J. *Enhanced adsorption of ammonia on metal-organic framework/graphite oxide composites: analysis of surface interactions.* Adv. Funct. Mater., **2010**, 20,111.

7. Petit, C.; Bandosz, T. J. *Synthesis, characterization, and ammonia adsorption properties of mesoporous metal-organic framework (MIL(Fe) graphite oxide composites: exploring the limits of materials fabrication.* Adv. Funct. Mater., **2011**, 21, 2108.

8. Petit, C.; Mendoza, B.; Bandosz, T. J. *Reactive Adsorption of Ammonia on Cu-Based MOF/Graphene Composites.* Langmuir, **2010**, 26, 15302.

9. Poirier, E.; Chahine, R.; Benard, P.; Lafi, L.; Dorval-Douville, G.; Chandonia, P. A.; *Hydrogen Adsorption Measurements and Modeling on Metal-Organic Frameworks and Single-Walled Carbon Nanotubes*. Langmuir**, 2006,** 22, 8784.

10. Ping, S.; Yaoqi, L.; Bei, H.; Junzhi, Y.; Jie, Z. Xingguo, L. *Hydrogen storage properties of two pillared-layer Ni(II) metal-organic frameworks*. Microporous Mesoporous Mater., **2011**, 142, 208.

11. Proch, S.; Herrmannsdofer, J.; Kempe, R.; Kern, C.; Jess, A.; Seyfarth, L.; Senker, *Pt@MOF-177: synthesis, room-temperature hydrogen storage and oxidation catalysis.* J. Chem. Eur. J. 2008, 14, 8204.

12. Pundt, A.; Kirchheim, R. *Hydrogen in metals: Microstructural Aspects*. Annu. Rev. Mater. Res., **2006**, 36, 555.

13. Purewal, J.; Liu, D.; Sudik, A.; Veenstra, M.; Yang, J.; Maurer, S.; Muller, U.; Siegel, D.J. *Improved Hydrogen Storage and Thermal Conductivity in High-Density MOF-5 Composites* J. Phys. Chem. C, **2012**, 116, 20199.

Q

1. Qin, W.; Cao, W.; Liu, H.; Li, Z.; Li, Y. *Metal–organic framework MIL-101 doped with palladium for toluene adsorption and hydrogen storage.* RSC Adv., **2014**, 4, 2414.

R

1. Rallapalli, P. B. S.; Raj, M. C.; Patil, D. V.; Prasanth, K. P.; Somani, R. S.; Bajaj H. C. *Activated carbon @MIL-101(Cr): a potential metal-organic framework composite material for hydrogen storage,* Int. J. Energy Res., **2013**, 37, 746.

2. Rather, S.; Zacharia, R.; Hwang, S. W.; Naik, M.; Nahm, K. S. *Hyperstoichiometric hydrogen storage in monodispersed palladium nanoparticles.* Chem. Phys. Lett., **2007**, 438, 78–84.

3. Reimer, L. *Scanning Electron Microscopy. Physics of image formation and microanalysis*. Springers, Germany, **1998.**

4. Rosi, N. L.; Eckert, J.; Eddaoudi, M.; Vodak, D. T.; Kim, J.; Keefe, M. O.; Yaghi, O. M. *Hydrogen Storage in Microporous Metal-Organic Frameworks.* Science, **2003**, 300, 1127.

5. Rowsell J. L. C.; Yaghi, O. M. *Metal–organic frameworks: a new class of porous materials.* Microporous Mesoporous Mater., **2004**, 73, 3.

6. Rowe, M. D.; Thamm, D. H.; Kraft, S. L.; Boyes, S. G. *Polymer-Modified Gadolinium Metal-Organic Framework Nanoparticles Used as Multifunctional Nanomedicines for the Targeted Imaging and Treatment of Cancer.* Biomacromolecules, **2009**, 10, 983 – 993.

7. Rondeau, R. E.; Harrah. L. A. *Slush Baths*. J. Chem. Eng. Data, **1965**, 10, 84.

8. Ruthven, D. M.; Sun, M. S. *Principle of Adsorption and Adsorption Processes*, *Chapter-1*, Wiley-Interscience, New York, **1984**.

9. Ruthven, D. M.; Farooq, S. *Concentration of a trace component by pressure swing adsorption*. Chem. Eng. Sci., **1994**, 49, 51.

10. Ryan, P.; Broadbelt, L. J.; Snurr, R. Q. *Is catenation beneficial for hydrogen storage in metal–organic frameworks.* Chem. Commun., **2008**, 44, 4132.

S

1. Sabo, M.; Henschel, A.; Frode, H.; Klemm, E.; Kaskel, S. *Solution infiltration of palladium into MOF-5: synthesis, physisorption and catalytic properties.* J. Mater. Chem., **2007**, 17, 3827.

2. Saito, A.; Foley, H. C. *Curvature and parametric sensitivity in models for adsorption in micropores.* Aiche Journal, **1991,** 37, 429.

3. Saha, D.; Wei, Z.; Deng, S. *Hydrogen adsorption equilibrium and kinetics in metal–organic framework (MOF-5) synthesized with DEF approach.* Separation Purification Technol., **2009**, 64, 280.

4. Saha, D.; Deng, S.; Yang, Z. *Hydrogen adsorption on metal-organic framework (MOF-5) synthesized by DMF approach.* J. Porous Mater., **2009**, 16, 141.

5. Saha, D.; Deng, S. *Hydrogen Adsorption on Metal-Organic Framework MOF-177.* Tsinghua Science Technol., **2010**, 15(4), 363.

6. Sahu, D.; Mishra, P.; Edubilli, S.; Verma, A.; Gumma, S. *Hydrogen Adsorption on Zn-BDC, Cr-BDC, Ni-DABCO and Mg-DOBDC Metal Organic Frameworks.* J. Chem. Eng. Data, **2013**, 58(11), 3096.

7. Sahu, D.; Mishra, P.; Das, N.; Verma, A.; Gumma S. *The Net Adsorption of Hydrogen on Palladium Nanoparticles.* DOI: 10.1142/S0218625X1450022X

8. Sunita, S.; John, P.; Carole, R.; George, T.; Grace, O. *The U.S. Department of Energy's National Hydrogen Storage Project: Progress towards meeting hydrogen-powered vehicle requirements.* Catal. Today, **2007**, 120, 246.

9. Schlapbach, L.; Zuttel, A. *Hydrogen storage for mobile applications*. Nature, **2001**, 414, 353.

10. Schüth, F.; Sing, K. S. W.; Weitkamp, J. *Handbook of porous solids*. Wiley-VCH, Weinheim, Vol.2, **2002.**

11. Shekhah, O.; Hirai, K.; Wang, H.; Uehara, H.; Kondo, M.; Diring, S.; Zacher, D.; Fischer, R. A.; Sakata, O.; Kitagawa, S.; Furukawa, S.; Woll, C. *MOF-on-MOF heteroepitaxy: perfectly oriented [Zn_2(ndc)$_2$(dabco)]n grown on [Cu_2(ndc)$_2$(dabco)]n thin films.* Dalton Trans., **2011**, 40, 4954.

12. Sheppard, D. A.; Buckley, C. E. *Hydrogen adsorption on porous silica*. Int. J. Hydrogen Energy, **2008**, *33*, 1688.

13. Sheppard, D. A.; Maitland, C. F.; Buckley, C. E. *Preliminary results of hydrogen adsorption and SAXS modelling of mesoporous silica: MCM-41*. J. Alloys Comp., **2005,** 404-406, 405.

14. Stéphanie-Victoire, F.; *de*-Lara C. E. *Adsorption and coadsorption of molecular hydrogen isotopes in zeolites. II. Infrared analyses of H_2, HD, and D_2 in NaA*, J. Chem. Phys., **1998**, 109, 6469.

15. Stucket, N. R.; Wang, L. F.; Yang, R. T. *Characteristic of hydrogen storage by spillover on Pt-doped carbon and catalyst-bridged metal organic framework.* Langmuir, **2010**, 26, 11963.

16. Srinivas, G.; Zhu, Y.; Piner, R.; Skipper, N.; Ellerby, M.; Ruoff, R. *Synthesis of graphene-like nanosheets and their hydrogen adsorption capacity.* Carbon, **2010**, 48, 630.

17. Suh, M. P.; Cheon, Y. E.; Lee, E. Y. *Reversible Transformation of ZnII Coordination Geometry in a Single Crystal of Porous Metal-Organic Framework* $[Zn_3\ (ntb)_2\ (EtOH)_2]$*•4EtOH.* Chem. Eur. J., **2007**, 13, 4208.

18. Sumida, K.; Horike, S.; Kaye, S. S.; Herm, Z. R.; Queen, W. L.; Brown, C. M.; Grandjean, F.; Long, G. J.; Anne, D.; Long, J. R. *Hydrogen storage and carbon dioxide capture in an iron-based sodalite-type metal–organic framework (Fe-BTT) discovered via high-throughput methods.* Chem. Sci., **2010**, 1, 184

19. Suh, M. P.; Park, H. J.; Prasad, T. K.; Lim, D. W. *Hydrogen Storage in Metal Organic Frameworks.* Chem. Rev., **2012**, 112, 782.

20. Sumida, K.; Brown, C. M.; Herm Z. R.; Chavan, S.; Bordig, S.; Long, J. R. *Hydrogen storage properties and neutron scattering studies of* Mg_2*(dobdc) a metal–organic framework with open* Mg^{2+} *adsorption sites*. Chem. Commun., **2011**, 47, 1157.

21. Sun, M. S.; Shah, D. B.; Xu, H. H.; Talu, O. *Adsorption Equilibria of C1 to C4 Alkanes,* CO_2*, and* SF_6 *on Silicalite.* J. Phys. Chem. B, **1998**, 102, 1466.

22. Szostak, R. *Molecular Sieves Principles of Synthesis and Identification*, Blackie Academic & Professional, London, **1998**.

T

1. Talyzin, A. V.; Szabo, T.; Dekany, I.; Langenhorst, F.; Sokolov, P. S.; Solozhenko, V. L. *Nanocarbons by high-temperature decomposition of graphite oxide at various pressures*. J. Phys. Chem. C, **2009**, 113(26), 11279.

2. Takagi, H.; Hatori, H.; Soneda, Y.; Yoshizawa, N.; Yamada, Y. *Adsorptive hydrogen storage in carbon and porous materials.* Mater. Sci. Eng., B, **2004**, 108, 143.

3. Tan, C.; Yang, S.; Champness, N. R.; Lin, X.; Blake, A. J.; Lewis, W.; Schroder, M. *High capacity gas storage by a 4,8-connected metal–organic polyhedral framework.* Chem. Commun., **2011**, 47, 4487.

4. Tsao, C. S.; Yu, M. S.; Wang, C. Y.; Liao, P. Y.; Chen, H. L.; Jeng, U.; Tzeng, Y. R.; Chung, T. Y.; Wu H.C. *Nanostructure and Hydrogen Spillover of Bridged Metal-Organic Frameworks.* J. Am. Chem. Soc., **2009**, 131, 1404.

5. Trung, T. K.; Trens, P.; Tanchoux, N.; Bourrelly, S.; Llewellyn P. L.; Loera-Serna, S.; Serre, C.; Loiseau, T.; Fajula, F.; Férey, G. *Hydrocarbon Adsorption in the Flexible Metal Organic Frameworks MIL-53(Al, Cr).* J. Am. Chem. Soc., **2008**, 130, 16926.

6. Tranchemontagne D. J.; Hunt, J. R.; Yaghi, O. M. *Room temperature synthesis of metal-organic frameworks: MOF-5, MOF-74, MOF-177, MOF-199, and IRMOF-0.* Tetrahedron, **2008,** 64, 8553.

7. Turner, S.; Lebedev, O.; Schroder, F.; Esken, D.; Fischer, R. A.; Tendeloo, G. V. Direct *Imaging of Loaded Metal-Organic Framework Materials (Metal@MOF-5)* Chem. Mater., **2008**, 20, 5622.

V

2. Vajo, J. J.; Skeith, S. L.; Mertens, F. *Altering Hydrogen Storage Properties by Hydride Destabilization through Alloy Formation: LiH and MgH_2 Destabilized with Si.* J. Phys. Chem. B, Lett., **2005**, 109, 3719.

3. Vix-Guterl, C.; Frackowiak, E.; Jurewicz, K.; Friebe, M.; Parmentier, J.; Beguin, F. *Electrochemical energy storage in ordered porous carbon materials. Carbon*, **2005**, *43*, 1293.

4. Vimont, A.; Goupil, J. M.; Lavalley, J. C.; Daturi, M.; Surblé, S.; Serre, C.; Millange, F.; Férey, G.; Audebrand, N. *Investigation of Acid Sites in a Zeotypic Giant Pores Chromium(III) Carboxylate.* J. Am. Chem. Soc., **2006**, 128, 3218.

W

1. Walker, G. *Solid State Hydrogen Storage*. CRC Press, Washington, DC, **2008**.

2. Wang, P.; Kang, X. *Hydrogen-rich boron-containing materials for hydrogen storage*, Dalton Trans., **2008**, 5400.

3. Wang, L.; Stuckert, N. R.; Chen, H.; Yang R. T. Effects of Pt *Particle Size on Hydrogen Storage on Pt-Doped Metal-Organic Framework IRMOF-8* J. Phys. Chem. C, **2011**, 115, 4793.

4. Wang, Y.; Fang, M.; Li, Y.; Liang, J.; Shi, J.; Chen, G.; Cheng, P. *A porous 3d-4f heterometallic metal–organic framework for hydrogen storage* Int. J. Hydrogen Energy, **2010**, 35, 8166

5. Wang, S. *Ordered mesoporous materials for drug delivery.* Microporous Mesoporous Mater., **2009**, 117, 1.

6. Wang, X. S.; Ma, S. Q.; Rauch, K.; Simmons, J. M.; Yuan, D. Q.; Wang, X. P.; Yildirim, T.; Cole, W. C.; Lopez, J. J.; *de*-Meijere, A.; Zhou, H. C. *Metal-Organic Frameworks Based on Double-Bond-Coupled Di-Isophthalate Linkers with High Hydrogen and Methane Uptakes.* Chem. Mater., **2008**, 20, 3145.

7. Wang, L. F.; Yang, R. T. N*ew sorbents for hydrogen storage by hydrogen spillover -a review*. Energy Environ. Sci., **2008**, 1,268.

8. Wang, Z.; Yang, R. T. *Enhanced hydrogen storage on Pt-doped carbon by plasma reduction.* J. Phys. Chem. C, **2010**, 114, 5956.

9. Wei, Z.; Hui, W.; Taner, Y. *Enhanced H_2 adsorption in isostructural metal-Organic Frameworks with Open Metal Sites: Strong Dependence of the Binding Strength on Metal Ions*. J. Am. Chem. Soc., **2008**, 130, 15268.

10. Wieser, M. E. *Atomic weights of the elements 2005*. Pure Appl. Chem., **2006**, 78, 2051.

11. Wiley, B.; Herricks, T.; Sun Y.; Xia, Y. *Polyol Synthesis of Silver Nanoparticles: Use of Chloride and Oxygen to Promote the Formation of Single-Crystal, Truncated Cubes and Tetrahedrons.* Nano Lett., **2004**, 4, 1733.

12. Wu, H.; Zhou, W.; Yildirim, T. *Enhanced H2 Adsorption in Isostructural Metal-Organic Frameworks with Open Metal Sites: Strong Dependence of the Binding Strength on Metal Ions* J. Am. Chem. Soc., **2009**, 131, 4995.

13. Weston, M. H.; Farha, O. K.; Hauser, B. G.; Hupp, J. T.; Nguyen, S. B. T. *Synthesis and Metalation of Catechol-Functionalized Porous Organic Polymers* Chem. Mater., **2012**, 24, 1292.

14. Wong-Foy, A. G.; Matzger, A. J.; Yaghi, O. M. *Exceptional H_2 Saturation Uptake in Microporous Metal-Organic Frameworks.* J. Am. Chem. Soc., **2006**, 128, 3494.

15. Wu, Y. *Hydrogen Storage via Sodium Borohydride Current Status, Barriers, and R&D Roadmap.* GCEP –Stanford University, **2013.** (http://gcep.stanford.edu/pdfs/hydrogen_workshop/Wu.pdf)

16. Wu, C.; Gao, Q.; Hu, J.; Chen, Z.; Shi, W. *Rapid preparation, characterization and hydrogen storage properties of pure and metal ions doped mesoporous MCM-41. Microporous* Mesoporous Mater., **2009**, 117,165.

X

1. Xiang, Z.; Hu, Z.; Yang, W.; Cao, D. *Lithium doping on metal-organic frameworks for enhancing H_2 Storage.* Int. J. Hydrogen Energy, **2012**, 37, 946.

2. Xu, C.; Wang, X.; Zhu, J. W. *Graphene -metal particle nanocomposites*. J. Phys. Chem. C, **2008**, 112, 19841.

3. Xiong, Y.; Cai, H.; Wiley, B .J.; Wang, J.; Kim, M. J.; Xia, Y. *Kinetically Controlled Synthesis of Triangular and Hexagonal Nanoplates of Palladium and Their SPR/SERS Properties*. J. Am. Chem. Soc., **2007,** 129, 3665.

Y

4. Yang, R. T. *Gas Separation by Adsorption Processes, Chapter-1*. **1997**, Imperial College Press, London.

5. Yan, Y.; Lin, X.; Yang, S.; Blake, A. J.; Dailly, A.; Champness, N. R.; Hubberstey, P.; Schroder, M. *Exceptionally high H_2 storage by a metal–organic polyhedral Framework.* Chem. Commun., **2009**, 45, 1025.

6. Yan, Y.; Telepeni, I.; Yang, S.; Lin, X.; Kockelmann, W.; Dailly, A.; Blake, A. J.; Lewis, W.; Walker, G. S.; Allan, D. R.; Barnett, S. A.; Champness, N. R.; Schroder, M. Metal-Organic *Polyhedral Frameworks: High H_2 Adsorption Capacities and Neutron Powder Diffraction Studies,* J. Am. Chem. Soc., **2010**, 132, 4092.

7. Yaghi, O. M.; O'Keeffe, M.; Ockwig, N. W.; Chae, H. K.; Eddaoudi, M.; Kim, J. *synthesis and the design of new materials.* Nature, **2003**, *423*, 705.

8. Yang, S. H.; Lin, X.; Dailly, A.; Blake, A. J. Hubberstey, P.; Champness, N. R.; Schroder, M. *Enhancement of H_2 Adsorption in Coordination Framework Materials by Use of Ligand Curvature.* Chem. Eur. J., **2009**, 15, 4829.

9. Yang, S. H.; Lin, X.; Blake, A. J.; Walker, G. S.; Hubberstey, P.; Champness, N. R.; *Schroder, M. Cation-induced kinetic trapping and enhanced hydrogen adsorption in a modulated anionic metal–organic framework.* Nat. Chem., **2009**, 1, 487.

10. Yang, S. J.; Choi, J. Y.; Chae, H. K.; Cho, J. H.; Nahm, K. S.; Park, C. R. *Preparation and Enhanced Hydrostability and Hydrogen Storage Capacity of CNT@MOF-5 Hybrid Composite.* Chem. Mater., **2009**, 21, 1893.

11. Yartys, V. A.; Vajeeston, P.; Riabov A. B. *Crystal chemistry and metal-hydrogen bonding in anisotropic and interstitial hydrides of intermetallics of rare earth (R) and transition metals (T), RT_3 and R_2T_7.* Mater. Technol., **2008,** 223, 674.

12. Yan, Y.; Telepeni, I.; Yang, S.; Lin, X.; Kockelmann, W.; Dailly, A.; Blake, A. J.; Lewis, W.; Walker, G. S.; Allan, D. R.; Barnett, S. A.; Champness, N. R.; Schroder, M. J. Am. Chem. Soc., **2010**, 132, 4092.

13. Yoo, Y.; Jeong , H. K. *Rapid fabrication of metal organic framework thin films using microwave-induced thermal deposition.* Chem. Commun., **2008**, 2008, 2441.

14. Yamauchi, M.; Ikeda, R.; Kitagawa, H.; Takata, M. *Nanosize Effects on Hydrogen Storage in Palladium.* J. Phys. Chem. C, **2008**,112, 3294.

15. Yang, Y.; Shukla, P.; Wang, S.; Rudolph, V.; Chenc X. M.; Zhu, Z. *Significant improvement of surface area and CO_2 adsorption of Cu–BTC via solvent exchange activation.* RSC Adv., **2013**, 3, 17065.

16. Yang, J.; Zhao, Q.; Li, J.; Dong, J. *Synthesis of metal–organic framework MIL-101 in TMAOH-$Cr(NO_3)_3$-H_2BDC-H_2O and its hydrogen-storage behaviour.* Microporous Mesoporous Mater., **2010**, 130, 174.

17. Yuan, D.; Zhao, D.; Sun, D.; Zhou, H. C. *An Isoreticular Series of Metal–Organic Frameworks with Dendritic Hexacarboxylate Ligands and Exceptionally High Gas-Uptake* Capacity. Angew. Chem., Int. Ed., **2010**, 49, 5357.

18. Yuan, D.; Zhao, D.; Zhou, H. C. *Pressure-Responsive Curvature Change of a "Rigid" Geodesic Ligand in a (3,24)-Connected Mesoporous Metal-Organic Framework.* Inorg. Chem., **2011**, 50, 10528.

Z

1. Zhou, L.; Zhou, Y.; Sun, Y. *A comparative study of hydrogen adsorption on superactivated carbon versus carbon nanotubes.* Int. J. Hydrogen Energy, **2004**, 29, 475.

2. Zlotea, C.; Campesi, R.; Cuevas, F.; Leroy, E.; Dibandjo, P.; Volkringer, C.; Loiseau, T.; Ferey, G.; Latroche M. *Pd nanoparticles embedded into a metal-organic framework: synthesis, structural characteristics, and hydrogen sorption properties.* J. Am. Chem. Soc., **2010**, 132, 2991.

3. Zhou, H.; Liu, X.; Zhang, J.; Yan, X.; Liu,Y.; Yuan, A. *Enhanced room-temperature hydrogen storage capacity in Pt-loaded graphene oxide/HKUST-1 composites* Int. J. Hydrogen Energy, **2014**, 39(5), 2160.

4. Zlotea, C.; Campesi, R.; Cuevas, F.; Leroy, E.; Dibandjo, P.; Volkringer, C.; Loiseau, T.; Ferey, G.; Latroche M; Pd *Nanoparticles Embedded into a Metal-Organic Framework: Synthesis, Structural Characteristics, and Hydrogen Sorption Properties.* J. Am. Chem. Soc. **2010**, *132*, 2991.

5. Zhao, M.; Zhao.; Deng, K.; He, L.; Liu, Y.; Li, G.; Zhao, H.; Tang Z. *Core−Shell Palladium Nanoparticle@Metal−Organic Frameworks as Multifunctional Catalysts for Cascade Reactions*. J. Am. Chem. Soc., **2014**, 136, 1738.

6. Zhu, Z. H.; Lu, G. Q.; Smith, S. C. *Comparative study of hydrogen storage in Li- and K-doped carbon materials—theoretically revisited*. Carbon, **2004**, 42, 2509.

7. a) Zuttel, A.; Naturwissenschaften, **2004**, 91,157. b) Zuttel, A.; *Model for the hydrogen adsorption on carbon nanostructures.* Appl. Phys. A, **2004**, 78, 941.

APPENDIX: A

Measured Isotherm Data on

Studied Adsorbents

Table A1: Excess Adsorption Isotherm Data

Adsorbent	**T, K**	**P, bar**	**Amount adsorbed mmol g^{-1}**	**T, K**	**P, bar**	**Amount adsorbed mmol g^{-1}**
Pd NPs	293	0.0	0.00	324	0.0	0.00
		0.01	0.72		0.01	0.60
		0.01	1.04		0.02	0.77
		0.02	1.73		0.02	0.70
		0.03	2.23		0.04	0.81
		0.05	2.35		0.07	0.87
		0.09	2.39		0.1	2.27
		0.11	2.40		0.12	2.29
		0.13	2.42		0.14	2.23
		0.16	2.44		0.16	2.40
		0.19	2.47		0.19	2.39
		0.27	2.43		0.31	2.38
		0.4	2.46		0.45	2.46
		0.6	2.60		0.61	2.45
		1.13	2.60		0.76	2.51
		1.27	2.53		0.90	2.47
		2.05	2.70		1.0	2.46
		2.73	2.71		1.33	2.57
		4.5	2.73		2.05	2.42
		8.2	2.87		2.76	2.59
		12.09	2.95		4.11	2.73
		16.17	3.05		8.09	2.81
		20.07	3.20		12.05	2.80
		26	3.35		16.19	2.79
					20.01	2.86
					26	2.86

Adsorbent	T, K	P, bar	Amount adsorbed mmol g^{-1}	T, K	P, bar	Amount adsorbed mmol g^{-1}
Pd NPs	364	0.0	0.00	392	0.0	0.00
		0.01	0.34		0.01	0.65
		0.02	0.57		0.02	0.72
		0.02	0.62		0.03	0.78
		0.04	0.69		0.03	0.72
		0.07	0.69		0.05	0.82
		0.10	0.75		0.1	0.87
		0.12	0.71		0.12	0.90
		0.14	0.82		0.13	0.91
		0.17	0.79		0.16	0.94
		0.2	0.79		0.19	0.99
		0.3	1.70		0.27	1.00
		0.44	2.13		0.43	1.32
		0.64	2.24		0.6	2.29
		0.77	2.31		0.75	2.35
		0.93	2.34		0.89	2.36
		1.03	2.29		0.99	2.35
		1.29	2.38		1.26	2.40
		2.1	2.35		2.2	2.52
		2.77	2.43		2.86	2.46
		4.48	2.53		4.49	2.50
		8.16	2.40		8.18	2.59
		12.13	2.47		12.14	2.59
		16.07	2.53		16.11	2.57
		20.09	2.52		20.09	2.51
		26	2.55		26	2.43
MCM 41	296	0.0	0.00	92	0.0	0.00
		2.3	0.05		0.1	0.56
		4.0	0.02		0.4	1.34
		8.0	0.09		0.65	1.47
		12.0	0.17		1.0	1.90
		16.6	0.21		2.0	2.86
		20.3	0.22		4.0	3.38
		26	0.23		8.1	4.82
		37	0.31		11.7	5.32
		53	0.45		16.1	5.83
		74	0.93		19.7	5.98
		104	1.09		26	6.57
					39	6.91
					52	7.03
					75	7.57
					101	8.16

Adsorbent	T, K	P, bar	Amount adsorbed mmol g^{-1}	T, K	P, bar	Amount adsorbed mmol g^{-1}
Zn-BDC	297	0.0	0.00	169	0.0	0.00
		1.1	0.02		0.2	0.29
		4.0	0.05		0.45	0.34
		8.1	0.07		1.1	0.42
		12.2	0.10		5.0	0.80
		16.0	0.14		10.0	1.17
		26	0.22		17.5	1.57
		40	0.35		33	2.12
		53	0.46		52	2.66
		68	0.58		70	3.03
		92	0.76		94	3.37
		102	0.86			
Zn-BDC	136	0.0	0.00	101	0.0	0.00
		0.3	0.10		0.1	0.68
		0.6	0.22		0.3	1.68
		1.0	0.33		0.5	1.95
		2.0	0.84		1.0	2.55
		4.1	1.39		2.0	2.78
		8.2	2.00		4.0	3.58
		13.5	2.44		8.6	4.00
		20.3	2.76		13.5	4.17
		25.7	3.21		20.2	4.25
		38	3.74		26	4.32
		53	4.27		38	4.30
		69	4.63		54	4.36
		92	4.67		69	4.48
					92	4.42
Cr-BDC	297	0.0	0.00	165	0.0	0.00
		0.3	0.07		0.3	0.13
		1.0	0.09		0.7	0.25
		2.1	0.21		1.3	0.44
		4.0	0.25		2.8	0.87
		7.1	0.34		5.7	1.47
		10.7	0.48		9.4	2.20
		16.0	0.67		14.9	2.99
		21.4	0.81		25.7	4.49
		26	0.94		37	5.75
		34	1.17		52	6.59
		45	1.43		70	7.79
		67	1.98		96	9.12
		90	2.47			
		101	2.71			

Adsorbent	T, K	P, bar	Amount adsorbed mmol g^{-1}	T, K	P, bar	Amount adsorbed mmol g^{-1}
Cr-BDC	136	0.0	0.00	92	0.0	0.00
		0.15	0.04		0.1	1.80
		0.7	0.39		0.3	3.57
		2.2	1.03		1.0	6.04
		4.1	1.89		2.2	8.19
		8.0	3.22		4.0	10.39
		12.7	4.30		6.8	12.28
		19.2	5.85		10.8	14.05
		26	6.83		16.0	15.45
		37	8.70		22.1	16.47
		67	10.85		26	17.30
		94	12.46		34	18.25
					45	19.00
					68	19.09
					91	19.12
					103	19.43
Ni-DABCO	297	0.0	0.00	194	0.0	0.00
		1.1	0.03		0.4	0.07
		2.1	0.14		1.0	0.20
		4.2	0.22		2.2	0.34
		8.0	0.48		4.3	0.70
		13.5	0.59		8.0	1.20
		19.3	0.91		13.5	1.83
		25.7	1.13		19.7	2.64
		38	1.57		25.4	3.24
		53	2.02		38	4.32
		68	2.48		52	5.39
		88	2.99		68	6.25
					91	7.23

Adsorbent	T, K	P, bar	Amount adsorbed mmol g^{-1}	T, K	P, bar	Amount adsorbed mmol g^{-1}
Ni-DABCO	145	0.0	0.00	90	0.0	0.00
		0.2	0.17		0.2	1.75
		0.65	0.42		0.3	3.10
		1.0	0.70		0.7	6.00
		2.0	1.34		1.0	7.13
		4.0	2.35		1.8	10.94
		8.1	4.05		4.0	14.25
		13.4	5.58		6.7	15.51
		19.3	6.94		11.5	17.10
		25.4	7.96		17.3	17.82
		37	10.23		25.4	18.26
		52	11.55		38	18.74
		73	13.75		53	19.08
		92	14.35		75	19.06
					94	19.25
MOF 205	296	0.0	0.00	193	0.0	0.00
		1.1	0.34		0.1	0.04
		2.0	0.47		0.3	0.03
		4.1	0.52		0.7	0.16
		8.0	0.66		1.0	0.13
		12.2	0.64		2.05	0.27
		16.1	0.75		4.05	0.92
		20.0	0.89		8.1	1.12
		25.9	1.15		12.1	1.87
		37	1.51		16.0	2.31
		54	1.93		20.3	3.00
		75	2.50		25.8	2.83
		104	3.16		38	4.31
					52	5.15
					75	6.60
					103	7.60

Adsorbent	T, K	P, bar	Amount adsorbed mmol g^{-1}	T, K	P, bar	Amount adsorbed mmol g^{-1}
MOF 205	140	0.0	0.00	91	0.	0.00
		0.05	0.27		0.04	0.91
		0.1	0.42		0.1	1.65
		0.3	0.81		0.2	2.22
		0.7	1.65		0.3	3.49
		1.0	2.28		0.5	4.24
		2.0	3.10		0.6	4.45
		4.0	5.89		0.7	5.33
		8.0	7.84		1.0	6.98
		12.1	8.90		1.3	7.75
		16.1	9.51		2.0	9.92
		21.6	10.50		3.0	12.50
		26	11.30		3.9	14.12
		37	13.21		5.0	16.22
		53	14.64		6.0	17.60
		74	16.20		7.0	18.93
		101	17.38		8.1	19.63
					9.5	21.30
					11.0	22.36
					12.1	23.43
					16.0	25.38
					20.0	26.96
					24.2	28.30
					29	28.95
					32	29.31
					52	30.00
					74	28.99
					104	27.17
Mg- DOBDC	298	0.0	0.	192	0.0	0.00
		0.2	0.09		0.4	0.06
		0.4	0.1		0.7	0.31
		0.7	0.12		1.1	0.50
		1.0	0.15		2.1	0.85
		2.0	0.18		4.1	1.54
		4.0	0.21		8.1	2.67
		8.0	0.52		13.5	3.81
		13.3	0.8		20.0	5.34
		20.0	0.99		25.9	6.33
		26	1.3		37	7.94
		37	1.82		53	9.22
		52	2.2		67	10.71
		67	2.71		76	11.71
		80	3.07			

Adsorbent	T, K	P, bar	Amount adsorbed mmol g^{-1}	T, K	P, bar	Amount adsorbed mmol g^{-1}
Mg- DOBDC	133	0.0	0.0	101	0.0	0.00
		0.1	1.04		0.1	1.99
		0.4	2.1		0.9	7.77
		0.7	2.84		2.0	9.82
		1.0	3.3		4.0	11.60
		2.0	4.47		8.0	13.35
		4.0	5.87		12.1	14.46
		7.9	7.76		20.2	15.61
		13.3	9.55		25.9	16.13
		19.9	11.12		37	16.48
		25.7	12.14		52	17.25
		37	13.42		68	17.32
		52	14.64		78	18.22
		67	15.6			
		77	16.24			
Co- DOBDC	297	0.0	0.00	91	0.0	0.00
		1.1	0.01		0.1	5.56
		2.2	0.07		0.3	7.07
		4.0	0.13		0.5	8.20
		8.0	0.36		1.0	9.56
		12.1	0.46		2.2	10.95
		16.0	0.60		4.2	12.29
		20.0	0.72		8.6	13.70
		25.9	0.94		12.2	14.34
		37	1.31		15.9	14.55
		52	1.74		20.2	14.86
		74	2.23		25.9	14.86
		104	2.85		37	15.14
					50	14.29
					73	13.43
					104	12.59

Adsorbent	T, K	P, bar	Amount adsorbed mmol g^{-1}	T, K	P, bar	Amount adsorbed mmol g^{-1}
Cu-BTC	297	0.0	0.00	192	0.0	0.00
		1.1	0.10		0.2	0.15
		5.4	0.24		0.4	0.34
		13.4	0.54		0.7	0.47
		25.5	0.90		1.1	0.77
		38	1.54		2.0	1.28
		52	1.94		4.1	2.41
		68	2.27		8.0	3.01
		88	2.64		13.4	3.61
		113	3.16		20.4	4.15
					26	4.54
					37	5.20
					52	6.05
					74	7.11
					105	8.13
Cu-BTC	101	0.0	0.00			
		0.1	3.01			
		0.2	5.12			
		0.4	5.80			
		0.7	7.42			
		1.0	9.68			
		2.0	11.90			
		4.0	13.61			
		8.0	14.53			
		12.9	16.51			
		20.0	16.91			
		25.7	16.99			
		37	16.93			
		52	16.31			
		73	14.94			
		103	13.52			

Adsorbent	T, K	P, bar	Amount adsorbed mmol g^{-1}	T, K	P, bar	Amount adsorbed mmol g^{-1}
Cr-BDC/Li	298	0.0	0.00	189	0.0	0.00
		1.0	0.16		0.6	0.05
		2.0	0.12		1.0	0.19
		4.1	0.16		2.3	0.43
		8.2	0.25		4.2	0.86
		13.5	0.42		8.1	1.54
		19.9	0.58		12.0	2.25
		25.6	0.79		16.4	3.08
		37	1.09		20.6	3.66
		54	1.58		25.6	4.36
		73	2.07		37	5.56
		103	2.79		53	6.78
					75	8.19
					105	9.69
Cr-BDC/Li	138	0.0	0.00	92	0.0	0.00
		0.1	0.10		0.2	2.67
		0.3	0.40		0.5	4.56
		0.5	0.88		0.7	5.54
		1.0	1.52		1.0	6.68
		2.2	2.67		2.1	9.02
		4.0	3.98		3.8	12.38
		8.0	6.01		7.9	16.15
		12.0	7.43		12.2	18.78
		16.2	8.53		16.3	21.05
		19.7	9.18		20.4	22.95
		26	10.25		25.7	25.14
		37	11.69		37	28.16
		52	13.16		52	29.89
		74	14.82		74	30.10
		104	16.33		96	29.58
					103	30.01

Adsorbent	T, K	P, bar	Amount adsorbed mmol g^{-1}	T, K	P, bar	Amount adsorbed mmol g^{-1}
Cu-BTC/Li	296	0.0	0.00	188	0.0	0.00
		1.1	0.04		0.4	0.13
		2.2	0.13		0.7	0.19
		3.8	0.18		1.1	0.27
		8.1	0.39		2.0	0.47
		13.4	0.55		4.0	0.91
		20.0	0.81		8.2	1.83
		25.6	1.05		13.4	2.59
		37	1.42		20.0	3.64
		52	1.91		25.8	4.32
		74	2.43		37	5.34
		104	3.06		52	6.70
					74	8.00
					103	9.00
Cu-BTC/Li	91	0.0	0.00			
		0.1	4.04			
		0.3	7.85			
		0.7	10.22			
		1.0	11.83			
		2.0	14.50			
		4.0	16.95			
		8.2	19.26			
		13.2	20.48			
		20.1	21.21			
		25.1	21.38			
		51	20.87			
		75	19.91			
		103	18.79			
Cr-BDC/1.9 Pd-IGO	297	0.0	0.00	92	0.0	0.00
		2.5	0.18		0.1	0.63
		4.6	0.10		0.4	2.21
		8.5	0.22		1.1	3.23
		12.4	0.29		2.4	6.81
		16.5	0.42		4.2	8.70
		20.3	0.45		7.6	14.27
		25.7	0.66		12.0	16.48
		37	0.93		16.2	17.66
		52	1.30		19.85	18.06
		74	1.72		25.9	19.01
		99	2.27		37	19.90
					52	20.11

Adsorbent	T, K	P, bar	Amount adsorbed mmol g^{-1}	T, K	P, bar	Amount adsorbed mmol g^{-1}
Cr-BDC/4.6 Pd-IGO	297	0.0	0.00	107	0.0	0.00
		1.1	0.04		0.1	1.67
		4.5	0.11		0.3	3.64
		8.3	0.23		1.1	6.67
		13.8	0.34		4.5	12.02
		19.9	0.56		8.8	14.64
		25.6	0.62		13.4	16.39
		37	0.95		20.2	17.55
		52	1.34		25.5	18.41
		74	1.81		37	18.83
		98	2.31		48	18.75
Cr-BDC/6.4 Pd-IGO	296	0.0	0.00	101	0.0	0.00
		4.2	0.02		0.6	4.75
		8.3	0.13		1.1	6.74
		16.3	0.35		4.3	10.70
		25.8	0.60		8.0	15.44
		37	0.90		15.9	18.59
		52	1.23		25.8	20.35
		74	1.71		37	21.03
		103	2.27		51	20.92
Cr-BDC/21 Pd-IGO	297	0.0	0.00	95	0.0	0.00
		1.0	0.23		0.1	2.15
		3.9	0.35		0.3	4.25
		8.0	0.57		0.7	7.03
		13.3	0.83		1.2	9.30
		20.0	0.88		4.3	13.43
		26	1.01		8.3	16.22
		37	1.29		13.4	18.55
		52	1.78		20.2	20.48
		74	2.02		25.2	20.92
		99	2.45		37	21.87
					49	22.38

Adsorbent	T, K	P, bar	Amount adsorbed mmol g^{-1}	T, K	P, bar	Amount adsorbed mmol g^{-1}
Cr-BDC/1.9 Pt-AC	298	0.0	0.00	90	0.0	0.00
		2.1	0.03		0.05	0.15
		4.0	0.09		0.3	0.39
		8.0	0.22		0.9	2.89
		12.1	0.31		2.3	4.68
		16.0	0.39		3.7	8.71
		20.0	0.53		8.0	11.85
		26	0.57		12.3	13.49
		37	0.96		16.0	14.19
		54	1.28		20.4	14.90
		74	1.74		26	15.59
		102	2.25		37	16.43
					51	15.89
					77	15.20
					104	14.69
Cr-BDC/1.4 IGO	296	0.0	0.00	90	0.0	0.00
		1.1	0.10		0.1	1.40
		4.2	0.18		0.6	5.58
		8.1	0.25		1.1	7.14
		16.2	0.46		4.7	10.23
		26	0.68		8.3	13.84
		38	0.94		16.2	16.04
		53	1.22		25.7	17.20
		76	1.70		36	17.79
		100	2.06		48	17.94
Cr-BDC/1.9 Pt-AC/Li	298	0.0	0.00	91	0.0	0.00
		4.0	0.13		0.1	1.70
		8.3	0.24		0.6	5.35
		12.3	0.28		1.0	6.91
		20.1	0.48		3.8	10.95
		26	0.64		8.1	13.97
		37	0.99		15.9	16.69
		51	1.30		25.6	18.41
		74	1.91		37	19.49
		102	2.55		51	19.88

Adsorbent	T, K	P, bar	Amount adsorbed mmol g^{-1}	T, K	P, bar	Amount adsorbed mmol g^{-1}
Cr-BDC/1.9 Pd-IGO/Li	298	0.0	0.00	104	0.0	0.00
		1.0	0.01		0.1	1.13
		4.4	0.16		0.6	5.74
		8.7	0.30		1.1	7.08
		16.1	0.57		4.2	11.48
		25.9	0.94		8.6	15.28
		37	1.26		15.9	17.29
		53	1.86		25.8	18.98
		75	2.70		37	19.87
		100	3.32		49	20.72
Cr-BDC/6.4 Pd-IGO/Li	296	0.0	0.00	96	0.0	0.00
		1.1	0.01		0.1	1.96
		4.5	0.13		0.6	5.27
		8.5	0.26		1.0	7.42
		13.8	0.39		4.4	13.34
		20.0	0.60		8.5	16.54
		25.3	0.77		13.4	18.79
		37	1.10		19.0	20.40
		53	1.52		25.7	21.47
		75	2.07		37	22.72
		97	2.56		49	23.08
Cr-BDC/21 Pd-IGO/Li	295	0.0	0.00	103	0.0	0.00
		1.0	0.03		0.1	2.47
		4.3	0.12		0.3	3.90
		8.3	0.26		1.0	6.05
		12.1	0.36		4.4	13.37
		19.8	0.59		8.2	16.02
		25.8	0.78		13.2	18.27
		35	1.06		19.8	20.22
		52	1.58		25.3	20.68
		73	2.13		35	21.51
		89	2.49		53	21.73

Adsorbent	T, K	P, bar	Amount adsorbed mmol g^{-1}	T, K	P, bar	Amount adsorbed mmol g^{-1}
Cu-BTC/1.2 AC	295	0.0	0.00	91	0.0	0.00
		1.0	0.02		0.05	2.00
		2.0	0.04		0.5	5.08
		4.0	0.09		1.0	6.41
		8.0	0.19		2.3	7.54
		12.0	0.26		4.2	8.39
		16.0	0.31		8.0	9.22
		20.1	0.44		11.8	9.51
		27	0.47		16.2	9.85
		37	0.80		20.6	10.19
		53	0.89		26	9.91
		74	1.31		36	9.96
		100	1.51			
Cu-BTC/1.2 Pt-AC	297	0.0	0.00	91	0.0	0.00
		1.0	0.06		0.1	3.08
		1.9	0.12		0.2	5.34
		4.3	0.22		0.4	7.05
		8.5	0.34		0.7	8.09
		12.7	0.49		1.0	9.30
		16.6	0.61		1.9	10.92
		21.0	0.74		4.2	12.73
		26	0.91		8.0	13.99
		34	1.18		11.7	14.55
		52	1.63		16.2	15.04
		74	2.10		26	15.39
		98	2.69		44	15.25
Cu-BTC/3.3 Pt-AC	296	0.0	0.00	92	0.0	0.00
		2.0	0.10		0.1	2.93
		4.2	0.10		0.4	6.71
		8.0	0.21		0.5	7.96
		12.1	0.33		1.0	9.55
		16.0	0.44		2.2	11.65
		20.2	0.57		4.0	13.11
		25.7	0.71		8.1	14.48
		38	1.10		11.3	14.94
		53	1.42		15.9	15.31
		69	1.71		20.3	15.56
		101	2.20		26	15.63
					35	15.33

Adsorbent	T, K	P, bar	Amount adsorbed mmol g^{-1}	T, K	P, bar	Amount adsorbed mmol g^{-1}
Cu-BTC/7.1 Pt-AC	296	0.0	0.00	90	0.0	0.00
		1.0	0.04		0.02	1.60
		2.1	0.01		0.4	6.50
		4.0	0.11		0.9	8.57
		8.1	0.21		1.5	9.87
		12.2	0.34		2.9	11.34
		16.0	0.45		4.1	12.17
		20.3	0.59		8.2	13.51
		26	0.82		12.15	13.89
		38	1.10		16.3	14.37
		52	1.43		20.1	14.59
		75	1.88		25.9	14.60
		101	2.31		37	14.49
Cu-BTC/11 Pt-AC	297	0.0	0.00	92	0.0	0.00
		1.1	0.02		0.1	0.33
		2.0	0.06		0.3	3.98
		4.3	0.11		1.1	6.98
		8.4	0.22		2.3	8.27
		12.4	0.32		4.0	9.32
		20.1	0.47		7.9	10.22
		25.8	0.36		12.25	10.86
		36	0.77		16.3	10.95
		51	1.00		20.4	11.35
		73	1.32		25.8	11.38
		100	1.62		36	11.26
Cu-BTC/31 Pt-AC	298	0.0	0.00	101	0.0	0.00
		1.4	0.01		0.05	1.33
		2.6	0.04		0.4	3.72
		5.3	0.13		1.05	4.78
		8.9	0.18		2.9	7.06
		13.2	0.24		4.3	7.57
		20.4	0.37		8.1	8.36
		26	0.45		12.0	8.80
		38	0.63		20.1	9.07
		52	0.88		24.9	9.12
		75	1.16		37	9.02
		102	1.41			

Adsorbent	T, K	P, bar	Amount adsorbed mmol g^{-1}	T, K	P, bar	Amount adsorbed mmol g^{-1}
Cu-BTC/3.7 Pd-GO	296	0.0	0.00	90	0.0	0.00
		1.0	0.04		0.03	1.39
		2.1	0.09		0.4	6.44
		4.1	0.20		0.6	7.77
		8.3	0.29		1.1	9.49
		12.2	0.35		1.9	11.07
		16.0	0.44		4.2	12.77
		20.1	0.57		8.1	14.13
		26	0.70		11.8	14.65
		38	0.96		16.1	15.02
		53	1.24		20.2	15.14
		75	1.60		25.7	15.13
		101	1.99		37	14.97
Cu-BTC/3.3 IGO	297	0.0	0.00	97	0.0	0.00
		1.1	0.02		0.1	0.21
		4.3	0.11		0.5	0.69
		8.5	0.22		1.1	8.59
		16.3	0.43		4.0	11.85
		25.6	0.65		8.2	13.14
		38	0.93		15.8	13.88
		53	1.21		25.6	13.98
		75	1.62		37	13.88
		101	1.97			
Cu-BTC/3.7 Pd-IGO	297	0.0	0.00	106	0.0	0.00
		1.1	0.03		0.1	0.36
		2.5	0.08		0.2	4.80
		4.2	0.16		0.8	7.25
		8.4	0.30		1.2	10.47
		12.3	0.35		2.4	12.93
		16.1	0.51		4.3	14.62
		25.8	0.90		8.4	15.71
		37	1.26		12.7	15.92
		55	1.72		15.7	17.38
		75	2.17		20.2	17.35
		102	2.73		25.7	16.82
					37	16.13

Adsorbent	T, K	P, bar	Amount adsorbed mmol g^{-1}	T, K	P, bar	Amount adsorbed mmol g^{-1}
Cu-BTC/8 Pd-IGO	295	0.0	0.00	102	0.0	0.00
		1.0	0.00		0.1	3.12
		4.1	0.13		0.3	6.50
		8.2	0.26		1.1	10.56
		16.0	0.51		4.2	14.65
		25.9	0.78		7.9	16.09
		37	1.10		15.8	18.00
		51	1.47		24.9	18.21
		70	1.78		37	17.97
		104	2.45			
Cu-BTC/10 Pd-IGO	297	0.0	0.00	113	0.0	0.00
		2.1	0.02		0.1	0.18
		4.0	0.07		0.5	1.24
		8.3	0.09		1.1	3.25
		12.2	0.35		2.0	4.63
		20.1	0.61		8.2	9.28
		25.8	0.76		15.9	11.21
		37	1.06		25.4	12.21
		52	1.42		37	12.72
		74	1.92			
		100	2.37			
Cu-BTC/37 Pd-IGO	297	0.0	0.00	91	0.0	0.00
		1.1	0.03		0.05	1.69
		4.0	0.11		0.4	4.45
		8.6	0.26		1.0	6.49
		13.8	0.41		4.5	8.09
		20.5	0.55		8.6	10.50
		26	0.71		13.6	12.35
		37	0.96		20.0	12.97
		53	1.30		27.0	13.37
		76	1.71		37	13.21
		96	2.04			

Adsorbent	T, K	P, bar	Amount adsorbed mmol g^{-1}	T, K	P, bar	Amount adsorbed mmol g^{-1}
Cu-BTC/1.2 Pt-AC/ Li	297	0.0	0.00	92	0.0	0.00
		1.1	0.03		0.03	1.89
		2.0	0.10		0.3	5.57
		4.3	0.19		0.5	8.14
		8.3	0.30		1.1	10.32
		12.2	0.41		2.1	12.58
		16.0	0.56		4.2	14.56
		20.2	0.67		8.2	16.23
		25.7	0.85		12.4	17.07
		37	1.17		16.4	17.47
		53	1.56		26	17.84
		75	2.04		37	17.73
		102	2.53			
Cu-BTC/3.3 Pt-AC/ Li	297	0.0	0.00	100	0.0	0.00
		1.0	0.03		0.05	1.98
		2.2	0.09		0.2	5.26
		4.2	0.13		0.5	7.96
		8.1	0.29		1.0	10.33
		12.0	0.42		2.3	12.64
		16.2	0.54		4.3	14.40
		20.2	0.66		8.3	15.80
		25.9	0.83		12.0	16.75
		37	1.16		16.0	17.09
		52	1.52		19.9	17.14
		75	2.04		26	17.21
		99	2.50		37	16.92
Cu-BTC/7.1 Pt-AC/ Li	297	0.0	0.00	99	0.0	0.00
		1.0	0.01		0.1	4.23
		2.3	0.06		0.4	7.50
		4.3	0.13		1.0	10.49
		8.2	0.29		2.2	12.54
		12.2	0.45		4.5	14.39
		16.0	0.48		8.2	15.61
		20.3	0.58		12.2	16.89
		25.7	0.76		16.3	17.27
		38	1.06		20.1	17.48
		51	1.43		26	17.58
		72	1.89		37	17.28
		103	2.37			

Adsorbent	T, K	P, bar	Amount adsorbed mmol g^{-1}	T, K	P, bar	Amount adsorbed mmol g^{-1}
Cu-BTC/11 Pt-AC/ Li	297	0.0	0.00	99	0.0	0.00
		1.1	0.05		0.2	1.80
		4.4	0.18		0.4	6.83
		8.2	0.30		0.9	9.45
		16.3	0.56		4.3	14.12
		25.6	0.84		7.7	15.45
		37	1.16		16.0	16.73
		52	1.55		25.8	17.10
		75	2.11		37	17.13
		100	2.59			
Cu-BTC/3.7 Pd-GO/Li	297	0.0	0.00	100	0.0	0.00
		1.0	0.06		0.01	0.14
		2.1	0.12		0.4	7.05
		4.2	0.18		0.6	8.41
		8.4	0.34		1.1	10.68
		12.8	0.49		2.0	12.51
		19.4	0.70		4.2	14.61
		25.9	0.91		7.9	16.16
		37	1.24		12.1	17.02
		52	1.62		16.1	17.47
		73	2.11		20.2	17.70
		101	2.64		26	17.79
					37	17.59
Cu-BTC/3.7 Pd-IGO/Li	298	0.0	0.00	97	0.0	0.00
		4.4	0.18		0.1	3.18
		9.1	0.14		0.3	6.33
		16.4	0.40		1.1	10.26
		25.6	0.63		4.3	14.45
		36	1.24		7.5	17.28
		51	1.09		16.2	18.64
		74	1.78		25.5	18.80
		101	2.28		37	18.63
Cu-BTC/8 Pd-IGO/Li	296	0.0	0.00	98	0.0	0.00
		1.1	0.03		0.03	1.78
		4.1	0.16		0.4	6.55
		8.3	0.28		1.0	8.45
		13.5	0.45		4.2	14.43
		20.2	0.64		8.3	15.92
		26	0.80		12.2	16.76
		37	1.04		20.1	17.27
		53	1.42		26	17.41
		75	1.82		37	17.30
		93	2.13			

Adsorbent	T, K	P, bar	Amount adsorbed mmol g^{-1}	T, K	P, bar	Amount adsorbed mmol g^{-1}
Cu-BTC/10 Pd-IGO/Li	296	0.0	0.00	95	0.0	0.00
		1.1	0.03		0.1	0.55
		4.3	0.16		0.3	3.02
		8.1	0.31		1.1	9.96
		13.4	0.49		4.6	11.70
		20.0	0.72		7.6	15.16
		25.9	0.92		13.1	17.10
		37	1.28		19.4	17.70
		53	1.75		26	17.98
		75	2.28		37	17.97
		94	2.65			
MOF-205/2.3 Pt-AC	298	0.0	0.00	93	0.0	0.00
		1.1	0.05		0.1	1.36
		3.6	0.11		0.3	2.41
		9.1	0.24		0.6	3.24
		13.0	0.34		1.1	5.44
		17.1	0.42		2.2	7.74
		20.7	0.50		4.2	10.82
		26	0.64		8.3	13.91
		37	0.78		12.0	15.62
		53	1.21		16.6	17.25
		74	1.57		20.6	18.18
		102	2.10		25.8	18.96
					37	19.99
					52	19.75

Research Publications

International Journals:

1. **Hydrogen Adsorption on Zn-BDC, Cr-BDC, Ni-DABCO and Mg-DOBDC Metal Organic Frameworks.**

Debjyoti Sahu, Prashant Mishra, Satyannarayana Edubilli, Anil Verma, Sasidhar Gumma, J. Chem. Engg. Data, 2013, 58(11), 3096.

2. **The Net Adsorption of Hydrogen on Palladium Nanoparticles.**

Debjyoti Sahu, Prashant Mishra, Nitun Das, Anil Verma, Sasidhar Gumma, Surface Rev. Lett. DOI: 10.1142/S0218625X1450022X

Conference Proceedings:

1. Debjyoti Sahu, Anil Verma, and Sasidhar Gumma, "Hydrogen Storage in Metal Organic Frameworks" *Advancements in Hydrogen Production and Storage I,* **AIChE Annual Meeting 2013, San Francisco, CA USA**.

2. Debjyoti Sahu, Anil Verma, and Sasidhar Gumma, Evaluation of Hydrogen Sorption in Nickel and Palladium Nanoparticle" **COCHIN NANO 2011, Cochin, India.**

3. D. Sahu, A. Verma and S. Gumma, Synthesis of Nickel Nanoparticles using Template Assisted Electrodeposition Technique, **CHEMCON 2010, Chidambaram, India.**